DISSERTATION

zur

Erlangung der Doktorwürde (Dr. rer. nat.)

der

Gesamtfakultät für Mathematik, Ingenieur- und Naturwissenschaften

der

Universität Heidelberg

vorgelegt von

Philipp Mainik

aus Hannover

Tag der mündlichen Prüfung

17.10.2025

DISSERTATION

3D/4D microprinting of biomaterials

Gutachter

Prof. Dr. Eva Blasco

Prof. Dr. Franziska Thomas

„'Don't be an idiot.' Changed my life."

Dwight Schrute, The Office

ACKNOWLEDGEMENTS

Before diving into the scientific part of this thesis, I want to take the time and thank my family, friends, and all the teachers, supervisors, and mentors who have made this scientific journey possible. It is your contribution in shaping and supporting me in various important aspects in life.

Dear Eva! I am very grateful for having started my scientific journey at your side. I still remember the first meeting and the beginning of my master's thesis. Since then, your continuous patience, trust, support, and guidance have offered me the space to make mistakes, learn, and grow up. The possibility to dive into the topics of light-based 3D/4D printing and polymeric materials has allowed me to evolve from my background in (polymer) chemistry to discover the beauty of material science. Additionally, you have shown me how to communicate scientifically and how to handle difficult situations. All your offered opportunities to being involved have allowed me to see and learn a lot about science and people – including myself. I have not forgotten your advice the day when I started my PhD journey. Thank you for being a fantastic supervisor and mentor who always takes the time when needed!

Christoph! You started as a mentor and quickly became a close friend. I want to thank you for training me on the devices, especially the Nanoscribe, and for showing me all the procedures in detail. Although some of them could be shortened easily by 45 minutes to avoid seizures, I adopted and used many of these small routines and procedures. Your positive influence in the role of a senior PhD candidate and later postdoctoral researcher in these years was important. You always took the time and opportunity to listen and support me in my ideas – some of which I must admit seemed sometimes crazy. You allowed me to find my way without pushing me in a certain direction. Thank you for taking care of so many things and being there for me!

Arriving at our shared office 03.101 has brought a huge smile to my face even on my early travelling Monday mornings. Sharing this time with you – Fabian, Finn, and Christoph – showed me how important fantastic colleagues and a comfortable atmosphere are, especially in times with long to-do lists. Our mixture of shared humor, relaxed attitude, as well as

seriousness where necessary has made my life easy in so many ways. Thank you for making this time so easy! Es war mir ein Fest.

Niklas. Knowing that a great colleague and former fellow student started exploring biomaterials too, makes life easier. Thank you for your support and our conversations!

Johannes and Lilli. Seeing both of you thrive makes me very happy because it reminds me of how I started as a master's and continued as a PhD. Being able to share my experience as a senior PhD reminds me that this system is running in circles and how important it is to ensure that it keeps going. I hope I will have an impact on you like the one which I have received. Keep going and you will shine! Hola hombre, Johannes. It is a pleasure seeing you discover the field of polymer chemistry and material science. You have evolved fast and learned a lot. Your topic has started differently, but that is how the most exciting and not explored scientific discoveries and connections are made. I cannot find enough words to thank Eva and you for being able to take and learn in this role!

Li-Yun, Marcus, Britta, Samantha, and Clara. You have accompanied me for a long time starting from my master's thesis to my PhD. Thank you as well as the whole Blasco group for the numerous events, activities, and experiences that we have shared!

Moreover, I want to thank all my collaborators and colleagues in and outside of the "3D matter made to order" Cluster. Interdisciplinary research is nearly impossible to do without a great team and continuous scientific exchange. Here, I want to thank especially Cassian, Magdalena, Camilo, Jonathan, Alberto, Ronald, Irene, Dominik, Götz, Prof. Gräter, Prof. Tanaka, Prof. Bastmeyer, Prof. Wittbrodt, Prof. Schröder, Prof. Steeb, and Prof. Wegener. It was a pleasure working with you!

The last 10 years have not been the way without the support of my family and friends. I am grateful for having you in my life. You let me remember about the world outside of research. This includes the friends I made during my studies such as Konrad and Ilya, but also the friends who followed me during this period. Here, I want to thank the friends who have seen me growing up: Viktor, Dimi, and my friends from school in Frankfurt. Thank you, Moritz, Konsti, Leo, Max, Lucas, Daniel, Louis und Chrisi for our unique group. It is amazing to see who we have become. I am looking forward to the next chapters of our lives!

Спасибо моей семье за ценности, которым я научился и которые принял в детстве и юности. Без вашего мужества и решения переехать в Германию я бы не испытал всего этого. Спасибо, папа и мама, за то, что вы сделали всё это возможным для меня. Не сдаваться при первых же трудностях и решать проблемы с помощью трудолюбия и терпения - этому я научился у вас. Спасибо, что вы меня этому научили. Спасибо тебе, Лина, за то, что я всегда могу на тебя положиться. Спасибо, дедушка, за время, проведённое вместе за математикой во Франкфурте, прежде чем я поддался юношескому порыву и увлёкся химией. И спасибо тебе, бабушка, за твою поддержку! Я до сих пор хорошо помню, как делился с тобой своим интересом к химии материалов. Я вас всех люблю, целую и обнимаю.

Sonya. Ich bin unendlich dankbar dafür, so einen verständnisvollen, ehrlichen und liebevollen Sonnenschein wie dich an meiner Seite zu wissen. Danke, mein Schatz!

ABSTRACT

In the last few decades, 3D printing has emerged as a preferred alternative to conventional polymer manufacturing. This transformation has been driven by new key technologies for manufacturing as well as by the development of new materials for these arising technologies. Among those technologies, light-based 3D printing particularly stands out due to its capability to produce 3D objects fast and precisely. The rising interest and demand for new materials, *i.e.* photocurable inks, for specifically designed applications are driving forces for innovations in this field. This thesis focusses especially on the design of new biomaterial inks for 3D laser printing at the microscale and expanding their application in *in vivo* microprinting. The presented new biomaterials cover synthetic as well as natural-based systems and focus on implementing new material properties and functionalities. In detail, this includes the expansion of printable synthetic materials to very soft synthetic materials by introducing a new ink design for multiphoton 3D laser printing based on supramolecular interactions. This new synthetic ink design allows for 3D printing of very soft materials which are highly desired in bioapplications. In addition to addressing current limitations of synthetic biomaterial ink, a natural-based biomaterial ink based on collagen is presented. The microprinted collagen hydrogels exhibited cell-adhesive properties and were composed of a highly porous collagen network. After characterizing the static material properties, the printed collagen was studied for its temperature-responsive folding motif. The fully reversible shrinkage and recovery of printed collagen upon heating and cooling was attributed to the folding and unfolding of the collagen binding motif – experimentally as well as theoretically. The new responsive mechanism based on polypeptide folding or unfolding opens new opportunities to equip and use natural-based biomaterials with stimuli-responsive properties. Moving toward application, this thesis also covers the implementation of biomaterials in *in vivo* microprinting. For this purpose, a suitable synthetic biomaterial ink is chosen to meet several important criteria for multi-photon 3D laser printing directly in developing organisms of medaka fish and fruit flies. In this collaborative study, the effect of the ink microinjection, multiphoton 3D laser printing process, and printed material on the development of the organisms is studied and evaluated. The presented framework opens new opportunities for *in vivo* microfabrication paving the way towards printed microimplants and drug delivery devices.

ZUSAMMENFASSUNG

In den letzten Jahrzehnten hat sich der 3D-Druck als Alternative zur herkömmlichen Polymerprozessierung etabliert. Diese Transformation wurde zum einen durch neue 3D-Drucktechniken sowie durch die Verfügbarkeit neuer Materialien vorangetrieben. Unter diesen Technologien sticht insbesondere der lichtbasierte 3D-Druck hervor, da er die schnelle und präzise Herstellung von 3D-Objekten ermöglicht. Das steigende Interesse an neuen lichthärtende Tinten und Materialien ist die treibende Kraft für Innovationen in diesem Bereich. In dieser Arbeit werden neue Biomaterial-Tinten für den 3D-Laserdruck im Mikromaßstab vorgestellt und neue Anwendungen dieser Biomaterial-Tinten im Mikrodruck in lebenden Organismen untersucht. Die neuen vorgestellten Biomaterial-Tinten umfassen sowohl synthetische als auch natur-basierte Systeme und konzentrieren sich auf die Implementierung neuer Materialeigenschaften und Funktionalitäten. Im Einzelnen umfasst dies die Erweiterung der druckbaren synthetischen Materialien auf sehr weiche synthetische Materialien, die in Bioanwendungen sehr gefragt sind. Dies gelingt durch die Einführung eines neuen Tintenkonzepts für den Multiphotonen-3D-Laserdruck durch die Nutzung supramolekularer Wechselwirkungen. Zusätzlich zur Überwindung der derzeitigen Einschränkungen synthetischer Biomaterialtinten wird eine natur-basierte Kollagentinte vorgestellt. Die gedruckten, hochporösen Kollagenhydrogele weisen zelladhäsive Eigenschaften auf. Darüberhinaus wird das gedruckte Kollagen hinsichtlich seines temperatursensitiven Proteinfaltungsmotivs untersucht. Erhitzen und Abkühlen führt jeweils zu einer vollständig reversiblen Schrumpfung und Anschwellen des gedruckten Kollagens, das sowohl experimentell als auch theoretisch auf das Falten und Entfalten des Kollagenbindungsmotivs zurückgeführt wird. Dieser neue auf Proteinfaltung basierende Mechanismus eröffnet neue Möglichkeiten, Proteine als responsive Materialien nutzen zu können. In dieser Arbeit wird zudem der 3D-Mikrodruck von Biomaterial-Tinten in entwickelnden Organismen gezeigt. Zu diesem Zweck wird eine Tinte vorgestellt, die mehrere wichtige Kriterien für den Multiphotonen-3D-Laserdruck direkt in sich entwickelnden Organismen von Medaka-Fischen und Fruchtfliegen erfüllt. In dieser gemeinsamen Studie wird die Wirkung der Injektion, des 3D-Laserdruckverfahrens und des gedruckten Materials auf die Entwicklung der Organismen untersucht und bewertet. Der vorgestellte Rahmen eröffnet neue Möglichkeiten für die In-vivo-Mikrofabrikation und ebnet den Weg für gedruckte Implantate und neue Möglickeiten zur Medikamentenverabreichung.

ABBREVIATIONS

%	percent
°C	degree Celsius
2D	two-dimensional
3D	three-dimensional
4D	four-dimensional
Å	Ångstrom
AAc	acrylic acid
AAm	acrylamide
AcOH	acetic acid
BAPO	2-hydroxy-4'-(2-hydroxyethoxy)-2-methylpropiophenone
BDEABP	4,4'-bis(diethylamino)benzophenone
CAD	computer aided design
CD	circular dichroism
CDIC	circular differential interference contrast
CLIP	continuous liquid interface production
cm	centimeter
cm^{-1}	wavenumber
ColMA	collagen methacrylamide
cryo-EM	cryo-electron microscopy
DEI	deep eutectic ink
DES	deep eutectic system
DLP	digital light processing
DMAAm	*N*,*N*-dimethylacrylamide
DMD	digital mirror device
D_p	penetration depth
e	Euler number
$\vec{E}$	electric field
E_c	critical exposure energy
ECM	extracellular matrix
EDTA	ethylenediaminetetraacetic acid

FDM	fused deposition modeling
GelMA	gelatin methacryloyl
h	Planck constant
h	hour
HEA	2-hydroxyethyl acrylate
IR	infrared
Irgacure2959	4'-(2-hydroxyethoxy)-2-methylpropiophenone
ITX	4-(propan-2-yl)-9H-thioxanthen-9-one
Ivocerin	bis(4-methoxybenzoyl)diethylgermanium
J	Joule
keV	kilo electronvolt
kPa	kilopascal
LAP	lithium phenyl-2,4,6-trimethylbenzoylphosphinate
LED	light emitting diode
M	mol per liter
M	molecular weight
mdeg	millidegree
mg	milligram
MHz	megahertz
mL	milliliter
mm	millimeter
MPa	megapascal
MPL	multiphoton lithography
MPLP	multiphoton 3D laser printing
mW	milliwatt
N	Newton
NIPAAm	*N*-isopropyl acrylamide
NIR	near infrared
nm	nanometer
NMR	nuclear magnetic resonance
P	polarization
PC	polycarbonate

P_{CL}	crosslinking probability
PDES	polymerizable deep eutectic solvent
PDMS	poly(dimethylsiloxane)
PEGDA	poly(ethylene glycol) diacrylate
PLA	polylactic acid
ppm	parts per million
REF	rat embryonic fibroblast
RGD	arginine-glycine-aspartic acid
RhodBMA	rhodamine B methacrylate
S	singlet state
s	second
SEM	scanning electron microscopy
SLA	stereolithography
SV	volume swelling factor
T	triplet state
T	Temperature
TEM	transmission electron microscopy
TGA	thermogravimetric analysis
$T_{n\text{-}i}$	nematic to isotropic phase transition temperature
TPLP	two-photon 3D laser printing
UV	ultraviolet
V	volume
vis	visible
wt	weight
α	alpha
λ	wavelength
µL	microliter
µm	micrometer
ν	frequency
$\chi^{(n)}$	susceptibility of order n

TABLE OF CONTENTS

LIST OF PUBLICATIONS & CONFERENCE CONTRIBUTIONS

The results of this thesis have been published and presented at conferences. Shared first co-authorships are indicated with a mark († - equal contribution).

Peer-reviewed journal articles presented in this thesis:

1. **Philipp Mainik**, Christoph A. Spiegel, Jonathan L. G. Schneider, Martin Wegener, and Eva Blasco. "Deep Eutectic Inks for Multiphoton 3D Laser Microprinting." *Adv. Mater.* (**2025**): 2507640.

2. **Philipp Mainik**, Camilo Aponte-Santamaría, Magdalena Fladung, Ronald Ernest Curticean, Irene Wacker, Götz Hofhaus, Martin Bastmeyer, Rasmus R. Schröder, Frauke Gräter, and Eva Blasco. "Responsive 3D printed microstructures based on collagen folding and unfolding." *Small* 21.3 (**2024**): 2408597.

3. Cassian Afting†, **Philipp Mainik**†, Clara Vazquez-Martel, Tobias Abele, Verena Kaul, Girish Kale, Kerstin Goepfrich, Steffen Lemke, Eva Blasco, and Joachim Wittbrodt. "Minimal-invasive 3D laser printing of microimplants in organismo." *Adv. Sci.* (**2024**): 2401110.

Other peer-reviewed journal articles and contributions:

4. Alberto Concellón, **Philipp Mainik**, Clara Vazquez-Martel, Cristina Álvarez-Solana, and Eva Blasco. "4D Printing of Liquid Crystal Emulsions for Smart Structures with Multiple Functionalities." *Angew. Chem.* 64.10 (**2025**): e20242116.

5. **Philipp Mainik**†, Christoph A. Spiegel†, and Eva Blasco. "Recent Advances in Multi-Photon 3D Laser Printing: Active Materials and Applications." *Adv. Mater.* 36.11 (**2023**): 2310100.

6. **Philipp Mainik**, Li-Yun Hsu, Claudius W Zimmer, Dominik Fauser, Holger Steeb, and Eva Blasco. "DLP 4D Printing of Multi-Responsive Bilayered Structures." *Adv. Mater. Technol.* 8.23 (**2023**): 2300727.

7. Raquel Royo, **Philipp Mainik**, Carlos Benitez-Martin, Raquel Andreu, Eva Blasco, Francisco Najera, and Belén Villacampa. "Highly Efficient Photoninitiators Based on 4H-

Pyranylidene Derivatives for Two-Photon Laser Printing." *Adv. Mater. Technol.* 8.23 (**2023**): 2300571.

8. Li-Yun Hsu, **Philipp Mainik**, Alexander Münchinger, Sebastian Lindenthal, Tobias Spratte, Alexander Welle, Jana Zaumseil, Christine Selhuber-Unkel, Martin Wegener, and Eva Blasco. "A Facile Approach for 4D Microprinting of Multi-Photoresponsive Actuators." *Adv. Mater. Technol.* 8.1 (**2023**): 2200801.

9. Clara Vazquez-Martel, **Philipp Mainik**, and Eva Blasco. "Natural and Naturally Derived Photoinitiating Systems for Light-Based 3D Printing." *Organic Materials* 4.04 (**2022**): 281.

Filed patent application together with Heidelberg University:

1. **Philipp Mainik**, Christoph Alexander Spiegel, Eva Blasco Pomar. Deep Eutectic Inks for Multiphoton 3D Laser Microprinting. EP25151765. Filing date: **14.01.2025.**

Conference contributions:

1. **Philipp Mainik**, Li-Yun Hsu, Claudius W Zimmer, Dominik Fauser, Holger Steeb, and Eva Blasco. "DLP 4D Printing of Multi-Responsive Bilayered Structures.", French, Swiss and German Conference on Photochemistry, Photophysics and Photosciences CP2P'23, Conference, Mulhouse, France, **May 2023**, poster presentation.

2. **Philipp Mainik**, Cassian Afting, Clara Vazquez-Martel, Tobias Abele, Verena Kaul, Girish Kale, Kerstin Goepfrich, Steffen Lemke, Joachim Wittbrodt, and Eva Blasco. "Minimal-invasive 3D laser printing of microimplants in organismo.", Towards Holistic Understanding of Life, Winter School 2024, Kyoto, Japan, **February 2024**, poster presentation with flash talk. Contribution was awarded with poster prize.

3. **Philipp Mainik**, Eva Blasco. "3D printing of biomaterials.", Future 3D Additive Manufacturing – The 3DMM2O Conference 2024, Conference, Kloster Schöntal, Germany, **April 2024**, poster presentation with flash talk.

4. **Philipp Mainik**, Camilo Aponte-Santamaría, Magdalena Fladung, Ronald Ernest Curticean, Irene Wacker, Götz Hofhaus, Martin Bastmeyer, Rasmus R. Schröder, Frauke Gräter, and Eva Blasco. "Responsive 3D printed collagen microstructures.",

Makromolekulares Kolloquium – MAKRO 2025, Conference, Freiburg, Germany, **February 2025**, poster presentation with flash talk.

5. **Philipp Mainik**, Eva Blasco. “3D/4D microprinting of biomaterials.”, EPF European Polymer Congress 2025, Conference, Groningen, Netherlands, **June 2025**, poster presentation with flash talk.

I. Introduction & Outline

Polymers have become an important class of material which can be found in various aspects of our daily life, ranging from construction, coatings, (food) packaging, and coatings, to contact lenses, drug delivery, wound dressings, and hygiene products. The numerous applications rely on the chemical and structural tunability of polymers offering a range of achievable properties. Main chemical properties of a polymer are attributed to the monomer composition and types of repeating units. The architecture of polymers is tuned by varying the polymer length, sequence of various employed monomers, shape of the polymer, and by adding crosslinks between polymer chains. The combination of employed monomers together with the architecture of the polymer gives access to a variety of material functionalities, making them a tunable and versatile class of materials for the plethora of daily life products.

Despite being omnipresent in daily life products, polymer research is currently progressing rapidly due to ecological, economical, and social demand for more sustainable solutions as well as for more specialized and personalized applications. Major current topics include the development of sustainable and closed-loop recyclable (bio)polymers, new synthesis methods for precise architecture-defined polymers, and the implementation of advanced properties and functions. In addition to these large overarching topics, current progress is also driven by new and easily accessible manufacturing technologies. 3D (three-dimensional) printing, also known as additive manufacturing, plays a crucial role in this context since it allows the manufacturing of material (precursors) into desirable 3D geometries from a digital model. This process is achieved by fabricating the structure with the help of volumetrically controlled polymer deposition either by starting from a molten polymer or single monomers. In this context, light-based techniques such as digital light processing or multiphoton 3D laser printing are excellent manufacturing techniques offering lateral resolution down to dozens of micrometers or even in the nanometer range. Both methods rely on the *in-situ* spatially controlled polymerization of monomer precursor mixtures leading to the polymer deposition during fabrication. In addition to the fabrication of static 3D structures, light-based 3D printing is also an excellent tool for advancing applications with additional material functionalities for functional soft robotics, optics & photonics, microfluidics, and

biomedicine. These advanced applications are enabled by 3D printed structures which offer various stimuli-responsive features. Depending on the printed responsive material, different stimuli-responsive features can be achieved leading to desired structural or functional property changes upon exposure to physical or chemical stimuli such as temperature, light, or pH. The combination of this additional control of material properties in another dimension, *i.e.* time, with 3D printed structures is often referred to as 4D (four-dimensional) printing.

Based on these perspectives, the aim of this thesis was to design new biomaterials for light-based 3D/4D printing at the microscale and explore the possibility of combining printed biomaterials in new advanced applications. For this purpose, the different main projects were split into different objectives dealing with topics such as 3D microprinting, responsive behavior, and biocompatibility. In these presented interdisciplinary projects, the 3D and 4D printed biomaterials have been studied by mechanical characterization, *in-vivo* or single cell biocompatibility assays, theoretical simulation, and advanced electron microscopy imaging techniques.

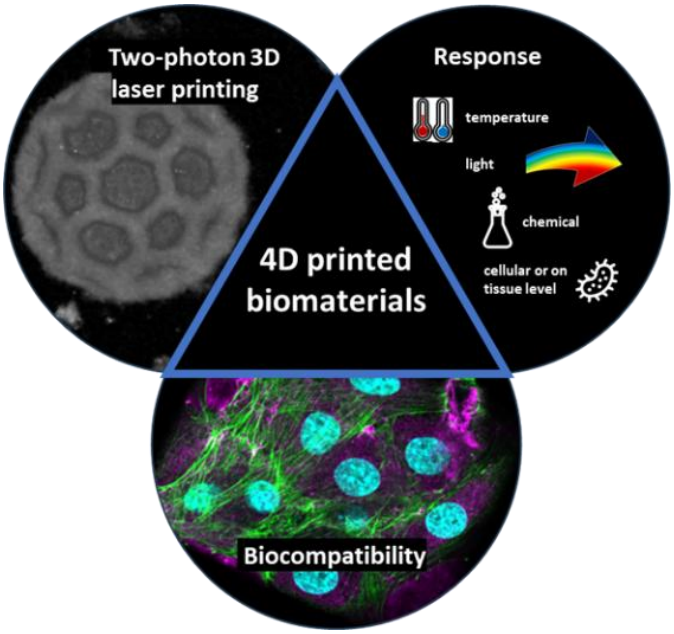

Figure 1: Overview of three key aspects for all three PhD projects on 3D/4D printing of biomaterials.

This thesis covers the theoretical background, scientific results, and conclusion in five chapters. After this introduction and outline section, *Chapter 2* introduces the theoretical concepts and techniques to provide the reader with the background on 3D/4D printing of biomaterials. This includes a description of the available additive manufacturing techniques,

employed photochemistry, previously reported biomaterials, and stimuli-responsive materials for 4D microprinting. *Chapter 3* deals with the scientific results obtained for different explored biomaterials and their applications. This chapter is separated by the followed research directions with varying topics from overcoming manufacturing paradigms, design of new biomaterials, to advancing new biomedical applications. *Chapter 4* provides a summary and discussion of the results based on the scientific findings. Finally, *Chapter 5* offers a reflection on future perspectives of this research direction.

II. Theoretical Background

The rise of today's polymer chemistry has started with the description of high molecular weight compounds by Hermann Staudinger, around 100 years ago. [1] More than a century later, an entire interdisciplinary field of research had evolved around *macromolecules* dealing with varying different monomer compositions, architectures, physical behaviors, manufacturing techniques, and applications. [2,3] To narrow down the large topic of polymer chemistry, this section deals first with processing and manufacturing polymeric materials. After introducing additive manufacturing and essential technical aspects, current state-of-the-art photopolymerization for vat photopolymerization is presented. Last, the variety of accessible functional (bio)materials is introduced – focusing on materials which have been prepared using multiphoton 3D laser printing (MPLP).

1. POLYMER PROCESSING & MANUFACTURING

Polymers are omnipresent in our daily life for various applications ranging from construction materials for damping or sealing to consumer products like packaging, plastic bottles, or clothes. [3,4] All these applications heavily rely on the processing of bulk polymeric materials. Polymer processing is a crucial step, because it defines various macro- and microscopic properties, thus mechanical properties, material porosity, and applicability. [5,6] Most employed industrial processing steps are polymer extrusion, injection molding, and extrusion blow molding. [5] All these industrial processing steps are usually performed by liquefying synthesized polymers. This step is possible for polymeric materials consisting of single linear or branched not-crosslinked polymer chains, because the comparably weak interchain interactions can very often be overcome at high temperatures leading to macroscopic material creeping. [7] These polymeric materials are therefore called *thermoplasts*.

Covalent crosslinking between the different chains improves the mechanical stability of the bulk polymeric materials but constrains the movement of the chains at high temperatures. Polymer networks cannot show material creeping like thermoplasts and are also often called *thermosets*. [2] For thermosets, which are generally not meltable, injection molding is usually

performed with a liquid pre-polymer or monomer solution which is crosslinked in the mold by heating or irradiation. [5,8]

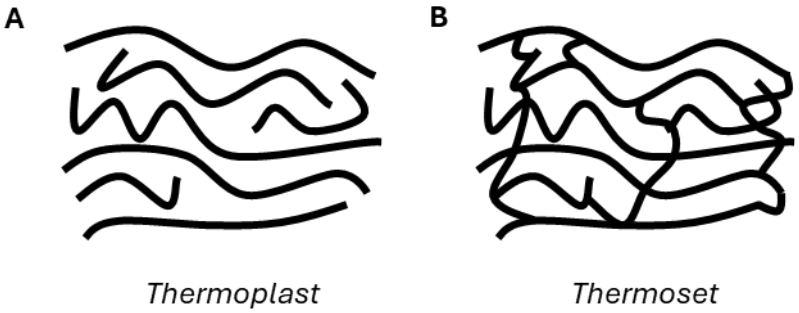

Figure 2: Thermoplast and thermoset bulk polymeric materials.

Although proven to be applicable for large scale bulk polymer manufacturing, these processing methods highly rely on a specific structure to be repeated and do not allow fine-tuning of geometrical parameters in a simple and specified manner. [9] Moreover, these large-scale manufacturing set-ups are very often bound to a specific location which requires sending these manufactured components. Although being cheap on a large scale, rapid prototyping and manufacturing-on-demand is currently addressed by new technological progress. [9]

To overcome existing limitations on slow prototyping and manufacturing-on-demand, new material processing technologies have been developed in the last decades. [10] By using 3D printing, also known as additive manufacturing, bulk materials are manufactured in a stepwise manner by adding separate material parts during processing. Today, many methods for additive manufacturing are already well-established or in their early promising stages for broad application. [10] All methods have the same initial starting point prior to manufacturing: the design of a suitable 3D model. The versatility of accessible 3D structures as well as the fast implementation of changes make 3D printing superior for rapid prototyping and manufacturing-on-demand compared to traditional polymer processing. After its creation, the created 3D model is used for the preparation of the printing file by the desired 3D printer. In this step, the desired additive manufacturing method and its manufacturing process, *i.e.* layer-by-layer, line-by-line, or volumetric, pre-defines the subsequent 3D printing execution protocol. [10] In general, the different additive manufacturing techniques are distinguished based on the employed setup into seven different categories:

1. **Material extrusion:** This method utilizes a nozzle which is used to selectively dispense material on the substrate or already printed structures. The material can be, for example, a thermoplastic polymer which melts in the nozzle such as polylactic acid (PLA) or polycarbonate (PC) using fused deposition modeling (FDM). In addition to these very frequently applied materials, 3D dispersible hydrogel or photoresist liquids can be used and cured during the nozzle extrusion by parallel irradiation. [10]
2. **Material jetting:** These additive manufacturing methods utilize droplets which are selectively deposited using a nozzle such as in inkjet printing. Inkjet printing is a common technique for commercial paper printers but has also been established for the selective deposition of conductive or dielectric inks onto (flexible) substrates for printed electronics. [10]
3. **Binder jetting:** Binder jetting uses selective deposition of a binder onto substrates which is afterwards used for binding and fusing layers of solid powders. This method is especially interesting for binding layers of ceramic materials. [10]
4. **Sheet lamination:** This additive manufacturing process is performed by directly bonding separate layers directly onto each other. [10]
5. **Directed energy deposition:** Directed energy deposition is used to deposit and melt/fuse materials at the same time. This is achieved by depositing the material precursor with nozzle(s) while a laser or electron beam provides thermal energy. [10]
6. **Powder bed fusion:** In powder bed fusion, thermal annealing of a powdered precursor bed is performed in a spatially controlled fashion by using thermal energy of a laser or electron beam. Methods such as (selective) laser sintering are especially interesting for the fabrication of metals, but it can also be employed for polymers. [10]
7. **Vat photopolymerization:** Vat photopolymerization is performed by spatially controlled photopolymerization of liquid (pre-polymer) ink. This can be achieved by employing different light sources and irradiation setups. This method includes MPLP and digital light processing (DLP) 3D printing. [10]

All additive manufacturing methods show similarities but also vary in terms of printing setups and more importantly applicability for different materials. In the following section, the different accessible printing processing and requirements are discussed for vat photopolymerization in detail.

2. LIGHT-BASED 3D PRINTING

Vat photopolymerization is the additive manufacturing method of choice for creating 3D structures from monomers or pre-polymers using light. [10] Light offers an excellent source of energy because it can be focused on mirrors or objectives in a volumetrically controlled manner either by using light emitting diodes or (femtosecond-pulsed) lasers. [11]

In fact, vat photopolymerization methods originally developed as stand-alone 3D fabrication techniques but have similarities and conceptual origins in 2D (two-dimensional) photolithography. In photolithography, the substrate is first covered with a thin film of photosensitive ink, *i.e. photoresist*, which is subsequently irradiated with spatial resolution using a photomask. [12] Depending on the employed ink, irradiation can enable either photodegradation or photocrosslinking of the material in the irradiated regions. In positive photoresists, exposure to ultraviolet (UV) light induces a change in polymer structure making it soluble in the subsequent washing step. [12] In contrast to that, the exposed area in negative photoresists is photocrosslinked with UV light and remains on the substrate in the washing step. Thus, employing the photomask and irradiation with UV light enables the highly precise generation of thin polymer film structures. [12]

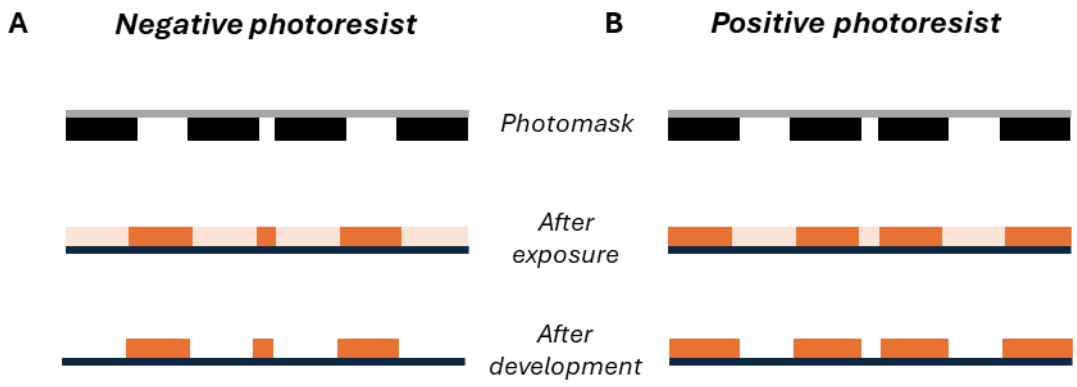

Figure 3: Photoresists in 2D photolithography. A) Irradiated regions of negative photoresists become insoluble. B) Irradiated regions of positive photoresists become soluble for the development.

Transferring the concept of 2D photolithography to 3D vat photopolymerization techniques is typically achieved by employing negative photoresists. [10] Before dealing with ink design on the molecular level, the different available setups for vat photopolymerization are briefly discussed in the following sections.

2.1 STEREOLITHOGRAPHY

Stereolithography (SLA) printing is the oldest 3D printing technology and typically offers the fabrication of hundreds of micrometers to dozens of centimeters scaled structures. [10] It was developed in the 1980s, thus building the foundation for commercial light-based 3D printing technologies in the last decades. [13] In the first setups for SLA, a UV laser was focused on a photopolymerizable ink which was placed in a vat with a movable platform. In this step, the suitable laser light excites the photoinitiator or photosensitizer in a one-photon absorption process to an excited state. The subsequently forming species are able to induce the desired polymerization reaction. [10]

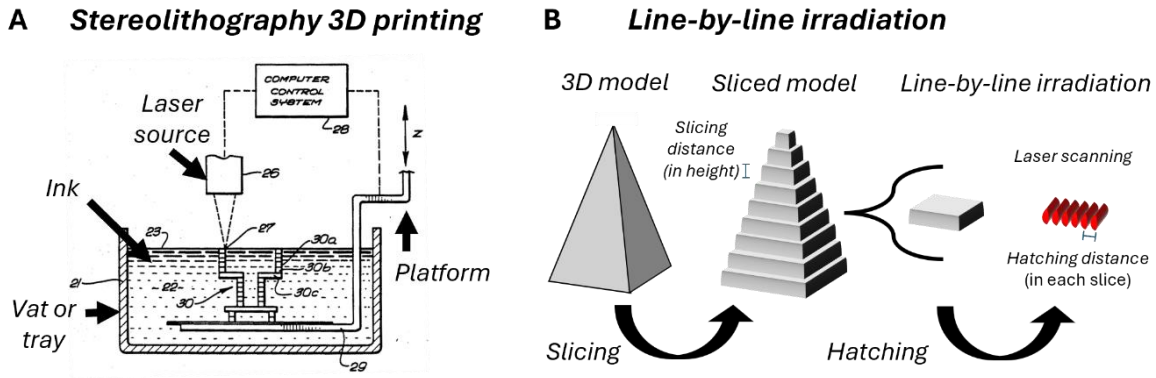

Figure 4: Stereolithography. A) Original drawing of the stereolithographic 3D printing setup proposed by Hull in 1986. [13] B) Printing process of line-by-line irradiation.

Selective photopolymerization is achieved by moving the laser focus on top of the solution in a line-by-line (x, y) manner. After finishing with the first layer, the platform is mechanically lowered allowing the selective photopolymerization of the adjacent layer (z). With this line-by-line (hatching in x,y) and layer-by-layer (slicing in z) separation of the desired computer aided design (CAD) model, the final desired 3D solid object is photopolymerized with volumetric control. [10] SLA offers a high spatial resolution which can be further tuned by changing the spot size of the focused laser beam. [14] Moving the laser line-by-line together with the curing time of the single layers makes this process quite time-consuming for larger scaled structures. For this reason, the initial SLA setup was improved over time. [10] One of them was the implementation of a projection approach instead of a scanning approach. [15] This new printing process is called digital light processing 3D printing.

2.2 DIGITAL LIGHT PROCESSING 3D PRINTING

Compared to earlier SLA, several changes were implemented in DLP 3D printing to improve the printing process and increase the accessibility of the setup. [10] First, the irradiation setup in DLP was inverted to reduce the amount of necessary printable ink in the vat. Second, the laser source was replaced by a light emitting diode (LED). This replacement included the use of an array of digital mirrors, *i.e. digital mirror device* (DMD), instead of the previously employed galvano-mirrors for moving the laser in *xy*. [10] In DLP, the DMD is located and oriented in a way that incident light can be either reflected into the ink or not. By switching the single individual mirrors in the DMD, a pixelated irradiation pattern is obtained yielding parallel photopolymerization in one layer. This parallelization without the need for single line movement and reduced waiting times increase the printing speed. [10]

The printing process is performed by moving the platform in the ink-containing vat and irradiate the desired pattern for the single slice. Afterwards, the platform is moved upwards by the slicing distance and the next layer is irradiated. The final 3D printed structure is carefully removed from the platform and typically thoroughly washed with solvent to remove residues of uncured ink. This step is called *development* and can furthermore include additional post-curing with UV light to improve mechanical material properties. [16]

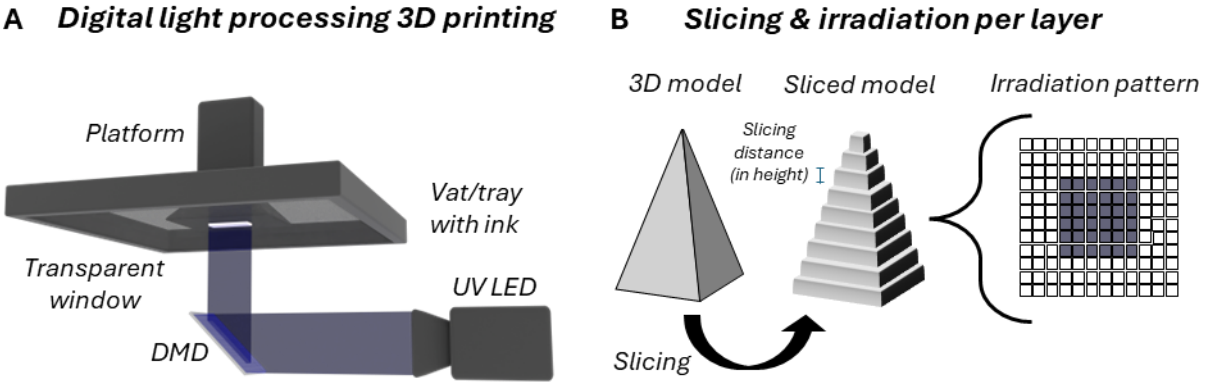

Figure 5: Digital light processing. A) Printing set-up with the digital mirror device (DMD) which can be navigated independently to irradiate or not irradiate the ink in a spatially controlled way using an ultra-violet light emitting diode (UV LED). B) Printing process of layer-by-layer irradiation.

Prior to starting the 3D printing process, a printing file containing all necessary mechanical and irradiation parameters needs to be prepared. This file includes information about the 3D model such as slicing thickness (*z*) and the irradiation patterns (*xy*), parameters about the movement of the platform, as well as the irradiation intensity and irradiation times per slice.

The printing parameters such as irradiation intensity and irradiation time per slice need to be determined experimentally beforehand. [16] In DLP 3D printing these are related to the *curing behavior* of the ink. The curing behavior describes the photopolymerization behavior of the ink for varying irradiation conditions. Two important parameters are used to quantify the amount of irradiation energy for achieving a certain layer thickness: the critical exposure energy E_c and penetration depth D_p. [17,18] Both parameters are determined by recording an *energy-cure depth curve* which is also called *Jacob's working curve*. [19]

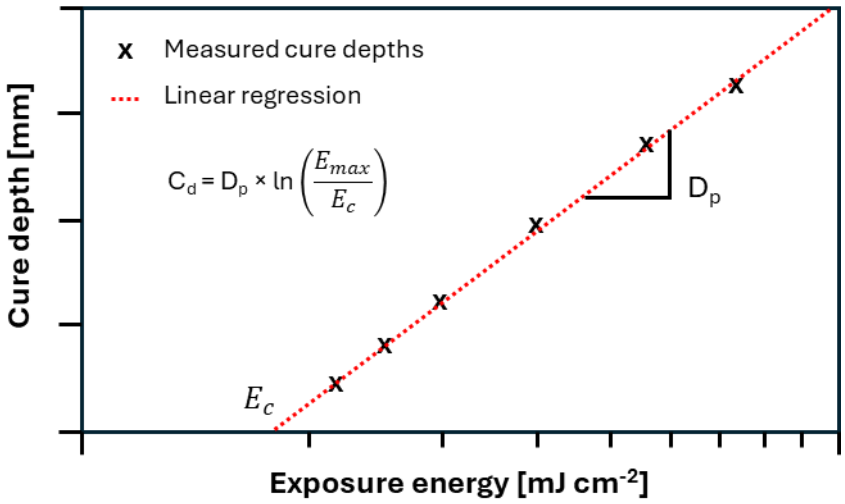

Figure 6: Jacob's working curve for the calculation of the critical exposure energy E_c and penetration depth D_p. Prior to performing the linear regression, the measured cure depths are plotted against the set exposure energies on a logarithmic scale. [17–19]

For this purpose, different irradiation energy exposures are applied onto ink droplets, and after removing unpolymerized ink, the obtained photopolymerized spots are measured for their thickness. This procedure yields varying cure depths as a function of the exposure energy. Usually, the exposure energy is varied by changing the irradiation times. The energy can then be calculated by multiplying the irradiation times with the constant (lamp) irradiation intensity.

Due to the description of light-based absorption processes by the Lambert-Beer law, linear regression of the measured curve in logarithmic representation of the exposure energy is performed. [17,18] The linear regression yields the two important parameters E_c and D_p. The crititcal energy E_c provides a measure of exposure energy which is necessary to yield gelation of the ink. The penetration depth D_p describes the slope with which the spot thickness increases with increasing exposure energy. [17,18] It furthermore equals the D_p the penetration depth of ink which reduces the irradiation energy to e^{-1} (≈ 37 %) of the surface irradiation

energy. [19] Both quantitative parameters are important for understanding the curing behavior of an ink and its potential in DLP 3D printing. After characterizing the curing behavior, the measured parameters are used to calculate the irradiation time for a certain slicing thickness during the printing file preparation.

The resolution of the DLP 3D printed structures highly depends on technical and chemical parameters. Most importantly, the lateral resolution in *xy* is determined by the pixel size of the irradiation pattern. [10] The pixel size is connected to the size of individual mirrors on the DMD as well as to the distance between the DMD and the projection plane. [20] Chemical ink properties such as viscosity or curing speed influence the movement of activated monomers, thus having an impact on the lateral resolution too. [21,22] The lateral resolution is usually between 10–50 µm. [10] The axial resolution in *z* depends on the set slicing distance and accuracy of the mechanical platform movement. It usually ranges from 25–100 µm. [10] Moreover, it is important to keep in mind that the final resolution of the object also highly depends on the *development*, *i.e.* post-printing material treatment. This treatment can significantly affect the size of the printed structure by swelling or shrinkage. This size change needs to be considered especially when removing or replacing the ink with another (liquid) medium of choice.

Although DLP 3D printing is an established technique today, it has furthermore served as an excellent starting point for next-generation vat photopolymerization techniques. Most of these new techniques aim to increase printing speed. This can be seen by the new printing techniques which have emerged in the last decade, *e.g.* continuous liquid interface production (CLIP) or volumetric 3D printing. [23,24] For example, the patented technology for CLIP by the company CARBON3D employs an oxygen-permeable membrane window in the vat to enable oxygen polymerization inhibition during continuous pulling and irradiation of the desired structure. [25] The continuous pulling of the structures speeds up the recoating step which is often the most time-consuming operation during DLP 3D printing. [10] In addition to increasing the printing speed, CLIP improves the axial resolution of the objects by avoiding stepwise irradiation. [10] An alternative approach towards rapid vat photopolymerization is the use of volumetric 3D printing technologies. [26] Volumetric 3D printing describes the process of creating irradiated 3D volumes instead of sequentially applied 2D patterns such as in SLA, DLP 3D printing, or CLIP. This can be achieved, for example by using rotational setups, up-conversion processes, or dual-wavelength photoinitiators. [26–29]

2.3 MULTIPHOTON 3D LASER PRINTING

2.3.1 Nonlinear Optics

MPLP, often also called two-photon 3D laser printing (TPLP), direct laser writing, or multiphoton lithography (MPL), is a vat photopolymerization technique which was pioneered by Kawata and co-workers in 1997. [30] MPLP allows the fabrication of (micro)structures with submicron resolutions. [31–33] This technique and is achieved by using multiphoton absorption processes for the spatially controlled photoinitiation. Multiphoton absorption is a nonlinear optical process, in which multiple photons are absorbed simultaneously. [34] The basis for this phenomenon relies on the light-induced polarization P of molecules by the incoming light, *i.e.* electromagnetic wave:

$$P = \chi^{(1)}\,\vec{E} + \chi^{(2)}\,\vec{E}\vec{E} + \chi^{(3)}\,\vec{E}\vec{E}\vec{E} + higher\ order\ terms, \tag{1}$$

where $\chi^{(n)}$ is the susceptibility of order n and $\vec{E}$ is electric field of incident light. [35] In everyday life, the electric field $\vec{E}$ of light is usually too low to induce second, third or even higher terms of polarization since these tabulated high-order susceptibilities in solids are typically very low. [36] Here, the first term is typically sufficient to describe one-photon absorption and scattering phenomena. By moving to high-energy light sources such as (pulsed) lasers, other types of optical phenomena can be observed. [36] This includes, for example, second, third, or higher order harmonic generation scattering or absorption. [36] By selecting a suitable laser power, these effects are only observed in a small volume, *i.e.* focal point. [34] Thus, applying multiphoton absorption in the photoinitiation process allows to photopolymerize inks in a desired focal point inside of the ink. [34] Moving the focal point inside of the ink droplet or container leads to spatially controlled photopolymerization along the desired trajectory. The process starts with the simultaneous absorption of multiple photons by a photosensitizer or photoinitiator molecule. [34] In a Jablonsky scheme, this process is depicted by the multiphoton absorption *via* a “virtual state”. Next, the excited photosensitizer or photoinitiator molecule can undergo thermal relaxation from a singlet to another excited triplet state before inducing or forming reactive species. The reactive species start the subsequent polymerization reaction in MPLP. [34]

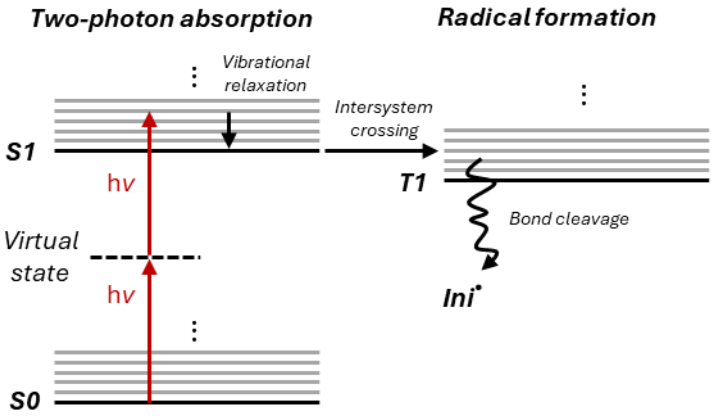

Figure 7: Two-photon absorption induced radical photoinitiation mechanism. [34]

2.3.2 Printing Setups

The technology behind MPLP has evolved rapidly in the last two and a half decades since Kawata and coworkers presented it for the first time in 1997. [30] In the last two decades, this new technology has been commercialized by different vendors facilitating the accessibility of printing setups as well as commercially accessible inks. [37] In this thesis, a commercially available Nanoscribe Photonic Professional GT2 system was used for printing. In general, this setup allows microfabrication in two distinct modes, namely oil-immersion and dip-in mode. The dip-in mode or DiLL is a patented configuration by Nanoscribe GmbH. [38] These two modes refer to the preparation of the substrate and the placement of the ink. [37]

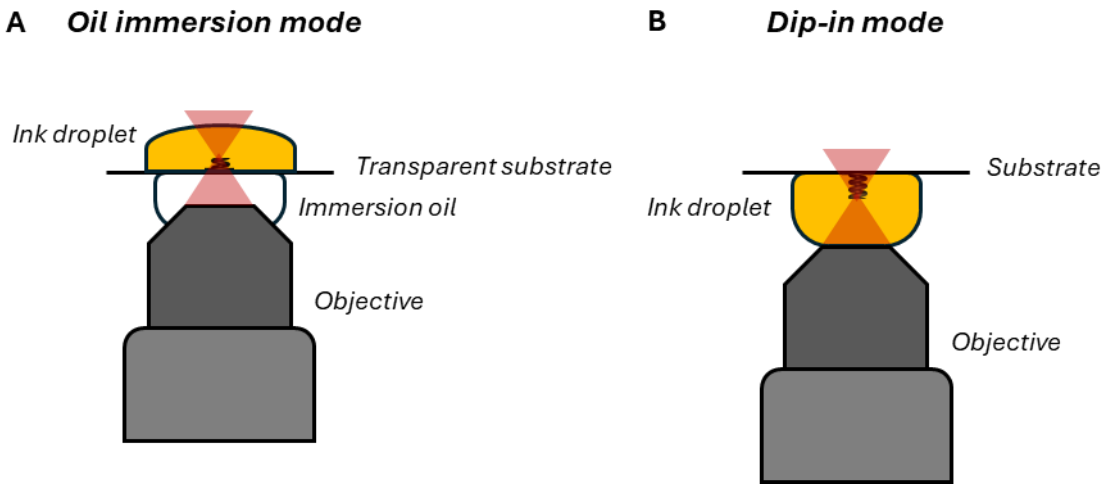

Figure 8: Two printing configurations commonly applied for MPLP. A) In oil immersion mode, the objective is used in combination with immersion oil to print in an ink droplet on top of an optically transparent substrate. B) In dip-in mode, the objective immersed in the ink and printing occurs directly on the substrate. This mode enables printing on non-transparent substrates.

In oil-immersion mode, the objective is covered with an immersion oil and placed below the optically transparent substrate. The light beam exits the objective and reaches the ink after traversing the oil and substrate. In this standard configuration, the accessible structure height is limited to the working distance of the objective and the substrate thickness. [34] Prior to printing, the suitable substrate is mounted on the substrate holder, and a drop of ink is applied on top of the substrate. This configuration is often applied to screen different inks.

In contrast to that, the dip-in configuration gives access to prepare also structures up to multiple millimeters in size by circumventing working distance limitations and transparent substrate requirements. [34] In this configuration, the ink droplet is placed between the objective and the substrate. By lowering the objective during printing, the structure is printed upside down. This mode typically requires larger amounts, *i.e.* volumes, of ink. Available inks for MPLP in oil immersion are not necessarily suitable for printing in dip-in mode configuration since upscaling is not straightforward. [39] This printing configuration requires the maintenance of a stable connection between the objective and the substrate.

An interesting alternative printing mode was recently presented by the company UpNano GmbH with their vat mode. [39,40] In this mode, the structure is pulled out of a vat similar to the DLP printing setup. In this setup, no constant connection or meniscus between substrate and objective is required allowing fabrication of macroscopic structures with micrometer resolution. [39]

2.3.3 Printing Process

The printing process is usually described by two models – the threshold dose model and accumulation dose model. [32,41] Following the threshold dose model, the printing of the separate irradiated volume units, *i.e.* voxels, is achieved by irradiation in a simple binary model. If the energy threshold for achieving photopolymerization is surpassed for each voxel during printing, the polymerized structure is crosslinked enough to remain stable during development. In addition to that, if the induced suitable photoenergy remains below this photocuring threshold, no photopolymerization occurs. [32,41] Although this model explains the printing process in a simplified manner, the oversimplification does not explain different phenomena related to the resolution limit of printed objects. The accumulation dose model assumes that multiple exposures with suitable photoenergy lead to additive energy accumulation in the irradiated voxel. [32,41] Following this model, a stable photopolymerized

material is obtained after development only if the total accumulated energy dose is surpassed. The accumulation dose model reflects better on the achievable resolution of the printing process – especially when the multiphoton absorption process is considered for the photoinitiation step. [41] For example, thin structural features typically require larger exposure energies compared to solid volumes where printing of several lines next to each other leads to an energy accumulation. [41]

MPLP has multiple important printing parameters which highly influence the structure outcome. Different parameters are set by the utilized setup such as laser wavelength and pulse duration – others can be set by the user during sample preparation or printing file generation. For example, the selection of the printing objective already partially predefines the achievable voxel size. The easily tunable settings in the printing file generation include, for example, the distance between scanned lines during printing, *i.e.* slicing and hatching distance, as well as the laser power and the scanning speed.

2.3.4 Technological Challenges

Current technological progress focuses on pushing the targeted miniaturization to its limits, significantly increasing the printing speeds, or achieving printability with lower energy laser sources. [31] Employing stimulated emission depletion in the controlled photoinitiation process with another laser source allows, for example, the printing of structures with a minimum feature size down to 9 nm. [42] In addition to tackling the miniaturization limits, technological progress also focuses on extending the accessible fabrication dimensions from microstructures to the mesoscale and macroscale. This step involves the key to increasing printing rate and developing highly sensitive inks. To increase the achievable printing speed, laser sources with higher maximum power can be applied together with a parallelization approach using multiple foci systems towards volumetric approaches. [43–45] Another approach is to use grayscale lithography to modulate the irradiation voxel size by changing the laser power during printing. By doing so, very smooth surfaces can be achieved, and less printing time is spent. [31,46]

In the following section, the polymerization mechanisms and the employed chemistry of photopolymerization in vat photopolymerization is described.

3. CHEMISTRY OF LIGHT-BASED 3D PRINTING

Polymerizations can be classified depending on their mechanisms either as a *step-growth polymerization* and *chain-growth polymerization*. [3] The decision on which polymerization mechanisms, *i.e.* step-growth or chain-growth, depends on the molecular structure of the monomers and desired polymer.

In step-growth polymerization the reaction and bond formation of the involved monomer's functional groups leads to their deactivation. [3] Thus, the formation of the bulk polymer material proceeds in a stepwise manner and high molecular weight polymers are achieved only for high conversions of functional groups following Carother's equation. [47] Thereby, step-growth polymerization is also highly sensitive to the ratio of both involved molecular functional groups in the bond formation. [3]

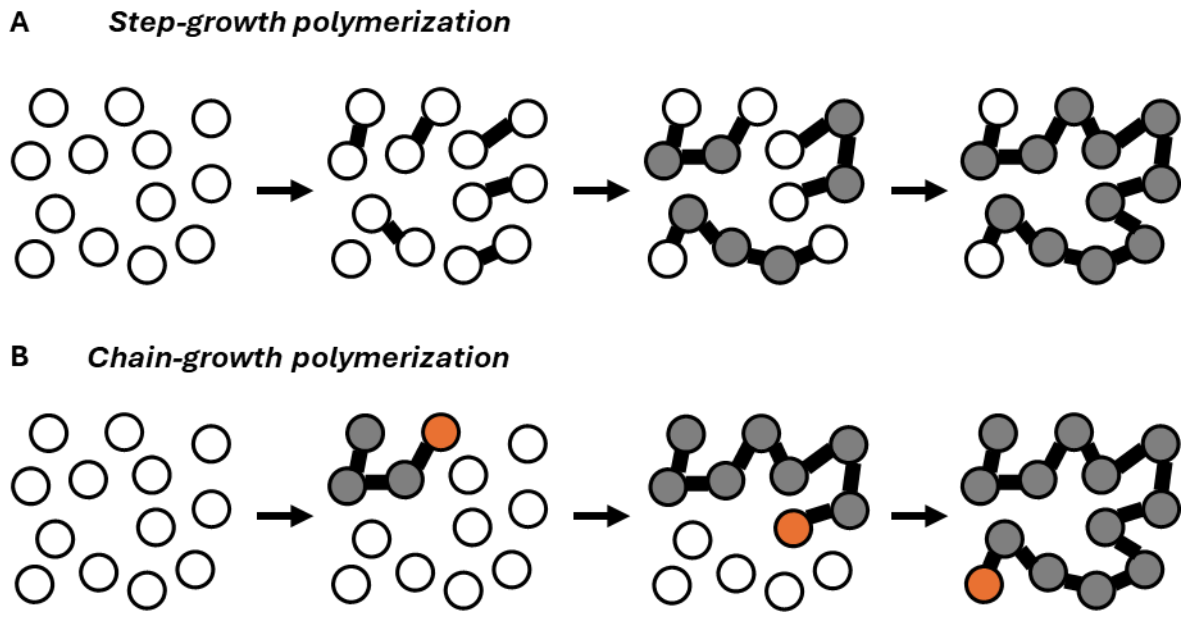

Figure 9: Step- and chain-growth polymerization mechanisms. In white are the reactive monomers, in grey the fully converted monomers, and in orange is the growing reactive chain.

In contrast to that, chain-growth polymerization proceeds in three steps: initiation, chain growth, and termination. [3] After the initiation of a reactive chain, the polymerization mechanism proceeds by inserting monomers iteratively into the growing reactive chain. The growing reactive chain remains active as long as no termination reaction deactivates it. The obtained mass distribution depends on the number of active chain initiation events as well as the kinetics and possible termination reactions. [3]

3.1 PHOTOPOLYMERIZATION PROCESS

Successful vat photopolymerization requires fast photocuring during the printing process. [10] For this reason, photocurable inks with fast photochemically induced reaction mechanisms are typically employed. Especially, (meth)acrylic monomers exhibit fast radical polymerization kinetics together with a chain-growth mechanism. [10] Moreover, the chain-growth mechanism supports a fast increase in polymer mass compared to step-growth mechanisms which follow the previously mentioned Carother's equation. [47] In the following, the reaction mechanism of commonly utilized free radical (photo)polymerization is described step-by-step. [5,48]

The first key step for successful photopolymerization is the photoinitiation process. This process starts with the absorption of one or multiple photons by the photoinitiator or photosensitizer. Photoinitiators are typically categorized for their radical formation mechanism into Norrish type I and Norrish type II photoinitiators. [48]

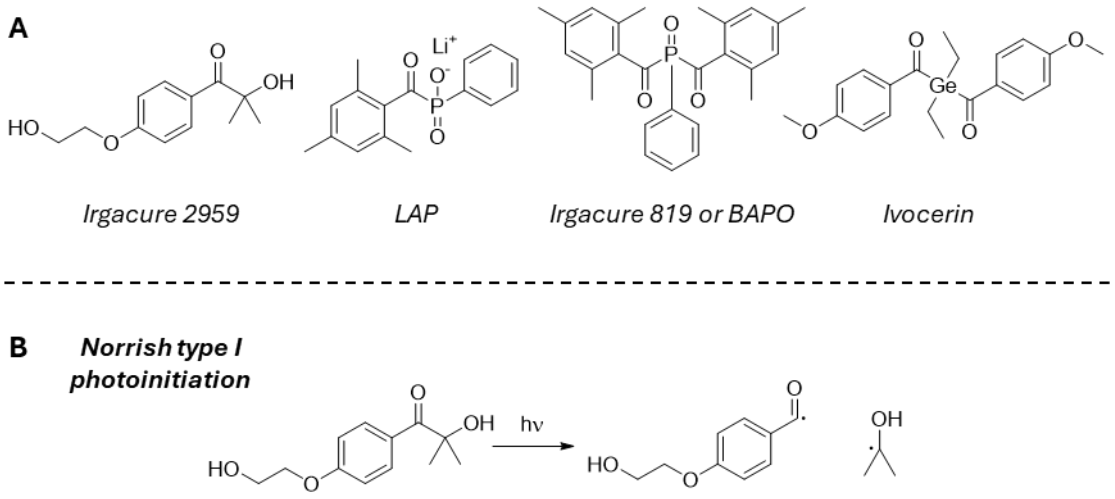

Figure 10: A) Commonly employed Norrish type I photoinitiators such as Irgacure 2959, LAP, BAPO, or Ivocerin. B) The initiation mechanism of the Irgacure 2959 in a Norrish type I mechanism. [48]

Norrish type I photoinitiators show photodissociation, often *via* an α-bond cleavage, upon irradiation. Commonly employed photoinitiators in this class include for example 2-hydroxy-4'-(2-hydroxyethoxy)-2-methylpropiophenone (Irgacure 2959), phenylbis(2,4,6-trimethylbenzoyl) phosphine oxide (Irgacure 819 or BAPO), lithium phenyl-2,4,6-trimethylbenzoylphosphinate (LAP), or bis(4-methoxybenzoyl)diethylgermanium (Ivocerin). [49] In all these initiators, the α-bond breaks upon suitable light irradiation leading to the

formation of two active radical species which can serve for chain-growth during polymerization. [48]

Norrish type II photoinitiators have a different initiation mechanism because they involve a hydrogen abstraction for radical formation. Their photoinitiation mechanism starts with the absorption of suitable light energy by a photosensitizer. In the next step, the photosensitizer typically abstracts a hydrogen radical from a co-initiation species, often an amine co-initiator. After the hydrogen abstraction, both formed radical species can initiate the subsequent chain-growth. [48,50]

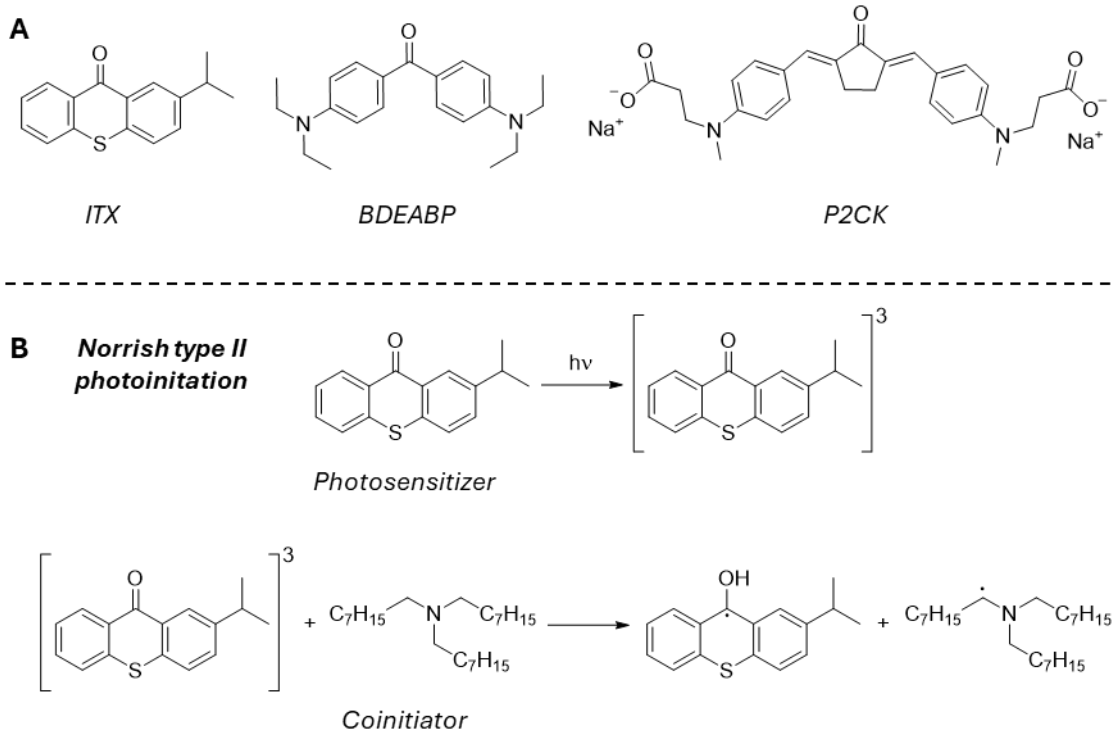

Figure 11: A) Commonly employed Norrish type II photoinitiators such as ITX, BDEABP, or P2CK. B) The initiation mechanism of the ITX in a Norrish type II mechanism. [48]

The choice of photoinitiation system is linked to the employed photopolymerization technique and desired printing wavelength. [51] Norrish type I photoinitiators are frequently employed in both, DLP 3D printing as well as MPLP. However, while being the standard choice for DLP 3D printing, these photoinitiators often do not show efficient multiphoton absorption. [52] For this purpose, Norrish type II systems such as 4-(propan-2-yl)-9H-thioxanthen-9-one (ITX), 4,4'-bis(diethylamino)benzophenone (BEABP), or the photoinitiator P2CK have proven to be more effective in initiating under these conditions. [52] The high multiphoton absorption cross-section as well as effective intra- and intermolecular hydrogen

abstraction ensures highly efficient photoinitiation. [48,53] However, a major drawback of these systems is their residual presence in printed structures which can lead to strong undesired autofluorescence. [54]

After successful photoinitiation, the next step involves radical chain-growth polymerization. [5] For this purpose, rapidly polymerizable monomers are preferred because they offer fast mass growth, *i.e.* printing speed. This can be achieved using acrylic monomers such as (meth)acrylates and (meth)acrylamide. [55]

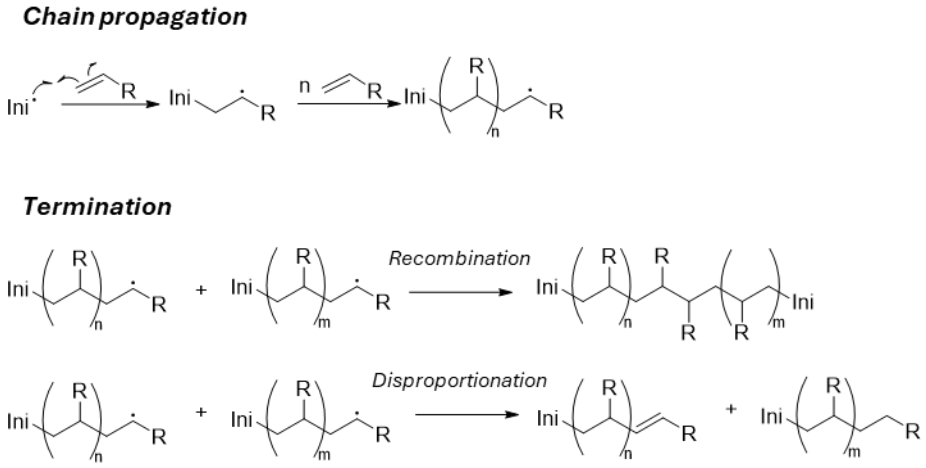

Figure 12: Mechanism of free radical polymerization after formation of initiating radical species. [5]

During polymerization of the different monofunctional acrylic monomers, linear chains are formed. Using multifunctional monomers, *e.g.* di-, tri-, and tetraacrylates, provides access to crosslinked polymeric materials. [34,55] In addition to acrylate systems, another frequently used class of radically polymerizable monomers employ thiol-ene photopolymerization. [34,55] Compared to acrylic systems, these systems can be come with various advantages – especially when biocompatible hydrogels are desired – such as better biocompatibility, lower shrinkage, and lower required light doses for photocuring. [10,34,40,49,55–57] Nevertheless, poor thermal storage stability as well as strong odor of these thiol-ene based systems make them usually less attractive to work with.

The polymerization process is stopped by a termination step which can occur by radical recombination or disproportionation. [5] In addition to the combination or disproportionation of growing chains, this step is often connected to the presence of dissolved oxygen in the ink. The oxygen reacts with the radical and thereby hinders additional chain-growth. [25]

An alternative to radical photopolymerization is the use of epoxy-functionalized monomers and the use of photoacid generators for starting the cationic chain-growth polymerization. Epoxy-based polymerization typically leads to less shrinkage of printed structures but comes typically at the cost of slow polymerization rates compared to radical polymerization.[10]

3.2 PREPARATION OF INKS

The obtained photopolymerized materials possess properties which are related to the employed monomers as well as the polymer architecture. [58–60] This modular principle gives access to a wide range of tunable additional functionalities. Development of new inks for vat photopolymerization such as DLP 3D printing or MPLP follows a rational process in an iterative protocol. The process starts with the selection of desired and targeted material properties in the final 3D printed structures (*e.g.*, mechanical, optical, responsive, or other functional properties). First, the ink is designed around synthesized or selected accessible mono- and multifunctional monomers for the implementation of the desired properties. Next, other ink components are chosen based on their compatibility with the printing process and the desired properties. Frequently employed additional ink components are suitable solvents, non-polymerizable additives, or photoinitiators. The prepared inks are tested for their printability, and the process optimized.

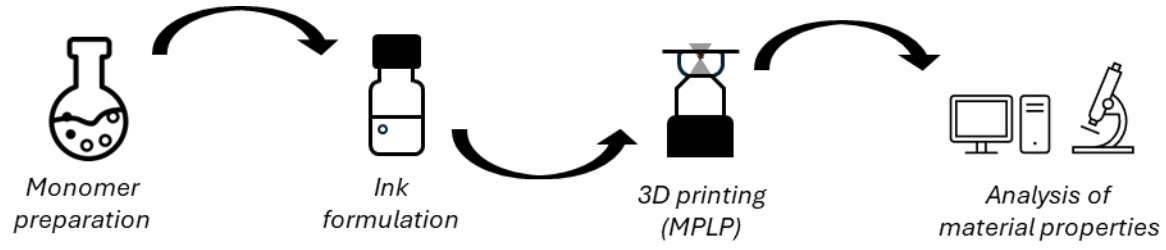

Figure 13: Process of ink development. After deciding the targeted material properties, the process involves the formulation of monomers into inks which are tested for their printability. The process is re-evaluated at an earlier point in the development chain until the desired properties are achieved.

3.3 CURRENT TRENDS IN INK FORMULATIONS

The interest in expanding the scope of accessible structures and materials for a variety of users across disciplines such as engineering, physics, chemistry, biology, and medicine is the driving force for recent innovation in printable inks.

For example, photochemical approaches using multiple wavelengths during 3D printing have attracted attention in recent years. These involved the development of new methods and photochemical reactions by using multiple wavelengths of light simultaneously. For example, multiple wavelength photoinitiators for volumetric 3D printing using xolography holds great potential for new photochemical concepts. [27] In this regard, employing orthogonal photochemistry by printing with multiple wavelengths is a promising approach to combine multiple materials into 3D multimaterial structures during printing. [61,62]

Many recently presented ink formulations aim for establishing bio-based, degradable, and recyclable vat photopolymerized 3D structures. Reported bio-based systems typically employ natural resources, for example vegetable oils, for the synthesis of multifunctional photocrosslinkable monomers. [63,64] Moreover, innovative concepts for breaking and reforming crosslinks were introduced in 3D printing to achieve recyclable systems. [65]

In addition to progressing sustainability in 3D printing, inks for biohybrid materials have been recently presented to achieve living materials. In this approach, inks are combined with bacteria, yeast, or mycelium, which could be used for modulating material properties. [66–68] Mixing inks with mammalian cells is attractive for application in tissue engineering. [66,69]

For 3D printed bioelectronic materials, a new class of ink formulations based on polymerizable deep eutectic systems (PDESs) is currently raising interest in vat photopolymerization. [70–74] PDESs are liquid deep eutectic mixtures prepared from Lewis or Brønsted acids and bases, where one of the components is polymerizable. [75–77] These liquid eutectics with tunable polarity are readily accessible by mixing the components at elevated temperatures. [75–77] Furthermore, a low volatility and tunable viscosity make PDESs also highly attractive for dissolving a variety of polar and apolar compounds. [75–77]

Since this thesis focused on materials for MPLP, the next section introduces accessible functional state-of-the-art materials focusing on stimuli-responsive materials and biomaterials.

4. STATE-OF-THE-ART MATERIALS FOR MULTIPHOTON 3D LASER PRINTING

Functional materials play a key role in the development of new applications on the microscale. [31,59,78,79] The functionality can be incorporated into the material either physically by additives or covalently using functional monomers. [78] In state-of-the-art ink design for MPLP, functional monomers are typically combined with crosslinkers and a suitable photoinitiator. [79,80] In many cases, the crosslinking density very often must be sufficiently low to ensure the desired material functionality. [80] However, since crosslinking is very important for MPLP to achieve printability and mechanical stability of the 3D printed microstructures, state-of-the art ink design often requires optimization of the ratio of functional monomers to crosslinker. [80]

The next section will deal in detail with addition of and control over stimuli-responsive, shape-morphing material properties in 3D microprinted structures.

4.1 BEYOND STATIC 3D STRUCTURES

Developing structures which can respond, interact, and adapt to environmental changes are of great interest for developing signaling cascades and robotics applications. By introducing stimuli-responsive behavior into static structures, they can for example change their shape, exert forces onto other structures, move in a controlled manner, or induce further signals. [78,80] Among a plethora of those materials, organic stimuli-responsive polymers have been previously designed to respond to external stimuli such as temperature, light, electric fields, pH, humidity, and other chemical signals. [78] From a chemical point-of-view, stimuli-responsive materials possess molecular structures which can respond to the stimulus of interest. [81] For example, light-induced changes start with the absorption of light and continue with internal electronic or molecular rearrangement processes which can also lead to thermal processes. [81] Similar to light, thermal energy induces electronic and molecular changes which can affect the interaction of molecular groups. [81] The choice for a desired stimulus and response influences the suitability stimuli-responsive polymer class. Embedding stimuli-responsive features in 3D printed structures is often called *4D printing*. [82] The additional dimension is the accessible material change upon applying a certain

stimulus. This provides another dimension of control over the shape, stiffness, size, or any other material property. [78,80] Thus, 4D printing using MPLP offers an excellent technique for preparing stimuli-responsive structures for soft robotics, optics and photonics, microfluidics, and biological applications. [78] Four different classes of stimuli-responsive polymers have played a crucial role in the development of 4D printed structures using MPLP: responsive hydrogels, shape memory polymers, liquid crystalline elastomers, and (magnetic) composite materials. The following section deals with MPLP of the first three classes, namely responsive shape memory polymers, liquid crystal elastomers, and responsive hydrogels.

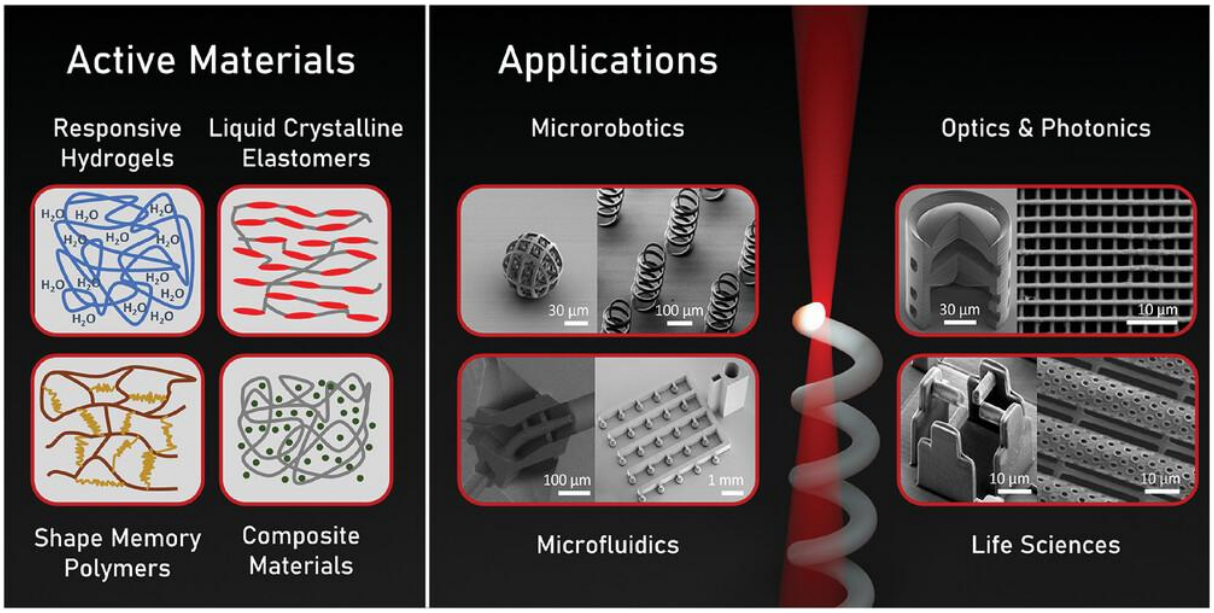

Figure 14: Active materials involved in providing stimuli-responsive properties for 4D microprinting using MPLP. [78]

4.1.1 Shape Memory Polymers

Shape memory polymers are a class of polymers which can change their shape upon applying an external stimulus. [83] In temperature-responsive shape memory polymers, a temporary, *i.e.* programmed, shape transforms back upon heating into the material's permanent shape. [83] Programming is performed by heating the permanent shape above the polymer's glass or crystallization transition temperature. In this step, the material typically shows significantly softer mechanical properties allowing the deformation of the softened material to a temporary shape. Fixing the programming strain in the shape memory polymer is achieved by cooling the material in its temporary shape below the glass or crystallization transition temperature. [83] The response is usually based on the release of induced, *i.e.*

programmed, strains upon heating the programmed material back above the polymer's glass or crystallization transition temperature. Upon melting at the transition temperature, softening of the material allows the material to release its strain and recover its previously permanent state. [83]

Shape memory polymers were previously 3D printed using MPLP. Reported shape memory systems by Greer and coworkers or Blasco and coworkers are based on glass transitions of polymers such as poly(benzyl methacrylate) or poly(isobornyl acrylate). [84,85] The ink composition reported by Blasco and coworkers was printable with only minor changes using MPLP and DLP printing. [85]

4.1.2 Liquid Crystal Elastomers

Liquid crystal elastomers are a special class of stimuli-responsive polymers showing responsive behavior based on changes in liquid crystalline phases. [86] Liquid crystals possess unique physical properties by combining long-range order of crystals with the fluidity of liquids. Various liquid crystalline phases have been prepared which can be categorized based on the molecular orientation between suitable liquid crystalline molecules, often called mesogens. [86] The different liquid crystalline phases fix the mesogen orientation without limiting its fluid state. In the nematic phase, the mesogens show an alignment in a direction without an additional preference along the orientation axis. [86] Increasing thermal energy by heating can at a certain temperature overcome the orientation preference leading to an isotropic state. This temperature is called nematic-to-isotropic phase transition temperature $T_{n\text{-}i}$. Cooling the isotropic mixture back results in the recovery of the nematic phase. [86] Connecting mesogens in a low crosslinked network allows to use the reversible phase transitions in materials. For example, the orientation of mesogens in nematic liquid crystalline elastomers is along an alignment direction. Upon induced nematic-to-isotropic phase transition, the long-range orientation is lost leading to a contraction in the direction of alignment. [86] Thus, the application of liquid crystalline elastomers highly depends on the possibility to align the mesogens prior to crosslinking in the network. In thin film applications (< 100 µm), alignment of the mesogens is typically achieved by using coated surfaces in glass cells. [86,87]

By MPLP of (meth)acrylated mesogens in glass cells, liquid crystalline elastomers were successfully 4D printed and used for the preparation of stimuli-responsive microrobots.[88–92]

For example, Wiersma and coworkers prepared a light-fueled moving microrobot by incorporating a photo-responsive azobenzene in the printed structure. [92] The absorption of suitable light by the dye and the photo-thermal heating of the microrobot induced the desired nematic-to-isotropic phase transition. In another work, Wegener and coworkers used electrical field induced mesogen alignment during the MPLP process to achieve spatially controlled mesogen alignment in the printed structure. [93] In a follow-up work, Wegener and coworkers utilized this approach to 3D printing photo-responsive metamaterials using liquid crystalline elastomers. [94]

In addition to the actuation of nematic structures, Florea and coworkers presented MPLP of a cholesteric liquid crystalline elastomer structure. [95] The pitch distance of the printed structure was found to change its color in response to differences in humidity of the environment.

4.1.3 Responsive Hydrogels

Stimuli-responsive hydrogels are another class of stimuli-responsive polymer. [96] In responsive hydrogels, the responsive behavior is achieved by stimuli-induced differences in swelling behavior of the hydrogel network. [96–98] For example, incorporating different organic acids or bases lead to pH-responsive swelling or shrinkage in aqueous media close to their pK_a or isoelectronic point value. [96–98] Sitti and coworkers have incorporated pH responsive behavior in microprinted hydrogels by adding acrylic acid (AAc) and poly(ethylene glycol) diacrylate (PEGDA) in a hydrogel ink for MPLP to achieve on-demand pH responsive cargo release of the core of a printed drug carrier. [99] This pH responsive core was embedded into a temperature-responsive outer shell. For this purpose, Sitti and coworkers used a *N*-isopropyl acrylamide-containing (NIPAAm-containing) hydrogel ink formulation. Poly(NIPAAm) is a commonly employed temperature-responsive polymer in hydrogel formulations. [99] It possesses a critical solution temperature at around 32 °C which causes the polymer to shrink in aqueous solution slightly above room temperature. [100] In crosslinked hydrogels, this effect leads to shrinkage of the hydrogels upon heating. [100] The earliest example of microprinted poly(NIPAAm) using MPLP was reported by Bastmeyer and coworkers in 2019. [101]

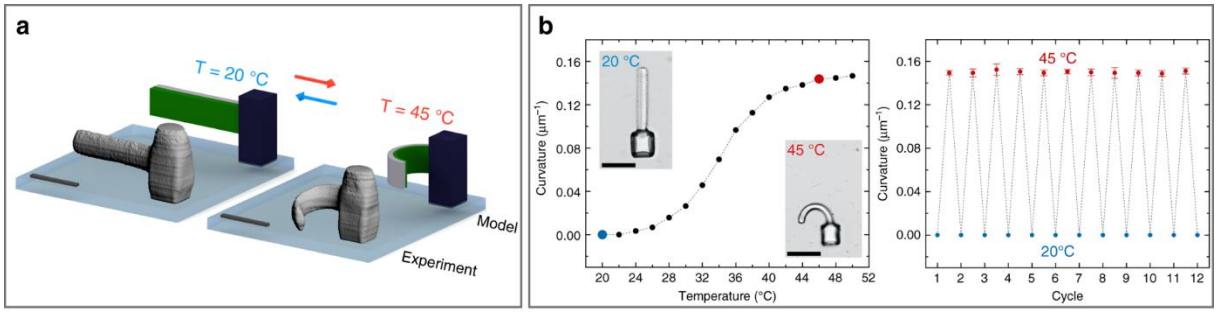

Figure 15: Reported MPLP of bilayered poly(NIPAAm)-containing actuator. [101]

In this first work, the authors have also shown the influence of the printing parameters in MPLP on the controlled shrinkage of bilayered structures. [101] Bending of their printed bilayered structures was achieved by printing with different printing parameters and thereby different crosslinking densities. The more crosslinked part of the bilayered beam showed less shrinkage compared to the less crosslinked beam part. This anisotropy led to the bending in a controlled way. [101] The combination of differently crosslinked materials serves as an excellent way to create anisotropic behavior in responsive hydrogel-based actuators. [97] Selhuber-Unkel and coworkers have investigated the response of the printed poly(NIPAAm) and employed it in microfluidic chips to trap particles. [102,103] Blasco and coworkers have recently developed oligo-ethylene glycol-based prepolymer inks to achieve responsive shrinkage at tunable temperatures between 40 °C and 80 °C. [104]

Responsive behavior was also implemented by Tanaka and coworkers by using adamantane-based host-guest systems. [105] This system allowed for selective chemically triggered decrosslinking, *i.e.* swelling response, in the presence of cells. Moreover, the authors presented multimaterial structures with this system allowing the controlled stretching of cells. [105]

Ensuring biocompatibility of printed materials is a crucial aspect for the development of crucial applications. The next section introduces biomaterials for MPLP.

4.2 3D MATERIALS FOR BIOAPPLICATIONS

Before going in detail on the variety of biomaterials, the first step includes the definition of the materials which we commonly consider as biomaterials. According to the broadly accepted definition from 2009, David F. Williams defined biomaterials in his book "On the nature of biomaterials" as following:

"*A biomaterial is a substance that has been engineered to take a form which, alone or as part of a complex system, is used to direct, by control of interactions with components of living systems, the course of any therapeutic or diagnostic procedure, in human or veterinary medicine.* " [106]

Based on this definition, the term *biomaterial* is linked to synthetic as well as natural materials intended for use with living systems in biomedical studies, diagnostics, implants, and therapeutics. Moreover, the term *biomaterial* can apply to ceramics or metals intended for bone replacement as well as to flexible substrates used in wearables and bioelectronics. Keeping this definition and the versatility of applications in mind, it is not necessarily related to *biodegradable* or *bio-derived materials*. [5] It is also not necessarily linked to *soft materials*. However, since many applications are connected to soft tissues, many soft biomaterials are interesting in those applications. A crucial requirement for this combination is often called *biocompatibility*. The biocompatibility of a material can be defined as the property of not producing an adverse effect when in contact with a living system. [107] Following this definition, biocompatible materials include bioinert materials and materials with a positive effect. Of course, the evaluation of the effect from a biocompatibility study depends on the material and final application in mind. [108]

Using additive manufacturing and especially vat photopolymerization for shaping biomaterials in 3D provides a range of new opportunities in tissue engineering for biomedical research and personalized medicine. For example, the precise processing of biomaterials with submicron, *i.e.* subcellular, resolution using MPLP is highly attractive for fabricating single-cell scaffolds for (bio)medical studies and implants. [40] In this thesis, the main effort was placed on developing new soft synthetic as well as natural material inks for 3D microprinting and advance possible applications of these 3D printed biomaterials. For this purpose, the next section focuses on soft 3D printable biomaterials using MPLP.

4.2.1 Synthetic Precursors

Synthetic polymers offer several advantages compared to pure natural polymers. The main advantage is the versatility of chemical compositions yielding highly tunable mechanical material properties, controllable swelling degree in aqueous media, and easily embedded additional functionality. For example, soft mechanical properties can be achieved by using poly(dimethylsiloxane)-based (PDMS-based) prepolymers in printable inks. [109–111]

This is performed by using (meth)acrylate-functionalized PDMS-prepolymers. A frequently employed PDMS-based ink is the commercially available IP-PDMS by the company Nanoscribe GmbH. [112] This ink gives access to soft hydrophobic printable elastomers. This hydrophobic material shows a low degree of swelling after printing and development facilitating its fabrication in more complex structures. The low cytotoxicity of printed IP-PDMS has provided the basis for numerous successful studies using this material in cell scaffolds and biophysical studies. [113,114]

For example, Tanaka and coworkers have recently fabricated different net structures from IP-PDMS and examined cell forces on these materials. [114] After printing different net geometries using MPLP, the authors seeded cells on the structures and investigated the net deformation during cell movement. [114] In another recent work, Selhuber-Unkel and coworkers have 3D printed an elastic structure using IP-PDMS, seeded cells inside of the elastic structure, and used a mechanical tip to mechanically stimulate the multicellular systems. [113]

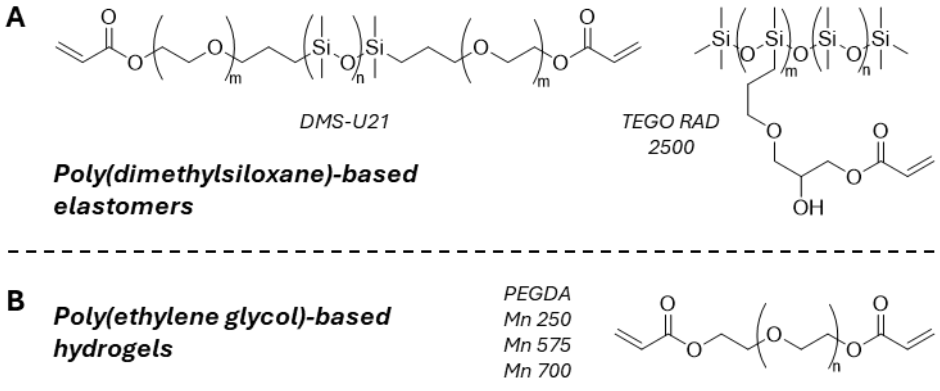

Figure 16: Frequently employed photopolymerizable synthetic precursors for MPLP.

Although IP-PDMS can be used for various studies, moving to hydrogels can provide access to even softer materials. [34] In hydrogels, non-covalently bound water ensures the structural stability of the material. Hydrogels are frequently employed in biological studies because they also come along with some further advantages. In addition to the soft and tunable mechanical properties, the intrinsic presence of water inside of the material comes along with improved nutrient supply. [115] In biological studies, the perfusion of hydrogels ensures cell viability, even if cells are directly encapsulated inside. [116] Commonly employed synthetic systems are poly(ethylene glycol)-based (PEG-based) hydrogels. For MPLP, PEG prepolymers are typically functionalized with (meth)acrylate groups and formulated in printable inks together with a photoinitiator and water. [40]

It is important to note that pure PEG-diacrylate (PEGDA) hydrogels possess cell repellent behavior making it crucial to add additives to promote cell-adhesion. For example, selectively cell-adhesive printed PEGDA-based inks can be achieved by adding acrylated polypeptides with cell-adhesion promoting sites (*e.g.* sequence motif "RGD"). [117]

PEGDA-based formulations have been previously printed for the fabrication of microrobots and cell scaffolds. [118,119] In 2021, Göpfrich and coworkers presented MPLP of a PEGDA-based ink for the preparation of intracellular structuring inside of giant unilamellar lipid vesicles. [120] Moreover, in recent years, the commonly employed PEG-based hydrogels have been step-by-step replaced in (bio)medical studies by alternative hydrogels, because long term exposure of human to these materials leads to the development of PEG-antibodies. [121,122]

4.2.2 Natural-Based Precursors

Implementing natural-based hydrogels in bioapplications comes along with multiple advantages. Natural-based hydrogel-forming polymers can be found in a plethora of tissues where they serve key components in the natural extracellular matrix (ECM). [40] The ECM was found to not only offer mechanical surrounding to cells, but to also play a crucial role in cell-cell as well as cell-matrix interactions. [123] Thus, using natural-based components from the ECM allows the fabrication of hydrogels with similar mechanical material properties and provides the possibility of including biochemical and biological cues to stimulate surrounding cells. Two frequently employed natural-based ECM components are poly(saccharides) and poly(peptides). [40] To enable MPLP, natural-based materials are usually chemically functionalized with (meth)acrylates or (meth)acrylamides using acryloyl

chloride or (meth)acryloyl anhydride. These reagents react with accessible amine or hydroxy groups of the natural prepolymers allowing additional photocrosslinking during MPLP. [40]

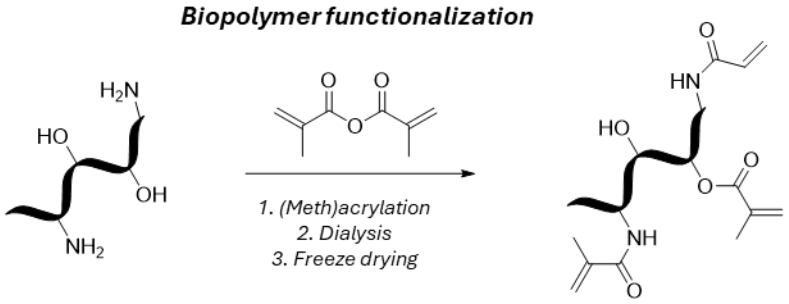

Figure 17: Functionalization procedure for photocrosslinkable natural-based precursors. [124]

4.2.2.1 Polysaccharide-Based Precursors

Polysaccharides are important components of the extracellular matrix with highly varying stiffness. For example, chitin is produced by arthropods as one of the main components of stiff exoskeletons, *i.e.* shells for protection. [125] In contrast to that, hyaluronic acid is a key component in the ECM of soft tissues because it retains water and thereby keeps the tissue elastic. [126] The broad range of natural occurrences of polysaccharides is related to the tunability in monosaccharides and their connectivity. The broad range of properties and accessible polysaccharide prepolymers makes this class of biopolymers attractive for MPLP. [127–132] Among those, hyaluronic acid is especially interesting for its biomedical role in mammalian tissues. [126] For this reason, different functionalization strategies have been employed to access printable hyaluronic acid. Chichkov and coworkers functionalized the polysaccharide prepolymers with methacrylate groups using glycidyl methacrylate. [129] To achieve the printability of their systems, the authors have moreover added PEGDA as another crosslinker to their ink. [129] To reduce the cytotoxicity of the printed material by avoiding unreacted (meth)acrylate groups, Liska and coworkers have functionalized the hyualuronic acid with vinyl esters using a lipase-catalyzed transesterification reaction. [133] The vinyl ester functionalized hyualuronic acid was printed using thiol-ene photopolymerization with dithiothreitol as dithiol agent. [133]

4.2.2.2 Polypeptide-Based Precursors

Polypeptide-based precursors are an excellent natural source of biopolymers. In nature, polypeptides and proteins are essential to ensure cell functions and cell interactions with their surroundings. [134] Preparation of polypeptide scaffolds for tissue engineering is a crucial part of mimicking natural tissues which often consist of a mixture of different types of collagens and their denatured, partially hydrolyzed form gelatin. [135]

Collagen, for example, as one of the most abundant proteins in animals is essential to maintain mechanical stability of the ECM. [136] Moreover, this protein induces alignment in tissues and plays a crucial role in signaling pathways. [137,138] Collagen can be found in various types where collagen type I is the most abundant. [139] The different types of collagens vary in their polypeptide-sequence, chain combinations, length, and post-modifications. [139] These variations in collagen structure lead to different properties and function in different tissues.[139] Collagen has various hierarchical levels of structure formation.

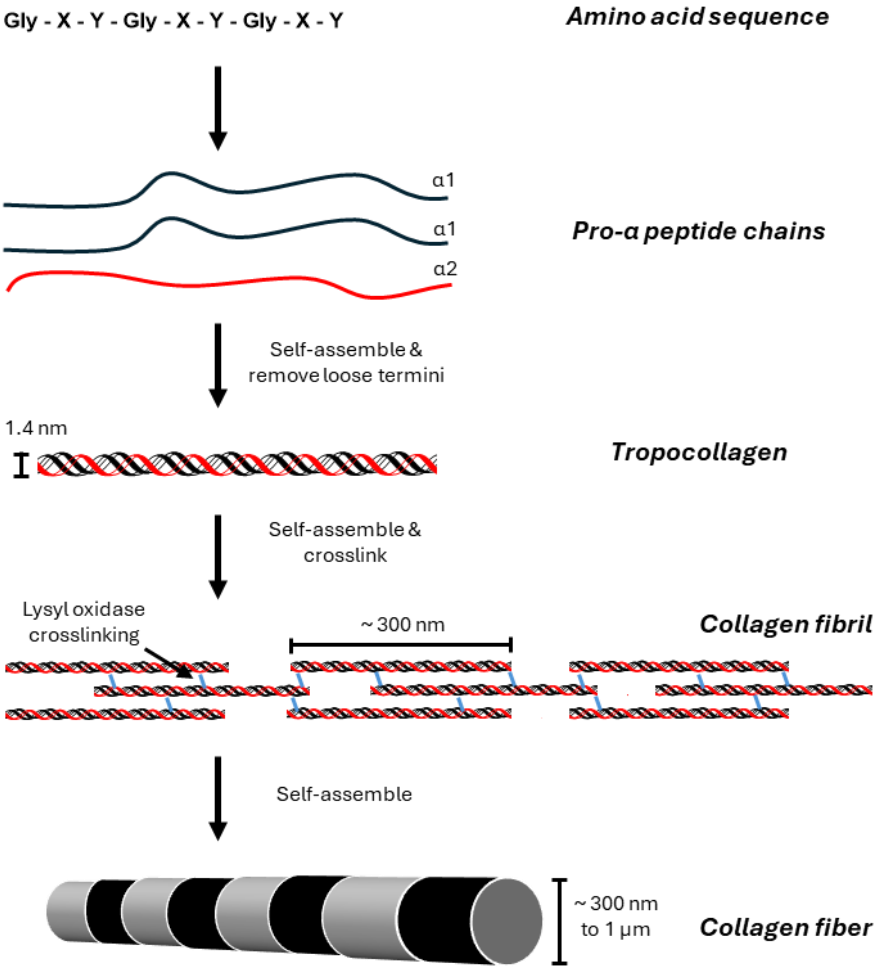

Figure 18: Collagen self-assembly at different hierarchical levels. [140]

Its smallest element, *i.e.* primary structure, is built from a sequence of amino acids with the repeating tripeptide sequence of glycine-X-Y, where X and Y are mostly proline and hydroxyproline with regular mutations at the positions X and Y, respectively. [139] This primary structure forms a polyproline II helical secondary structure which assembles with two more collagen polyproline II helices into a trihelical quaternary structure. [139] The stability of this quaternary structure is closely connected to the ratio of proline and hydroxyproline in the primary structure. Increasing the content of hydroxyproline was found to also increase the folding stability of the quaternary structure. [139] In nature, the unfolding, *i.e.* melting, temperature of different collagen sources was found to depend on the tissue. [141] For example, collagen extracted from Antarctic fish skin unfolds, *i.e.* melts, slightly above the body temperature the fish faces (5 °C-6 °C). In collagen extracted from rat skin, melting occurs around 37 °C. [141]

In addition to the other hierarchical levels, the separate trihelical quaternary structures can assemble into fibrils of several hundreds of nanometers and fibers of centimeter scale depending on the environment and tissue. [139] Research on collagen assembly across different scales has gained rapid evolution in the last decades due to new accessible powerful computational methods and simulations. [142–144] Up to today, potential folding and assembly mechanisms of collagen *in vivo* remain a vividly discussed topic. [145] Understanding this process in detail could offer new biomedical opportunities to understand and manipulate wound healing and aging processes. [139]

To study and use collagen in hydrogels, it is typically purified from natural sources such as bovine, rat, or fish. [139] In this step, the water-insoluble fibers are usually treated with acids at low pH to break the quaternary assembly. [139,146,147] The solubility of collagen in this medium highly depends on the source and degree of chemical crosslinking between the separate trihelical structures. [146] Increasing the pH of the soluble collagen solution yields gelation with reformation of fibril or fiber assembly. [146] This assembly is further highly preferred with increasing temperature. [146] For this purpose, soluble collagen is usually dissolved at low temperatures before inducing gelation at relevant temperatures for cell cultures. [148]

To achieve collagen gelation during vat photopolymerization and explicitly MPLP, soluble collagen can be printed with photosensitizers such as riboflavin or rose bengal which are supposed to induce oxidative crosslinking of amino acid side chains upon irradiation. [149,150]

However, this process was found to show low efficiency, thus required high laser powers. An attractive alternative to increase the printability is the functionalization of the amines and hydroxy groups in the side chains with photopolymerizable groups. This can be achieved by methacrylation or incorporating groups for subsequent thiol-ene crosslinking. [151,152] So far, MPLP of collagen methacrylamide (ColMA) has only been achieved by using custom setups or cooling of the ink during the printing process to avoid undesired gelation. [152]

In contrast to soluble collagen, gelatin is composed of hydrolyzed short polypeptides, *i.e.* collagen primary structure fragments, which can be obtained by treating collagen with enzymes or harsh pH conditions over time. [153,154] This treatment changes the chemical properties of the material entirely since it does not form fibrils or fibers anymore. Due to this fragmentation, gelatin dissolves readily in aqueous conditions at temperatures above 30 °C. [153,154] Similar to collagen, gelatin possesses cell-adhesive properties making it highly attractive for the fabrication of cell scaffolds. [155] Chemical (photo)crosslinking of gelatin improves the mechanical properties of the hydrogels, making them suitable as scaffolds for cell culture. This can be achieved in the same way as for the other biopolymers, *e.g.* (meth)acrylation. [155] Gelatin methacryloyl (GelMA) is an established hydrogel material in vat photopolymerization and MPLP. [155–158] It is typically dissolved in concentrations of 20 wt% to 40 wt% in aqueous solution with a suitable photoinitiator. After spatially controlled photochemical crosslinking, the residual GelMA is removed by slightly heating the printed structures in an aqueous medium. GelMA has been previously used for the fabrication of cell scaffolds and biocompatible microrobots. [155–158]

For example, Nelson and coworkers have prepared enzymatically degradable helical microswimmers in 2018 using GelMA. [159] After MPLP, the authors incorporated iron oxide nanoparticles and were able to control the movement of the microswimmers upon applying magnetic fields. Furthermore, the 3D printed GelMA matrix was degradable in the presence of collagenase, a hydrolytically active enzyme, making the system interesting as a controllable biomedical cargo. [159]

III. Cumulative Part

1. DEEP EUTECTIC INKS FOR MULTIPHOTON 3D LASER MICROPRINTING

Bibliographic reference

Philipp Mainik, Christoph A. Spiegel, Jonathan L. G. Schneider, Martin Wegener, and Eva Blasco. “Deep Eutectic Inks for Multiphoton 3D Laser Microprinting.” Adv. Mater. (2025): 2507640.

Author contribution

Philipp Mainik has contributed to the *methodology* (lead), *validation* (lead), *formal analysis* (lead), *investigation* (lead), *data curation* (lead), *writing – original-draft* (lead), *writing – review & editing* (lead), and *visualization* (lead).

Patent reference

The results of this work have been used for an invention disclosure and patent application together with Heidelberg University:

Philipp Mainik, Christoph Alexander Spiegel, Eva Blasco Pomar. Deep Eutectic Inks for Multiphoton 3D Laser Microprinting. EP25151765. Filing date: 14.01.2025.

Formblatt Kumulative Dissertation

1. Publikation/*Publication*:
Vollständige bibliographische Referenz/*Complete bibliographic reference:*

Philipp Mainik, Christoph A. Spiegel, Jonathan L. G. Schneider, Martin Wegener, and Eva Blasco. "Deep Eutectic Inks for Multiphoton 3D Laser Microprinting." Adv. Mater. (2025): 2507640.

2. Erst- oder gleichberechtigte Autorenschaft/*First or equal authorship*: Ja/*Yes*☒ Nein/*No* ☐

Veröffentlicht/*Published* ☑
Zur Veröffentlichung angenommen/*Accepted* ☐
Eingereicht/*Submitted* ☐
Noch nicht eingereicht/*Not yet submitted* ☐

4.* Beteiligungen/*Contributions**

Contributor Role	**Doktorand/in/ *Doctoral Student***	**Co-Autor/in 1/ *Co-author* 1**	**Co-Autor/in 2/ *Co-author 2***
Name, first name	Mainik, Philipp		
Methodology	x		
Software			
Validation	x		
Formal analysis	x		
Investigation	x		
Resources			
Data Curation	x		
Writing-Original Draft	x		
Writing-Review&Editing	x		
Visualization	x		
Supervision			
Project administration			
Funding acquisition			

Kategorien des CRediT (Contributor Roles Taxonomy, https://credit.niso.org/)

Hiermit bestätige ich, dass alle obigen Angaben korrekt sind/*I confirm that all declarations made above are correct.*

Unterschrift/*Signature* _____ _____ _____
Doktorand/in/*Doctoral student* **Co-Autor/in 1/*Co-author 1*** **Co-Autor/in 2/*Co-author***

Betreuungsperson/Supervisor:
Hiermit bestätige ich, dass alle obigen Angaben korrekt sind und dass die selbstständigen Arbeitsanteile des/der Doktoranden/in an der aufgeführten Publikation hinreichend und signifikant sind/*I confirm that all declarations made above are correct and that the doctoral student's independent contribution to this publication is significant and sufficient to be considered for the cumulative dissertation.*

Prof Blasco, Eva | E Blasco | 8.8.2025
Name/*Name* | Unterschrift/*Signature* | Datum/*date*

Stand: Februar 2025

RESEARCH ARTICLE

ADVANCED MATERIALS
www.advmat.de

Deep Eutectic Inks for Multiphoton 3D Laser Microprinting

*Philipp Mainik, Christoph A. Spiegel, Jonathan L.G. Schneider, Martin Wegener, and Eva Blasco**

Multiphoton 3D laser printing of polymers has become a widespread technology for manufacturing 3D architectures on the micro- and nanometer scale, with booming applications in micro-optics, micro-robotics, and micro-scaffolds for biological cell culture. However, many applications demand material properties that are not accessible by conventional polymer inks. These include large stiffness, for which recent breakthroughs based on inorganic materials have been reported. Conversely, some applications require very low stiffness and high mechanical compliance. Existing solutions achieve softness by low crosslinking densities, at the inherent expense of deteriorated spatial resolution and structure quality. Herein, this apparent contradiction is resolved by introducing multiphoton inks based on deep eutectic systems, comprising Lewis or Brønsted acids/bases. The 3D printed materials support extremely large strains and bulk Young's moduli as low as 260 kPa under aqueous conditions, well suited for biological applications – at comparable ease of use and spatial resolution as well-established commercially available polymer inks.

1. Introduction

3D microfabrication by multiphoton 3D laser printing (MPLP), also known as multiphoton lithography or direct laser writing, offers unparalleled precision and versatility in 3D microfabrication, enabling the creation of complex structures with nanoscale resolution.[1–6] This technology is driving advancements across a wide range of cutting-edge applications, from optics and photonics[7–13] to soft-robotics,[14–20] and biology.[21–24] As demand for these applications grows, developing printable materials or inks that meet specific requirements is crucial. Recent advances in materials such as fused silica and metal oxides have enabled the fabrication of stiff 3D microstructures,[25–30] but achieving soft and elastic materials with high precision at these scales remains challenging.

Currently, the design of inks for MPLP typically involves the incorporation of multifunctional monomers, molecules equipped with multiple photopolymerizable moieties, which enable fast efficient polymerization for the generation of stable 3D microstructures.[31,32] Thus, good printability is very often inevitably linked to the generation of highly crosslinked polymer networks and stiff materials. Therefore, the design of inks for 3D-printed soft and elastic structures typically involves an iterative process to find an optimum between desired mechanical properties and printability.[5] Reducing the crosslinking density and thereby reducing the stiffness, is usually achieved by either adding monofunctional monomers or solvents which significantly impact the printability by lowering achievable printing speeds and structural quality. Therefore, a major limitation of today's printable materials for MPLP is the lack of functional soft materials that enable fast and precise fabrication.[6,33,34] Filling this missing gap with a suitable material approach is of particular interest for advanced (biomedical) applications in the life sciences and flexible electronics.

One approach to overcome this challenge is the use of dynamic bonds, which allow fine-tuning of the crosslinking density and thus mechanical characteristics after printing. So far, reported strategies usually require multiple steps of chemical synthesis limiting wide-range applicability.[35–37] As an alternative, inks using supramolecular interactions based on ionic or hydrogen bonding could offer easily accessible and versatile systems. We have identified deep eutectic systems (DESs) as a promising class of materials for this approach.[38,39] DESs are liquid eutectic mixtures comprised of Lewis or Brønsted acids and bases. These mixtures are readily accessible, possess low volatility as well as tunable viscosity, and offer excellent media for dissolving a variety of polar and apolar compounds.[38,39] Polymerizable DESs,

P. Mainik, C. A. Spiegel, E. Blasco
Institute for Molecular Systems Engineering and Advanced Materials (IMSEAM)
Heidelberg University
69120 Heidelberg, Germany
E-mail: eva.blasco@uni-heidelberg.de
P. Mainik, C. A. Spiegel, E. Blasco
Institute of Organic Chemistry (OCI)
Heidelberg University
69120 Heidelberg, Germany
J. L. Schneider, M. Wegener
Institute of Applied Physics
Karlsruhe Institute of Technology (KIT)
76131 Karlsruhe, Germany
M. Wegener
Institute of Nanotechnology
Karlsruhe Institute of Technology (KIT)
76344 Eggenstein-Leopoldshafen, Germany

The ORCID identification number(s) for the author(s) of this article can be found under https://doi.org/10.1002/adma.202507640

DOI: 10.1002/adma.202507640

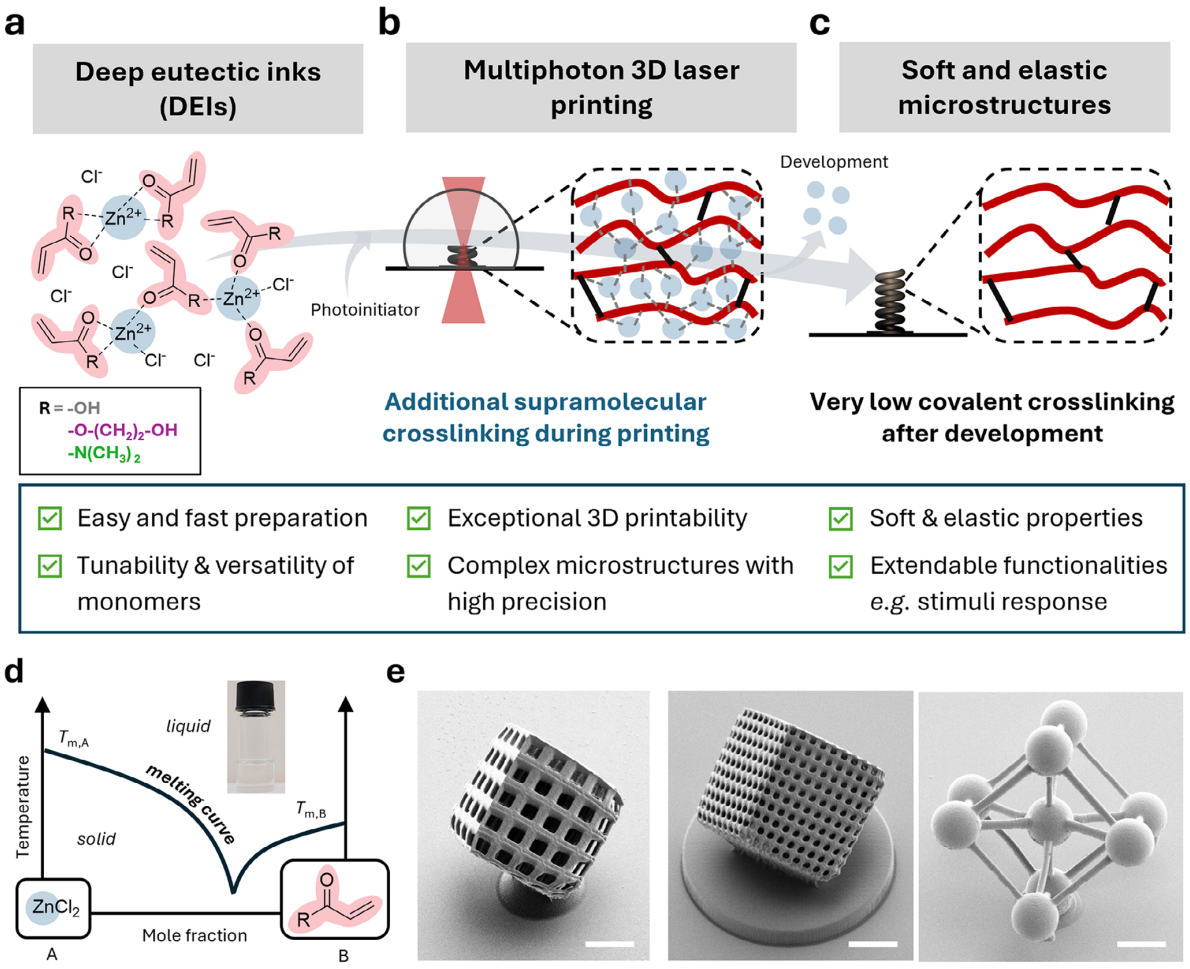

Figure 1. Deep eutectic systems (DESs) as versatile printable materials for multiphoton 3D laser printing (MPLP) enabling complex and soft 3D microstructures. a) We introduce deep eutectic mixtures based on acrylic acid (AAc), 2-hydroxyethyl acrylate (HEA), and *N*,*N*-dimethylacrylamide (DMAAm) and zinc chloride ($ZnCl_2$). The zinc ions interact with the acrylic monomers through ion-dipole and hydrogen bonds, forming "multi-functional" monomers that facilitate rapid photocrosslinking during the printing process. b) The supramolecular crosslinking enables fast printing and enhances the structural stability of the printed objects, allowing for the fabrication of 3D microstructures with intricate geometries and fine features. c) Developing and disrupting the supramolecular ion-dipole and hydrogen bonds results in a low-density crosslinked network that leads to highly elastic and soft 3D microstructures. d) Schematic illustration of the DEI phase diagram, where a transparent ink is formed from the 1:2 $ZnCl_2$/monomer mixtures (shown in the photograph). e) Exemplary scanning electron microscopy (SEM) images of 3D complex microstructures fabricated from DEIs. Scale bars 100 µm.

which contain at least one component that allows polymerization, have very recently raised interest in different fields.[40–46] However, this material class is completely unexplored for the fabrication of functional 3D/4D microstructures using MPLP.

Herein, we present for the first time the use of DESs for fast and efficient MPLP of soft and flexible 3D structures with high resolution. The printable mixtures consist almost entirely of monofunctional acrylic monomers with zinc chloride (**Figure 1**). Their unique supramolecular interactions facilitate outstanding printing performances with a wide range of readily available acrylic monomers and only minimal amounts of multifunctional monomers (<5 wt%). This enables rapid fabrication of soft, elastic, and even multi-responsive structures ranging from µm to mm sizes with high fidelity, that is unattainable by conventional printable materials.

2. Results and Discussion

2.1. Identification and Characterization of Suitable Deep Eutectic Systems

To bridge the current challenge of efficient MPLP of soft and elastic 3D/4D micro- to millimeter-sized structures, we explored DESs which provide supramolecular bonds during microprinting and can easily break during the development step leading to a low crosslinked network (Figure 1). In particular, deep eutectic

ADVANCED SCIENCE NEWS
www.advancedsciencenews.com

ADVANCED MATERIALS
www.advmat.de

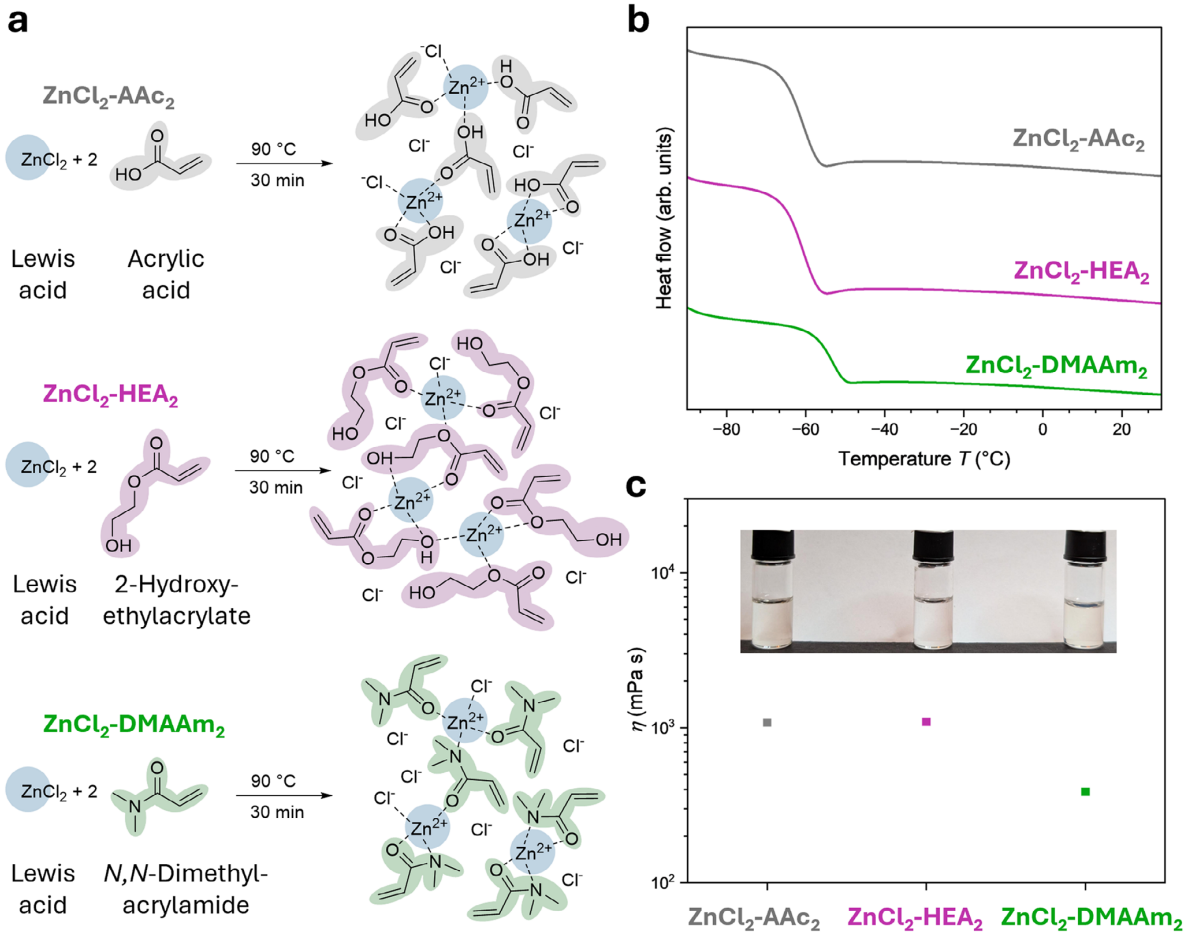

Figure 2. Preparation and characterization of DESs. a) Three different deep eutectic systems (DESs) were easily prepared by mixing acrylic monomers (acrylic acid, 2-hydroxyethyl acrylate, or *N,N*-dimethylacrylamide) with zinc chloride as a Lewis acid in a molar ratio of 2:1 at 90 °C for 30 min. b) DSC thermograms of the formed DESs, demonstrating their deep eutectic behavior. The three systems show glass transitions far below room temperature and the absence of additional melting transitions of the acrylic monomers. The thermographs are presented in stack with an offset for clarity. c) Dynamic viscosities of prepared DESs measured by rotational rheology at shear rates of 1000 s^{-1} with photograph of the prepared mixtures showing their optical transparency.

mixtures based on a metal halide and photopolymerizable acrylic monomers were explored. Zinc chloride was chosen as a suitable metal halide with a filled d^{10} shell for the preparation of colorless deep eutectic mixtures using different acrylic monomers – acrylic acid (AAc), 2-hydroxyethyl acrylate (HEA), and *N,N*-dimethylacrylamide (DMAAm) – in a 1:2 ratio $ZnCl_2$/monomer. Here, the zinc chloride is expected to form ion-dipole or hydrogen bonds with the acrylic monomers providing supramolecular entities that act as "multi-functional" monomers enabling fast crosslinking during MPLP. Afterward, the metal halide can be easily removed leaving behind a slightly crosslinked material.

The DESs were prepared in a facile way by stirring both components vigorously at elevated temperatures (90 °C) in a molar ratio *x* of 2:1 acrylic monomer to zinc chloride (see **Figure 2** and Experimental Section). After 30 min, the zinc chloride and acrylic monomers fully mixed into a colorless liquid which became highly viscous after cooling it to room temperature. The liquid state of the mixtures clearly indicated a phase transition below room temperature and deep eutectic behavior. The observed deep eutectic behavior was confirmed by performing differential scanning calorimetry (DSC) of all the analyzed mixtures (Figure 2). Importantly, the thermograms showed different behavior compared to the single components. For example, the melting point of acrylic acid at T_m = 9.5 °C was absent in the acrylic acid mixtures, instead a new glass transition appeared at T_g = −53.8 °C (Figure S1, Supporting Information). Similarly, the two DESs $ZnCl_2$-HEA_2 and $ZnCl_2$-$DMAAm_2$ also exhibited glass transitions at temperatures far below room temperature, i.e., −60.7 and −53.3 °C, respectively. The thermograms align well with previously reported behavior of deep eutectic mixtures.[47,48] The preparation of DESs with other molar ratios *x* was also possible allowing precise fine-tuning of the glass transition

(Figure S2, Supporting Information) as well as dynamic viscosity (see Figures S3 and S4, Supporting Information). ^{1}H NMR experiments indicated the presence of supramolecular interactions between the zinc chloride and the acrylic monomers (see Supporting Information).

The optical properties of the obtained DESs were also investigated. First, we determined the refractive indices (Figure S12, Supporting Information), which range from $\eta_{20\,^{\circ}C} = 1.48$–$1.52$ at the wavelength of the femtosecond pulsed laser $\lambda = 780$ nm. This range is comparable to indices of various commercially available inks (IP-S, IP-Dip, IP-L, OrmoComp, IP-Visio, and PO4) frequently used in MPLP.[49] Additionally, we have performed UV-vis and IR spectroscopy to study the absorption of the deep eutectic mixtures (see Supporting Information). Importantly, the three colorless mixtures showed no absorption between $\lambda = 380$–800 nm making it highly suitable for light-based laser printing at $\lambda = 780$ nm (Figure S13, Supporting Information). In addition to that, no photocuring was observed even after exposing them for 5 min to UV irradiation ($\lambda = 380$–400 nm). The stability under ambient light conditions facilitates future handling of the DESs. FTIR spectroscopy of $ZnCl_2$-AAc_2, $ZnCl_2$-HEA_2, and $ZnCl_2$-$DMAAm_2$ confirmed the presence of supramolecular interactions between zinc chloride and the employed monomers (Figures S14–S16, Supporting Information).

2.2. MPLP of Deep Eutectic Inks

Once thoroughly characterized, the DESs were formulated into deep eutectic inks (DEIs). MPLP of the DEIs was performed using a commercial printing set-up (Photonic GT2, Nanoscribe GmbH), which is based on a femtosecond laser at center wavelength $\lambda = 780$ nm. For this purpose, we first dissolved suitable photoinitiators known for efficient multiphoton polymerization such as phenylbis(2,4,6-trimethylbenzoyl)phosphine oxide (BAPO) or bis(diethylamino)benzophenone (BDEABP) directly in the DESs (**Figure 3** and Experimental Section). To investigate the printing performance of the optimized DEIs, we 3D printed benchmark boat microstructures (dimensions of 50 µm × 25 µm × 40 µm) with varying laser power and scanning speed (Figure S17, Supporting Information). Even without the addition of any covalent crosslinkers, micrometer-scale buckyballs with dimensions of 54 µm × 54 µm × 50 µm were successfully printed using a laser power of 20 mW and scanning speed of 40 mm s^{-1} (see Video S1 and Figure S18, Supporting Information).

Nevertheless, we found that the presence of very low amounts of covalent multifunctional crosslinker, i.e., PEGDA-M_n 700 (4-5 wt%), in the DEIs was beneficial to ensure the stability of the printed structures throughout development and in different media. Thus, we maintained a constant molar ratio of 86.5:1 employed acrylic monomer in the deep eutectic mixture to covalent multifunctional crosslinker PEGDA-M_n 700 in the final DEIs (Figure 3). The three prepared DEIs exhibited a broad printability window allowing exceptional printing speeds (>20 mm s^{-1}) at low laser powers (10-15 mW) (Figures S19–S21, Supporting Information), respectively. It should be noted that, in contrast to the frequently employed multifunctional monomers such as tri- or tetra-acrylates, the DEIs contained only very low amounts of covalent multifunctional photopolymerizable crosslinker (4-5 wt%). Nevertheless, the DEIs printability was found to reach the printing performance of these commonly used, highly sensitive materials for MPLP such as, for example, the commercially available IP-S (Nanoscribe GmbH) or of a custom-made ink composed of 99.5 wt% pentaerythritol triacrylate (PETA) and 0.5 wt% 7-diethylamino-3-thenoylcoumarin (DETC) (Figures S22 and S23, Supporting Information). This suggests that zinc chloride forms photocrosslinkable entities with acrylic monomers in the DESs mimicking the behavior of multifunctional photopolymerizable crosslinkers during printing. For example, a comparative ink with similar molar ratios, but without zinc chloride (Tables S1 and S2, Supporting Information), was not printable using the same range of printing parameters as depicted in Figure S24 (Supporting Information) and showed only a very narrow printability window leading solely to unstable microstructures even when using high laser power and low scanning speed (Figure S25, Supporting Information). The printability as well as the resolution of the printed DEIs was found to be similar or better compared to that of the commercially available soft material ink IP-PDMS (Nanoscribe GmbH) (see Table S3 and Figures S27–S30, Supporting Information).

To study the shape fidelity of the printed DEIs in water, we 3D printed free-standing net microstructures with dimensions of 25 µm × 25 µm × 10 µm and analyzed their deviations from the model by using confocal fluorescence microscopy. Quantitative analysis of the printed net microstructures revealed excellent shape fidelity for DEI1 and DEI2. The printed DEI3 showed minor relative deviations of ≈10% by swelling in water indicating hydrophilic properties (see Table S4 and Figure S31, Supporting Information).

To demonstrate printability, the three DEIs formulations were also used for the fabrication of complex free-standing larger millimeter-sized 3D structures such as an "Eschenheimer Turm" printed with DEI1, "Eiffel tower" printed with DEI2, or "Michelangelo's David" printed with DEI3 (Figure 3). The 3D-printed structures showed excellent shape fidelity as evidenced by the recorded SEM images. Furthermore, to show the stability of a mechanically highly demanding, delicate structure in water, we added rhodamine B methacrylate (0.01 wt% of total ink mass) as a fluorescent dye to DEI1 to perform confocal fluorescence microscopy after printing. This enabled, for example, the confocal imaging and 3D construction of a 3D microprinted "Atomium" with dimensions of 600 µm × 600 µm × 600 µm in aqueous media (Video S2, Supporting Information).

2.3. In-Depth Characterization of Printed Material

The resulting chemical composition of the printed materials was investigated spectroscopically and thermogravimetrically (see Supporting Information). The development process with isopropanol and water was found to remove almost all zinc ions resulting in a very low crosslinked network by breaking the supramolecular ion-dipole and hydrogen bonds. Residual traces of zinc ions could be successfully removed by employing an additional development step with a chelat binding ligand solution. Thus, the presence of zinc chloride plays a crucial role in the printability, but also can be easily removed having an impact on the final properties of the 3D printed materials.

ADVANCED SCIENCE NEWS
www.advancedsciencenews.com

ADVANCED MATERIALS
www.advmat.de

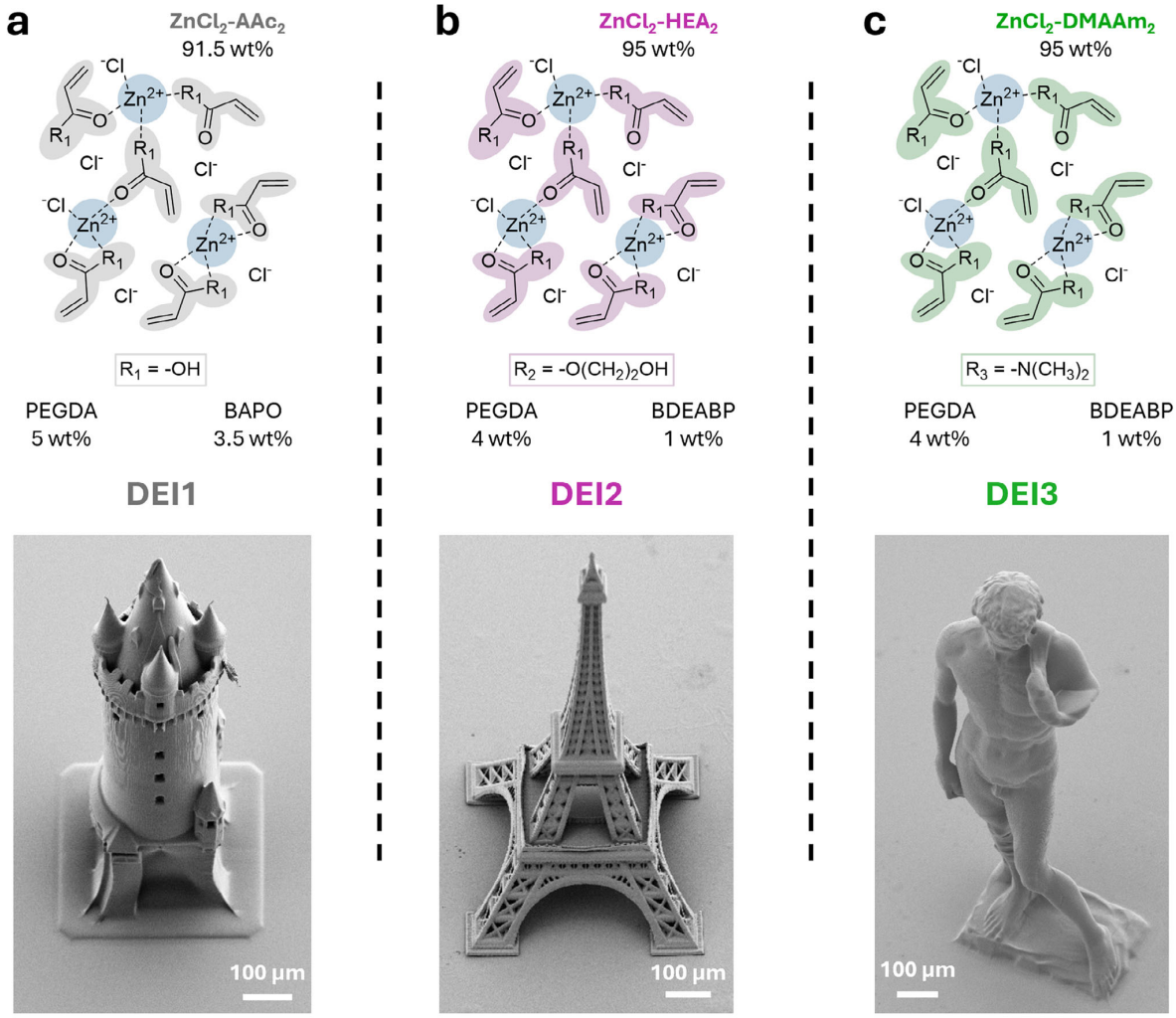

Figure 3. 3D microprinting in dip-in mode MPLP using DEIs. a) Ink composition of DEI1 (top) and exemplary SEM image of DEI1 printed "Eschenheimer Turm" (bottom). b) Ink composition of DEI2 (top) and SEM image of DEI2 printed "Eiffel tower" (bottom). c) Ink composition of DEI3 (top) and SEM image of DEI3 printed "Michelangelo's David". Notes: The inks have been prepared from the identified DESs $ZnCl_2$-AAc_2, $ZnCl_2$-HEA_2, $ZnCl_2$-$DMAAm_2$ as monomers, BAPO or BDEABP as photoinitiator, and small amounts of covalent crosslinker PEGDA M_n 700 as indicated for each case. The presence of very low amounts of PEGDA ensures better stability of the printed structures during development while keeping the main features of the materials.

As a next step, we studied the mechanical properties of the 3D printed DEIs using a custom-built compression set-up for measurements in the dry state and in water. For this purpose, we printed and analyzed cylindrical pillars of 400 µm in diameter and 300 µm in height (**Figure** 4 and Supporting Information).

The printed DEIs demonstrated a broad, tuneable range of Young's moduli in compression, ranging from 36 MPa in the dry state to 0.26 MPa in aqueous media (see Figure 4; Figures S37–S48 and Tables S5–S8, Supporting Information). These values are attributed to the low covalent crosslinker concentrations in the DEI formulations, which enable much softer mechanical properties than those observed in current commercial dip-in-compatible inks (Figure 4; Table S9, Supporting Information). For example, commercial inks such as IP-Q and IP-S exhibit Young's moduli in the GPa regime (3100 and 2100 MPa, in the dry state respectively). Compared to softer materials such as DE-GRAD (50–60 MPa) and particularly to IP-PDMS (15.3 MPa), DEIs offer a more versatile material platform, covering a wider mechanical spectrum in the low-modulus regime, while avoiding the limitations of hydrophobic, PDMS-based chemistries. DEIs exhibited Young´s moduli between 0.26 and 10 MPa under aqueous conditions. The significant variation in Young's modulus—spanning over two orders of magnitude—between the dry state and in water can be explained by material swelling. For the hydrophilic DEI1 and DEI3, based on poly(acrylic acid) and poly(dimethylacrylamide), Young's moduli in water were

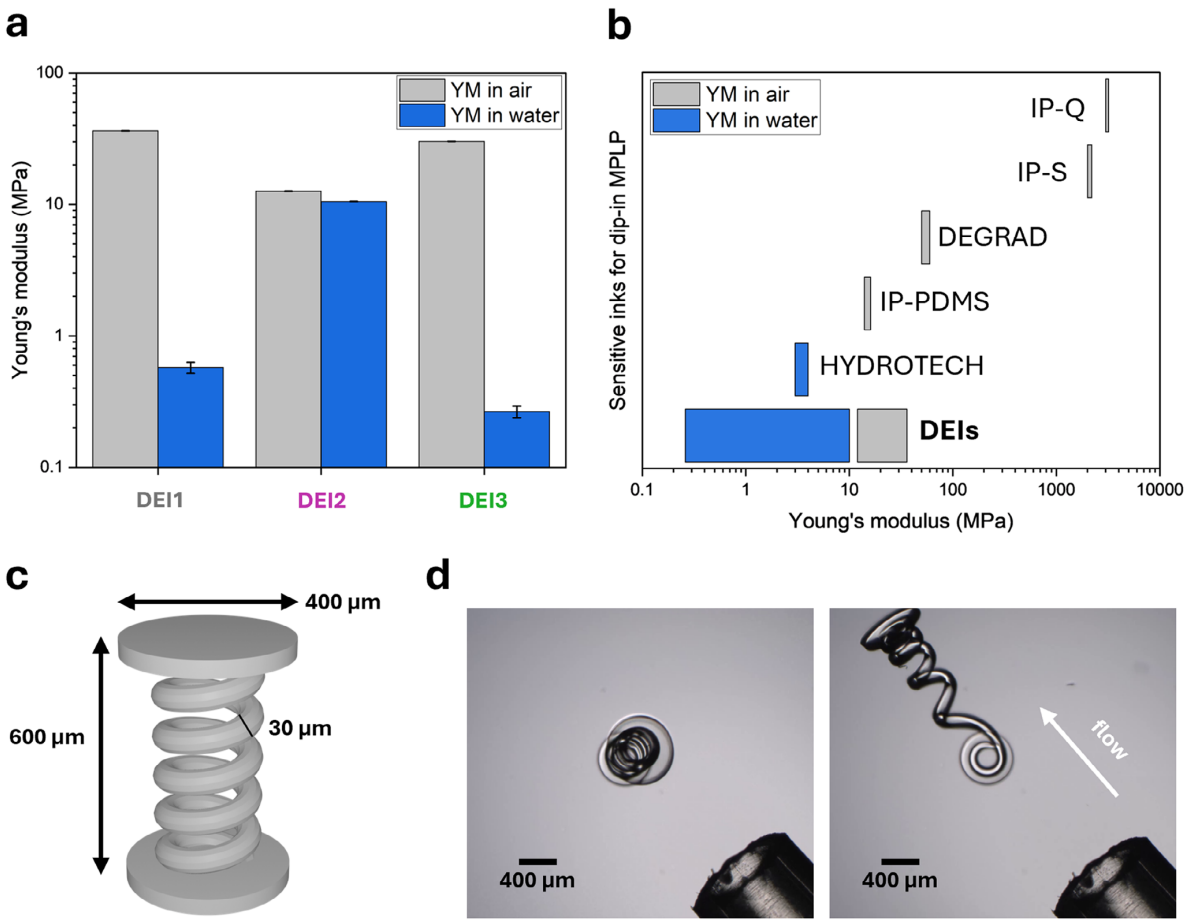

Figure 4. Mechanical characterization of the printed DEIs. The mechanical properties have been investigated quantitatively by compression experiments and qualitatively by flow-induced stretching/bending. a) Young's moduli of 3D printed DEIs in the dry state and in water have been determined by studying the compression of printed pillars with 400 µm diameter and 300 µm height, respectively. The Young's modulus has been calculated from force-strain displacement curves in the linear regime (see Tables S5 and S6, Supporting Information). b) Comparison of mechanical properties of different available material inks for dip-in mode MPLP. DEIs extend the range of accessible materials to the range of low Young's moduli (Table S9, Supporting Information).[50–52] c) 3D model of spring with dimensions of 600 µm in height, 100 µm in diameter, and 30 µm in thickness. d) 3D printed helical spring has been subjected to a water flow induced by a microliter pipette (Video S4, Supporting Information). The optical microscopy images have been recorded without flow (left) and with flow (right).

notably lower. In contrast, DEI2 showed similar Young's moduli both in air and in water. The printed pillars were compressible up to strain of 40% without observing any defects (Video S3, Supporting Information). It should be noted that conventional hydrogel inks often suffer from bad mechanical stability and are not comparable with DEI systems in terms of printability performance. To the best of our knowledge, the only commercially available hydrogel ink compatible with the dip-in mode for printing larger structures is HYDROTECH INX© X200, which exhibits a Young Modulus ≈3–4 MPa in aqueous media. However, DEIs not only cover this range but also reach significantly lower stiffness values in water—down to 260 kPa—thereby enabling the fabrication of highly compliant, responsive microstructures as demonstrated below.

To demonstrate the elastic material properties, we printed free-standing helical spring structures of DEI1 with dimensions of 600 µm in height, 100 µm in diameter, and 30 µm in thickness. After placing the springs in water, we induced a periodic flow with a microliter pipette (Figure 4; Video S4, Supporting Information). We observed a significant bending response of the spring. Stopping the flow resulted in the recovery of the 3D-printed initial state confirming the elasticity of the 3D-printed DEI.

2.4. Extending Functionality

We further demonstrated the versatility of the new ink design approach by first mixing the DESs with other monofunctional monomers. This allowed, for example, for the preparation of

ADVANCED SCIENCE NEWS
www.advancedsciencenews.com

ADVANCED MATERIALS
www.advmat.de

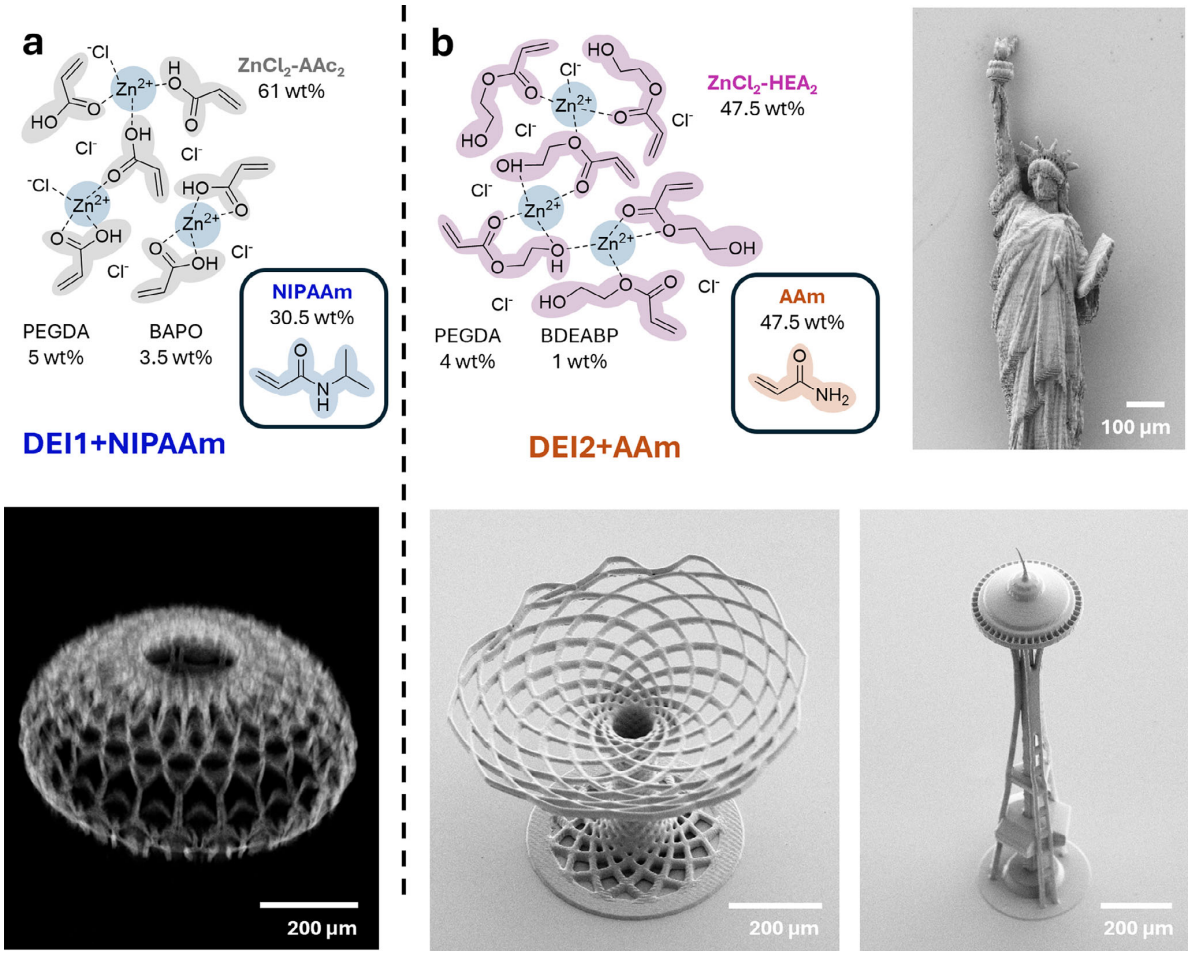

Figure 5. Functional 3D microstructures from DEIs. Further functionalities are introduced by mixing the different DEIs with other acrylic monomers. To prove the versatility, we have combined two identified DEIs, i.e., DEI1 and DEI2, with *N*-isopropylacrylamide (NIPAAm) – a well-known monomer leading to thermoresponsive polymers – or with acrylamide (AAm), respectively. a) DEI1+NIPAAm (top) has been employed to print, for example, the "Al Wasl Dome". A 3D reconstruction of the dome structure has been obtained using confocal fluorescence microscopy and verified its mechanical stability (bottom). Furthermore, the temperature-response of DEI1+NIPAAm has been studied in printed buckyball microstructures as well as multimaterial microgrippers (see Supporting Information). b) DEI2+AAm (top) has been successfully used for 3D microprinting of mechanically demanding structures such as, for example, the "Statue of liberty", "Seattle space needle", or the "Albero della vita" with high shape fidelity. SEM images of these printed structures are shown (right and bottom).

multicomponent DESs with monomers that could not be used with zinc chloride alone. For example, we combined the previously identified DESs with *N*-isopropyl acrylamide (NIPAAm) as well as acrylamide (AAm) (see Tables S10 and S11, Supporting Information). Both monomers showed good solubility in the identified DESs and were used for the preparation of the two DEIs, i.e., DEI1+NIPAAm and DEI2+AAm (**Figure 5**). Both exhibited printability in a printing parameter range similar to the three previously identified DEIs (Figures S50 and S55, Supporting Information). Printed DEI1+NIPAAm showed the expected multiresponsive behavior and could also be combined with other DEIs in multimaterial structures offering, for example, targeted directional actuation of responsive 3D structures (see Videos S5 and Video S6, and Figures S51–S54, Supporting Information). Furthermore, the addition of rhodamine B methacrylate (0.01 wt% of total ink mass) to DEI1+NIPAAm allowed for confocal fluorescence imaging of a delicate 3D printed "Al Wasl Dome" structure with dimensions of 600 µm × 600 µm × 400 µm (Video S7, Supporting Informations; Figure 5). DEI2+AAm was used to print a millimeter-scaled "Statue of liberty," the "Seattle space needle," and the "Albero della vita" with a laser power of 50 mW and scanning speed of 20 mm s^{-1} (Figure 5; Figure S56, Supporting Information). The recorded SEM images confirm the high quality and stability during printing of the mechanically demanding, very thin, and delicate structures. The optical microscopy images (Figure S57, Supporting Information) of the printed statue showed several fine detailed features such as the crown, face, and fire of the statue. Inspired by buildings constructed for the world

exhibition, we also printed the structurally demanding "Atomium". SEM images of this microarchitecture are included (Figure S58, Supporting Information).

3. Conclusion

The use of DESs in MPLP is proved to be an excellent approach to overcome existing limitations in combining the desired excellent printability of highly crosslinked materials with targeted soft mechanical properties. This goal is achieved by exploiting the present supramolecular interactions in the printing process which are later easily broken in the subsequent development step. Following this approach, the identified and presented DEI models exhibit exceptional printability performances with only a very low and tunable amount of covalent multifunctional crosslinker. This leads to a very low crosslinking density, which results in soft and elastic mechanical properties as well as significantly increasing responsive behavior in 4D microprinting applications. Furthermore, by adding other functional monomers, the functionality of the printed (multimaterial) structures can be easily extended while maintaining excellent printability.

Future efforts will effectively integrate DESs materials into applications in soft robotics, cell scaffold fabrication, metamaterial design, optics and photonics, sensors, and microelectromechanical systems. In addition to that, we believe our work on DEIs for 3D microprinting represents just the beginning of a wealth of new possibilities for ink design. The versatility and simplicity of the ink preparation significantly facilitates its handling for potential users across disciplines, thus ensuring its broad applicability.

4. Experimental Section

Materials: All chemicals and solvents were purchased from commercial suppliers and used without prior purification. In detail, zinc (II) chloride was purchased from TCI chemicals. Acrylic acid (AAc), 2-hydroxyethyl acrylate (HEA), polyethylene glycol diacrylate (M_n 700), *N,N*-dimethylacrylamide, BAPO, BDEABP, zincon, EDTA, and polyacrylic acid (M_n 20 000) were purchased from Merck. *N*-isopropylacrylamide (NIPAAm) and acrylamide (AAm) were purchased from BLDpharm. HPLC-grade isopropanol and water used in this work were purchased from Fisher Scientific. All chemicals, mixtures, inks, and samples were stored and handled under yellow light.

Preparation of DESs: DESs were prepared by adding the acrylic monomer to a flask with zinc (II) chloride in varying molar ratios. The prepared batches typically ranged from 5 g to 12 g by mass in total. The flask was heated to 90 °C for 30–60 min and vigorously stirred until a homogeneous, transparent, and liquid mixture was afforded. The obtained DESs remained liquid after cooling to room temperature and were used for the preparation of the ink.

Characterization of DESs: DSC was performed to characterize the deep eutectic behavior using the DSC 250 of TA Instruments in a temperature interval between 40 and −80 °C. The shown data is recorded from the second heating cycle.

The flow properties of the DESs were measured by rotational rheometry using a HAAKE MARS rheometer. The shear rate was varied between 1 and 1000 s^{-1} in 30 steps. The measured viscosity at 1000 s^{-1} is described in the results section.

1H NMR spectra were recorded using a Bruker Avance III 300 NMR spectrometer at room temperature and 300 MHz. The acrylic monomers were recorded in $CDCl_3$ as a solvent. The DESs were recorded in WILMAD NMR tubes with a coaxial insert tube filled with $CDCl_3$.

Refraction indices were determined at 20 °C for varying wavelengths using a Schmidt+Haensch ATR L refractometer. UV-vis spectroscopy and FT-IR of the deep eutectic mixtures were measured with a Jasco V-770 and a Jasco FT/IR-4600 spectrometer, respectively.

Preparation of DEIs: DEIs were prepared by mixing the DESs of interest with PEGDA as a covalent crosslinker in a molar ratio of 0.0116 mol% (4-5 wt%) polymerizable molecules. The photoinitiator, i.e., BAPO or BDEABP, was selected based on solubility in the DEI and added in a concentration of 3.5 or 1.0 wt%, respectively. Rhodamine B methacrylate was added to the DEI in a concentration of 0.01 wt% to achieve covalent incorporation of a fluorescent dye for confocal microscopy imaging.

Silanization Procedure: Glass coverslips (Marienfeld, 170 ± 5 µm) were washed with isopropanol and acetone and dried with pressurized nitrogen. Subsequently, the surface of all slides was activated for 1 min by plasma treatment using a TDK PiezoBrush. Afterward, the coverslips were immersed in a 4 mM solution of 3-(trimethoxysilyl)propyl acrylate in toluene for 1.5 h. Last, the acrylate-functionalized coverslips were washed twice in toluene and once in acetone and used as substrates for microprinting.

Multiphoton 3D Laser Printing: MPLP was performed with a commercially available set-up (Photonic Professional GT2, Nanoscribe GmbH & Co. KG) using a 63× objective (NA = 1.4), 25× objective (NA = 0.8) or 10× objective (NA = 0.3) from Zeiss for focusing the femtosecond laser with a center wavelength of 780 nm. All microstructures were printed using an oil immersion (63× and 25×) or dip-in (10×) configuration. The procedure reported by Toulouse et al. was used for the 10× objective.[53] Before printing, GWL files were generated with the Describe software (Nanoscribe GmbH) from previously designed STL files of desired geometries by setting slicing and hatching to 300 nm (25×) or 5 µm and 1 µm (10×) for all printed geometries, respectively. The structures were developed in isopropanol or propylene glycol methyl ether acetate depending on the printed material to remove uncured ink. After development, the printed structures were subjected to air drying before analysis. The printing parameters for the shown demonstrating structures are included in the Supporting Information.

Optical Microscopy: Optical images were recorded with a Zeiss Axio Imager M2 microscope using a 5× long-distance Zeiss objective (NA = 0.13) or a LD Plan-Neofluar 20×/0.4 Korr Ph M27 objective (NA = 0.4) and an Axiocam 705 microscope camera.

Scanning Electron Microscopy: All SEM images were acquired using a Zeiss Supra 55VP (Carl Zeiss AG) instrument at 3–5 kV in secondary electron mode. Prior to imaging, the structures were sputter coated with a Pt–Pd layer of 12 nm. The structures were imaged from in top view or in side view (40°).

Confocal Laser Scanning Microscopy: Confocal fluorescence microscopy was performed using a Nikon A1R confocal microscope (10×, NA = 0.45 and 20×, NA = 0.75) equipped with GaAsP-detectors by exciting the covalently incorporated rhodamine B methacrylate dye with 561 nm laser and detecting the fluorescence at 595 nm. To enable confocal fluorescence imaging of DEI1 or DEI3, rhodamine B methacrylate was added as 0.01 wt% to the total ink mass. DEI2 was imaged using an excitation laser wavelength of 488 nm. Confocal imaging of printed IP-PDMS was performed using an excitation laser wavelength of 404 nm. The Atomium structure was recorded in HPLC grade water and the "Al Wasl Dome" structure was recorded in a solution of 70% ethanol and 30% HPLC water.

Analysis of Temperature-Responsive Behavior: Heating of printed structures was performed with a heating stage (LTS 420, Linkam Scientific Instruments) in the optical microscope. The transmission illumination mode was used for imaging. The investigated temperature program started at 25 °C and heated the *N*-isopropylacrylamide containing printed structures up to 60 °C using a gradient of 5 °C min^{-1}. The heated microstructures were subsequently cooled using a gradient of 5 °C min^{-1} back to room temperature. The swelling factor S_V was calculated by estimating the volume from the top area of the printed structure.

Analysis of pH- and Calcium-Responsive Behavior: Calcium-responsive behavior was analyzed by washing the 3D printed structures several times with a calcium chloride solution (0.24 g mL^{-1}). The pH response was

ADVANCED SCIENCE NEWS
www.advancedsciencenews.com

ADVANCED MATERIALS
www.advmat.de

analyzed by washing the structures several times with an aqueous sodium hydroxide solution with a pH of 10.6.

Characterization of Chemical Composition of 3D Printed DEI1: FT-IR spectra of 3D printed cubes (50 µm × 50 µm × 20 µm) were acquired using a Bruker Lumos II and averaged for five structures. UV-vis spectra of the Zincon solution (1 mL, 188 µM) were recorded with a Jasco V-770 spectrometer. Thermogravimetry (TGA) of 3D printed cubes (500 µm × 500 µm × 1 mm) was performed in a nitrogen flow (50 mL min^{-1}) using a TGA 2 of Mettler Toledo and heating from 30 to 600 °C with rate of 10 °C min^{-1}.

Mechanical Characterization of Printed DEIs: The mechanical characterization of the presented materials was performed by conducting uniaxial-loading experiments using a home-built setup (Figure S35A, Supporting Information). This setup was previously used in slightly different configurations.[54,55]

For each material, six pillar samples were printed on glass coverslips (Marienfeld, 170 µm ± 5 µm) with dimensions of 300 µm in height and 400 µm in diameter with the following printing parameter using the 10× objective and dip-in configuration: laser power 100%, scanning speed 20 mm s^{-1}, slicing 5 µm, and hatching 1 µm.

To prevent warping of the substrates during the measurements, all substrates were mounted onto cleaned soda-lime glass (Nanoscribe GmbH & Co. KG, 25 mm × 25 mm × 0.7 mm) and fixed via a thin layer of glue (UHU, Plast Special), distributed with a syringe. After mounting, the samples were air-dried for 24 h. Samples measured in aqueous media required additional preparation steps; therefore, optical transparent cuvettes (Brand GmbH & Co. KG, 12.5 mm × 12.5 mm × 45 mm) were cut into pieces (12.5 mm × 12.5 mm × 3 mm) and coated on the underside with UV-glue (Best Uvirapid 702, BEST Klebstoffe). The UV-glue allows for alignment and centering the cuvette pieces around the pillar arrays on the substrates, before curing and sealing them with an UV-LED flashlight for 2 min (Figure S35C, Supporting Information).

To obtain the effective spring constant and the Young's modulus of the materials, four out of six pillars for each material were measured as follows:

The substrate was placed and tightly fixed on the sample holder underneath the stamp. The stamp itself was centered around a pillar and loaded the pillar by a prescribed displacement normal to the substrate surface, gradually moving down along the *z*-direction by the translation stages. After reaching the maximum displacement, the stamp unloads the sample. During loading and unloading, the force is recorded by the force sensor. Loading and unloading cycles are repeated ten times with a delay time of 40 s between each cycle. To ensure sufficient initial contact between the stamp and the sample, the alignment is observed by the cameras. An illustration of a measurement cycle can be seen in Video S3 (Supporting Information).

For the measurements in aqueous media, the samples were stored 2 h in deionized water before conducting the experiments. In between the measurements, evaporated water was replaced with a pipette to prevent drying out of the samples.

Supporting Information

Supporting Information is available from the Wiley Online Library or from the author.

Acknowledgements

The authors acknowledge funding from the Deutsche Forschungsgemeinschaft (DFG, German Research Foundation) via the Excellence Cluster "3D Matter Made to Order" (EXC-2082/1-390761711), NSF-DFG Lead Agency Activity on Chemistry and Transport in Confined Spaces "NSF-DFG Confine" (BL1604/4-1), and the Carl Zeiss Foundation through the "Carl-Zeiss Foundation-Focus@HEiKA". The authors gratefully acknowledge the data storage service "SDS@hd" supported by the Ministry of Science, Research and the Arts Baden-Württemberg (MWK) and the German Research Foundation (DFG) through grant INST 35/1503-1 FUGG. The authors also express their gratitude to Rasmus R. Schröder, Irene Wacker, and Ronald E. Curticean for providing access and training to scanning electron microscopes. The authors also thank Finn Kröger and Fabian Lill for assistance with UV–vis and IR spectroscopy as well as Hoang Bao Duc Tran for performing scanning electron microscopy.

Open access funding enabled and organized by Projekt DEAL.

Conflict of Interest

Philipp Mainik, Christoph A. Spiegel, and Eva Blasco have filed a patent application on deep eutectic inks for MPLP.

Data Availability Statement

The data that support the findings of this study are openly available in heiData, a data repository of Heidelberg University at https://doi.org/10.11588/DATA/UP26J7, reference number 1011588.

Keywords

4D printing, light-based 3D printing, polymerizable deep eutectic solvents, soft materials, stimuli-responsive polymers

Received: April 24, 2025
Revised: June 13, 2025
Published online:

[1] M. Carlotti, V. Mattoli, *Small* **2019**, *15*, 1902687.
[2] J.-F. Xing, M.-L. Zheng, X.-M. Duan, *Chem. Soc. Rev.* **2015**, *44*, 5031.
[3] *Multiphoton Lithography: Techniques, Materials and Applications*, (Eds.: J. Stampf, R. Liska, A. Ovsianikov) Wiley-VCH, Wien, Austria **2017**.
[4] P. Mainik, C. A. Spiegel, E. Blasco, *Adv. Mater.* **2024**, *36*, 2310100.
[5] E. Skliutas, G. Merkininkaitė, S. Maruo, W. Zhang, W. Chen, W. Deng, J. Greer, G. von Freymann, M. Malinauskas, *Nat. Rev. Methods Primers* **2025**, *5*, 15.
[6] S. O'Halloran, A. Pandit, A. Heise, A. Kellett, *Adv. Sci.* **2023**, *10*, 2204072.
[7] T. Gissibl, S. Thiele, A. Herkommer, H. Giessen, *Nat. Photonics* **2016**, *10*, 554.
[8] S. Thiele, K. Arzenbacher, T. Gissibl, H. Giessen, A. M. Herkommer, *Sci. Adv.* **2017**, *3*, 1602655.
[9] H. Wang, W. Zhang, D. Ladika, H. Yu, D. Gailevičius, H. Wang, C.-F. Pan, P. N. S. Nair, Y. Ke, T. Mori, J. Y. E. Chan, Q. Ruan, M. Farsari, M. Malinauskas, S. Juodkazis, M. Gu, J. K. W. Yang, *Adv. Funct. Mater.* **2023**, *33*, 2214211.
[10] L. Siegle, S. Ristok, H. Giessen, *Opt. Express* **2023**, *31*, 4179.
[11] D. Gonzalez-Hernandez, S. Varapnickas, A. Bertoncini, C. Liberale, M. Malinauskas, *Adv. Opt. Mater.* **2023**, *11*, 2201701.
[12] C. A. Richards, C. R. Ocier, D. Xie, H. Gao, T. Robertson, L. L. Goddard, R. E. Christiansen, D. G. Cahill, P. V. Braun, *Nat. Commun.* **2023**, *14*, 3119.
[13] C. R. Ocier, C. A. Richards, D. A. Bacon-Brown, Q. Ding, R. Kumar, T. J. Garcia, J. van de Groep, J.-H. Song, A. J. Cyphersmith, A. Rhode, A. N. Perry, A. J. Littlefield, J. Zhu, D. Xie, H. Gao, J. F. Messinger, M. L. Brongersma, K. C. Toussaint, L. L. Goddard, P. V. Braun, *Light Sci. Appl.* **2020**, *9*, 196.
[14] M. Del Pozo, C. Delaney, M. Da Pilz Cunha, M. G. Debije, L. Florea, A. P. H. J. Schenning, *Small Struct.* **2022**, *3*, 2100158.

[15] L. V. Elliott, E. E. Salzman, J. R. Greer, *Adv. Funct. Mater.* **2021**, *31*, 2008380.
[16] C. A. Spiegel, M. Hackner, V. P. Bothe, J. P. Spatz, E. Blasco, *Adv. Funct. Mater.* **2022**, *32*, 2110580.
[17] H. Zeng, D. Martella, P. Wasylczyk, G. Cerretti, J.-C. G. Lavocat, C.-H. Ho, C. Parmeggiani, D. S. Wiersma, *Adv. Mater.* **2014**, *26*, 2319.
[18] H. Jia, J. Flommersfeld, M. Heymann, S. K. Vogel, H. G. Franquelim, D. B. Brückner, H. Eto, C. P. Broedersz, P. Schwille, *Nat. Mater.* **2022**, *21*, 703.
[19] D. Jin, Q. Chen, T.-Y. Huang, J. Huang, L. Zhang, H. Duan, *Mater. Today* **2020**, *32*, 19.
[20] X. Wang, X.-H. Qin, C. Hu, A. Terzopoulou, X.-Z. Chen, T.-Y. Huang, K. Maniura-Weber, S. Pané, B. J. Nelson, *Adv. Funct. Mater.* **2018**, *28*, 868.
[21] F. Klein, T. Striebel, J. Fischer, Z. Jiang, C. M. Franz, G. von Freymann, M. Wegener, M. Bastmeyer, *Adv. Mater.* **2010**, *22*, 868.
[22] C. Greant, B. van Durme, J. van Hoorick, S. van Vlierberghe, *Adv. Funct. Mater.* **2023**, *33*, 2212641.
[23] M. Dong, X. Wang, X.-Z. Chen, F. Mushtaq, S. Deng, C. Zhu, H. Torlakcik, A. Terzopoulou, X.-H. Qin, X. Xiao, J. Puigmartí-Luis, H. Choi, A. P. Pêgo, Q.-D. Shen, B. J. Nelson, S. Pané, *Adv. Funct. Mater.* **2020**, *30*, 1910323.
[24] S. Grebenyuk, A. R. Abdel Fattah, M. Kumar, B. Toprakhisar, G. Rustandi, A. Vananroye, I. Salmon, C. Verfaillie, M. Grillo, A. Ranga, *Nat. Commun.* **2023**, *14*, 193.
[25] J. Bauer, C. Crook, T. Baldacchini, *Science* **2023**, *380*, 960.
[26] Y. Wang, C. Yi, W. Tian, F. Liu, G. J. Cheng, *Nat. Mater.* **2024**, *23*, 1645.
[27] H. Hu, C. Deng, H. Gao, T. Han, S. Xue, Y. Tang, M. Zhang, M. Li, H. Liu, L. Deng, W. Xiong, *Adv. Mater.* **2024**, *36*, 2405053.
[28] F. Li, S.-F. Liu, W. Liu, Z.-W. Hou, J. Jiang, Z. Fu, S. Wang, Y. Si, S. Lu, H. Zhou, D. Liu, X. Tian, H. Qiu, Y. Yang, Z. Li, X. Li, L. Lin, H.-B. Sun, H. Zhang, J. Li, *Science* **2023**, *381*, 1468.
[29] A. Vyatskikh, R. C. Ng, B. Edwards, R. M. Briggs, J. R. Greer, *Nano Lett.* **2020**, *20*, 3513.
[30] T. Rosental, A. Ottomaniello, S. Mizrahi, N. Menda, M. Y. Moshkovitz Douvdevany, L. Larush, D. Savraeva, N. Jarach, V. Mattoli, S. Magdassi, *Addit. Manuf.* **2024**, *92*, 104388.
[31] C. Barner-Kowollik, M. Bastmeyer, E. Blasco, G. Delaittre, P. Müller, B. Richter, M. Wegener, *Angew. Chem.* **2017**, *56*, 15828.
[32] Y. Zhang, H. Yu, X. Zhang, J. Zheng, J. Wang, H. Guo, Y. Qiu, X. Wang, L. Liu, W. J. Li, *Adv. Funct. Mater.* **2024**, *34*, 2313922.
[33] A. Balena, M. Bianco, F. Pisanello, M. de Vittorio, *Adv. Funct. Mater.* **2023**, *33*, 2211773.
[34] G. Zyla, M. Farsari, *Laser Photonics Rev.* **2024**, *18*, 2301312.
[35] D. Gräfe, S. L. Walden, J. Blinco, M. Wegener, E. Blasco, C. Barner-Kowollik, *Angew. Chem.* **2020**, *59*, 6330.
[36] S. C. Gauci, K. Ehrmann, M. Gernhardt, B. Tuten, E. Blasco, H. Frisch, V. Jayalatharachchi, J. P. Blinco, H. A. Houck, C. Barner-Kowollik, *Adv. Mater.* **2023**, *35*, 2300151.
[37] D. Gräfe, M. Gernhardt, J. Ren, E. Blasco, M. Wegener, M. A. Woodruff, C. Barner-Kowollik, *Adv. Funct. Mater.* **2021**, *31*, 2006998.
[38] E. L. Smith, A. P. Abbott, K. S. Ryder, *Chem. Rev.* **2014**, *114*, 11060.
[39] B. B. Hansen, S. Spittle, B. Chen, D. Poe, Y. Zhang, J. M. Klein, A. Horton, L. Adhikari, T. Zelovich, B. W. Doherty, B. Gurkan, E. J. Maginn, A. Ragauskas, M. Dadmun, T. A. Zawodzinski, G. A. Baker, M. E. Tuckerman, R. F. Savinell, J. R. Sangoro, *Chem. Soc. Rev.* **2021**, *121*, 1232.
[40] L. Cai, G. Chen, J. Tian, B. Su, M. He, *Chem. Mater.* **2021**, *33*, 2072.
[41] G. Zhu, M. Liu, S. Weng, G. Zhang, Y. Hu, Z. Kou, C. Bo, L. Hu, S. Wu, Y. Zhou, *Chem. Eng. J.* **2023**, *472*, 144987.
[42] L. Cai, G. Chen, B. Su, M. He, *Chem. Eng. J.* **2021**, *426*, 130545.
[43] C.-W. Lai, S.-S. Yu, *ACS Appl. Mater. Interfaces* **2020**, *12*, 34235.
[44] M. L. Picchio, A. Dominguez-Alfaro, R. J. Minari, J. D. Mota-Morales, D. Mecerreyes, *J. Mater. Chem. C* **2024**, *12*, 11265.
[45] X. Luo, H. Wu, C. Wang, Q. Jin, C. Luo, G. Ma, W. Guo, Y. Long, *Chem. Eng. J.* **2024**, *483*, 149330.
[46] L. C. Tomé, D. Mecerreyes, *J. Phys. Chem. B* **2020**, *124*, 8465.
[47] A. Shishov, P. Makoś-Chełstowska, A. Bulatov, V. Andruch, *J. Phys. Chem. B* **2022**, *126*, 3889.
[48] R. Craveiro, I. Aroso, V. Flammia, T. Carvalho, M. T. Viciosa, M. Dionísio, S. Barreiros, R. L. Reis, A. Duarte, A. Paiva, *J. Mol. Liq.* **2016**, *215*, 534.
[49] M. Schmid, D. Ludescher, H. Giessen, *Opt. Mater. Express* **2019**, *9*, 4564.
[50] Nanoscribe GmbH & Co. KG, Products, Available photoresins for dip-in MPLP **2025**, https://www.nanoscribe.com/fileadmin/Nanoscribe/PDF/Product_Folder/Folder-Printing-Materials-2025.pdf (accessed: June 2025).
[51] BioINX, Products, DEGRAD photoresin for dip-in MPLP **2025**, https://bioinx.com/sites/default/files/product_files/Degrad%20INX%20ž100%20Product%20Information%20Sheet.pdf (accessed: June 2025).
[52] BioINX, Products, HYDROTECH photoresin for dip-in MPLP **2025**, https://bioinx.com/sites/default/files/product_files/hydrotech%20ž200%20product%20information%20sheet.pdf (accessed: June 2025).
[53] A. Toulouse, S. Thiele, K. Hirzel, M. Schmid, K. Weber, M. Zyrianova, H. Giessen, A. M. Herkommer, M. Heymann, *Opt. Mater. Express* **2022**, *12*, 3801.
[54] Y. Chen, J. L. G. Schneider, K. Wang, P. Scott, S. Kalt, M. Kadic, M. Wegener, *Nat. Commun.* **2024**, *15*, 8882.
[55] T. Frenzel, M. Kadic, M. Wegener, *Science* **2017**, *358*, 1072.

WILEY-VCH

Supporting Information

Deep Eutectic Inks for Multiphoton 3D Laser Microprinting

*Philipp Mainik, Christoph A. Spiegel, Jonathan L.G. Schneider, Martin Wegener, Eva Blasco**

P. Mainik, C. A. Spiegel, E. Blasco
Institute for Molecular Systems Engineering and Advanced Materials (IMSEAM), Heidelberg University, 69120 Heidelberg, Germany
E-mail: eva.blasco@uni-heidelberg.de

P. Mainik, C. A. Spiegel, E. Blasco
Institute of Organic Chemistry (OCI), Heidelberg University, 69120 Heidelberg, Germany

J. L.G. Schneider, M. Wegener
Institute of Applied Physics, Karlsruhe Institute of Technology (KIT), 76131 Karlsruhe, Germany

M. Wegener
Institute of Nanotechnology, Karlsruhe Institute of Technology (KIT), 76344 Eggenstein-Leopoldshafen, Germany.

Table of Contents

Differential scanning calorimetry of identified DESs

DSC measurements of $ZnCl_2$-AAc_x mixtures with varying molar ratio x were performed and compared to thermograms of the starting compounds, *i.e.* acrylic acid and zinc chloride. The characteristic peak in the thermogram at the melting temperature of acrylic acid (T_m = 10 °C) vanishes in the deep eutectic mixtures. Instead, a new glass transition appears in a temperature range between -66.4 °C to -45 °C.

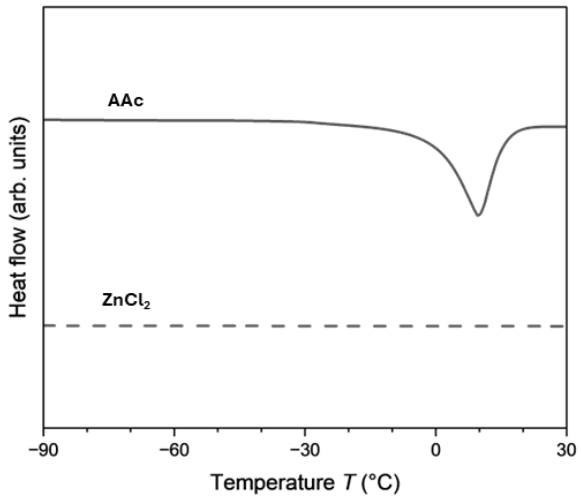

Figure S1: DSC thermogram of the starting compounds $ZnCl_2$ and acrylic acid. The stack is shown with an offset. The melting point of AAc vanishes in the DSC thermograms of the $ZnCl_2$-AAc_x.

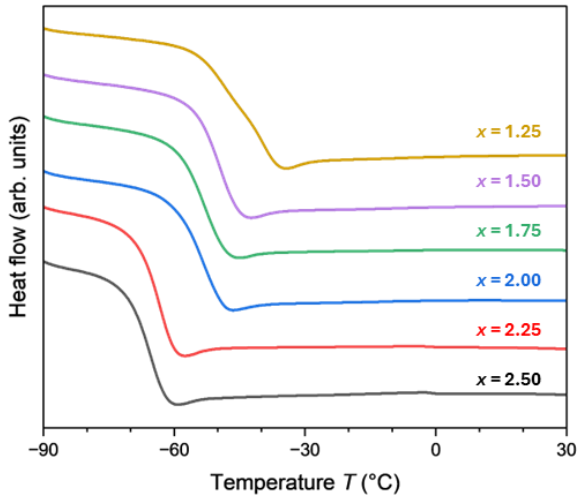

Figure S2: DSC thermogram of $ZnCl_2$-AAc_x with varying molar ratio x from 1.25 to 2.50. The stack is shown with an offset.

Rotational rheology of identified DESs

Rheological analysis of $ZnCl_2$ and acrylic acid containing DESs was performed by rotational rheology. Increasing the molar ratio x of the acrylic acid in the $ZnCl_2$-AAc_x systems allowed for tuning the dynamic viscosity in a range between 2×10^4 mPa s to 2×10^2 mPa s.

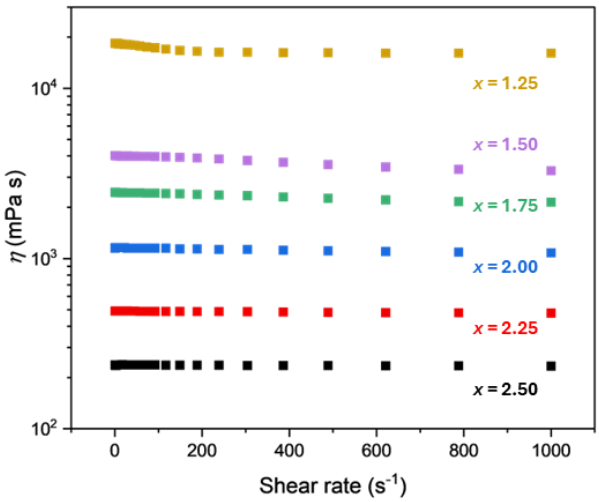

Figure S3: Rotational rheology measurements. Dynamic viscosity of DESs $ZnCl_2$-AAc_x for varying shear rates. Higher molar ratios x reduced the viscosity of the DES.

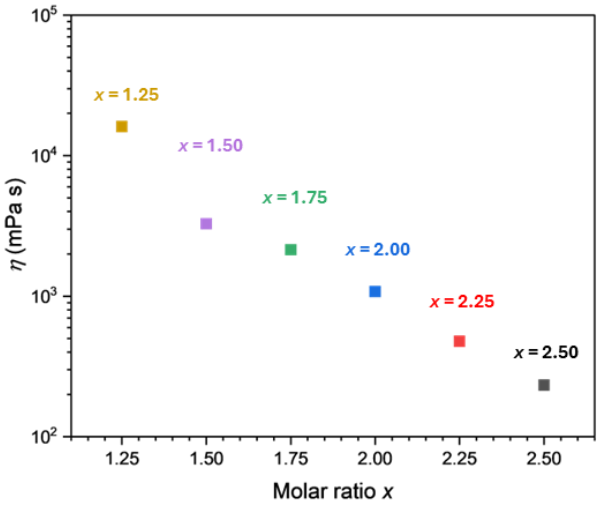

Figure S4: Tunable dynamic viscosity depending on the molar ratio x in $ZnCl_2$-AAc_x. The viscosity was determined at a shear rate of 1000 Hz by rotational rheology, respectively.

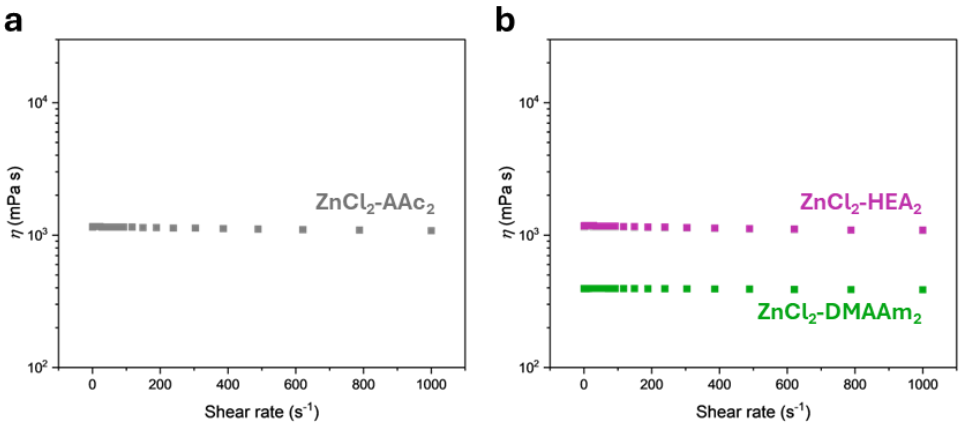

Figure S5: Dynamic viscosities of the three DESs for varying shear rates from rotational rheology measurements. $ZnCl_2$-AAc_2 (in **a**) and $ZnCl_2$-HEA_2 (in **b**) show similar viscosities. $ZnCl_2$-$DMAAm_2$ shows lower viscosities compared to the other two systems.

NMR spectroscopy of identified DESs

^{1}H NMR spectroscopy was performed of the starting acrylic monomers and the identified DESs. The acrylic monomers were dissolved and measured in $CDCl_3$. The DESs were measured using a coaxial insert tube filled with $CDCl_3$. In general, the DESs showed significant broadening of the ^{1}H NMR bands which can be related to the increase in viscosity.

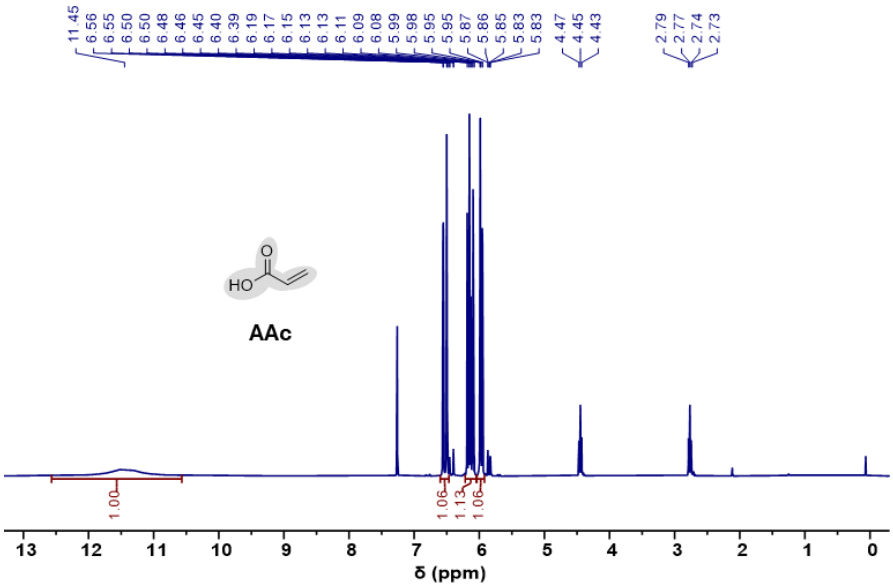

Figure S6: ^{1}H NMR spectrum (300 MHz, $CDCl_3$, room temperature) of acrylic acid.

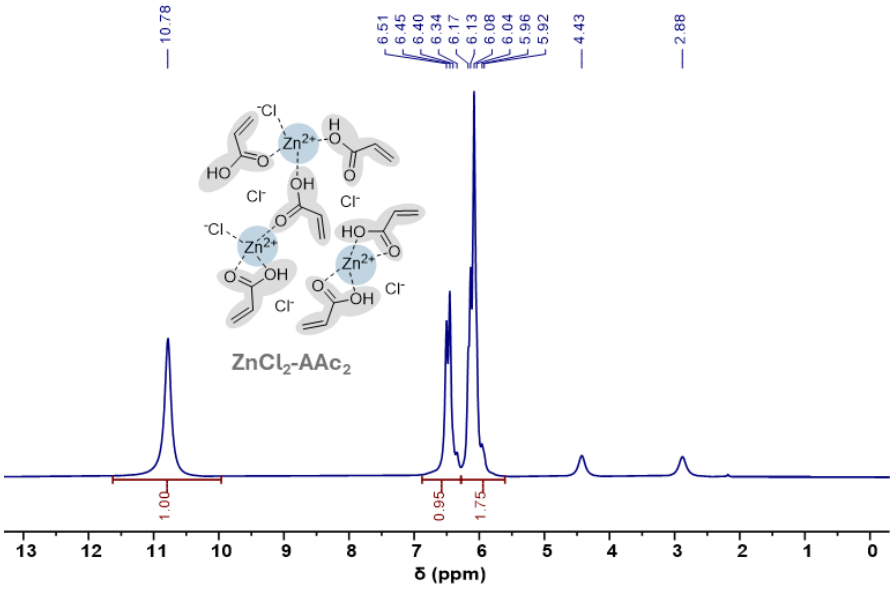

Figure S7: ^{1}H NMR spectrum (300 MHz, $CDCl_3$, room temperature) of $ZnCl_2$-AAc_2.

The δ-shift of the hydroxy proton in $ZnCl_2$-HEA_2 (compared to HEA) indicates a coordination of hydroxy groups to zinc ions (see **Figure S8** and **Figure S9**).

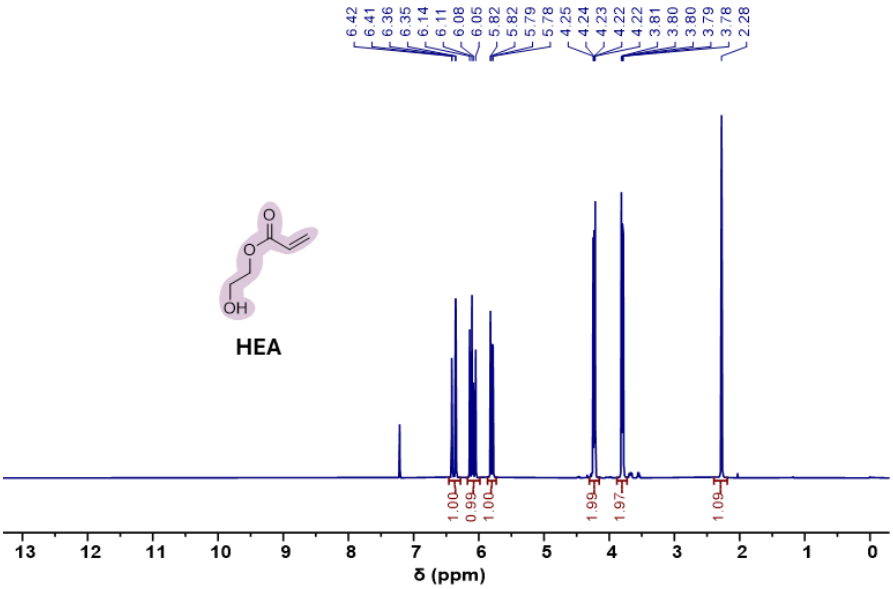

Figure S8: ^{1}H NMR spectrum (300 MHz, $CDCl_3$, room temperature) of 2-hydroxyethyl acrylate.

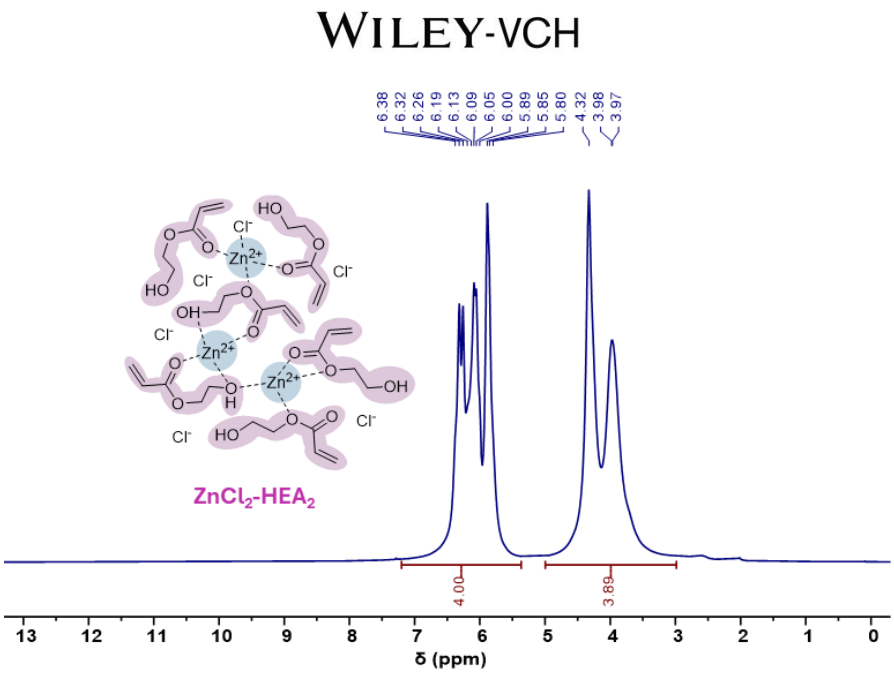

Figure S9: ^{1}H NMR spectrum (300 MHz, $CDCl_3$, room temperature) of $ZnCl_2$-HEA_2. In the DES, the signal for the hydroxy group is shifted towards higher ppm.

The doublet splitting of the methyl groups in $ZnCl_2$-$DMAAm_2$ (compared to DMAAm) indicate a strong coordination and polarization of the amide bond (see **Figure S10** and **Figure S11**).

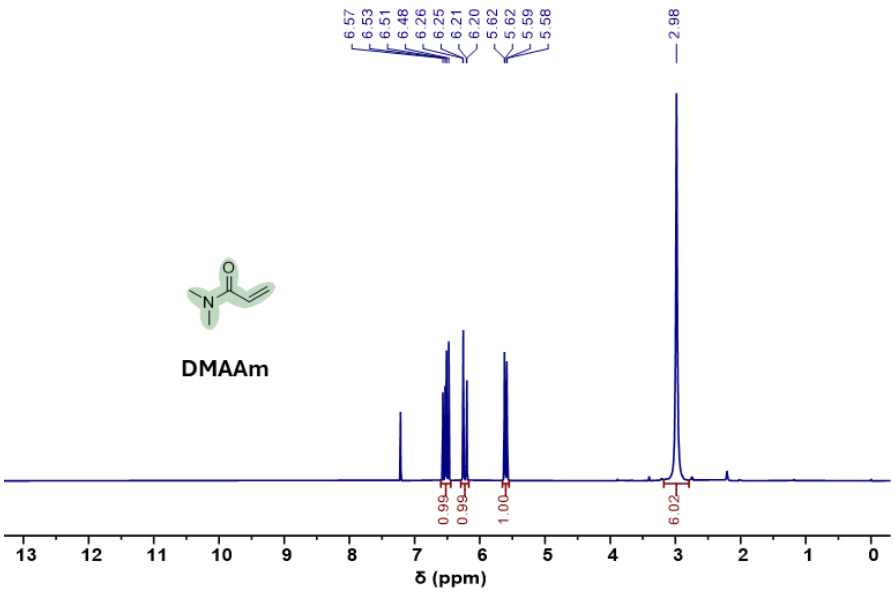

Figure S10: ^{1}H NMR spectrum (300 MHz, $CDCl_3$, room temperature) of *N*,*N*-dimethylacrylamide.

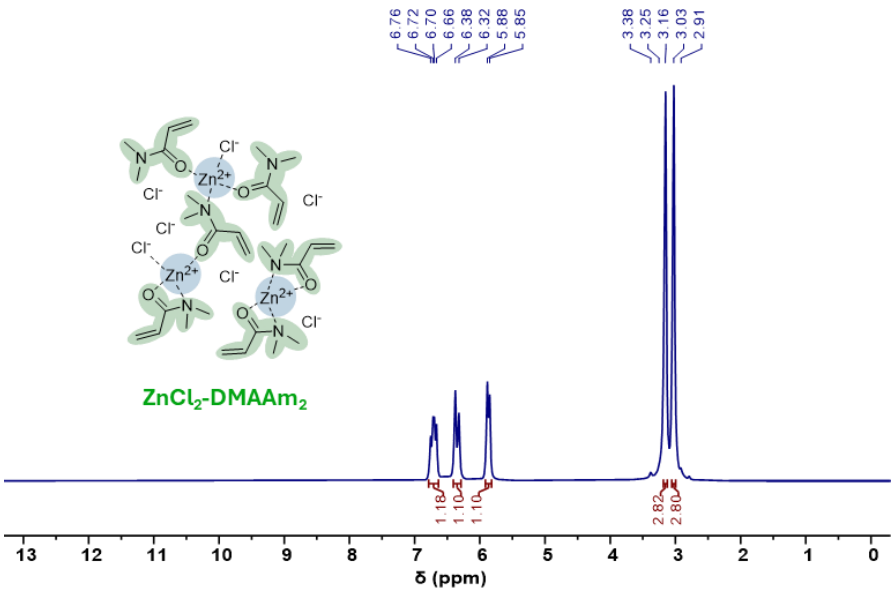

Figure S11: ^{1}H NMR spectrum (300 MHz, $CDCl_3$, room temperature) of $ZnCl_2$-$DMAAm_2$. The two methyl group signals are split in the DESs due to the strong polarization of the amide bond.

Optical properties of identified DESs

The three identified DESs $ZnCl_2$-AAc_2, $ZnCl_2$-HEA_2, and $ZnCl_2$-$DMAAm_2$ were analyzed for their optical properties such as refractive indices and absorption in the UV-vis and IR spectral range.

First, the refractive indices were measured using an ATR refractometer. The measured refractive indices of the three studied DESs ($\eta_{20°C}$ = 1.48-1.52 at λ = 780 nm) are comparable to indices of various commercially available inks (IP-S, IP-Dip, IP-L, OrmoComp, IP-Visio, and PO4) frequently used in MPLP. [1] In detail, for $ZnCl_2$-AAc_2 and $ZnCl_2$-HEA_2, the refractive index at the center wavelength of the femtosecond pulsed laser λ = 780 nm was found to be similar with $\eta_{20°C}$ = 1.479 and $\eta_{20°C}$ = 1.489, respectively (**Figure S12**). The refractive index of $ZnCl_2$-$DMAAm_2$ at 780 nm was slightly higher with $\eta_{20°C}$ = 1.519.

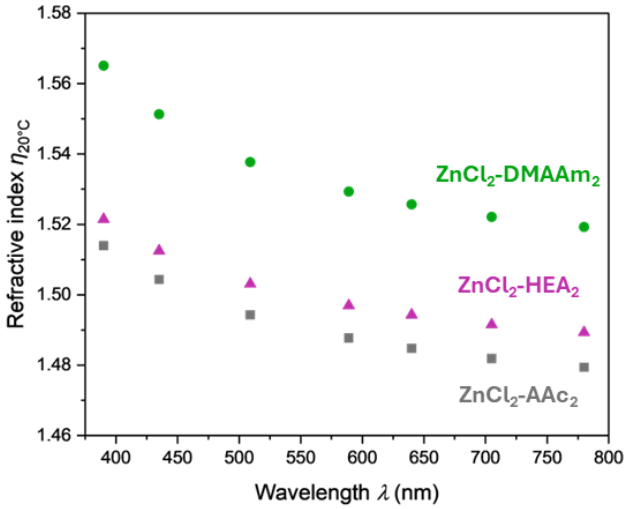

Figure S12: Refractive indices of investigated DESs at different wavelengths. The refractive indices are in a similar range compared to different commercially available inks such as IP-S, IP-Dip, IP-L, OrmoComp, IP-Visio, and PO4 which are frequently used in MPLP. [1]

After characterizing the refractive optical properties, we analyzed the optical absorption of the identified DESs by UV-vis spectroscopy. The colorless mixtures $ZnCl_2$-AAc_2 and $ZnCl_2$-HEA_2 did not exhibit any absorption in the range between 350 nm and 900 nm. The mixture $ZnCl_2$-$DMAAm_2$ did not show absorption between 400 nm and 900 nm. The high optical transparency in the visible and near IR range around make these mixtures highly suitable for multiphoton 3D laser printing.

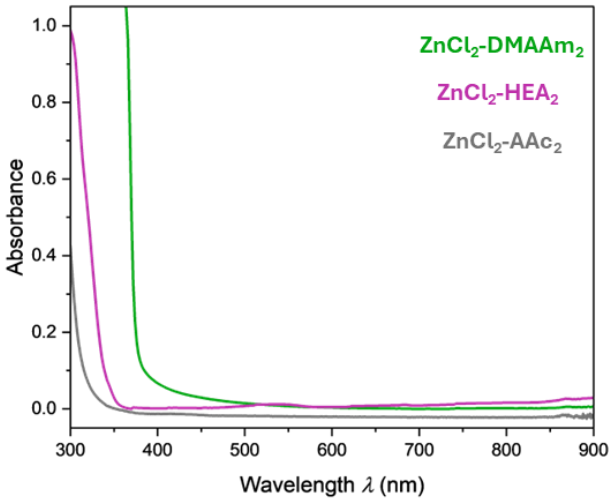

Figure S13: UV-vis spectra of investigated DESs. All DES are optically transparent and do not absorb light between 400 nm and 800 nm making them highly suitable for MPLP.

To extend the UV-vis analysis of the absorption properties to the IR spectral range, we have performed detailed FTIR spectroscopic analysis of $ZnCl_2$-AAc_2, $ZnCl_2$-HEA_2, and $ZnCl_2$-$DMAAm_2$ and compared them to the recorded spectra of pure monomers, *i.e.*, acrylic acid, 2-hydroxyethyl acrylate, and *N*,*N*-dimethylacrylamide, respectively (see **Figure S14** to **Figure S16).**

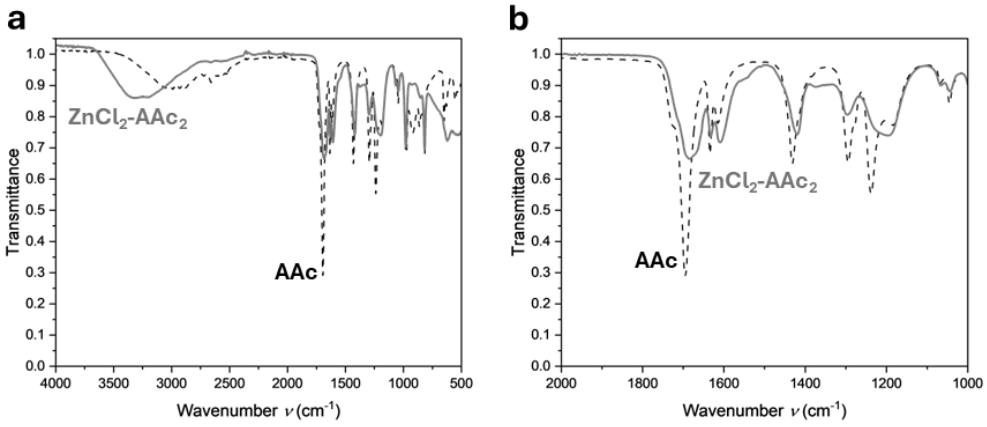

Figure S14: IR spectra of acrylic acid and $ZnCl_2$-AAc_2 in **a)** the full range from 4000 cm^{-1} to 500 cm^{-1} and **b)** a zoom-in from 2000 cm^{-1} to 1000 cm^{-1}. The broadening of the peaks compared to the monomer can be explained by the dynamic species in DES.

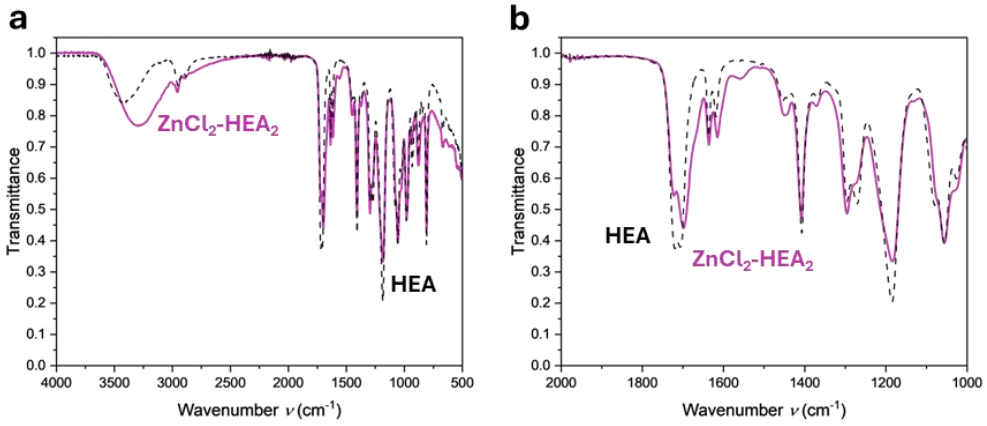

Figure S15: IR spectra of 2-hydroxyethyl acrylate and $ZnCl_2$-HEA_2 in **a)** the full range from 4000 cm^{-1} to 500 cm^{-1} and **b)** a zoom-in from 2000 cm^{-1} to 1000 cm^{-1}. The broadening of the peaks compared to the monomer can be explained by the dynamic species in DES.

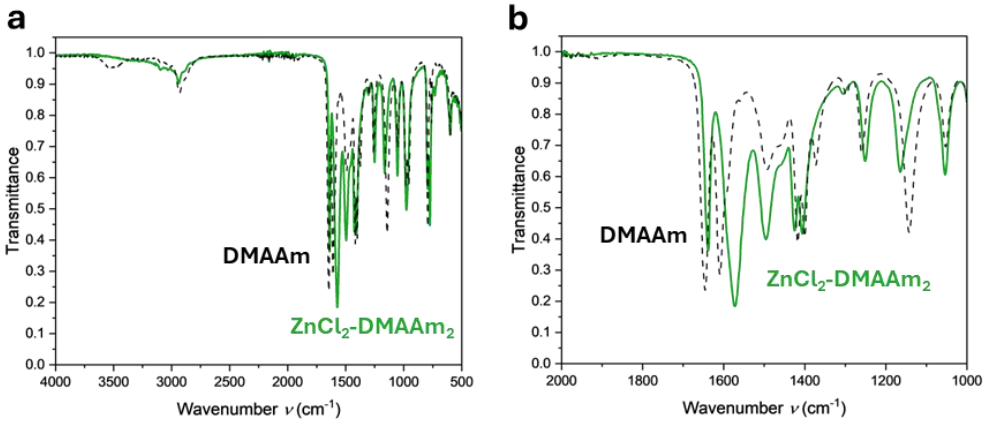

Figure S16: IR spectra of *N,N*-dimethylacrylamide and $ZnCl_2$-$DMAAm_2$ in **a)** the full range from 4000 cm^{-1} to 500 cm^{-1} and **b)** a zoom-in from 2000 cm^{-1} to 1000 cm^{-1}. The broadening of the peaks compared to the monomer can be explained by the dynamic species in DES.

In the FTIR spectra, we identified three general trends. First, the DESs show an altered intensity ratio between the C=O carboxyl group and the C=C double bond in the acrylic moiety compared to the pure monomers. Second, a bathochromic shift of the C=O band indicates that the zinc ions act as a Lewis acid and interact with the oxygen of the carboxyl group, thereby weakening the C=O double bond. Furthermore, the observed broadening of the peaks in the FTIR spectra suggests that different species are formed by ion-dipole interactions in the three characterized DESs.

Printing of DEIs without additional crosslinker

To demonstrate that certain conditions allowed also the preparation of covalent crosslinker-free microstructures, we printed an ink (HEA-pure) composed of 99 wt% $ZnCl_2$-HEA_2 and 1 wt% DEABP. We have further examined various printing parameters such as laser power and scanning speed to evaluate the printability window for this covalent crosslinker-free ink (**Figure S17**). The printed microstructures were categorized in three different categories for their quality. Green printing parameter set allowed for high structural fidelity. Using the yellow printing parameters allowed for printing of the solid boat part but were limited for the fine boat features. Red printing parameters did not show stable structures or led to microexplosions due to local heat accumulation during printing.

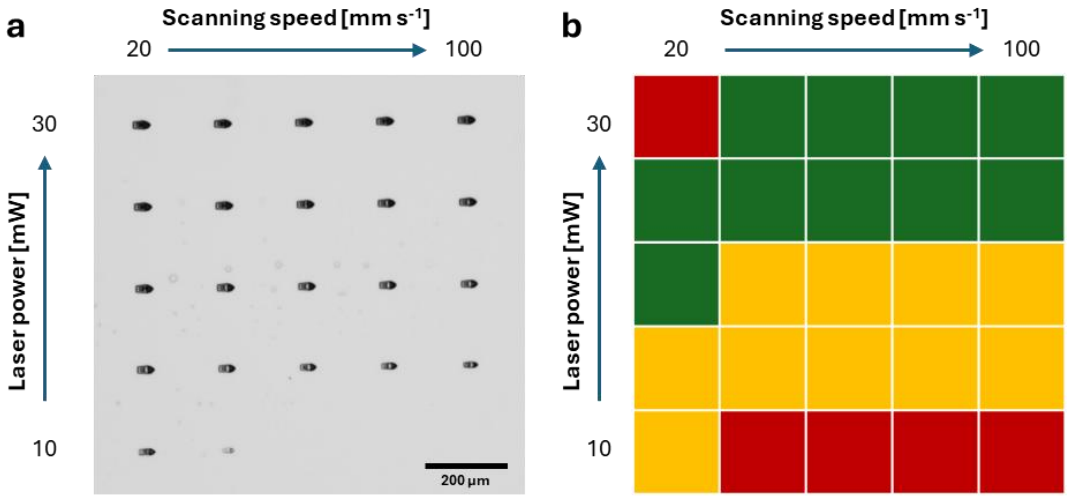

Figure S17: Printability window of a PEGDA-free ink composed solely of 99 wt% $ZnCl_2$-HEA_2 and 1 wt% DEABP for varying printing parameters. **a)** 3D printed benchmark boat structures (50 µm × 25 µm × 40 µm) and **b)** evaluation of printing parameters.

Moreover, we printed micrometric buckyballs using this covalent crosslinker-free ink (**Video S1**) and developed the microstructures in isopropanol. The 3D micrometric buckyballs did not dissolve and were imaged using optical microscopy (**Figure S18**).

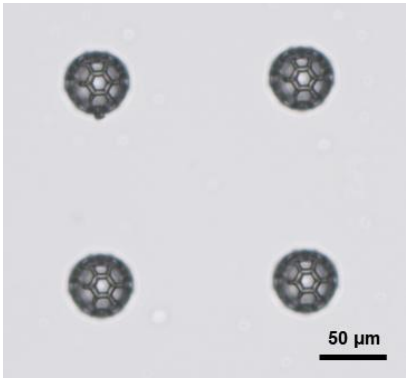

Figure S18: 3D printed buckyball (54 µm × 54 µm × 50 µm) with 99 wt% $ZnCl_2$-HEA_2 and 1 wt% DEABP after development in isopropanol (laser power 20 mW, scanning speed 40 mm s^{-1}).

Printability window of optimized DEIs

The prepared and optimized DEIs were analyzed for their performance in MPLP. For this purpose, 3D benchmark boat microstructures with dimensions of 50 µm × 25 µm × 40 µm were printed with varying printing parameters, *i.e.* laser power and scanning speed using the 25× objective.

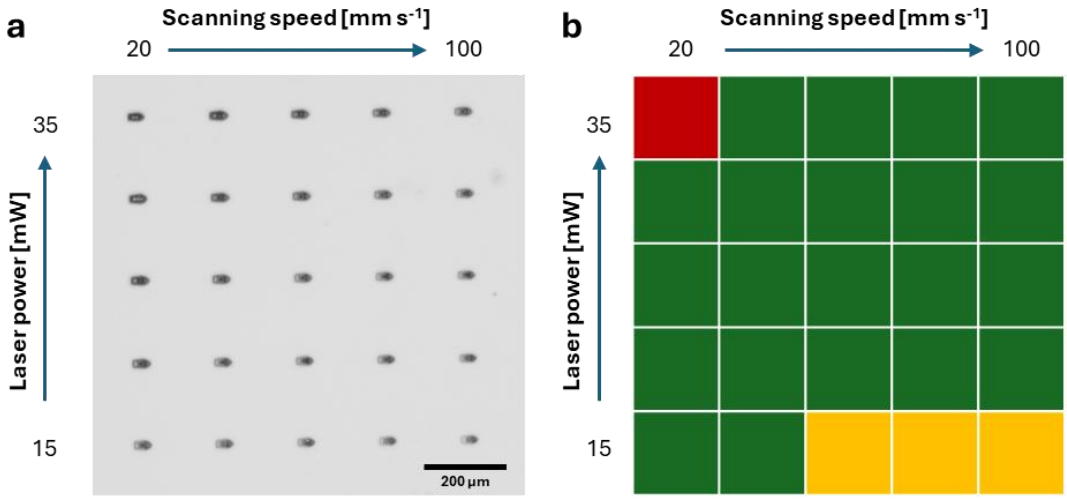

Figure S19: Printability window of DEI1 for varying printing parameters. **a)** 3D printed benchmark boat structures (50 µm × 25 µm × 40 µm) and **b)** evaluation of printing parameters.

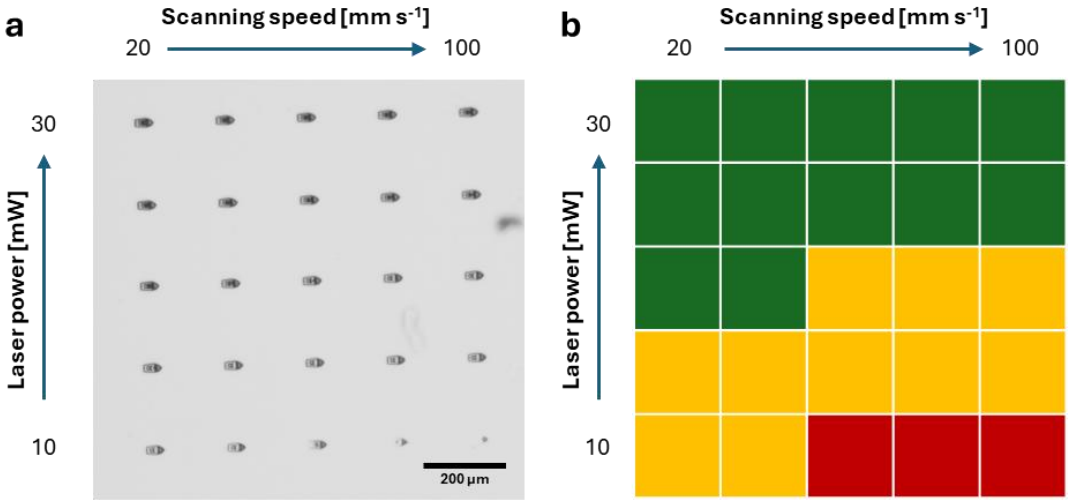

Figure S20: Printability window of DEI2 for varying printing parameters. **a)** 3D printed benchmark boat structures (50 µm × 25 µm × 40 µm) and **b)** evaluation of printing parameters.

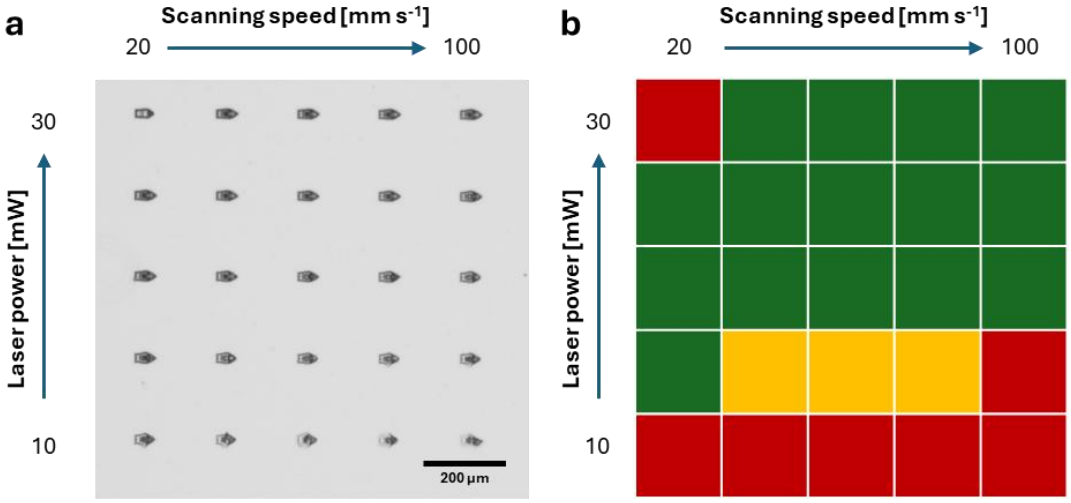

Figure S21: Printability window of DEI3 for varying printing parameters. **a)** 3D printed benchmark boat structures (50 µm × 25 µm × 40 µm) and **b)** evaluation of printing parameters.

Printability windows of highly sensitive reference systems (IP-S, PETA)

After printing the optimized DEIs, we compared the printing parameters to well-known frequently employed highly sensitive inks for MPLP. For this purpose, we selected IP-S (Nanoscribe GmbH) and a custom-made ink composed of 99.5 wt% PETA and 0.5 wt% DETC. Both materials show similar printability windows compared to the DEIs.

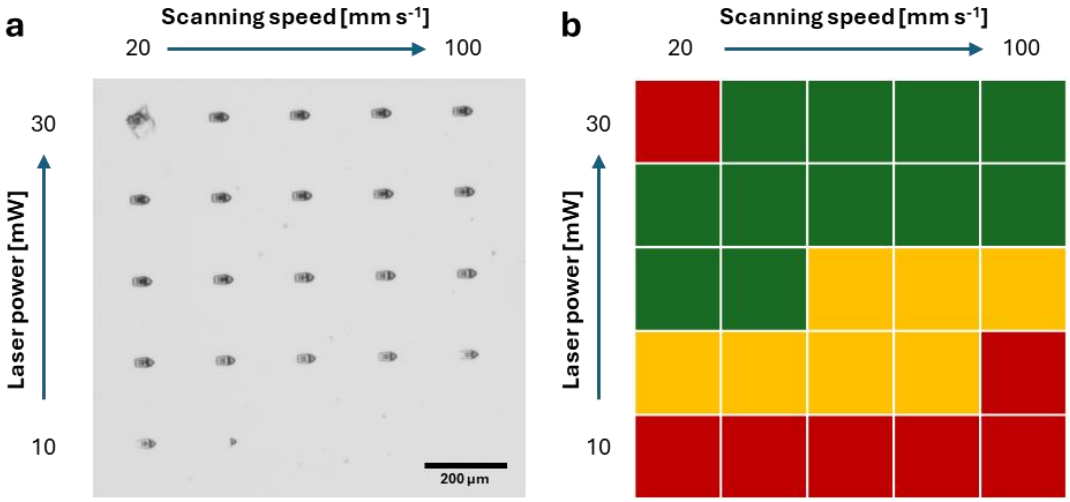

Figure S22: Printability window of IP-L (Nanoscribe GmbH) for varying printing parameters. **a)** 3D printed benchmark boat structures (50 µm × 25 µm × 40 µm) and **b)** evaluation of printing parameters.

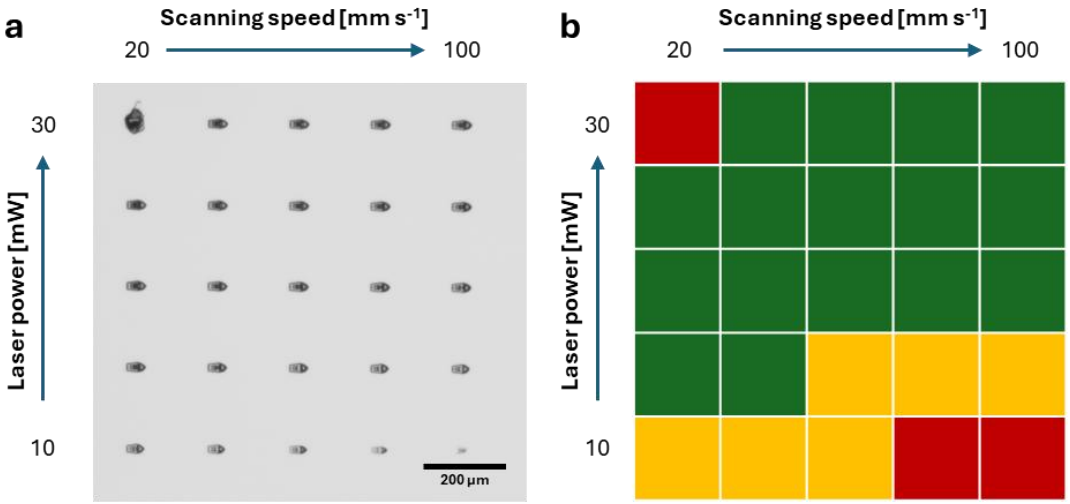

Figure S23: Printability window of PETA with 0.5 wt% DETC for varying printing parameters. **a)** 3D printed benchmark boat structures (50 µm × 25 µm × 40 µm) and **b)** evaluation of printing parameters.

Printability of optimized DEI and zinc-free comparative ink

In order to study the effect of zinc chloride on the printability of the ink, we first prepared a reference ink (RI1) without zinc chloride with similar mol% of acrylic monomers, covalent crosslinker PEGDA, and photoinitiator BAPO compared to DEI1 (see **Table S1** for DEI1 and **Table S2** for RI1).

Table S1: Ink composition of DEI1 with 5 wt% PEGDA.

Compound	wt%	M (g mol^{-1})	mol%	AAc-mol%
$ZnCl_2$-AAc_2	91.5	280.4	48.8%	97.7%
AAc	0	72.1	0%	0%
PEGDA	5	700.0	1.1%	-
BAPO	3.5	418.5	1.3%	-

Table S2: Ink composition of DEI1 with 5 wt% PEGDA without zinc chloride (RI1).

Compound	wt%	M (g mol^{-1})	mol%	AAc-mol%
$ZnCl_2$-AAc_2	0	280.4	0%	0%
AAc	84.7	72.1	97.7%	97.7%
PEGDA	9	700.0	1.1%	-
BAPO	6.3	418.5	1.3%	-

Next, the performance in MPLP of RI1 was compared to the performance of DEI1 (**Figure S24**). Printing of RI1 was not possible for the same broad range of printing parameters as for DEI1.

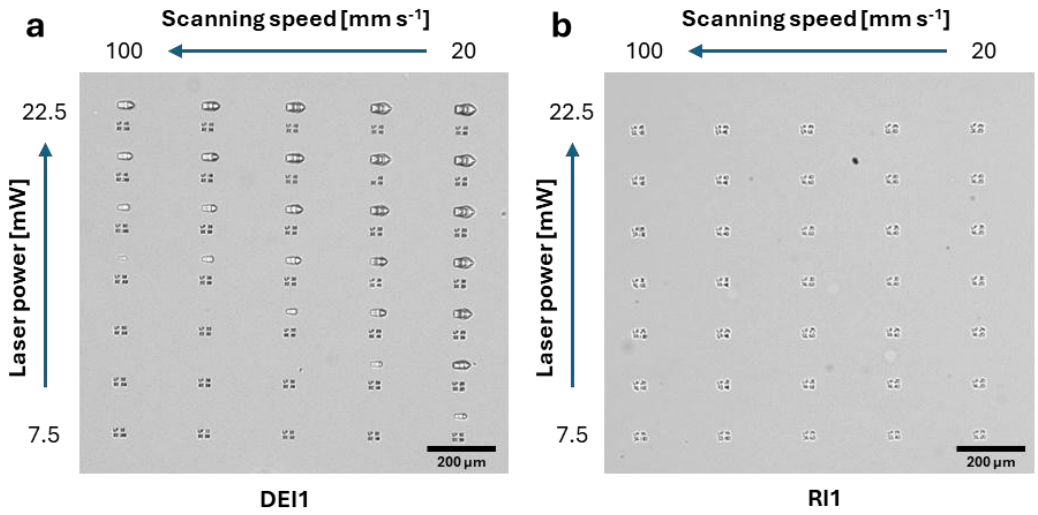

Figure S24: Printability windows of DEI1 (**a**) and RI1 (**b**) for printed boat structures (50 µm × 25 µm × 40 µm) with varying printing parameters. The ink formulations of both inks are summarized in **Table S1** for (**a**) and **Table S2** for (**b**).

By increasing the laser power, a very small printability window was found for MPLP. However, the 3D printed benchmark boat microstructures with these printing parameters were mechanically unstable (**Figure S25**).

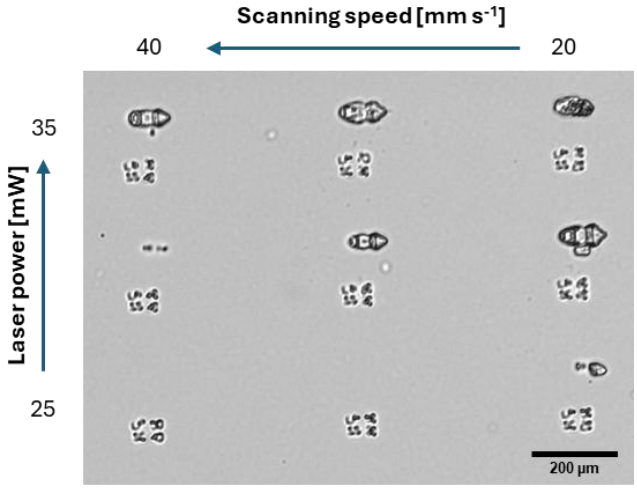

Figure S25: Printability window of RI1 (see also **b** in **Figure S24**) for printed boat microstructures (50 µm × 25 µm × 40 µm) with varying printing parameters and higher exposure doses. The ink formulation is summarized in **Table S2**.

Printability window of reference soft material ink (IP-PDMS)

After comparing the printability to highly sensitive inks, we compared the printing parameters also to the well-known frequently employed soft material ink IP-PDMS (Nanoscribe GmbH) for MPLP. Printing of the prepared DEIs was possible with a lower laser power compared to IP-PDMS.

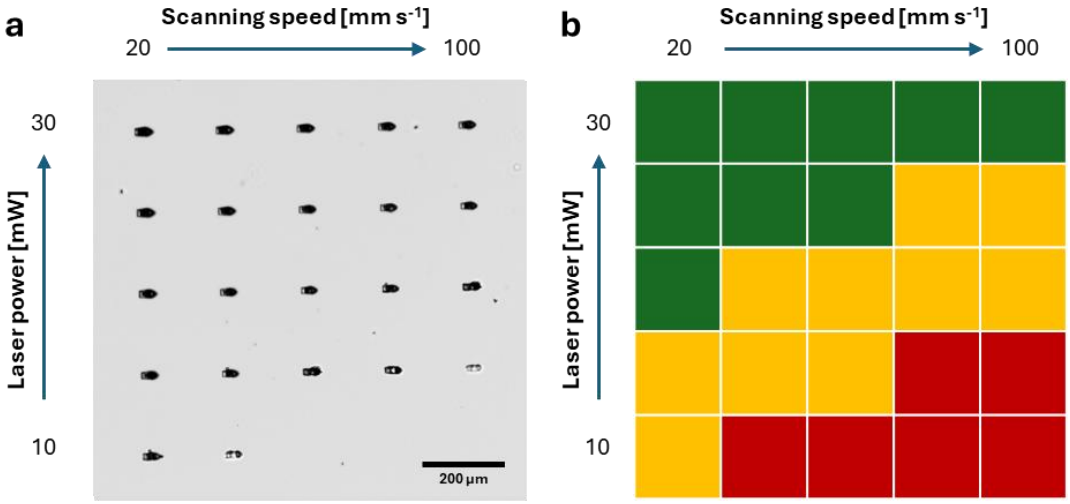

Figure S26: Printability window of IP-PDMS (Nanoscribe GmbH) for printed boat microstructures (50 µm × 25 µm × 40 µm) with varying printing parameters. **a)** 3D printed benchmark boat structures and **b)** evaluation of printing parameters.

Resolution tests

Lateral resolution was measured from printing single lines with varying distance from 0.4 µm and 1.6 µm as the distance at which the lines appear separated. To determine the highest possible resolution with the available setup, MPLP was performed using a 63× objective lens (NA = 1.4). The analysis was performed with optical microscopy and confocal fluorescence microscopy, respectively, and compared with the results obtained for IP-PDMS. We observed that the resolution in the dry and wet state was similar or even slightly better compared to that of the commercially available soft material ink IP-PDMS from Nanoscribe GmbH (**Table S3**).

Table S3: Achieved lateral resolution of the three selected main DEI systems in single line printing tests measured in the dry state from optical microscopy images and in the wet state from confocal fluorescence.

Compound	Resolution (dry state)	Resolution (wet state)
DEI1	1.0 µm	1.0 µm
DEI2	1.0 µm	1.0 µm
DEI3	1.0 µm	1.2 µm
IP-PDMS	1.2 µm	1.2 µm

The printed single lines for each material in **Table S3** are shown in **Figure S27**, **Figure S28**, **Figure S29**, and **Figure S30**.

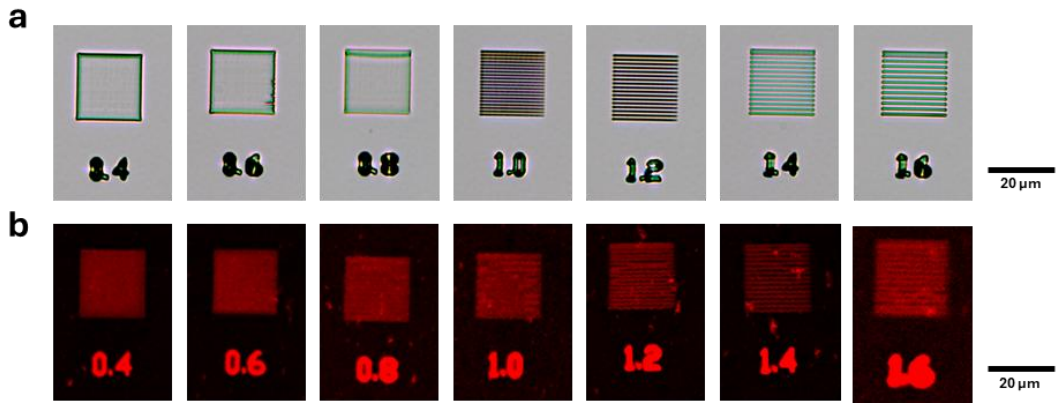

Figure S27: DEI1 single lines microprinted with a laser power of 5 mW and 0.1 mm s^{-1} focus velocity, and varying line pitch from 0.4 µm to 1.6 µm. **a)** Optical microscopy images in the dry state. **b)** Confocal fluorescence microscopy images in water using an excitation wavelength of 561 nm. The confocal images were recorded from rhodamine-B-methacrylate-incorporated structures.

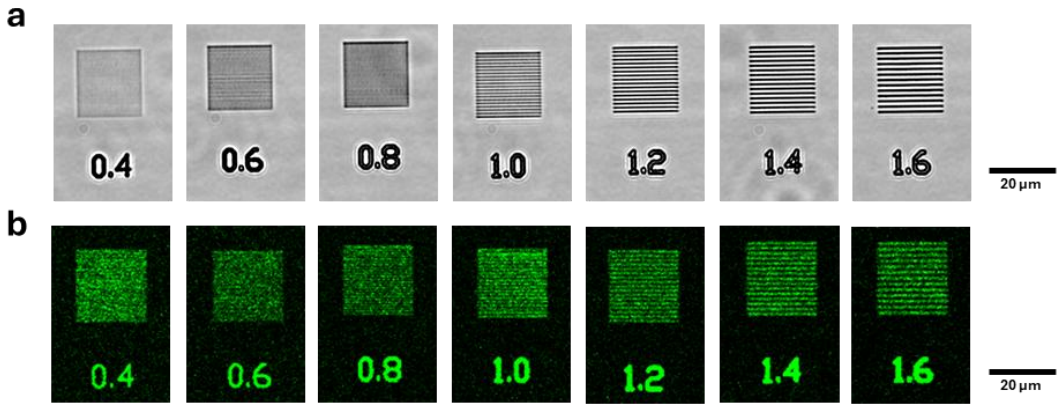

Figure S28: DEI2 single lines microprinted with a laser power of 5 mW and 0.1 mm s^{-1} focus velocity, and varying line pitch from 0.4 µm to 1.6 µm. **a)** Optical microscopy images in the dry state. **b)** Confocal fluorescence microscopy images in water using an excitation wavelength of 488 nm. The confocal images were recorded by using the autofluorescence of printed DEI2.

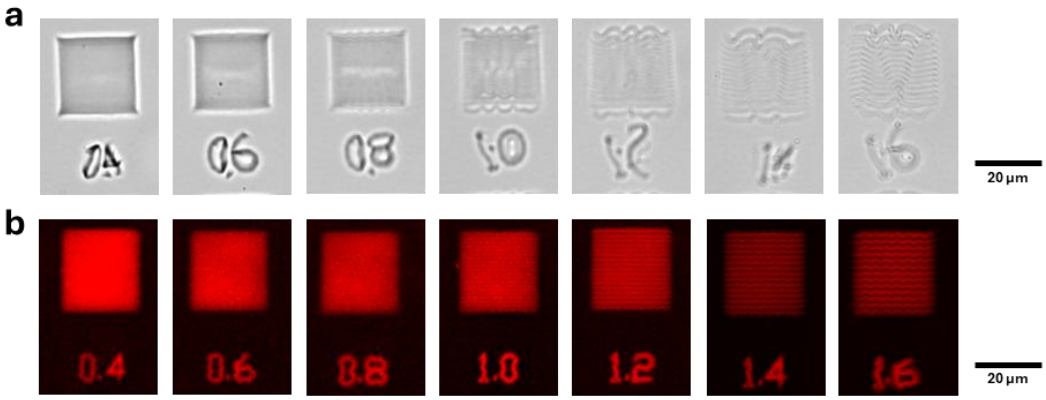

Figure S29: DEI3 single lines microprinted with a laser power of 15 mW and 0.1 mm s^{-1} focus velocity, and varying line pitch from 0.4 µm to 1.6 µm. **a)** Optical microscopy images in the dry state. **b)** Confocal fluorescence microscopy images in water using an excitation wavelength of 561 nm. The confocal images were recorded from rhodamine-B-methacrylate-incorporated structures.

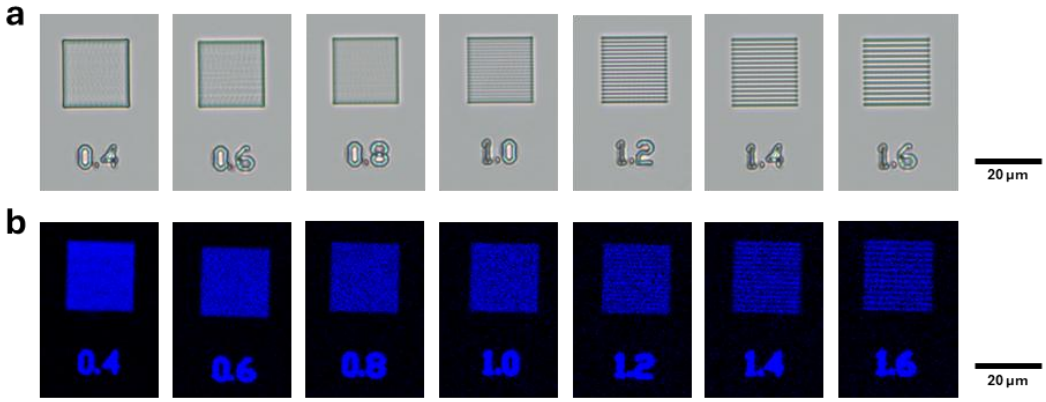

Figure S30: IP-PDMS single lines microprinted with a laser power of 5 mW and 0.1 mm s^{-1} focus velocity, and varying line pitch from 0.4 µm to 1.6 µm. **a)** Optical microscopy images in the dry state. **b)** Confocal fluorescence microscopy images in water using an excitation wavelength of 404 nm. The confocal images were recorded by using the autofluorescence of printed IP-PDMS.

Shape fidelity of printed structures in water

To show the achievable shape fidelity of DEI1, DEI2, and DEI3 in water, we printed hollow cylinders (outer and inner diameter 25 µm and 20 µm, respectively) with an enclosing net microstructure and performed confocal microscopy imaging of structures in water (**Figure S31**). The net microstructure consisted of 1 µm bars in the *xy*-plane with 2 µm × 2 µm windows.

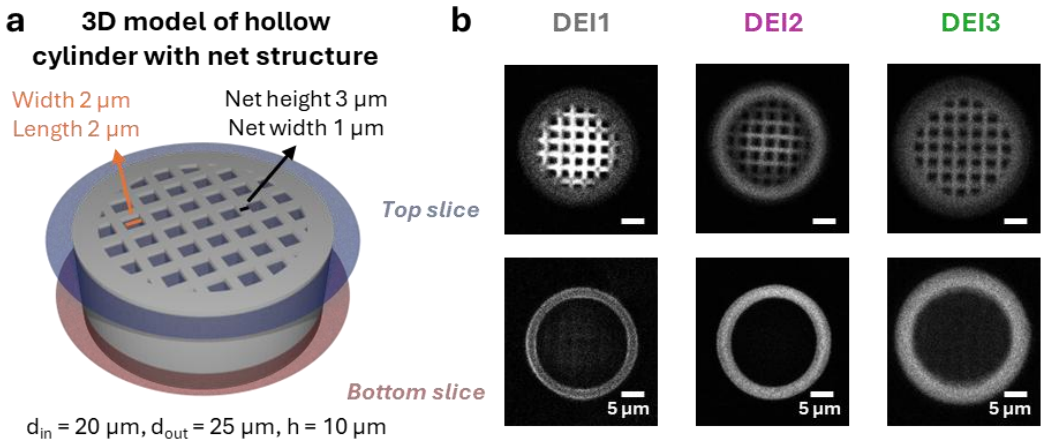

Figure S31: 3D printed net microstructure in water. **a)** 3D model of investigated hollow cylinder with net microstructure. The designed model was printed using the oil immersion mode with the 63× objective lens, a laser power of 30 mW, focus velocity of 10 mm s^{-1}, slicing of 0.3 µm, and hatching of 0.2 µm. **b)** Top and bottom slices of recorded confocal fluorescence microscopy images of the printed microstructures for DEI1 (with 0.01 wt% rhodamine B methacrylate) at 561 nm, DEI2 at 488 nm, and DEI3 at 488 nm.

To quantify the changes of the net microstructures in water to the 3D model, we used the top slice of the recorded stacks to measure the net widths and window withs (see **Table S4**). For this purpose, we measured the distances of 10 net widths and 10 window widths and averaged the outcome, respectively. DEI1 and DEI2 resembled with net widths of 0.97 µm and 1.00 µm the initially printed dimensions of 1.00 µm. DEI3 as the softest hydrophilic material in water with a net width of 1.14 µm showed minor relative deviations from the model dimensions due to swelling.

Table S4: Dimensions of the 3D printed net microstructures in water. The dimensions, *i.e.*, net and window width, were measured and analyzed from recorded confocal microscopy images at 10 different positions.

Net microstructure	Net width (µm)	Window width (µm)
Model	1.00	2.00
DEI1	0.97 ± 0.07	1.97 ± 0.13
DEI2	1.00 ± 0.09	2.06 ± 0.11
DEI3	1.14 ± 0.09	2.19 ± 0.09

Optical microscopy image of printed DEI1

The 3D printed ‘Eschenheimer Turm’ structure was imaged using optical microscopy in side view prior to sputter coating and SEM imaging (**Figure 3**). The flag on top of the tower collapsed during handling of dry samples.

Figure S32: Optical microscopy image (side view) of DEI1 3D printed medieval tower ‘Eschenheimer Turm’ before sputter coating.

Printing parameters for the shown buildings and statues

The building and statue 3D structures were obtained from thingiverse.com and used without modifications. All stl files were shared under common license allowing its free use and sharing for non-commercial purposes.

For DEI1, the 'Eschenheimer Turm' (https://www.thingiverse.com/thing:4855222; BY-NC 4.0), 'Atomium' (https://www.thingiverse.com/thing:112476; CC BY-NC-SA 4.0) and the modeled elastic spring were printed with 100% laser power and 20 mm s^{-1} scanning speed, respectively.

The 'Eiffel tower' (https://www.thingiverse.com/thing:2239567; CC BY-ND 4.0) was printed with DEI2 using 100% laser power and 20 mm s^{-1} scanning speed.

'Michelangelo's David' (https://www.thingiverse.com/thing:502967; CC BY-SA 3.0) was printed with DEI3 using 50% laser power and 40 mm s^{-1} scanning speed.

The 'Al Wasl Dome' (https://www.thingiverse.com/thing:6605755; CC BY-SA 3.0) was printed with DEI1+NIPAAm using 100% laser power and 10 mm s^{-1} scanning speed.

For DEI2+AAm, the 'Statue of liberty' (https://www.thingiverse.com/thing:4056644; CC BY 4.0), 'Atomium' (https://www.thingiverse.com/thing:112476; CC BY-NC-SA 4.0), and 'Space space needle' (https://www.thingiverse.com/thing:930296; CC BY-SA 3.0) were printed using 100% laser power and 20 mm s^{-1} scanning speed. The 'Albero della vita' (https://www.thingiverse.com/thing:922169; CC BY-SA 3.0) was printed using 100% laser power and 50 mm s^{-1} scanning speed.

FTIR spectroscopy of 3D printed DEI1

To study the chemical composition of the printed network, FTIR spectroscopy was performed on dry 3D printed DEI cubes (50 µm × 50 µm × 20 µm) using an FTIR microscope. 3D printed DEI1 was composed mainly of a very low crosslinked polyethylene glycol-crosslinked network with large amounts of AAc (**Figure S33**). The recorded spectra were similar to recorded FT-IR spectra of pure polyacrylic acid (PAA). In detail, the recorded FTIR spectra showed a large absorption band above ν = 3000 cm^{-1} showing the expected presence of free O-H groups. Compared to the IR spectra of $ZnCl_2$-AAc_2 (**Figure S14**), the C=O carboxyl band showed a hypsochromic shift back to higher wavenumbers (ν = 1698 cm^{-1}) and appeared very sharp resembling the one of pure acrylic acid. As expected from the very low amount of employed covalent crosslinker PEGDA-M_n700, the FTIR spectra showed only very minor unreacted acrylate C=C double bond signals around ν = 1560 cm^{-1} (see **Figure S33** and **Figure S14**).

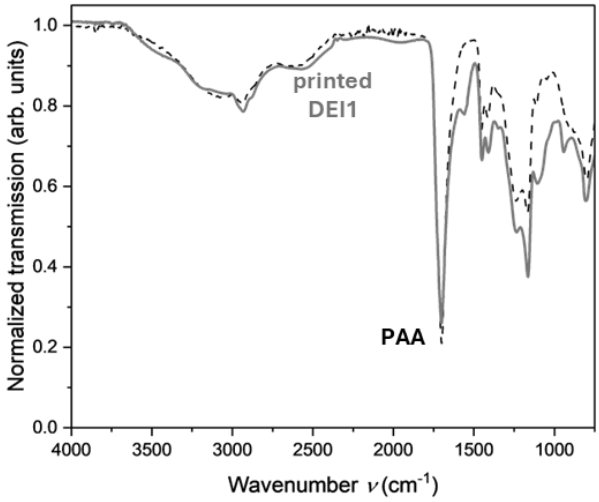

Figure S33: Recorded FTIR spectra of 3D printed DEI1 (50 µm × 50 µm × 20 µm) and polyacrylic acid (M_n 20000).

The recorded FTIR spectra of printed DEI2 and DEI3 follow the previously described trends for DEI1 such as a low content of present acrylates or hypsochromic shift (**Figure S34**).

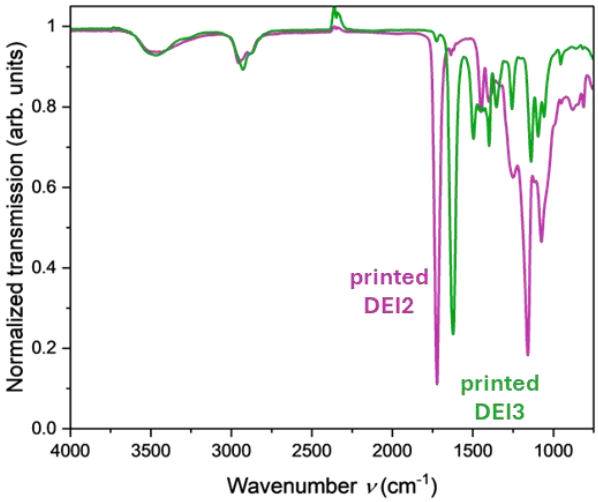

Figure S34: Recorded FTIR spectra of 3D printed cubes (50 µm × 50 µm × 20 µm) of DEI2 and DEI3.

Analysis of residual zinc ions

In addition to FTIR spectroscopy, we performed a highly sensitive UV-vis spectroscopic analysis using a zinc-binding organic dye (**Figure S35**) to investigate the chemical composition of the printed structures in-depth. To see if zinc ions are trapped and present in the DEI1 3D printed structures, we 3D printed millimeter-sized blocks with dimensions of 500 µm × 500 µm × 1000 µm and performed UV-vis spectroscopic analysis using zincon as a zinc-specific binding organic dye. After getting in contact with the 3D structures, the phosphate buffered zincon solution (188 µM) instantaneously showed a color change from orange to purple indicating the presence of zinc ions. The color change of the solution was observed in the recorded UV-vis spectra by a new band at 620 nm (**Figure S35**). A similar color change was detected after zincon solution got in contact with the ink DEI1. The observed color change and appearance of a new band at 620 nm align well with the complexation of zinc ions with zincon.[2]

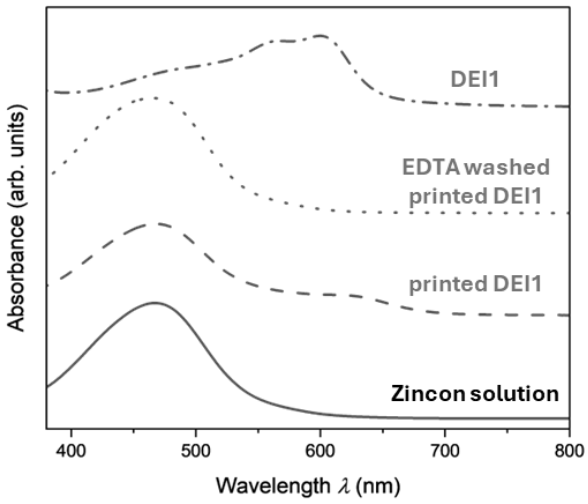

Figure S35: UV-vis spetra of zincon solution before and after contact with a 3D printed DEI1 structure, EDTA washed 3D printed DEI1 structure, and the DEI1 ink. The stack is shown with an offset. The additional EDTA wash does not lead to the color change of the zincon (analyte) solution indicating the absence of zinc ions.

Removing residual zinc ions was possible by performing an additional washing step with an aqueous solution with a chelat binding ligand, i.e. saturated aqueous ethylenediaminetetraacetic acid (EDTA) solution, which was expected to strongly bind to the transition metal. The additional development step removed residual zinc ions entirely from the printed PEG-

crosslinked acrylic acid network as shown by UV spectroscopic analysis. In detail, the zincon solution exhibited the same absorption behavior before and after contact to the EDTA washed DEI1 structure (**Figure S35**).

In addition to the spectroscopic analysis, we performed thermogravimetric analysis (TGA) of the 3D printed blocks with and without EDTA washing to study the thermal stability and amount of residue (**Figure S36**). Thermogravimetric analysis of the printed structures with and without residual zinc ions showed similar weight residues after heating to 600 °C indicating that the amount of zinc ions in the structures still present in the structures is very low (**Figure S36**).

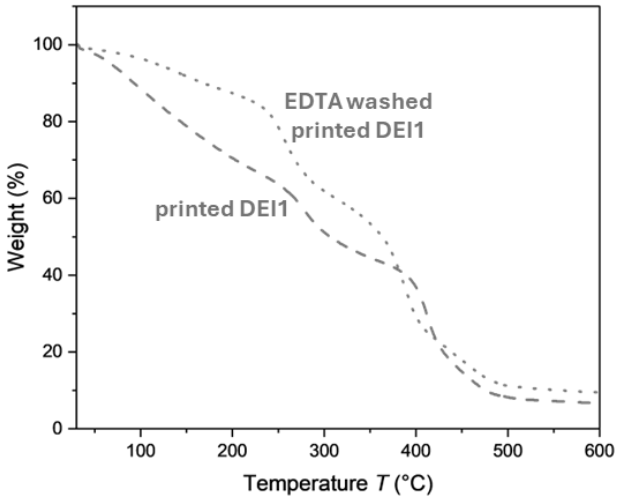

Figure S36: Thermogravimetric analysis of 3D printed DEI1 structures.

Furthermore, the printed structures with residual zinc showed a higher affinity to binding water from the atmosphere and a slightly increased thermal stability toward decomposition.

Mechanical characterization of printed DEIs

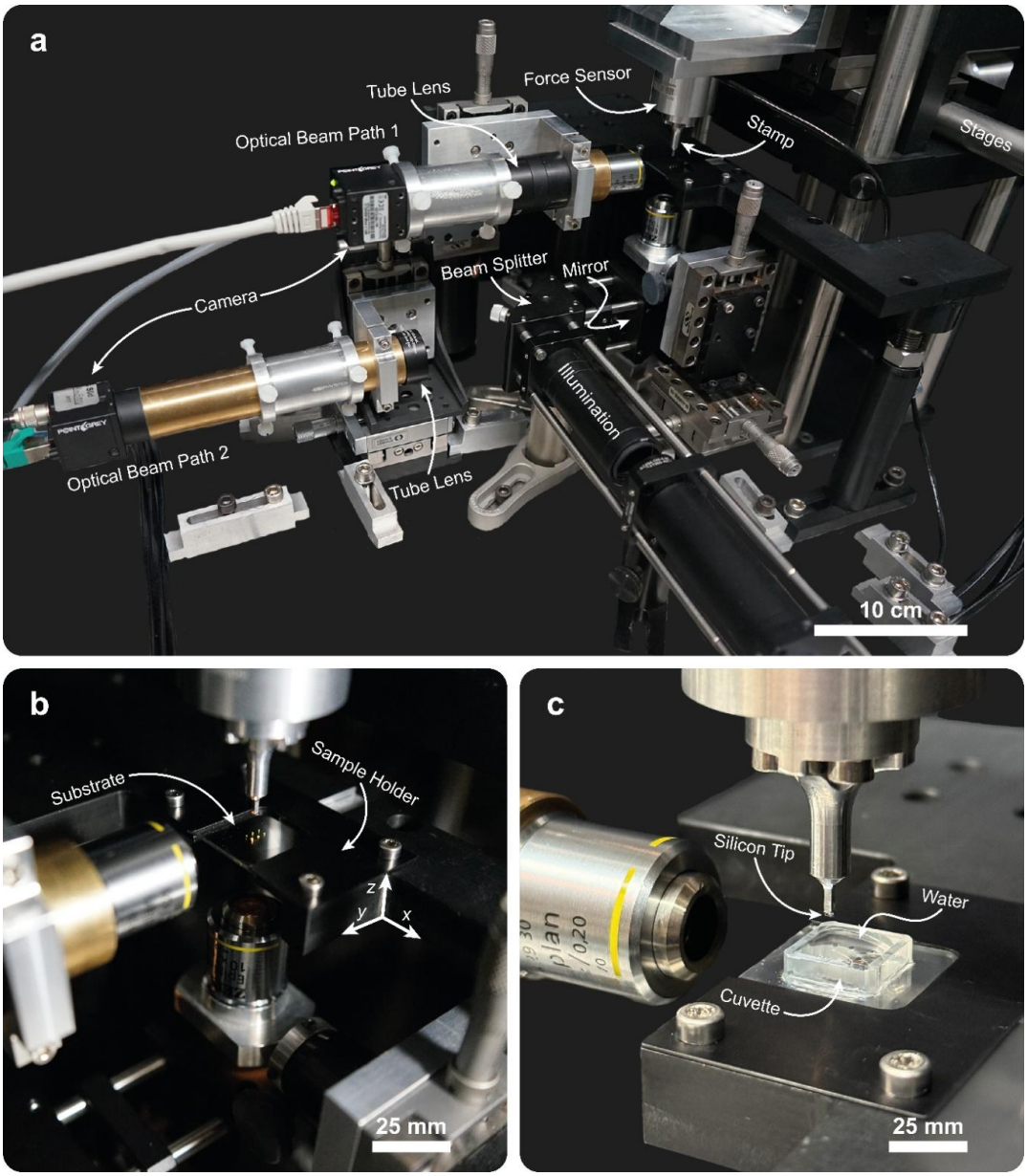

Figure S37: a) Overview of the home-built setup for uniaxial-loading experiments and mechanical characterization, illustrating the main parts of the setup. Bottom illumination of the substrate is included in optical beam path 2; back illumination and light sources are not depicted. **b)** Sample configuration for measurements in air, the substrate is fixed in the sample holder and placed underneath the custom-made stamp with silicon tip, in front of the two objective lenses. One pillar of the sample array is illuminated by the second optical-beam path. **c)** Sample configuration for measurements in aqueous media, the cuvette functions as sealed reservoir for deionized water during the measurements. Mounting of the substrate is the same as in **a**, displayed materials are DEI2+AAm (**a**) and DEI3 (**b**).

The main parts of the setup included two optical microscopes (optical beam path 1 and 2, ZEISS Epiplan 10×, NA = 0.2) with attached cameras (Point Grey Research, Blackfly BFLY-PGE-50H5C) for imaging the sample from the bottom and side during the experiment, a force sensor (ME-Meßsysteme, K3D35 500 mN) with a custom-made aluminum stamp (cross-section 1 mm^2), attached to automated translation stages (TRA25CC, Newport), and a sample holder. To provide a smoother surface of the stamp, a piece of silicon of the same cross-section was added to the tip. Illumination was provided by back illumination (Schott, KL 2500 LED) and from the bottom via optical beam path 2 (Schott, KL 1500 LCD), which is not depicted in **Figure S37A.** The setup was placed on an air-cushion optical table (RS 2000, Newport).

Measurements of dry samples were performed directly using the setup. For measuring the samples in water, a cuvette was glued to the glass slide. The cuvette functions as a reservoir to store and keep the samples in aqueous media. Both sample configurations are depicted in **Figure S37B** and **Figure S37C**.

The recorded force is a function of the prescribed displacement (**Figure S39**), the effective spring constant is obtained from the slope of a linear regression model fitted to the linear regime of the loading cycles. By calculating the Young's modulus from the effective spring constant, the change of the sample geometry of the different materials, through shrinkage after development or swelling in water, is included by taking pictures of the samples in the experimental setup before conducting the experiments and analyzing them with the software 'ImageJ' to measure the height and diameter of the samples. The Young's modulus for each sample is averaged over all loading cycles for each prescribed geometry corrected strain, and the modulus for each material is averaged over all measured samples. Geometry parameters and results of the Young's moduli are listed in **Table S5** and **Table S6**, respectively. Data analysis programmed in MATLAB, optical micrographs of the samples and supporting videos can be found in the data repository published with this work (DOI:10.11588/DATA/UP26J7).

Table S5: Results of mechanical characterization of 3D printed DEIs in air.

Printed Material	Height *h* (µm)	Diameter *d* (µm)	Strain linear regime	Corrected strain linear regime	Young's moduli in air (MPa)
HEA-pure	216.8 ± 6.0	291.6 ± 2.9	4%	5.5%	30.276 ± 0.068
DEI1	283.4 ± 4.8	309.6 ± 6.1	10%	10.6%	36.344 ± 0.070
DEI2	300.9 ± 2.8	386.5 ± 4.1	10%	10.0%	12.606 ± 0.046
DEI3	264.8 ± 4.0	367.8 ± 2.8	6%	6.8%	30.193 ± 0.043
DEI1+NIPAAm	276.0 ± 4.1	346.1 ± 2.7	6%	10.9%	35.897 ± 0.044
DEI2+AAm	294.4 ± 3.4	384.0 ± 3.2	10%	6.1%	14.364 ± 0.040

Table S6: Results of mechanical characterization of 3D printed DEIs in water.

Printed Material	Height *h* (µm)	Diameter *d* (µm)	Strain linear regime	Corrected strain linear regime	Young's moduli in water (MPa)
HEA-pure	252.0 ± 6.1	321.9 ± 3.3	4%	4.7%	5.679 ± 0.064
DEI1	390.5 ± 5.1	499.1 ± 6.1	10%	7.7%	0.575 ± 0.056
DEI2	297.6 ± 6.5	387.5 ± 1.2	10%	10.1%	10.526 ± 0.045
DEI3	463.8 ± 5.0	641.5 ± 2.5	6%	3.9%	0.265 ± 0.027
DEI1+NIPAAm	400.2 ± 5.8	490.0 ± 3.7	6%	7.5%	0.393 ± 0.042
DEI2+AAm	303.5 ± 6.8	404.7 ± 2.9	10%	5.9%	9.867 ± 0.053

The temporal measurement protocol for the first force loading and unloading cycle of the DEI2 measurement in air is depicted in **Figure S38** as an example. The time between the loading and unloading was 1.6 s for all measurements. The delay between the 10 cycles was set to 40 s.

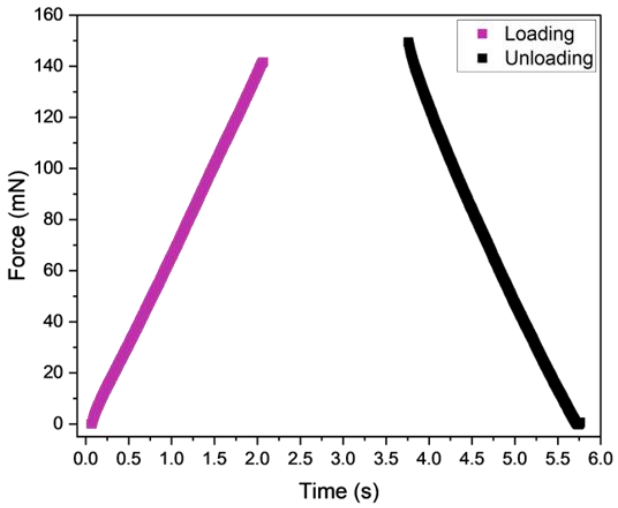

Figure S38: Selected data of first force loading and unloading cycle *versus* time for printed DEI2 cylinder in air.

The measured force-strain curves are depicted for one measured pillar of the six different materials, respectively. The corrected strain includes the geometry measurement obtained by 'ImageJ' for the Young's modulus calculation.

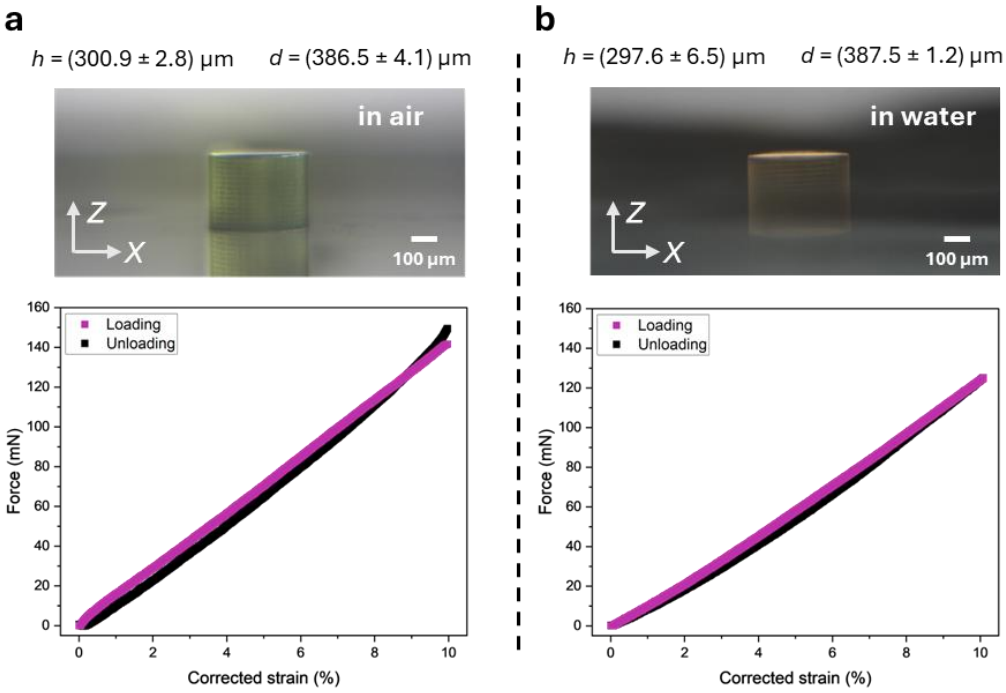

Figure S39: One measured force-strain loading and unloading cycle of one printed DEI2 cylinder in air (**a**) and in water (**b**).

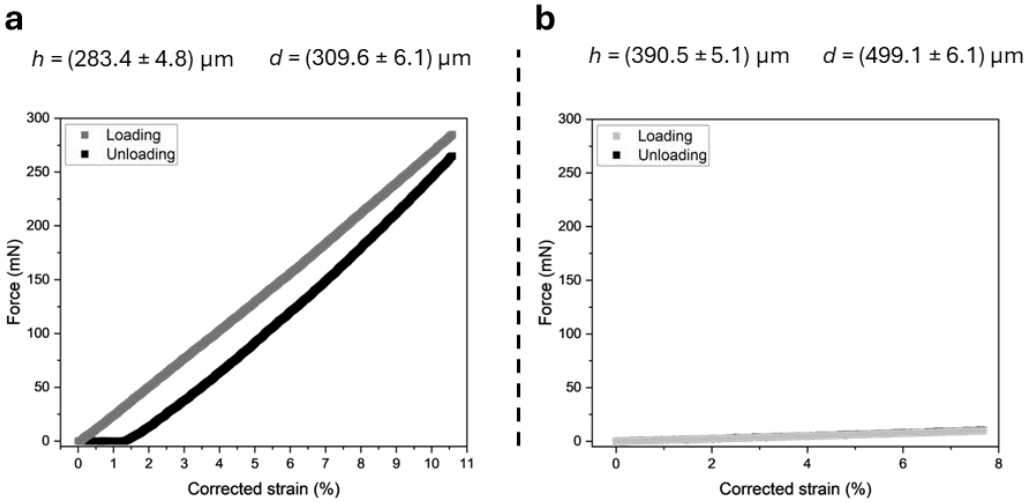

Figure S40: One measured force-strain loading and unloading cycle of one printed DEI1 cylinder in air (**a**) and in water (**b**).

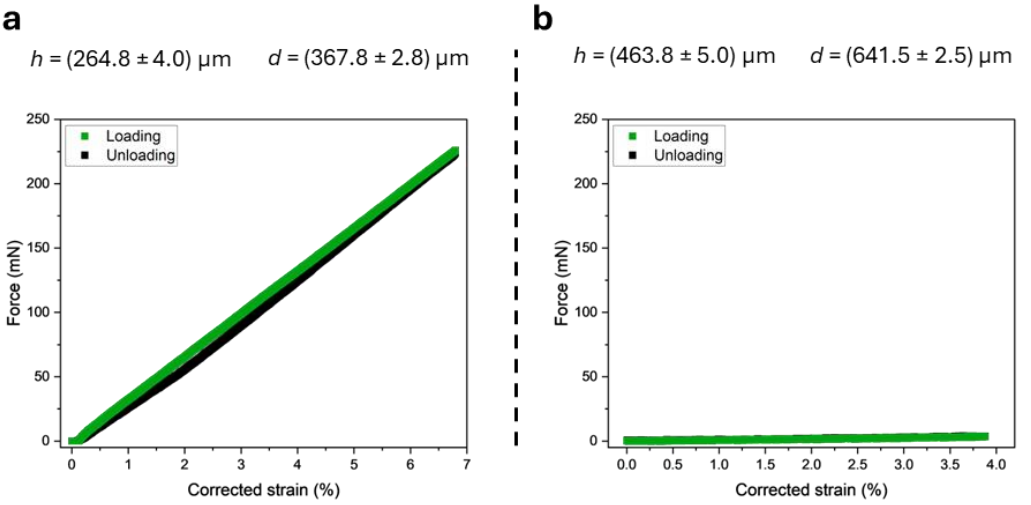

Figure S41: One measured force-strain loading and unloading cycle of one printed DEI3 cylinder in air (**a**) and in water (**b**).

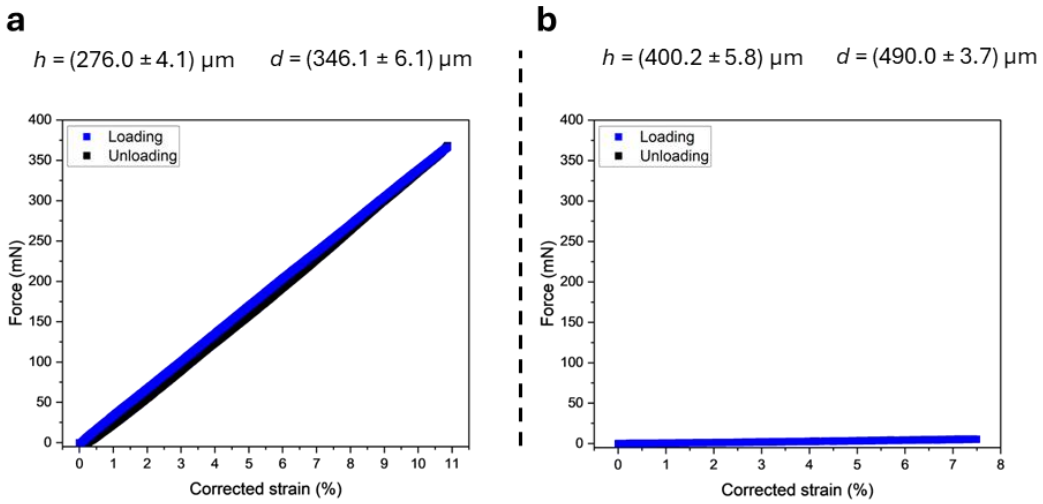

Figure S42: One measured force-strain loading and unloading cycle of one printed DEI1+NIPAAm cylinder in air (**a**) and in water (**b**).

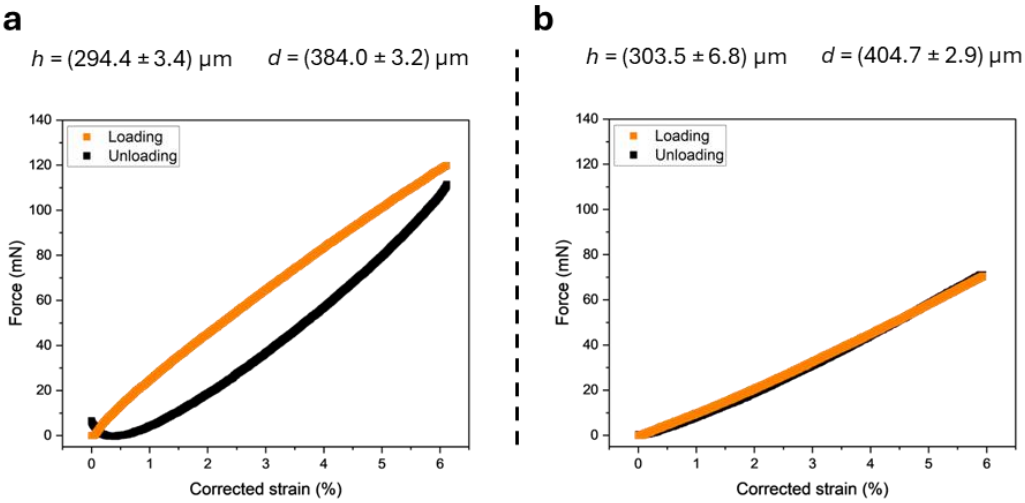

Figure S43: One measured force-strain loading and unloading cycle of one printed DEI2+AAm cylinder in air (**a**) and in water (**b**).

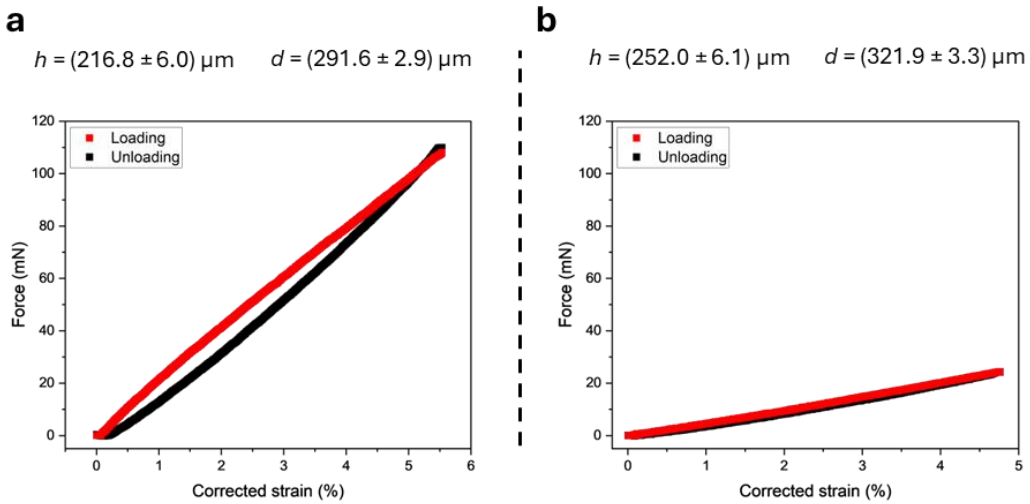

Figure S44: One measured force-strain loading and unloading cycle of one printed HEA-pure cylinder in air (**a**) and in water (**b**).

The Young's moduli of the printed HEA-pure, DEI1+NIPAAm, and DEI2+AAm are shown in **Figure S45**.

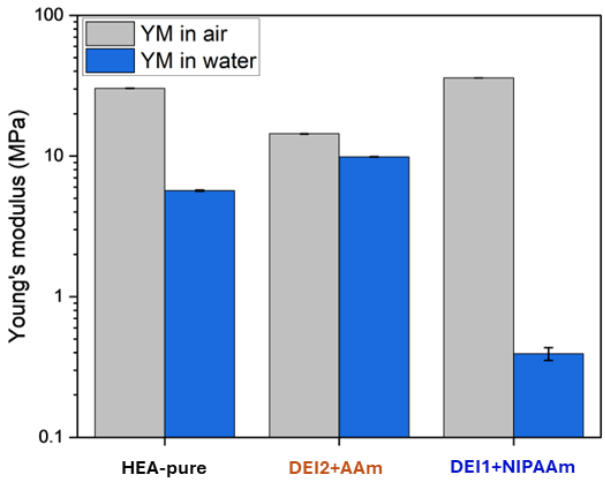

Figure S45: Young's moduli of HEA-pure, DEI2+AAm, and DEI1+NIPAAm, and IP-PDMS. The Young's moduli were calculated from force-strain displacement curves in the linear regime (see **Table S5** and **Table S6**).

To compare the compression measurements with a reference system, we have selected IP-PDMS (Nanoscribe GmbH) as a commercially available reference system. First, we verified

the reproducibility of measured Young's moduli of our setup. For this purpose, we printed a similar cubic structure with dimensions of 100 µm × 100 µm × 50 µm using the 25× objective, slicing and hatching 0.3 µm, laser power 50 mW, and scanning speed 80 mm s^{-1} as reported by Nanoscribe GmbH in their nanoindentation experiment. The sample was analyzed using the compression setup and showed Young's moduli of (15.290 ± 0.911) MPa. This value very much resembles the reported 15.3 MPa by Nanoscribe GmbH. [3]

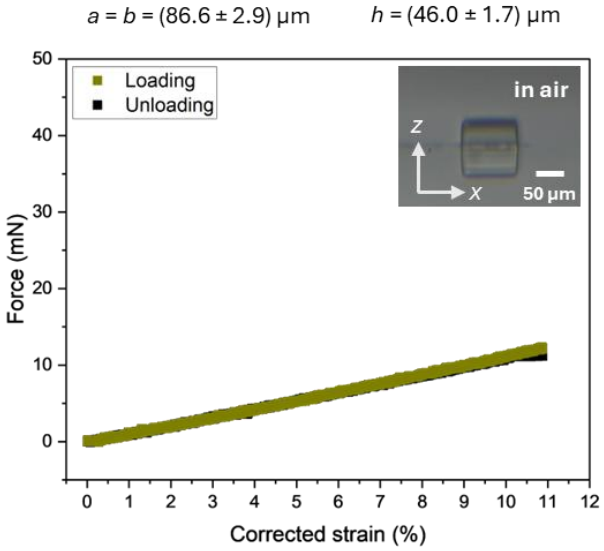

Figure S46: One measured force-strain loading and unloading cycle of one 3D printed IP-PDMS cube with dimensions of 100 µm × 100 µm × 50 µm in air as a reference measurement.

As a next step, we printed a cylinder of IP-PDMS of the same geometry as previously employed for the DEIs (**Figure S47**). To avoid heat accumulation, we reduced the laser power from 50 mW to 40 mW to use the same scanning speed of 80 mm s^{-1}. The Young's modulus of the printed cylinder was found to be (5.975 ± 0.204) MPa underlining the strong influence of the printing parameters on the resulting mechanical properties as it has been described previously for other inks. [4]

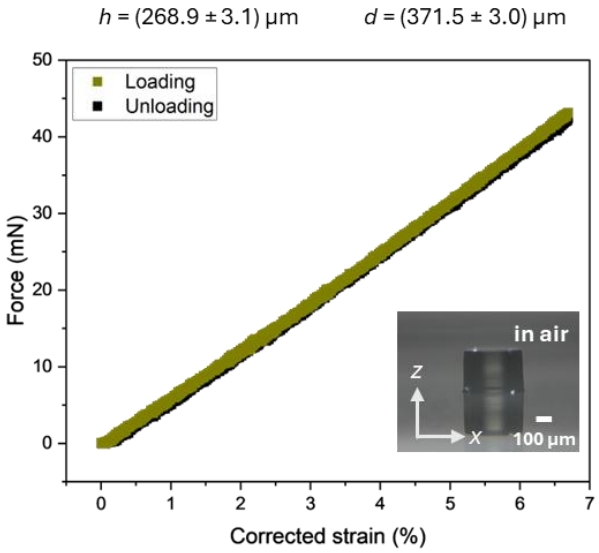

Figure S47: One measured force-strain loading and unloading cycle of the 3D printed IP-PDMS cylinder in air printed with the 25× objective. The cylinder (300 µm height, 400 µm diameter) has been printed with 80 mm s^{-1}, 40 mW, 0.3 µm slicing, and 0.3 µm hatching.

To finally compare the mechanical properties using similar printing conditions as the DEI, we printed and analyzed four cylinders of IP-PDMS with the 10× objective (with foil) [5], same geometry, and printing parameters as we previously employed for the DEIs (**Figure S48**). We observed a severe shrinkage of around 30% and 20% (pillars in air and in water) which was larger compared to that the shrinkage observed for the printed DEIs. The smaller printability window and severe shrinkage suggest that the used printing parameters do not offer relevant quality in structure fabrication. This was further supported by compression measurements of the printed IP-PDMS pillars yielding around (0.452 ± 0.121) MPa in air and (0.489 ± 0.068) MPa in water. This result highly deviated from the measured and reported Young's moduli 15.3 MPa by the vendor (Nanoscribe GmbH). [3] Thus, our results support the recommendation of Nanoscribe to use IP-PDMS with the 25× objective.

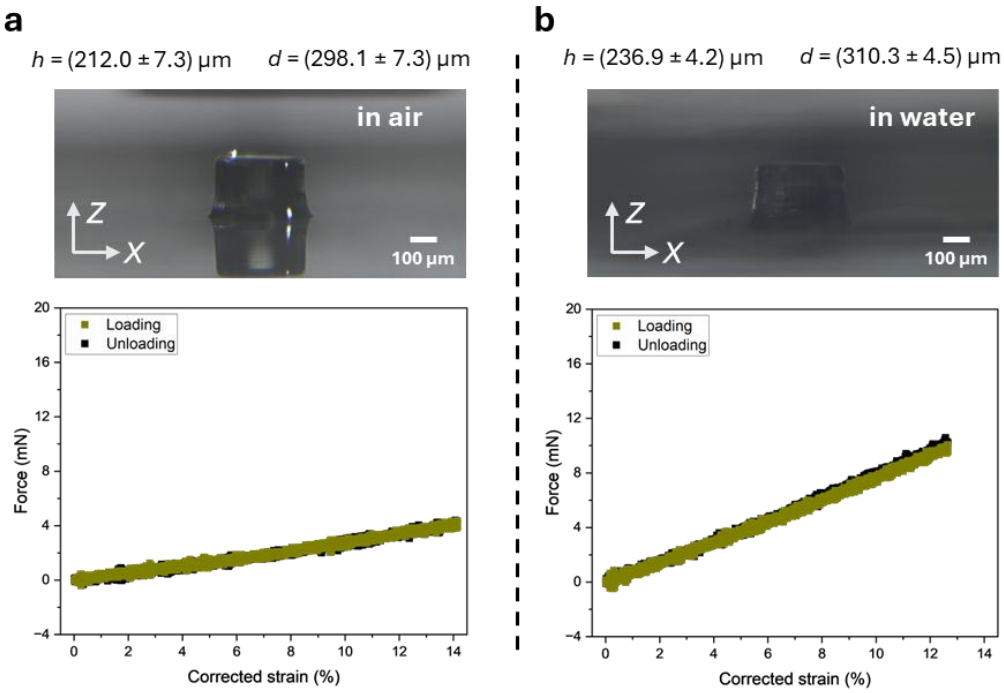

Figure S48: One measured force-strain loading and unloading cycle of one 3D printed IP-PDMS cylinder in air (**a**) and in water (**b**). The cylinder (300 µm height, 400 µm diameter) has been printed using the 10× objective and similar printing conditions as for the DEIs. The IP-PDMS cylinder shows severe shrinkage (20-30%) compared to the reference sample printed with the 25× objective (**Figure S47**).

The performed reference measurements using IP-PDMS (Nanoscribe GmbH) are summarized in **Table S7** and **Table S8**.

Table S7: Results of IP-PDMS reference measurements in compression experiments in air.

Objective	Geometry	Height h (μm)	Strain linear regime	Corrected strain linear regime	Young's moduli in air (MPa)
25×	Rectangular	46.0 ± 1.7	10%	10.9%	15.290 ± 0.911
25×	Cylindrical	268.9 ± 3.1	6%	6.7%	5.975 ± 0.204
10×	Cylindrical	212.0 ± 7.3	10%	14.2%	0.452 ± 0.121

Table S8: Results of IP-PDMS reference measurements in compression experiments in water.

Objective	Geometry	Height h (μm)	Strain linear regime	Corrected strain linear regime	Young's moduli in water (MPa)
10×	Cylindrical	236.9 ± 4.2	10%	12.7%	0.489 ± 0.068

Comparison of mechanical properties with available inks for dip-in mode MPLP

Table S9: Mechanical properties of reported inks available for MPLP preparation of larger structures in dip-in mode (measured * - dry and in ° - aqueous media). [6-8]

Inks for MPLP of larger structures using the dip-in mode	Young's modulus (MPa)
Nanoscribe IP-Q*	3100
Nanoscribe IP-S*	2100
DEGRAD INX© X100*	50 – 60
Nanoscribe IP-PDMS*	15.3
HYDROTECH INX© X200°	3 – 4
This work – DEIs*	**12 – 36**
This work - DEIs°	**0.26 – 10**

Extending functionality by mixing DEIs with N-isopropyl acrylamide

After printing a DEI with acrylamide, we selected *N*-isopropyl acrylamide (NIPAAm) as another monomer with responsive properties. To achieve multiresponsive behavior towards multiple stimuli such as temperature, pH, and calcium, [9,10] we aimed for combining NIPAAm with the previously identified DES $ZnCl_2$-AAc_2. Similar to acrylamide in $ZnCl_2$-HEA_2, NIPAAm, added in a 1:2 weight ratio, readily dissolved in the $ZnCl_2$-AAc_2 DES. It is worth noting that NIPAAm showed no lower critical solubility transition (LCST) in the mixture when heated to 50 °C (**Figure S49**), drastically extending its processing window.

Figure S49: Dissolved *N*-isopropyl acrylamide (33 wt%) in $ZnCl_2$-AAc_2 (67 wt%) at room temperature and 50 °C.

The NIPAAm mixed with $ZnCl_2$-AAc_2 was used to prepare an ink (DEI1+NIPAAm) together with PEGDA as crosslinker and BAPO as photoinitiator (**Table S10**).

Table S10: Ink composition of DEI1+NIPAAm with *N*-isopropyl acrylamide.

Compound	wt%	M (g mol^{-1})	mol%
$ZnCl_2$-AAc_2	61.0	280.4	43.3%
NIPAAm	30.5	113.2	53.6%
PEGDA	5	700.0	1.4%
BAPO	3.5	418.5	1.7%

DEI1+NIPAAm exhibited an excellent printability window as the other DEIs (**Figure S50**).

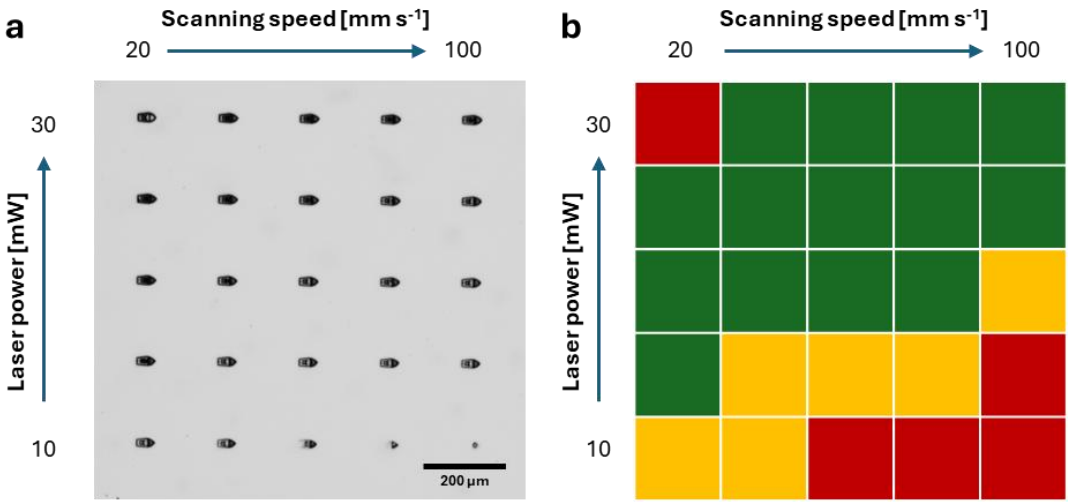

Figure S50: Printability window of DEI1+NIPAAm with *N*-isopropyl acrylamide. **a)** 3D printed benchmark boat structures (50 µm × 25 µm × 40 µm) and **b)** evaluation of the printing parameters.

3D printed temperature-, pH-, and calcium-responsive DEI1+NIPAAm

We 3D printed micrometric buckyballs with DEI1+NIPAAm in dimensions of 100 µm × 100 µm × 100 µm and recorded the printed structures upon heating and cooling between room temperature and 60 °C in water (**Video S5**).

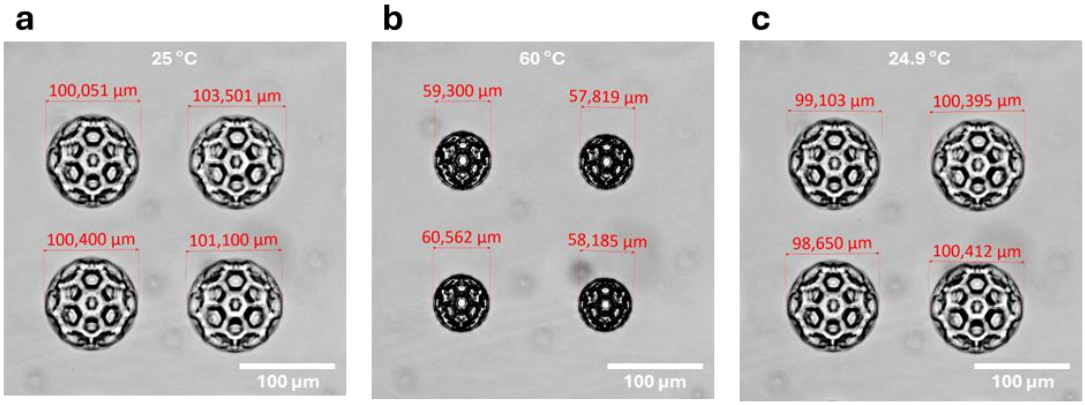

Figure S51: Temperature response of 3D printed buckyball (54 µm × 54 µm × 50 µm, laser power 20 mW, and scanning speed 40 mm s^{-1}) of DEI1+NIPAAm upon heating to 60 °C. The buckyballs shrink from a swelling factor of $S_V = 7$ (in **a**) to about $S_V = 1.3$ (in **b**) in volume. The dimensions recover upon cooling the microstructures back to room temperature (in **c**).

Upon heating, we observed large shrinkage of the buckyballs with a change in swelling factor from S_V = 7 at 25 °C to S_V = 1.0 at 60 °C with respect to the printed dimensions (**Figure S51**). This shrinkage was recovered when the buckyballs were cooled back to room temperature. The microprinted structures also exhibited the expected swelling or shrinkage upon addition of basic aqueous solution or calcium ions, respectively (see **Figure S52** and **Figure S53**).

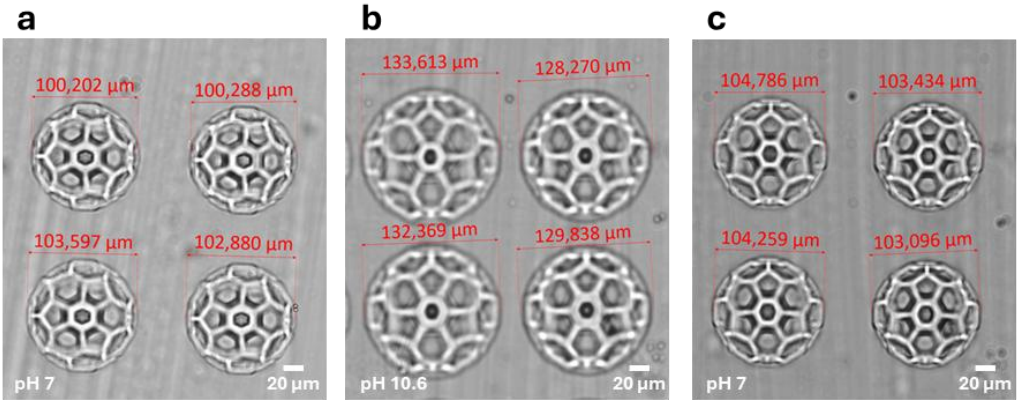

Figure S52: pH response of 3D printed buckyball (54 µm × 54 µm × 50 µm, laser power 20 mW, and scanning speed 40 mm s^{-1}) of DEI1+NIPAAm between pH = 7 and pH = 10.6. The buckyballs swell by a swelling factor of S_V = 7 (in **a**) to about S_V = 14.7 (in **b**) in volume. The dimensions recover upon bringing the microstructures back to pH = 7 (in **c**).

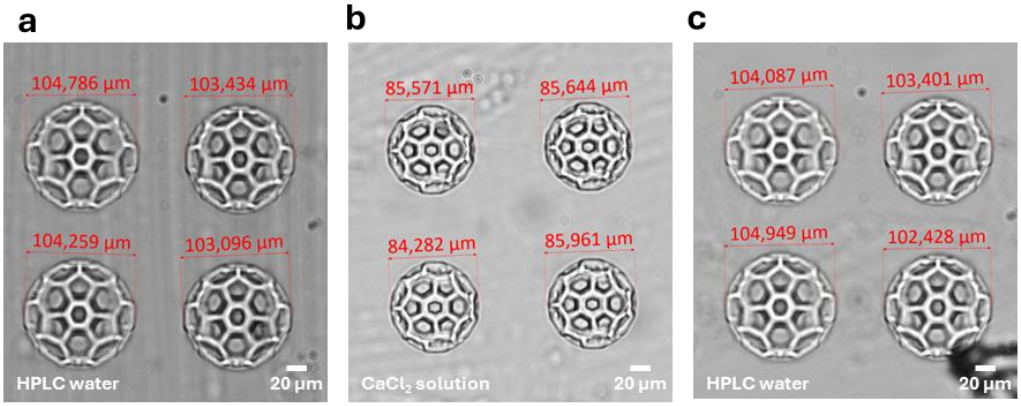

Figure S53: Calcium response of 3D printed buckyball (54 µm × 54 µm × 50 µm, laser power 20 mW, and scanning speed 40 mm s^{-1}) of DEI1+NIPAAm between HPLC water and aqueous calcium chloride solution (0.24 g mL^{-1}). The buckyballs shrink from a swelling factor of S_V = 7 (in **a**) to about S_V = 4 (in **b**) in volume. The dimensions recover upon washing the microstructures with HPCL water (in **c**).

To demonstrate the potential of combining different DEIs into multimaterial structures, we designed and printed gripper structures with dimensions of 620 µm × 620 µm × 240 µm. The

structural base for a bilayered actuator was printed with DEI3. The temperature-responsive layer was printed with DEI1+NIPAAm on top of the DEI3 base structure. The printed structures presented temperature-induced bending of the gripper arms upon heating and cooling between room temperature and 60 °C (**Figure S54** and **Video S6**).

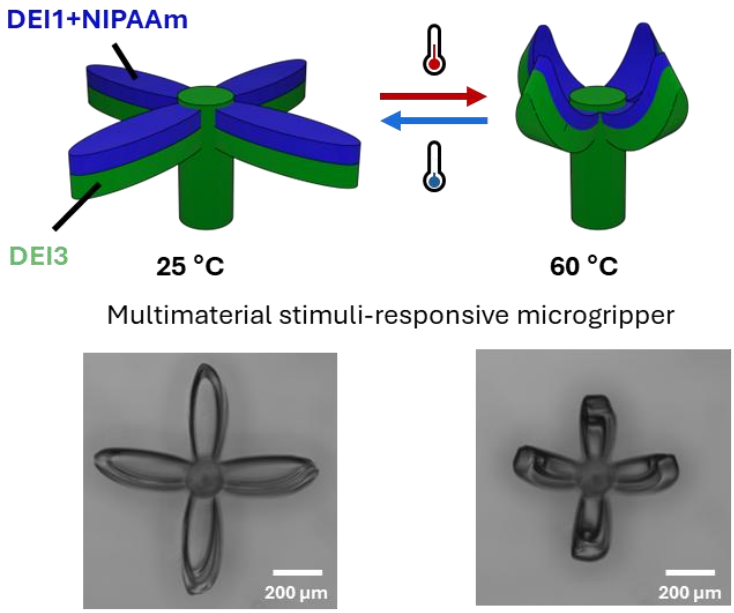

Figure S54: Temperature response of 3D printed multimaterial (DEI1+NIPAAm and DEI3) gripper (620 µm × 620 µm × 240 µm). Schematic representation (top) and optical microscopy images (bottom) of the observed temperature response.

Extending functionality by mixing DEIs with acrylamide

To show the versatility of DEIs, we mixed acrylamide, a monomer with a high melting point, in a 1:1 mass ratio with $ZnCl_2$-HEA_2. Since acrylamide was readily miscible in the DES, we prepared an ink (DEI2+AAm) by adding PEGDA and BDEABP (**Table S11**).

Table S11: Ink composition of DEI2+AAm with acrylamide.

Compound	wt%	M (g mol^{-1})	mol%
$ZnCl_2$-HEA_2	47.5	368.5	16.0%
AAm	47.5	71.1	83.9%
PEGDA	4	700.0	0.7%
BDEABP	1	324.5	0.4%

Remarkably, DEI2+AAm showed excellent printability using various laser powers and scanning speeds similar to DEI2 (**Figure S55**).

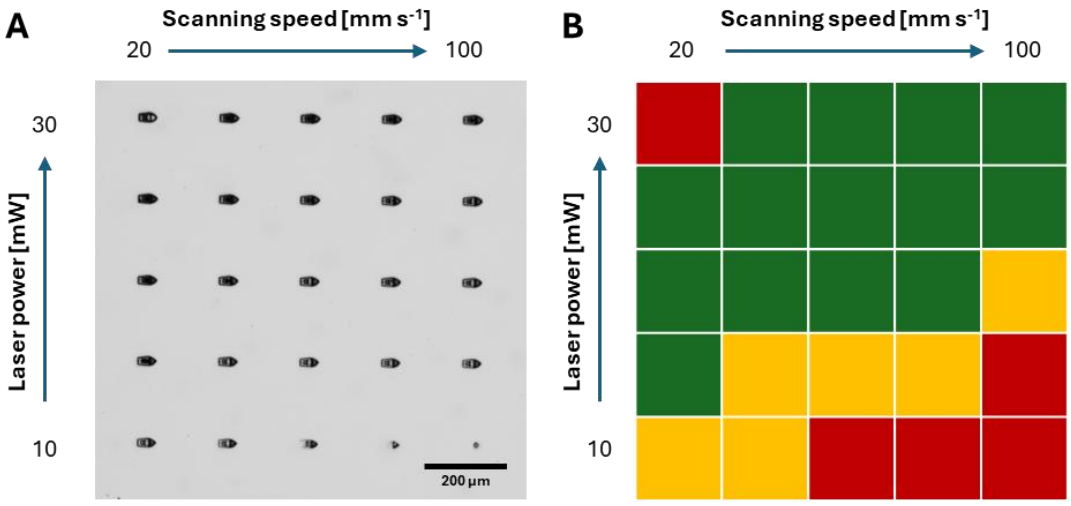

Figure S55: Printability window of DEI2+AAm for varying printing parameters. **a)** 3D printed benchmark boat structures (50 µm × 25 µm × 40 µm) and **b)** evaluation of printing parameters.

DEI2+AAm was used for MPLP of various structures such as a statue of liberty (2 mm height), space needle (1.5 mm height), 'Atomium' (600 µm), and 'Albero della vita' (600 µm).

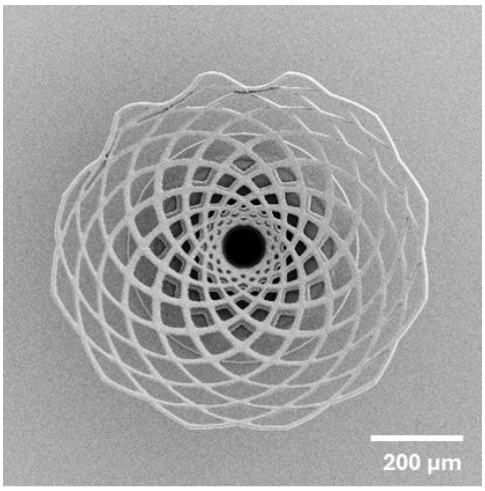

Figure S56: SEM image of DEI2+AAm 3D printed 'Albero della vita' in top view.

Figure S57: Optical microscopy image (side view) of DEI2+AAm printed statue of liberty before sputter coating.

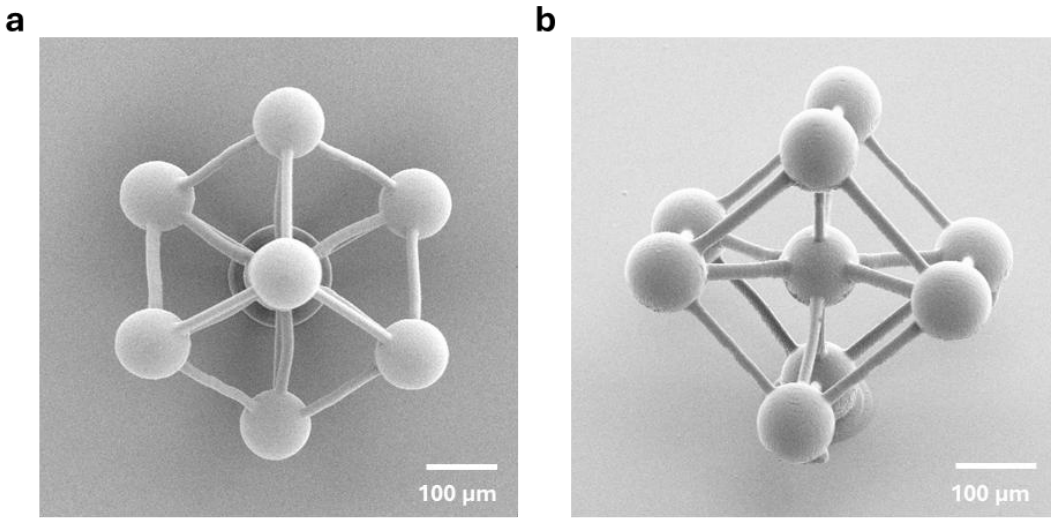

Figure S58: SEM images of DEI2+AAm 3D printed ‘Atomium’ **a)** in top view and **b)** in side view.

SEM images of 3D printed cubic grids

We have used DEI2 and DEI2+AAm for 3D printing cubic grids. The SEM images of the printed structures in **Figure 1** are shown from different angles in **Figure S59** and **Figure S60**.

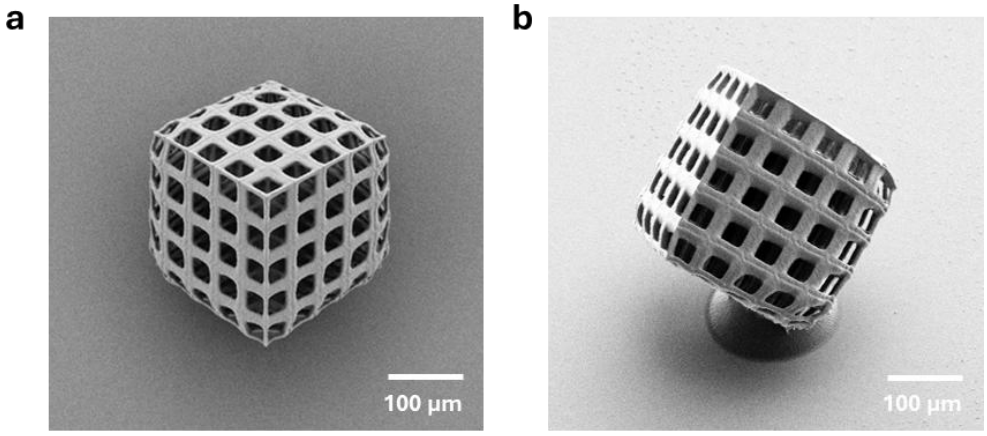

Figure S59: SEM images of DEI2 3D printed cubic grid **a)** in top view and **b)** in side view.

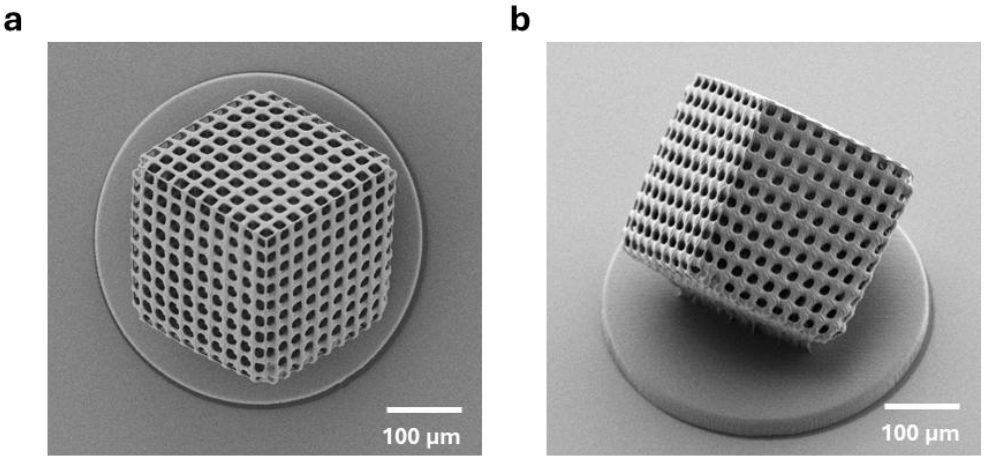

Figure S60: SEM images of DEI2+AAm 3D printed cubic grid **a)** in top view and **b)** in side view.

References

[1] M. Schmid, D. Ludescher, H. Giessen, *Opt. Mater. Express* **2019**, *9*, 4564.

[2] A. Kocyła, A. Pomorski, A. Krężel, *J. Inorg. Biochem.* **2017**, *176*, 53.

[3] Nanoscribe GmbH & Co. KG, Nanoguide, *IP-PDMS photoresin*, **April 2025**, https://support.nanoscribe.com/hc/en-gb/articles/360022218600-IP-PDMS.

[4] Q. Hu, G. A. Rance, G. F. Trindade, D. Pervan, L. Jiang, A. Foerster, L. Turyanska, C. Tuck, D. J. Irvine, R. Hague, R. D. Wildman, *Addit. Manuf.* **2022**, *51*, 102575.

[5] A. Toulouse, S. Thiele, K. Hirzel, M. Schmid, K. Weber, M. Zyrianova, H. Giessen, A. M. Herkommer, M. Heymann, *Opt. Mater. Express* **2022**, *12*, 3801.

[6] Nanoscribe GmbH & Co. KG, Products, A*vailable photoresins for dip-in MPLP*, **June 2025**, https://www.nanoscribe.com/fileadmin/Nanoscribe/PDF/Product_Folder/Folder-Printing-Materials-2025.pdf.

[7] BioINX, Products, DEGRAD *photoresin for dip-in MPLP*, **June 2025**, https://bioinx.com/sites/default/files/product_files/Degrad%20INX%20X100%20Product%20Information%20Sheet.pdf

[8] BioINX, Products, HYDROTECH *photoresin for dip-in MPLP*, **June 2025**, https://bioinx.com/sites/default/files/product_files/hydrotech%20X200%20product%20information%20sheet.pdf

[9] P. Schattling, F. D. Jochum, P. Theato, *Polym. Chem.* **2014**, *5*, 25.

[10] Y.-W. Lee, H. Ceylan, I. C. Yasa, U. Kilic, M. Sitti, *ACS Appl. Mater. Interfaces* **2021**, *13*, 12759.

2. RESPONSIVE 3D PRINTED MICROSTRUCTURES BASED ON COLLAGEN FOLDING AND UNFOLDING

Bibliographic reference

Philipp Mainik, Camilo Aponte-Santamaría, Magdalena Fladung, Ronald Ernest Curticean, Irene Wacker, Götz Hofhaus, Martin Bastmeyer, Rasmus R. Schröder, Frauke Gräter, and Eva Blasco. “Responsive 3D printed microstructures based on collagen folding and unfolding.” Small 21.3 (2024): 2408597.

Author contribution

Philipp Mainik has contributed to the *methodology* (lead), *validation* (lead), *formal analysis* (lead), *investigation* (lead), *data curation* (lead), *writing – original-draft* (lead), *writing – review & editing* (lead), and *visualization* (lead).

Formblatt Kumulative Dissertation

1. Publikation/*Publication*:
Vollständige bibliographische Referenz/*Complete bibliographic reference:*

Philipp Mainik, Camilo Aponte-Santamaría, Magdalena Fladung, Ronald Ernest Curticean, Irene Wacker, Götz Hofhaus, Martin Bastmeyer, Rasmus R. Schröder, Frauke Gräter, and Eva Blasco. "Responsive 3D printed microstructures based on collagen folding and unfolding." Small 21.3 (2024): 2408597.

2. Erst- oder gleichberechtigte Autorenschaft/*First or equal authorship*: Ja/*Yes*☒ Nein/*No* ☐

Veröffentlicht/*Published*	☑
Zur Veröffentlichung angenommen/*Accepted*	☐
Eingereicht/*Submitted*	☐
Noch nicht eingereicht/*Not yet submitted*	☐

4.* Beteiligungen/*Contributions**

Contributor Role	**Doktorand/in/ *Doctoral Student***	**Co-Autor/in 1/ *Co-author* 1**	**Co-Autor/in 2/ *Co-author 2***
Name, first name	Mainik, Philipp		
Methodology	x		
Software			
Validation	x		
Formal analysis	x		
Investigation	x		
Resources			
Data Curation	x		
Writing-Original Draft	x		
Writing-Review&Editing	x		
Visualization	x		
Supervision			
Project administration			
Funding acquisition			

Kategorien des CRediT (Contributor Roles Taxonomy, https://credit.niso.org/)

Hiermit bestätige ich, dass alle obigen Angaben korrekt sind/*I confirm that all declarations made above are correct.*

Unterschrift/*Signature* _____ _____ _____
Doktorand/in/*Doctoral student* **Co-Autor/in 1/*Co-author 1*** **Co-Autor/in 2/*Co-author***

Betreuungsperson/Supervisor:
Hiermit bestätige ich, dass alle obigen Angaben korrekt sind und dass die selbstständigen Arbeitsanteile des/der Doktoranden/in an der aufgeführten Publikation hinreichend und signifikant sind/*I confirm that all declarations made above are correct and that the doctoral student's independent contribution to this publication is significant and sufficient to be considered for the cumulative dissertation.*

Prof. Blasco, Eva — E. Blasco — 8.8.2025

Name/*Name* Unterschrift/*Signature* Datum/*date*

Stand: Februar 2025

RESEARCH ARTICLE

NANO · MICRO small
www.small-journal.com

Responsive 3D Printed Microstructures Based on Collagen Folding and Unfolding

*Philipp Mainik, Camilo Aponte-Santamaría, Magdalena Fladung, Ronald Ernest Curticean, Irene Wacker, Götz Hofhaus, Martin Bastmeyer, Rasmus R. Schröder, Frauke Gräter, and Eva Blasco**

Mimicking extracellular matrices holds great potential for tissue engineering in biological and biomedical applications. A key compound for the mechanical stability of these matrices is collagen, which also plays an important role in many intra- and intercellular processes. Two-photon 3D laser printing offers structuring of these matrices with subcellular resolution. So far, efforts on 3D microprinting of collagen have been limited to simple geometries and customized set-ups. Herein, an easily accessible approach is presented using a collagen type I methacrylamide (ColMA) ink system which can be stored at room temperature and be precisely printed using a commercial two-photon 3D laser printer. The formulation and printing parameters are carefully optimized enabling the manufacturing of defined 3D microstructures. Furthermore, these printed microstructures show a fully reversible response upon heating and cooling in multiple cycles, indicating successful collagen folding and unfolding. This experimental observation has been supported by molecular dynamics simulations. Thus, the study opens new perspectives for designing new responsive biomaterials for 4D (micro)printing.

1. Introduction

Natural extracellular matrices (ECMs) have served as an excellent source of inspiration for the design of cell scaffolds for biological and medical applications.[1,2] ECM-mimicking biomaterials and their processing in defined 3D structures have been gaining more and more interest in recent years.[3] Various advanced manufacturing techniques such as direct ink writing and light-based techniques relying on photopolymerization processes have been employed for these purposes.[4–8] Recently, two-photon 3D laser printing, also known as multi-photon lithography or direct laser writing, has attracted much attention. This 3D printing technology offers precise control in manufacturing on the micro- to nanometer scale, being highly suitable for the preparation of (single) cell 3D scaffolds with sub-cellular resolution.[9,10] In particular, polysaccharides (e.g., methacrylate chitosan or hyaluronic acid), as well as proteins (e.g., bovine serum albumin), cover a large range of biocompatible and easily accessible biomaterials exploited in the field.[11–24] These previously described bio-derived materials for two-photon 3D laser printing were mainly employed as non-responsive, structural hydrogels for the preparation of biocompatible cell scaffolds or microswimmers.

P. Mainik, E. Blasco
Institute for Molecular Systems Engineering and Advanced Materials (IMSEAM)
Heidelberg University
69120 Heidelberg, Germany
E-mail: eva.blasco@uni-heidelberg.de
P. Mainik, E. Blasco
Organic Chemistry Institute (OCI)
Heidelberg University
69120 Heidelberg, Germany
C. Aponte-Santamaría, F. Gräter
Heidelberg Institute for Theoretical Studies (HITS)
69118 Heidelberg, Germany
M. Fladung, M. Bastmeyer
Cell and Neurobiology
Zoological Institute
Karlsruhe Institute of Technology (KIT)
76131 Karlsruhe, Germany
R. E. Curticean, I. Wacker, G. Hofhaus, R. R. Schröder
BioQuant
Heidelberg University
69120 Heidelberg, Germany
M. Bastmeyer
Institute for Biological and Chemical Systems – Biological Information Processing (IBCS-BIP)
Karlsruhe Institute of Technology (KIT)
76344 Karlsruhe, Germany
F. Gräter
Interdisciplinary Center for Scientific Computing (IWR)
Heidelberg University
69120 Heidelberg, Germany

The ORCID identification number(s) for the author(s) of this article can be found under https://doi.org/10.1002/smll.202408597

DOI: 10.1002/smll.202408597

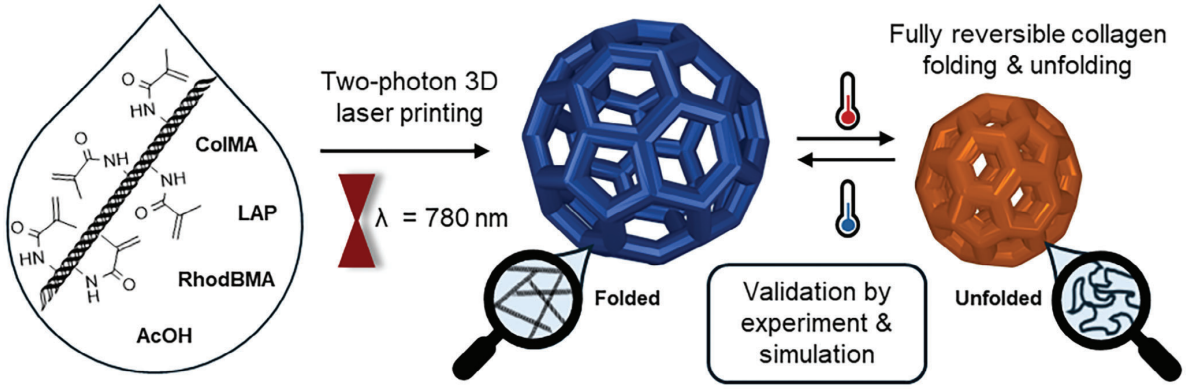

Figure 1. Two-photon 3D laser printing of collagen methacrylamide (ColMA) in the presence of a water-soluble photoinitiator (LAP), fluorescent dye (RhodBMA), and acetic acid (AcOH) at room temperature. The microprinted structures showed a fully reversible temperature-responsive behavior based on collagen folding and unfolding. The experimental observation was supported by molecular dynamics simulations.

Printability of these biomaterials is usually achieved either by functionalizing hydroxy or amine side groups of the biopolymers with photocrosslinkable thiol-ene or (meth)acrylate groups or by using photosensitizers which often imply the use of high doses.[25]

High-resolution 3D printing of collagen is of great interest since it is the major structural component in the ECM and hence, collagen microstructures are close to mimicking the ECM.[26] In ECMs, collagen provides exceptional mechanical stability while maintaining perfusive properties.[27,28] The mechanical stability originates from the assembly of collagen into triple helices which crosslink and form higher-order assemblies to fibrils and fibers. First studies in the direction of microprinting of ECMs employed native collagen type I in the presence of photosensitizers such as riboflavin or rose bengal to create 2D patterns by crosslinking the collagen.[29–33] Custom-made set-ups were necessary due to the high laser doses required, limiting its application in fabricating 3D scaffolds. One way to overcome these drawbacks is a chemical modification of collagen. This approach enabled efficient photocrosslinking of the collagen and therefore significantly lower energy doses are required for printing, making it more attractive for biomedical applications. For example, Tytgat et al. 3D printed isobornene- and thiol-functionalized recombinant collagen to encapsulate cells.[34] In another work, Shrestha et al. microprinted commercially accessible collagen type I methacrylamide (ColMA) for culturing retinal cells.[35] In the latter, the authors achieved improved printability compared to native collagen, but cooling the ink during printing was necessary to avoid its precipitation. In addition to these technical limitations, it remains unclear if the printing process allows collagen self-assembly as known in ECMs, as the retention of the secondary structure of collagen after 3D printing has not been demonstrated yet.

In this work, we present a robust and facile methacrylamide-functionalized collagen-based printable system that is stable at ambient conditions and can be printed with a commercially available setup. This approach offers fast microfabrication of biocompatible arbitrary 3D collagen structures increasing the versatility and applicability of current efforts. Moreover, we show temperature-responsive reversible collagen folding and unfolding not only in the ink but also 3D printed microstructures for the first time, leading to large and reproducible volume changes (**Figure 1**). The fully reversible temperature-dependent response is to the best of our knowledge the first demonstration of responsive self-assembly of collagen in (3D printed) materials.

2. Results & Discussion

2.1. 3D Microprinting of Collagen

The first step toward achieving an easily accessible approach for high-resolution 3D printing of collagen was the design of a printable formulation (ink) that is stable and compatible with two-photon 3D laser printing (Figure 1). We selected ColMA as a suitable starting material since it is easily accessible either commercially or by methacrylation of native collagen and exhibits increased thermal stability by reversibly forming physical gels between 4 and 34 °C.[36,37] In order to overcome the room temperature instability of previously reported collagen inks, the ColMA was dissolved in an acetic acid medium (0.02 M) in which native collagen exhibits increased thermal stability.[38–40] Before printing, the preservation of the collagen triple-helix structure, i.e., folded collagen, was verified by UV circular dichroism (UV-CD) spectroscopy (Figure S1, Supporting Information). The ColMA solution showed two characteristic bands at 200 and 220 nm resembling reported characteristic native collagen folding bands.[26,41,42] Thus, the collagen methacrylamide type I ink (collagen ink) was prepared by dissolving ColMA in a concentration of 8 mg mL^{-1} in 0.02 M acetic acid and adding lithium phenyl-2,4,6-trimethyl-benzoylphosphinate (LAP) (35 mg mL^{-1}), a water-soluble and biocompatible photoinitiator. Additionally, a fluorescence dye, methacryloxyethyl thiocarbamoyl rhodamine B (RhodBMA), was added to facilitate subsequent imaging of the 3D printed microstructures using confocal fluorescence microscopy. The methacrylate group enabled chemically covalent incorporation of the fluorescent dye in the printed structure. The collagen ink (pH 3.8) was characterized for its viscosity by rotational rheology and optical properties by refractometry as well as UV and infrared spectroscopy (Figures S3–S6,

ADVANCED SCIENCE NEWS
www.advancedsciencenews.com

NANO · MICRO small
www.small-journal.com

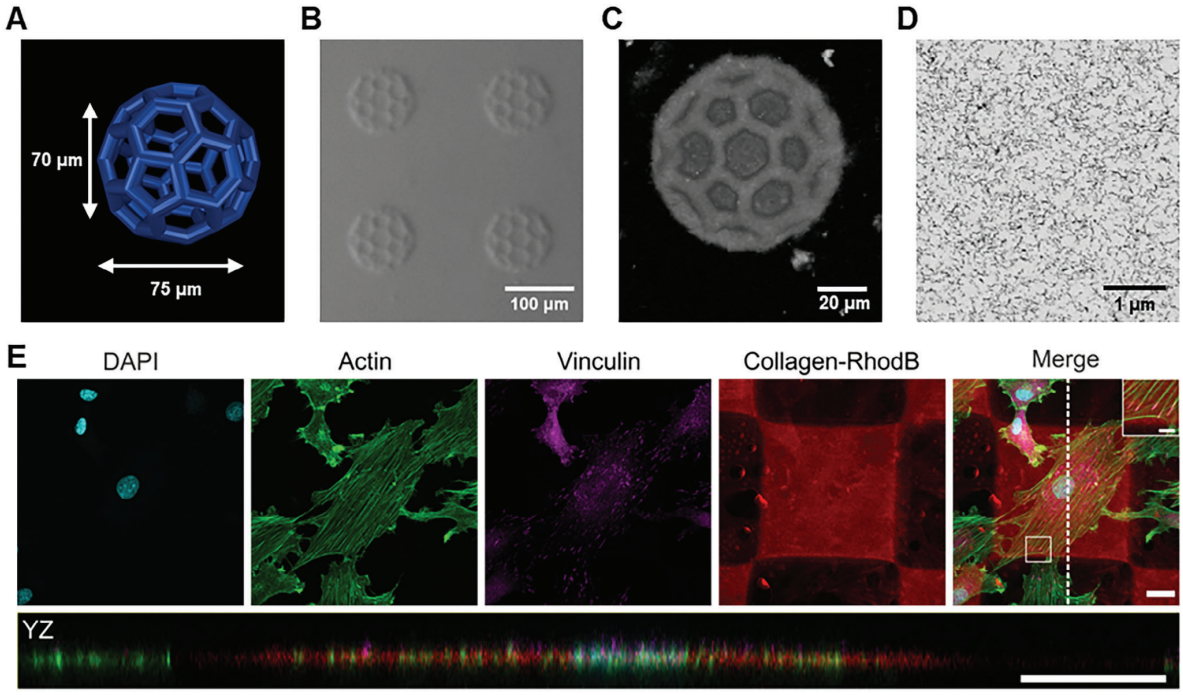

Figure 2. Two-photon 3D laser printing of collagen ink at room temperature. A) Model of empty buckyball as complex 3D microstructure with overhanging features in dimensions of 75 µm × 75 µm × 70 µm. B) Optical microscopy image acquired with CDIC contrast of micrometric buckyballs which were successfully printed with a laser power of 42 mW and scanning speed of 20 $mm^{-1}s^{-1}$. C) Top view (XY) on volumetric 3D reconstruction showing the porous free-standing features of microprinted collagen buckyballs acquired with confocal fluorescence microscopy. D) Large field of view scanning electron microscopy image of printed collagen nanostructure after embedding and sectioning showing the distribution of fibrils in the ultrathin section. The printed structure is composed of 13.2 nm ± 2.4 nm thick fibrils. E) Confocal images of immunocytochemical staining of rat embryonic fibroblast (REF) cells cultured on 3D laser-printed collagen blocks. Cells adhered to the printed scaffold (red) and exhibited an undisturbed actin organization (green). The magnification of the indicated area shows that focal adhesions, as visualized by Vinculin-staining (magenta), formed on the RhodBMA-labelled collagen blocks (red). Cells adhered to the top of the scaffolds as shown by the YZ-projection. The projection plane is indicated by a white dotted line in the merged image. Scale bars: 20 µm, magnification: 5 µm.

Supporting Information). Furthermore, we investigated the morphology of our collagen ink by cryo-transmission electron microscopy and found fibrils exhibiting thicknesses of 12.3 nm ± 2.5 nm (Figures S7,S8, Supporting Information). Importantly, the collagen ink was stable for several weeks at room temperature without showing precipitation or any significant change in printability.

The printability of the collagen formulation was tested using a commercial two-photon 3D laser printing set-up (Photonic GT2, Nanoscribe GmbH) with a 25× objective. As a first step, 3D cubic lattice microstructures with dimensions of 100 µm × 100 µm × 70 µm were printed with varying printing parameters such as laser powers ranging from 21 to 42 mW and scanning speeds from 20 to 60 $mm^{-1}s^{-1}$. The broad printability window for printing these microstructures is depicted in Figure S9 (Supporting Information). After removal of unpolymerized ink washing first with a 0.02 M acetic acid solution and subsequently with water (HPLC grade), the structures retained their printed dimensions. The 3D-printed collagen microstructures were stable at pH conditions between 2.6 and 10.8 (see Figure S10, Supporting Information). Furthermore, the fabrication of complex hollow 3D geometries, such as micrometric buckyballs (**Figure** 2A) with a diameter of ≈75 µm was successfully achieved, proving the good printability and versatility of the new collagen ink. First, the printed collagen was imaged by optical microscopy using contrast methods such as phase or circular differential interference contrast due to the high content of water in the 3D microstructures (Figure 2B). Additionally, confocal microscopy was employed to analyze the printed buckyballs in 3D (Figure 2C). A 3D reconstruction using experimental data proved the hollow features as expected from the model with good accuracy (see Figure S11, Supporting Information).

The precision of the printing process was further experimentally quantified by printing single parallel lines and analyzed using confocal microscopy. Resolved lines have been observed when printing with a distance of 1.5 µm between them (see Figure S12, Supporting Information). The minimum feature size was determined as 460 nm ± 70 nm by measuring the thickness of five separate lines.

As a next step, we aimed to analyze the internal nanostructure of the microprinted collagen by using electron microscopy to see how the fibrils in the ink translate into the printed collagen. The high-water content of the collagen microstructures (>99% in the collagen ink) led to an irreversible collapse upon simple

drying. Therefore, we have first replaced the water stepwise with ethanol and subsequently, acetone to perform either critical point drying or embedding the printed microstructures in epoxide resin. Critical point drying led to a partial collapse of the microstructures (see Figure S13, Supporting Information), so we focused on employing an embedding protocol. For this purpose, we prepared 3D blocks of 50 µm × 50 µm × 50 µm (laser power 42 mW and scanning speed of 25 $mm^{-1}s^{-1}$). The 3D-printed collagen micrometric blocks were embedded and sectioned, and the cross-sections were imaged by scanning electron microscopy (SEM). SEM images indicated a fibrillar network (see Figure 2D for a large field of view and Figures S14,S15, Supporting Information for the zoom-in). The average diameter of the fibrils in the printed collagen was found to be 13.2 nm ± 2.4 nm (Figure S16, Supporting Information). In addition to SEM, we performed TEM of 70 nm thick sections. The embedded printed collagen exhibited an internal fibrillar nanostructure (Figure S17, Supporting Information) as already suggested by SEM. The diameter obtained by TEM was 12.6 nm ± 2.3 nm (Figure S18, Supporting Information) and was found to be similar to the determined average from SEM. Comparing the fibrils in the ink with the fibrils observed in the microprinted collagen suggested that there is no apparent influence on the fibrils during the printing process (see Table S1, Supporting Information).

Next, biocompatibility, i.e., cell viability and immunocytochemical analysis, was addressed by culturing rat embryonic fibroblast cells on the 3D-printed collagen scaffolds. In detail, cells were seeded on arrays of 10 × 10 printed squares (100 µm × 100 µm, height 5 µm) as shown in Figure S19 (Supporting Information). For cell viability, live and dead cells were labeled with Calcein-AM and ethidium homodimer (EthD1) after 24 h, respectively. Additionally, cell nuclei were visualized with Hoechst. The obtained fluorescence images are depicted in Figure S20 (Supporting Information). Throughout three independent experiments, the majority of cells appeared positive for the live stain and negative for the dead stain. Statistical analysis with a total number of N = 473 cells verified > 99% of cells to be alive (Figure S21, Supporting Information). Immunocytochemical staining was performed to verify the adhesion and unaltered cytoskeletal organization of the cells. As depicted in Figure 2E and Figure S22 (Supporting Information), focal adhesions formed normally as shown by the vinculin staining and the actin skeleton appears to be undisturbed. The orthogonal projection in YZ shows that the cells are well spread and adhered to the top of the scaffold. These results indicate that the collagen ink did not significantly impact cell viability and did not interfere with the organization of the actin cytoskeleton or the formation of focal adhesions. Hence, the herein-used collagen ink exhibits good biocompatibility.

2.2. Response Study of the Collagen 3D Microstructures

Once we had characterized the internal fibrillar nanostructure of the 3D-printed collagen, we used temperature as a stimulus to study the response. It is well-known that heating of collagen leads to uncoupling of the triple helices.[26,37] Therefore, we were interested in exploiting this effect in 3D-printed collagen. First, we verified the temperature-induced unfolding of the collagen ink by UV-CD spectroscopy (see Figures S23–S25, Supporting Information). Upon heating above 37 °C, which is known to be the temperature range for unfolding or denaturation of collagen type I from mammalian sources,[43] the characteristic collagen UV-CD band at 220 nm started to vanish completely between 40 and 42 °C suggesting the successful unfolding of the collagen triple helix[40,41,43] Cooling the ColMA back to room temperature resulted in a slight recovery of the bands which could be entirely recovered by keeping the sample for 2 days at 4 °C similar as it has been observed for native collagen.[26]

Next, we investigated if the reversible self-assembly, i.e., unfolding and folding transition, also takes place in the 3D-printed collagen microstructures. To this aim, we printed the previously optimized 3D microstructures consisting of buckyballs with larger dimensions (≈100 µm diameter) (see **Figure 3A**). As a reference, frames of non-responsive commercial material (IP-S, Nanoscribe GmbH) were printed around. After two-photon 3D laser printing, the 3D printed buckyballs were observed by optical microscopy varying the temperature from 25 to 48 °C (and vice versa) with 1 °C min^{-1} (Video S1, Supporting Information). Upon heating, the micrometric buckyballs shrank isotropically. Cooling the heated microstructures back to room temperature fully recovered the initial dimensions of the buckyballs. The response in the same temperature range indicates that the reversible temperature-responsive unfolding also occurs in 3D-printed (crosslinked) collagen.

Quantitative analysis of this reversible temperature response was performed with cubic lattice structures with dimensions of 100 µm × 100 µm × 70 µm (Figure 3B and Video S2, Supporting Information). In detail, the top layer areas of cubic lattice structures were measured and used for calculating the volumetric swelling factor (S_V) with increasing temperature, respectively (Figure S26, Supporting Information). The onset point was observed at ≈41 °C, which is in good agreement with the transition temperature detected for the collagen unfolding by UV-CD spectroscopy (see Figure 3C). A total volume reduction of over 50% (S_V = 0.45) was found upon heating. This behavior was found to be reversible over multiple times (5 cycles) exhibiting similar volume changes (S_V = 0.45-0.50), i.e., shrinkage, upon heating and full recovery to the initial "swollen state" (S_V = 1.00-0.95) upon cooling (Figure 3D). The highly reproducible response proves reversible self-assembly and the absence of defects in the 3D-printed collagen microstructures.

To investigate the effect of the printing parameters on the response, we have printed the cubic lattices with increasing scanning speed in 20 $mm^{-1}s^{-1}$ step from 20 to 100 $mm^{-1}s^{-1}$, which should result in decreasing crosslinking density. (see Figures S27,S28, Supporting Information). Although the shrinking was found to be similar, the recovery rate upon cooling to room temperature decreased with the reduction of different crosslinking densities. For lower crosslinked structures, full recovery was observed after 1 h at room temperature. Enhancing recoveries with higher crosslinking were previously reported for the recovery of shape memory polymers suggesting that the mechanism of folding can be described as similar to the recrystallization process.[44–47]

Stochastic molecular dynamics simulations were performed to support the molecular basis of the shrinkage of collagen

ADVANCED SCIENCE NEWS
www.advancedsciencenews.com

NANO · MICRO small
www.small-journal.com

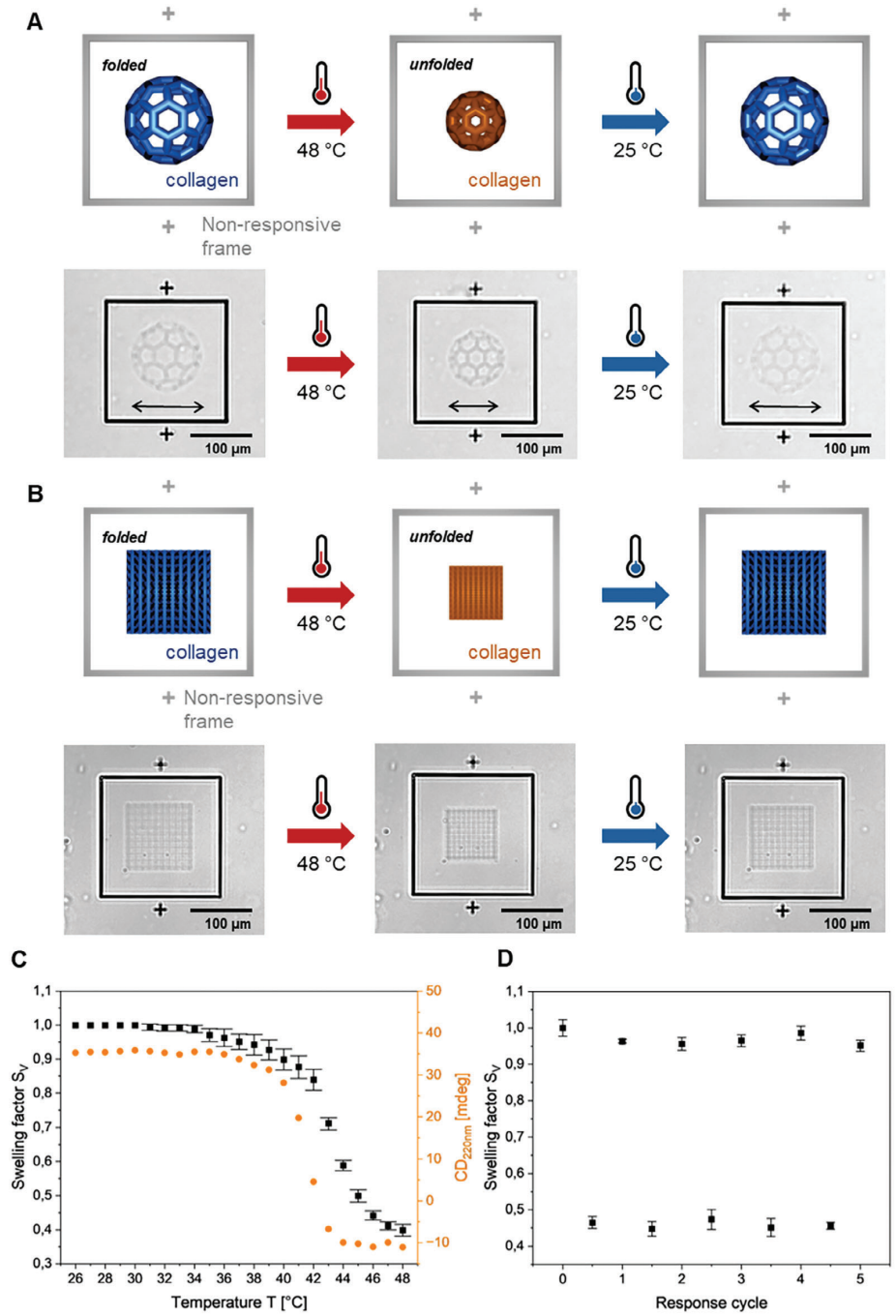

Figure 3. Analysis of the temperature response of 3D printed collagen microstructures. A,B): Temperature-response of two-photon 3D printed collagen buckyballs (diameter of ≈100 µm) and cubic lattice grids (100 µm × 100 µm × 70 µm) and a non-responsive frame of commercial printed IP-S (Nanoscribe GmbH). Models (up) and optical microscopy images (down). Upon heating, the microstructure shrinks due to collagen unfolding, and cooling the microstructures back to 25 °C entirely recovers the initially printed structure. Further images with multiple printed fields can be found in the Supporting Information (see Figure S26, Supporting Information). C) Volumetric swelling factor (S_V) of 3D microprinted cubic lattices (100 µm × 100 µm × 70 µm) upon heating (black). UV-CD signal at 220 nm of 5 µg mL^{-1} ColMA in 0.02 M acetic acid solution upon heating to different temperatures (orange). The change at 220 nm occurs due to the unfolding of collagen. D) Temperature response over multiple response cycles. The swelling factors are calculated from images at room temperature of cubic lattices before and after heating to 48 °C.

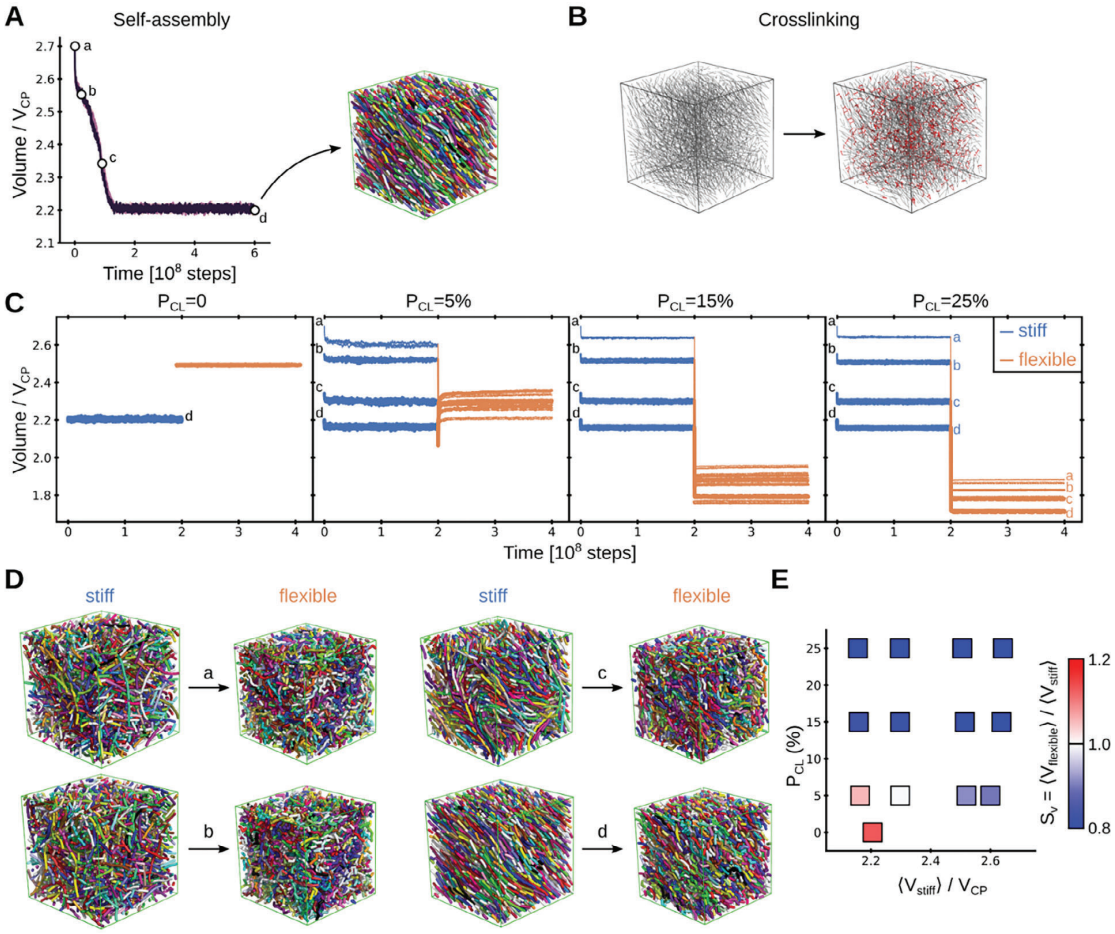

Figure 4. Reducing bending stiffness induces the shrinkage of crosslinked polymers in stochastic molecular dynamics simulations. A) Volume of the system during self-assembly of a mixture of semiflexible polymers ($n = 3$, lines). The volume is normalized by the theoretical closed packing volume, V_{CP}, and time is given in the integration steps. For each replica, four conformations with different volumes were selected (white circles, labeled a, b, c, d). The snapshot shows the last of such conformation (polymers shown as ribbons of different colors). B) Upon self-assembly, polymers were crosslinked with crosslinking probability P_{CL}, as exemplified here for one system (polymers in gray and crosslinks in red). C) Volume time traces are shown for a stage during which the crosslinked polymers were kept semi-rigid ("stiff": blue) and for a subsequent stage in which they were set fully flexible ("flexible": orange). N = 3 replicas were conducted for each of the four distinct initially considered volumes (different lines and labels a–d) and different crosslinking probability, P_{CL} (panels). For comparison, time traces for $P_{CL} = 0$ (no crosslinks) are also shown (here only one volume is applicable, corresponding to "d" in A). D) The shrinking process is illustrated for the four cases indicated in C for $P_{CL} = 25\%$. Polymers are shown as ribbons of different colors. E) The swelling factor, $Sv = \langle V_{flexible} \rangle / \langle V_{stiff} \rangle$, i.e., the ratio between the average volumes in the "flexible" and the "stiff" stages, respectively (<> denoting time average), was obtained as a function of the volume in the stiff stage ($\langle V_{stiff} \rangle$: x-axis) and the crosslinking probability (P_{CL}: y-axis). S_V is depicted in color according to the color scale at the right. Accordingly, shrinking upon flexibilization of the polymers is shown in blue and swelling in red.

microstructures by heating. For this purpose, we mimicked the microstructure as a mixture of semi-flexible crosslinked polymers. We initially let the mixture self-assemble under equilibrium conditions and chose conformations at four different stages during this process for further simulations (see **Figure** 4A). Subsequently, polymer chains were crosslinked with different crosslinking probability, P_{CL} (Figure 4B). Crosslinking helped to maintain the volume of the system almost constant, not only for the final stable conformation, with the lowest volume but also for conformations with larger volumes which would be unstable without crosslinks (Figure 4C).

Heating, above the phase transition temperature, transitioned collagen from a folded conformation into a random coil in experiments (see Figure 3C; Figures S23–S25, Supporting Information). Folded collagen triple helices display persistence lengths varying from few to several tens of nm,[48–50] meaning they are at least an order of magnitude stiffer than unfolded protein chains (for which persistence lengths are ≈1 nm).[51–53] We modeled this

ADVANCED SCIENCE NEWS
www.advancedsciencenews.com

NANO · MICRO small
www.small-journal.com

effect by reducing the bending stiffness of the individual polymer chains (by ≈25-fold in terms of their persistence length) while still maintaining the crosslinks between them (see Experimental Section). Accordingly, the system turned from a mixture of "stiff" into one of "flexible" crosslinked polymers (we note that our simplified coarse-grained approach ignores other potential factors such as the change in topology when three chains form from one helix). Remarkably, this caused the volume of the systems to reduce in the majority of the crosslinked cases (compare "stiff" and "flexible" stages in Figure 4C and see representative conformational transitions in Figure 4D). The swelling factor was computed here as a function of two key free parameters: the volume before the coil transition (i.e., the volume in the "stiff" stage, $<V_{stiff}>$) and the crosslinking probability (P_{CL}) (Figure 4E). Substantial shrinkage was observed for crosslinking probabilities above 15%, independently of $<V_{stiff}>$. Shrinkage was also observed for lower probabilities, but to a smaller extent and only provided that the initial volume was considerably high ($<V_{stiff}> > 2.4 \cdot V_{CP}$). In the absence of crosslinks, the system did not shrink but swelled instead (compare $P_{CL} = 0$ with $P_{CL} \neq 0$ in Figures 4C,E). In summary, our simulations demonstrate that a mixture of cross-linked polymers undergoes shrinking transitions, by loosening the bending rigidity of the constituent chains.

3. Conclusion

We have presented an easily accessible collagen ink suitable for two-photon 3D laser printing, which can be stored at room temperature for several weeks and be used with commercial printing set-ups, thereby significantly facilitating future applications. Furthermore, we have proved biocompatibility and preservation of fibrillar structure in the 3D printed collagen microstructures. Therefore, we believe that this approach paves the way for 3D laser printing of extracellular matrices to influence and support other biological studies on cell migration and tissue assemblies.[54–56] Moreover, we have demonstrated for the first time the full reversibility of temperature-induced self-assembly, i.e., folding and unfolding, of collagen in 3D printed materials. Strikingly, full reversibility was found in multiple cycles leading to recurring large volume changes. This makes the new response mechanism particularly interesting for the future development of responsive biomaterials, with tunable changes in volume and molecular structure. For example, the temperature transition of the folding-unfolding mechanism can be tuned either by varying the collagen source or by implementing synthetic collagen-mimicking fragments.[26,57,58] Thus, we also believe that these results provide an excellent platform for designing printed biomaterials that are responsive and whose properties can be modeled and predicted by theory.

4. Experimental Section

Chemicals & Materials: Bovine collagen type I methacrylamide (ColMA) was used as purchased from Advanced BioMatrix with the product name PhotoCol. The photoinitiator lithium phenyl-2,4,6-trimethylbenzoylphosphinate (LAP) and HPLC grade water were purchased from Fisher Scientific. Acetic acid (0.1 M) was purchased from Merck and diluted with HPLC-graded water to a concentration of 0.02 M. The fluorescent dye methacryloxyethyl thiocarbamoyl rhodamine B (RhodBMA) was purchased from Polysciences. All chemicals and samples were stored and handled under yellow light. SYLGARD 184 Silicone Elastomer Kit from Dow Chemical was used for the preparation of polydimethylsiloxane (PDMS) molds.

Preparation of Collagen Ink: ColMA (12 mg) was first dissolved in 1.5 mL of acetic acid (0.02 M) by vigorously stirring the lyophilized solid for 3 h at 4 °C. Next, LAP (10.5 mg) was dissolved in 300 µL water and added to the dissolved ColMA solution. Last, RhodBMA (1 mg) was added to 1 mL of water and sonicated for 15 min in a sonicator bath to get a saturated aqueous RhodBMA solution. After filtration of the solution with a syringe filter (0.2 µm), 300 µL of the saturated dye solution was added to obtain the final collagen ink.

Characterization of Collagen Ink: The pH was measured with METTLER TOLEDO S220 SevenCompact. The flow properties of the inks were measured by rotational rheometry using a HAAKE MARS rheometer with a measuring geometry of C60/1° Ti-L. The shear rate varied between 100 and 1500 s^{-1} in 30 steps. Refraction indices were determined at 20 °C and the two-photon laser printing wavelength 780 nm using a Schmidt+Haensch ATR L refractometer. UV–vis and FT–IR spectroscopy of the collagen ink was measured with a Jasco V-770 and a Jasco FT/IR-4600 spectrometer, respectively. UV–vis spectroscopy was performed using a Quartz cuvette (d = 2 mm). Before cryo-electron microscopy, 3 µL of the collagen ink was applied to a glow discharged (3s, Solarus Gatan) Quantifoil (2/1, copper) specimen support grid and blotted in a humidified atmosphere for 4 s (Vitrobot, Thermofisher). The sample was vitrified by plunging it into liquid ethane. Grids were mounted under liquid nitrogen in autogrids and stored. The ink was imaged using similar conditions as the TEM sections (see Sectioning and imaging using electron microscopy in Experimental Section).

Silanization Procedure: Glass coverslips (Marienfeld, 170 ± 5 µm) and indium tin oxide (ITO)-coated glass coverslips (SPI Supplies, 160–190 µm, 70—100 Ω sq^{-1}) were washed with isopropanol and acetone and dried with pressurized nitrogen. Subsequently, the surface was activated for 1 min by plasma treatment using a TDK PiezoBrush. The coverslips were immersed in a 4 mM solution of 3-(trimethoxysilyl)propyl methacrylate in toluene for 1.5 h. The methacrylate-functionalized coverslips were further washed twice in toluene and once in acetone and used as substrates for microprinting.

Two-Photon Laser Printing of 3D Collagen Microstructures: Two-photon laser printing was performed with a commercially available set-up (Photonic Professional GT2, Nanoscribe GmbH & Co. KG) in an oil immersion configuration and a femtosecond laser wavelength of 780 nm. All structures were printed using a 25× oil objective (NA = 0.8) from Zeiss for focusing the laser inside of the ink. Before printing, GWL files were generated with the Describe software (Nanoscribe) from previously designed STL files of desired geometries by setting slicing and hatching to 300 nm for all printed geometries, respectively. Before printing, a PDMS mold was prepared and placed on the methacrylate-functionalized coverslips (22 mm × 22 mm) to avoid evaporation of solvent during the printing process. Next, collagen ink (5–30 µL) was applied to the PDMS mold before the filled mold was covered with a round glass slide from the other side. The sandwich cell was inserted into the Nanoscribe GT2 and printed with scanning speeds ranging from 20 to 60 $mm^{-1}s^{-1}$ and laser powers in the range of 21–42 mW depending on the structure and experiment. After micro printing, the round coverslip and residual collagen ink were removed, and the structures were washed 5 times with ≈100 µL of acetic acid (0.02 M) and 5 times with 100 µL of water always ensuring the structures never dried. Last, the PDMS mold was closed with a round glass slide again to avoid solvent evaporation. It is important to note that the structures need to be kept in aqueous media throughout the whole procedure and analysis to avoid irreversible collapse of the collagen network upon drying.

Optical and Confocal Fluorescence Microscopy: Optical (fluorescence) microscopy images were recorded with a Zeiss Axio Imager M2 using a 5× long distance Zeiss objective (NA = 0.13) or an LD Plan-Neofluar 20×/0.4 Korr Ph M27 objective (NA = 0.4) and an Axiocam 705 microscope camera. Fluorescence images were recorded with a Zeiss Axio Imager Z1 using an excitation wavelength of 555 nm. Fluorescent z-stacks

of collagen microstructures were recorded with a Nikon A1R confocal microscope equipped with GaAsP-detectors using a 20× Nikon objective (NA = 0.8). A 559 nm diode laser was used for excitation, and the emission at 595 nm was collected. The structure was imaged in slices of 0.8 µm step width with a pinhole diameter of 1 au. Data was computed and analyzed using ImageJ. Cell viability assays were imaged using a Zeiss AxioObserver Z1 epifluorescence microscope, equipped with a heated incubation chamber and A-Plan 5× objective (NA = 0.12) and LD A-Plan 20× objective (NA = 0.35). Confocal fluorescence images of immunocytochemical staining were acquired with a Zeiss LSM800 confocal microscope equipped with a 40× oil immersion objective (NA = 1.4).

Embedding Protocol for Electron Microscopy: Scanning and transmission electron microscopy images were acquired after embedding two-photon 3D laser-printed collagen structures in epoxide resin. For this purpose, 50 µm × 50 µm × 50 µm cubes were first printed on ITO-coated glass coverslips and developed using the previously described development procedure with acetic acid (0.02 M) and HPLC water.

To avoid the collapse of collagen, a multi-step embedding protocol was followed for successful fixation, heavy-atom staining, dehydration, and critical point or embedding in an epoxide resin.

First, the structures were fixed by immersing them in 2.5% aqueous glutaraldehyde solution for 30 min. After washing the structures 3 times for 5 min with distilled water, the structures were immersed in a 3% aqueous tannic acid solution for 2 h at 4 °C. Removing the tannic acid solution and washing the printed structures 3 times for 5 min with distilled water was followed by staining and additional fixation with an aqueous solution of 2% OsO_4 and 1.6% $K_3[Fe(CN)_6]$ for 1 h at 4 °C. Washing the stained and fixed structures was performed twice for 5 min with distilled water before adding additional stain by immersing them in aqueous 2% uranyl acetate solution containing 25% ethanol at 4 °C overnight. On the next day, the stained and fixated structures were washed with a 25% ethanol-water mixture twice for 5 min before being fully dehydrated in consecutive steps. This dehydration was performed by increasing the ethanol content from 25, 50, 70, and 90 to 100% in 10 min steps. Next, the ethanol was replaced stepwise by 50 and 100% acetone following the same time steps.

For critical point drying, acetone was replaced in 25 iterations at 17 °C by carbon dioxane using a Leica CPD300. For the embedding procedure, the solvent was replaced stepwise by mixtures of 30 and 70% epoxide resin in acetone, for 2 h each, followed by 100% epoxide for 1 h before being embedded in flat silicon molds. The molds were transferred into a heating oven and kept at 65 °C for 2 days. Removal of the glass substrate from the embedded sample was facilitated by placing the substrate in liquid nitrogen. Printing on ITO-coated glass coverslips allowed easier separation of glass and embedding resin. It should be noted that 3D structures shrank to ≈70% of the original volume after fixation and embedding (see Figure S14, Supporting Information).

Sectioning and Imaging using Electron Microscopy: Resin blocks were trimmed and sectioned using a Powertome PC ultramicrotome (RMC Boeckeler, Tucson, USA) equipped with diamond knives (Diatome, Biel, Switzerland) for trimming (Trim20) and cutting (Ultra 35). For SEM imaging (Ultra 55, Carl ZEISS Microscopy, Oberkochen, Germany) 70 nm sections were collected on pieces of Si wafer and post-stained with 3% aqueous uranyl acetate followed by 3% aqueous lead citrate (Science Services, München, Germany). Hierarchical imaging at 1.5 keV landing energy using SE and ESB detectors was performed with the Atlas 5 software package (Carl ZEISS Microscopy). For TEM imaging 60 nm sections were collected on 200 mesh Quantifoil 2.2 Au grids (Quantifoil, Jena, Germany) and post-stained with 3% uranyl acetate for 1 min.

For TEM images of the printed material, 70 µm sections of the embedded and stained material were placed on a QF grid and observed in a Krios (Thermofisher) electron microscope at 300 kV, equipped with an autoloader. Images were taken under cryo and low dose conditions at a pixel size of 2.8 Å with a Gatan K3 camera operated in counting mode. At an underfocus ≈2 µm movies were collected with a total dose of ≈20 e/Å2 using EPU software (Thermo Fischer) and corrected for beam-induced motion (Motioncorr2 in Relion).

Cell Viability Assay: Rat embryonic fibroblast cells were seeded onto collagen scaffolds, fabricated by two-photon 3D laser printing, and cultivated in DMEM supplemented with 10% FCS from Pan-Biotech (Aidenbach, Germany) in a humidified incubator at 37 °C and 5% CO_2 overnight. Cell viability was verified using the LIVE/DEAD Viability/Cytotoxicity Kit from Invitrogen (Waltham, MA, USA), which applies calcein-AM and ethidium homodimer-1 (EthD1) to label live and dead cells, respectively. In addition, cell nuclei were stained with Hoechst 33342 from Invitrogen (Waltham, MA, USA). Labeling solutions were allowed to incubate for 30 min at 37 °C. Cells were imaged in PBS containing calcium and magnesium from Pan-Biotech (Aidenbach, Germany) using epifluorescence microscopy and a 5× or 20× objective lens. The excitation wavelengths were 401, 493, and 577 nm, respectively.

Live and dead cells were characterized using Fiji. First, a mask was created from the cell nuclei based on the Hoechst labeling. For live cells, a threshold was applied to the calcein-AM labeling to binarize the image. The binarized image was analyzed using the "analyze particles" plugin, restricting the particle size to 15-infinite µm. Detected particles, which did not correspond to a nucleus, were excluded from analysis. For dead cells, a threshold was applied to the EthD1-staining to cut off the fluorescence of the RhodBMA-labeled collagen. The previously created mask was applied to analyze the nuclei for EthD1-labeling using the "analyze particles" plugin, restricting the particle size to 5-infinite µm. If multiple particles were detected per nucleus, they were counted as one. Percentiles of live and dead cells were calculated using Microsoft Excel.

Immunocytochemical Staining: Immunostaining was performed to visualize the cell nuclei, focal adhesions, and actin cytoskeleton. Cells were fixed 24 h after seeding in 5% paraformaldehyde and permeabilized with PBS containing 0.1% Triton-X100. The samples were incubated with 5 µg mL^{-1} anti-Vinculin antibody (Invitrogen (Waltham, MA, USA)) in 1% (w/w) bovine serum albumin in PBS, followed by washing with PBS with 0.1% Triton-X100 and incubation with secondary antibody donkey anti-mouse Alexa Fluor 647 (Invitrogen (Waltham, MA, USA)), DAPI (10 µg mL^{-1}) and Alexa Fluor 488 Phalloidin (1.5 U mL^{-1}). Staining solutions were allowed to incubate for 1 h at room temperature in a humidity chamber.

Temperature-Responsive Reversible Folding and Unfolding Behavior: Heating of microprinted collagen was performed with a heating stage (LTS 420, Linkam Scientific Instruments) in the optical microscope. The transmission illumination mode with differential interference contrast and reflection mode with circular differential interference contrast were used for imaging. The investigated temperature programs started at 25 °C and heated the printed collagen to 48 °C using a gradient of 1 °C min^{-1}. The heated microstructures were subsequently cooled using a gradient of 1 °C min^{-1} back to room temperature. The swelling factor S_V was calculated by estimating the volume from the top area of the printed cubic lattice grids. The top layer area of five lattices was used as an average.

UV-CD spectra of the ColMA were recorded with a Jasco J-1700-CD spectrometer between 190 and 260 nm with a scanning speed of 100 nm min^{-1}. To detect the CD signal, ColMA was diluted with 20 mM acetic acid to a concentration of 5 µg mL^{-1} or below for the measurement. Heating of the ink was performed at a speed of 1 °C min^{-1} while measuring the temperature of the holder. After cooling the cuvette and recording a CD spectrum at 4 °C, the cuvette was stored for 2 days at 4 °C before remeasuring the CD signal.

Stochastic Molecular Dynamics Simulations: We modeled a fraction of the 3D-printed collagen microstructures as a mixture of semiflexible crosslinked polymers. The mixture was constituted of 200 chains, each one with a degree of polymerization of 50. Each chain was modeled as a series of beads (one per monomer) connected by harmonic springs, with a bonded interaction energy $V_{bond} = K_{bond}(d\text{-}2r)^2/2$. Here, K_{bond} is the elastic constant, d is the distance between consecutive beads, and 2r is the equilibrium distance. Pairs of beads i and j sterically repelled from each other, via consideration of the repulsive term of a Lennard-Jones potential $V_{rep} = 4\epsilon(\sigma/d_{ij})$.[12] Here, ϵ is the strength of the potential, σ relates to the radius of each bead (i.e., each monomer) via $r = \sigma(2^{1/6})/2$, and d_{ij} corresponds to the separation between beads. The repulsive

ADVANCED SCIENCE NEWS
www.advancedsciencenews.com

NANO · MICRO small
www.small-journal.com

potential was considered for all beads within a cutoff distance (d_{cutoff}) and it was excluded for neighbor bonded beads. The bending rigidity of the chains was imposed by introducing an angular potential between all triads of consecutive bonded beads of the form $V_{angle} = K_\theta[\cos(\theta)-\cos(\theta_0)]^2/2$, where K_θ is the strength of the potential, θ is the angle formed by the triad of beads and $\theta_0 = 180°$. Stochastic molecular dynamics were carried out to monitor the dynamics of the mixtures using the GROMACS MD package (version 2020.3) ("sd" integrator option).[59] For each bead, the friction coefficient was assumed to be $m\gamma$, where m is the bead mass and $1/\gamma$ is the relaxation time. The friction coefficient is related to the diffusion coefficient, D, via $D = k_BT/m\gamma$, where k_B is the Boltzmann constant and T the temperature. Langevin equations of motion were numerically solved at discrete time steps Δt. Neighbors were treated according to the Verlet buffer scheme.[60] The length was normalized by the separation between beads (related to) σ, time by the characteristic diffusion time of a bead $\tau = (2r)^2/D$, mass by the mass of a bead, and energy by k_BT (see list of simulation parameters in Table S2, Supporting Information).

The chains were assumed to adopt initial linear conformations and were placed at random positions and orientations, without overlap, in a cubic box of dimensions $(399.6\ \sigma)^3$. The box dimensions were reduced gradually in two consecutive steps, first, during 10^7 integration steps until the system reached a volume of $(48\ \sigma)^3$ and second, during 10^6 integration steps until the volume was $(30\ \sigma)^3$. From this point on, the system was simulated under equilibrium NPT conditions. The system was coupled to a Berendsen barostat to maintain the pressure constant at 1 bar (coupling time of 5 in GROMACS arbitrary units equivalent to $\approx 0.07937\ \tau$).[61] In addition, Langevin dynamics ensured the temperature stayed constant at 300 K (see resulting k_BT in Table S2, Supporting Information). In the first stage, the system was allowed to further self-assemble for $6{\cdot}10^8$ integration steps (simulation length $\approx 0.952{\cdot}10^6\ \tau$). N = 3 simulation replicas were conducted. Four configurations with different volumes were extracted from each replica for further simulations (times indicated with the white circles in Figure 4). In the second stage, crosslinks between chains were added. For the four selected configurations, pairs of monomers that belonged to different chains, but which were in close proximity (at a distance smaller than 2r) were connected by a harmonic spring with a crosslinking probability P_{CL} = 5, 15, or 25%. The elastic constant of the spring was set to K_{bond} and the equilibrium reference distance to 2r. Subsequently, the dynamics of the resulting crosslinked mixture were simulated during $2{\cdot}10^8$ integration steps (simulation length $\approx 0.317{\cdot}10^6\ \tau$). This stage was denoted as the "stiff" stage in Figure 4. In the third stage, the bending rigidity of the chains was removed by setting the angular interaction potential $V_{angle} = 0$. The crosslinked (now flexible) mixture was simulated during $2{\cdot}10^8$ integration steps (simulation length $\approx 0.317{\cdot}10^6\ \tau$). Note that crosslinks between chains were maintained during this stage. This stage was denoted as the "flexible" stage in Figure 4. The persistence length of a single chain in isolation was predicted to be ≈50r, in the "stiff" stage, and 2r, in the "flexible" stage (i.e., a ≈25-fold decrease upon release of the angular constraints). For comparison, simulations without crosslinks ($P_{CL} = 0$) were also carried out. In this case, the last $2{\cdot}10^8$ integration steps of the self-assembly process, for which the system already equilibrated (see Figure 4A), were considered as the "stiff" stage. For the "flexible" stage, additional simulations were conducted removing the angular restraints, starting from the final configuration upon self-assembly.

The volume of the system was monitored throughout the different stages. It was normalized by the theoretical closed packing volume, $V_{CP} = (32/\pi){\cdot}V_{mon}{\cdot}N \approx 1.35{\cdot}V_{mon}{\cdot}N$, for N = 10 000 monomers, each one with a volume $V_{mon} = 4\pi r^3/3$. The swelling factor was computed as $Sv = \langle V_{flexible}\rangle/\langle V_{stiff}\rangle$, with $\langle V_{flexible}\rangle$ and $\langle V_{stiff}\rangle$ being the average volumes during the "flexible" and the "stiff" stages, respectively (<> denotes time average over the last 10^8 steps of each stage combining the $n = 3$ replicas).

Supporting Information

Supporting Information is available from the Wiley Online Library or from the author.

Acknowledgements

The authors acknowledge the funding from the Deutsche Forschungsgemeinschaft (DFG, German Research Foundation) via the Excellence Cluster "3D Matter Made to Order" (EXC-2082/1-390761711), the Carl Zeiss Foundation through the "Carl-Zeiss Foundation-Focus@HEiKA" and the Klaus Tschira Foundation. Further, the authors acknowledge support by the state of Baden-Württemberg through bwHPC, the German Research Foundation (DFG) through the grants INST 35/1597-1 FUGG and INST 35/1503-1 FUGG as well as the data storage service SDS@hd supported by the Ministry of Science, Research and the Arts Baden-Württemberg (MWK). The authors acknowledge the access to the Nikon Imaging Center Heidelberg and InnovationLab. The authors thank Clara Vazquez-Martel for fruitful discussions. The authors also thank Fabian Lill and Pia Klee for their assistance with UV-CD measurements.

Open access funding enabled and organized by Projekt DEAL.

Conflict of Interest

The authors declare no conflict of interest.

Data Availability Statement

The data that support the findings of this study are openly available in heiDATA, the Open Research Data institutional repository for Heidelberg University at https://doi.org/10.11588/data/WTFEHF.

Keywords

4D printing, extracellular matrix, self-assembly, stimuli-responsive materials, two-photon laser printing

Received: October 15, 2024
Published online: November 27, 2024

[1] K. A. Kyburz, K. S. Anseth, *Ann. Biomed. Eng.* **2015**, *43*, 489.
[2] M. P. Lutolf, J. A. Hubbell, *Nat. Biotechnol.* **2005**, *23*, 47.
[3] E. A. Guzzi, M. W. Tibbitt, *Adv. Mater.* **2020**, *32*, 1901994.
[4] K. S. Lim, J. H. Galarraga, X. Cui, G. C. J. Lindberg, J. A. Burdick, T. B. F. Woodfield, *Chem. Rev.* **2020**, *120*, 10662.
[5] V. G. Muir, J. A. Burdick, *Chem. Rev.* **2021**, *121*, 10908.
[6] M. A. S. R. Saadi, A. Maguire, N. T. Pottackal, M. S. H. Thakur, M. M. Ikram, A. J. Hart, P. M. Ajayan, M. M. Rahman, *Adv. Mater.* **2022**, *34*, 2108855.
[7] C. Mendes-Felipe, L. Pérez-Álvarez, L. Ruiz-Rubio, J. L. Vilas-Vilela, *Emerg. Mater.* **2020**, *3*, 453.
[8] J. L. Ifkovits, J. A. Burdick, *Tissue Eng.* **2007**, *13*, 2369.
[9] C. Greant, B. van Durme, J. van Hoorick, S. van Vlierberghe, *Adv. Funct. Mater.* **2023**, *33*, 2212641.
[10] R. Link, K. Weißenbruch, M. Tanaka, M. Bastmeyer, U. S. Schwarz, *Adv. Funct. Mater.* **2024**, *34*, 2302145.
[11] M. R. Lee, I. Y. Phang, Y. Cui, Y. H. Lee, X. Y. Ling, *Small* **2015**, *11*, 740.
[12] I. Zergioti, A. Karaiskou, D. G. Papazoglou, C. Fotakis, M. Kapsetaki, D. Kafetzopoulos, *Appl. Phys. Lett.* **2005**, *86*, 163902.
[13] D. Serien, K. Sugioka, *ACS Biomater. Sci. Eng.* **2020**, *6*, 1279.
[14] B. Kaehr, J. B. Shear, *Proc. Natl. Acad. Sci. U.S.A.* **2008**, *105*, 8850.
[15] A. Ovsianikov, A. Deiwick, S. Van Vlierberghe, P. Dubruel, L. Möller, G. Dräger, B. N. Chichkov, *Biomacromolecules* **2011**, *12*, 851.
[16] A. Ovsianikov, S. Mühleder, J. Torgersen, Z. Li, X. Qin, S. Van Vlierberghe, P. Dubruel, W. Holnthoner, H. Redl, R. Liska, J. Stampfl, *Langmuir* **2014**, *30*, 3787.

[17] D. Gong, N. Celi, L. Xu, D. Zhang, J. Cai, *Mater. Today Chem.* **2022**, *579*, 152165.
[18] F. A. Pennacchio, C. Fedele, S. D. Martino, S. Cavalli, R. Vecchione, P. A. Netti, *ACS Appl. Mater. Interfaces* **2018**, *10*, 91.
[19] F. A. Pennacchio, C. Casale, F. Urciuolo, G. Imparato, R. Vecchione, P. A. Netti, *Biomater. Sci.* **2018**, *6*, 2084.
[20] P. Sanjuan-Alberte, J. Vaithilingam, J. C. Moore, R. D. Wildman, C. Tuck, M. R. Alexander, R. J. M. Hague, F. J. Rawson, *Polymers* **2021**, *13*, 1038.
[21] S. Engelhardt, E. Hoch, K. Borchers, W. Meyer, H. Krüger, G. E. M. Tovar, A. Gillner, *Biofabrication* **2011**, *3*, 025003.
[22] X. Wang, X. Qin, C. Hu, A. Terzopoulou, X. Chen, X.-Z. Chen, T.-Y. Huang, K. Maniura-Weber, S. Pané, B. J. Nelson, *Adv. Funct. Mater.* **2018**, *28*, 1804107.
[23] M. Taale, B. Schamberger, F. Taheri, Y. Antonelli, A. Leal-Egaña, C. Selhuber-Unkel, *Adv. Funct. Mater.* **2023**, *34*, 2302356.
[24] H. Jia, J. Flommersfeld, M. Heymann, S. K. Vogel, H. G. Franquelim, D. B. Brückner, H. Eto, C. P. Broedersz, P. Schwille, *Nat. Mater.* **2022**, *21*, 703.
[25] K. D.a Silva, P. Kumar, Y. E. Choonara, L. C. Du Toit, V. Pillay, *J. Biomed. Mater. Res.* **2020**, *108*, 2324.
[26] M. Meyer, *Biomed. Eng. Online* **2019**, *18*, 24.
[27] K. M. Chrobak, D. R. Potter, J. Tien, *Microvasc. Res.* **2006**, *71*, 185.
[28] S. O. Sarrigiannidis, J. M. Rey, O. Dobre, C. González-García, M. J. Dalby, M. Salmeron-Sanchez, *Mater. Today Bio.* **2021**, *10*, 100098.
[29] B. S. Shavkuta, M. Y. Gerasimov, N. V. Minaev, D. Kuznetsova, V. V. Dudenkova, I. A. Mushkova, B. E. Malyugin, B. Malyugin, S. L. Kotova, P. Timashev, P. S. Timashev, S. V. Kostenev, B. N. Chichkov, V. N. Bagratashvili, *Laser Phys. Lett.* **2018**, *15*, 015602.
[30] A. Bell, M. Kofron, M. Kofron, V. Nistor, *Biofabrication* **2015**, *7*, 035007.
[31] L. P. Cunningham, M. P. Veilleux, P. J. Campagnola, *Opt. Express* **2006**, *14*, 8613.
[32] M. Gebinoga, J. Katzmann, U. Fernekorn, J. Hampl, F. Weise, M. Klett, A. Läffert, T. A. Klar, A. Schober, *Eng. Life Sci.* **2013**, *13*, 368.
[33] S. Basu, L. P. Cunningham, G. D. Pins, K. A. Bush, R. Taboada, A. R. Howell, J. Wang, P. J. Campagnola, *Biomacromolecules* **2005**, *6*, 1465.
[34] L. Tytgat, A. Dobos, M. Markovic, L. van Damme, J. van Hoorick, F. Bray, H. Thienpont, H. Ottevaere, P. Dubruel, A. Ovsianikov, S. van Vlierberghe, *Biomacromolecules* **2020**, *21*, 3997.
[35] A. Shrestha, B. N. Allen, L. A. Wiley, B. A. Tucker, K. S. Worthington, *J. Ocul. Pharmacol. Ther.* **2020**, *36*, 42.
[36] I. D. Gaudet, D. I. Shreiber, *Biointerphases* **2012**, *7*, 25.
[37] K. E. Drzewiecki, A. S. Parmar, I. D. Gaudet, J. R. Branch, D. H. Pike, V. Nanda, D. I. Shreiber, *Langmuir* **2014**, *30*, 11204.
[38] J. Gross, D. Kirk, *J. Biol. Chem.* **1958**, *233*, 355.
[39] T. Hayashi, Y. Nagai, *J. Biochem.* **1973**, *73*, 999.
[40] C. Mu, D. Li, W. Lin, Y. Ding, G. Zhang, *Biopolymers* **2007**, *86*, 282.
[41] W. T. Brinkman, K. Nagapudi, B. S. Thomas, E. L. Chaikof, *Biomacromolecules* **2003**, *4*, 890.
[42] K. E. Drzewiecki, D. R. Grisham, A. S. Parmar, V. Nanda, D. I. Shreiber, *Biophys. J.* **2016**, *111*, 2377.
[43] E. Leikina, M. V. Mertts, N. Kuznetsova, S. Leikin, *Proc. Natl. Acad. Sci. U.S.A* **2002**, *99*, 1314.
[44] X. Xiao, D. Kong, X. Qiu, W. Zhang, Y. Liu, S. Zhang, F. Zhang, Y. Hu, J. Leng, *Sci. Rep.* **2015**, *5*, 14137.
[45] T. Calvo-Correas, N. Gabilondo, A. Alonso-Varona, T. Palomares, M. A. Corcuera, A. Eceiza, *Eur. Polym. J.* **2016**, *78*, 253.
[46] R. Chen, Q. Cheng, F. Gao, J. Zhong, L. Shen, C. Lin, Y. Lin, *Eur. Polym. J.* **2021**, *147*, 110304.
[47] X. L. Wu, S. F. Kang, X. J. Xu, F. Xiao, X. L. Ge, *J. Appl. Polym. Sci.* **2014**, *131*, 40559.
[48] Y.-L. Sun, Z.-P. Luo, A. Fertala, K.-N. An, *Biochem. Biophys. Res. Commun.* **2002**, *295*, 382.
[49] N. Rezaei, A. Lyons, N. R. Forde, *Biophys. J.* **2018**, *115*, 1457.
[50] K. Ghavanloo, *J. Biol. Phys.* **2017**, *43*, 525.
[51] A. Sarkar, S. Caamano, J. M. Fernandez, *J. Biol. Chem.* **2005**, *280*, 6261.
[52] J. Danielsson, A. Andersson, J. Jarvet, A. Gräslund, *Magn. Reson. Chem.* **2006**, *44*, S114.
[53] A. Hoffmann, A. Kane, D. Nettels, D. E. Hertzog, P. Baumgärtel, J. Lengefeld, G. Reichardt, D. A. Horsley, R. Seckler, O. Bakajin, B. Schuler, *Proc. Natl. Acad. Sci. U.S.A.* **2007**, *104*, 105.
[54] K. Siemsen, S. Rajput, F. Rasch, F. Taheri, R. Adelung, J. Lammerding, C. Selhuber-Unkel, *Adv. Healthcare Mater.* **2021**, *10*, 2100625.
[55] C. M. Denais, R. M. Gilbert, P. Isermann, A. L. McGregor, M. te Lindert, B. Weigelin, P. M. Davidson, P. Friedl, K. Wolf, J. Lammerding, *Science* **2016**, *352*, 353.
[56] O. Guillaume, O. Kopinski-Grünwald, G. Weisgrab, T. Baumgartner, A. Arslan, K. Whitmore, S. Van Vlierberghe, A. Ovsianikov, *Acta Biomater.* **2023**, *165*, 72.
[57] M. Goodman, M. Bhumralkar, E. A. Jefferson, J. Kwak, E. Locardi, *Biopolymers* **1998**, *47*, 127.
[58] F. Dewan, M. Kirchner, F. Masoud, Z. Sami, Y. Xu, *Biomacromolecules* **2023**, *24*, 5871.
[59] M. J. Abraham, T. Murtola, R. Schulz, S. Páll, J. C. Smith, B. Hess, E. Lindahl, *SoftwareX* **2015**, *1*, 19.
[60] S. Páll, B. Hess, *Comput. Phys. Commun.* **2013**, *184*, 2641.
[61] H. J. C. Berendsen, J. P. M. Postma, W. F. van Gunsteren, A. DiNola, J. R. Haak, *J. Chem. Phys.* **1984**, *81*, 3684.

Supporting Information

Responsive 3D printed microstructures based on collagen folding and unfolding

Philipp Mainik [1,2], Camilo Aponte-Santamaría [3], Magdalena Fladung [4], Ronald Ernest Curticean [5], Irene Wacker [5], Götz Hofhaus [5], Martin Bastmeyer [4,6], Rasmus R. Schröder [5], Frauke Gräter [3,7], Eva Blasco [1,2]*

*corresponding author (eva.blasco@uni-heidelberg.de)

Affiliations

[1] Institute for Molecular Systems Engineering and Advanced Materials (IMSEAM), Heidelberg University, 69120 Heidelberg, Germany.

[2] Organic Chemistry Institute (OCI), Heidelberg University, 69120 Heidelberg, Germany.

[3] Heidelberg Institute for Theoretical Studies (HITS), 69118 Heidelberg, Germany.

[4] Cell and Neurobiology, Zoological Institute, Karlsruhe Institute of Technology (KIT), 76131 Karlsruhe, Germany.

[5] BioQuant, Heidelberg University, 69120 Heidelberg, Germany.

[6] Institute for Biological and Chemical Systems - Biological Information Processing (IBCS-BIP), Karlsruhe Institute of Technology (KIT), 76344 Karlsruhe, Germany.

[7] Interdisciplinary Center for Scientific Computing (IWR), Heidelberg University, 69120 Heidelberg, Germany.

Supporting Information

Outline

1. Characterization of collagen-based ink

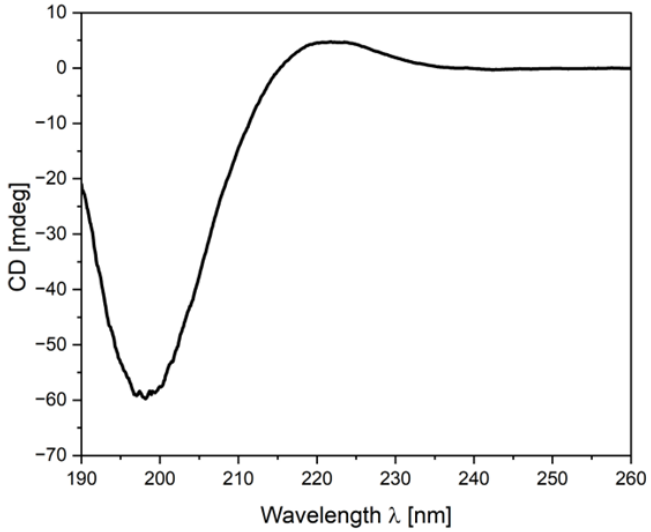

Figure S1: UV-CD spectrum of ColMA (2 µg/mL) in 0.02 M acetic acid aqueous solution at 25 °C.

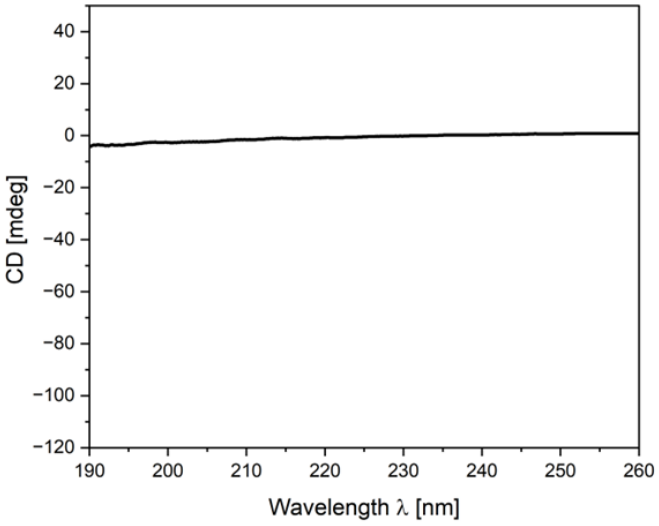

Figure S2: Reference UV-CD spectrum of 0.02 M acetic acid aqueous solution at 25 °C.

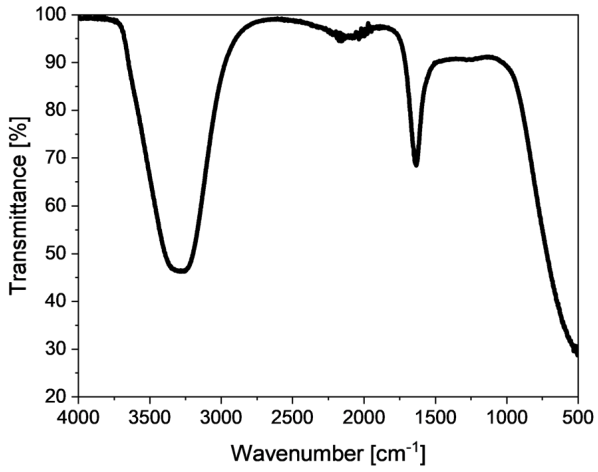

Figure S3: IR spectrum of the collagen methacrylamide ink showing two main absorption bands. The band at 3300 cm^{-1} corresponds to the O-H vibrational band of water. The band at 1600 cm^{-1} is in the region C=O vibration of the polypeptide backbone.

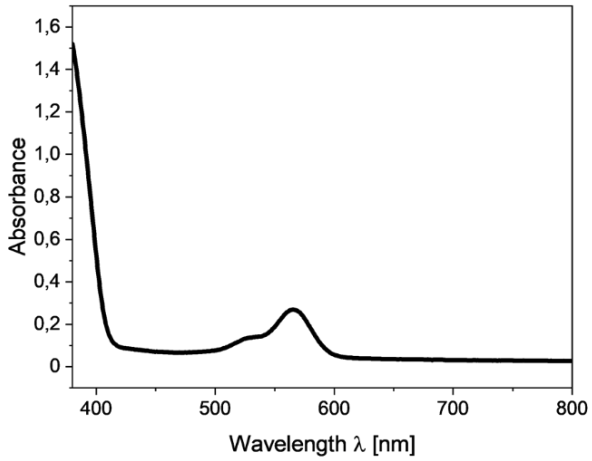

Figure S4: UV-vis spectrum of the collagen ink in a quartz cuvette with d = 2 mm showing strong absorption of the photoinitiator LAP below 400 nm. The two absorption bands between 500 nm and 600 nm correspond to rhodamine B methacrylate. Importantly, no additional absorption in the printing region at 780 nm was observed.

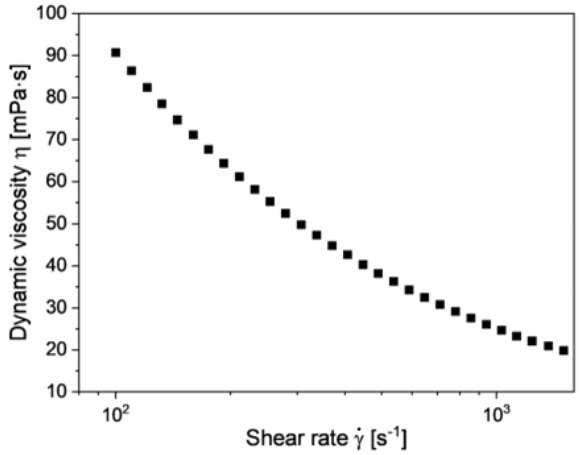

Figure S5: Measured dynamic viscosity at 25 °C for varying shear rates from 100 s^{-1} to 1500 s^{-1} using rotational rheology.

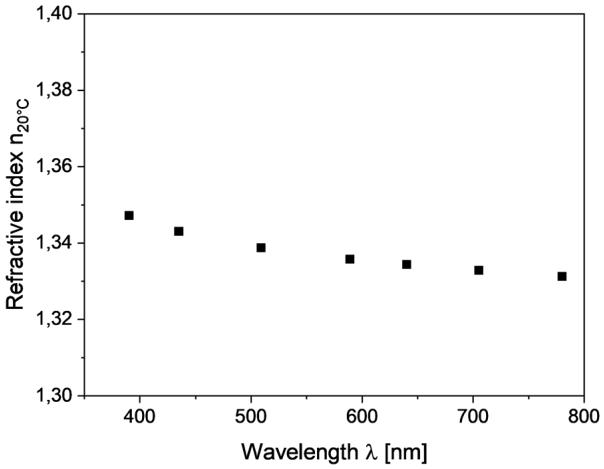

Figure S6: Measured refractive indices at 20 °C between 380 nm and 780 nm.

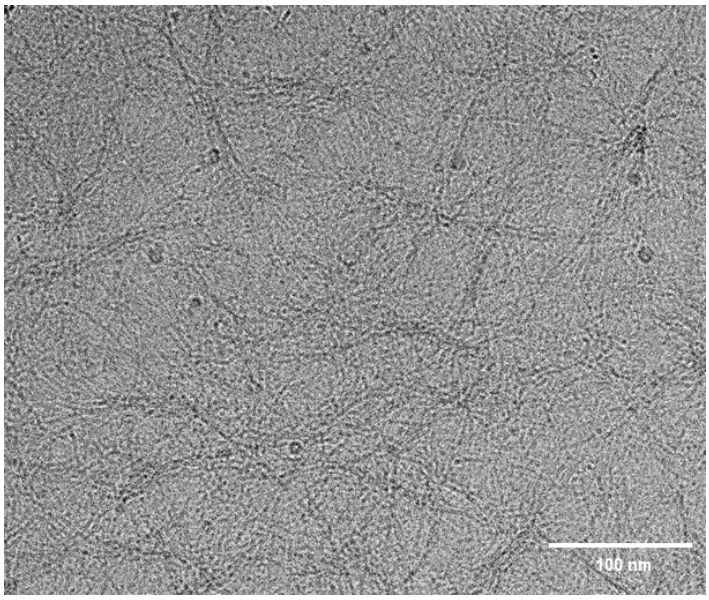

Figure S7: Cryo-EM imaging of collagen ink showing the collagen fibrils of around 13 nm diameter. Fibrils are visible due to the (phase) contrast of the protein versus water.

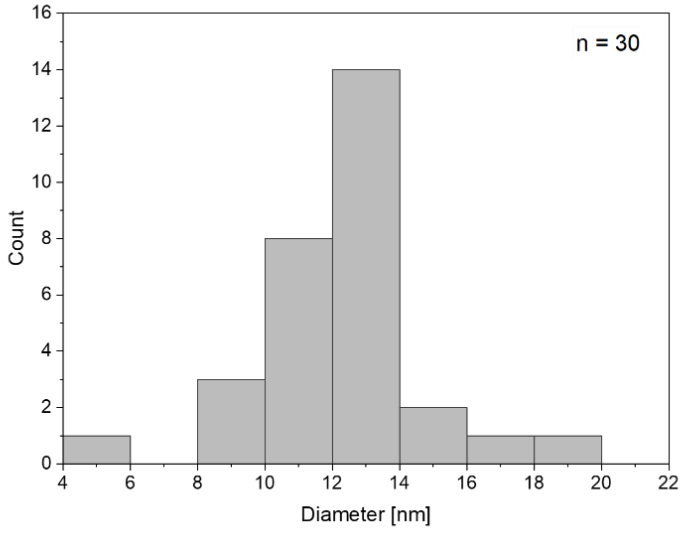

Figure S8: Histogram of n = 30 measured fibril diameters in the cryo-EM image. The average of measured diameters was calculated to 12.3 nm ± 2.5 nm.

2. 3D microprinting of collagen and material characterization

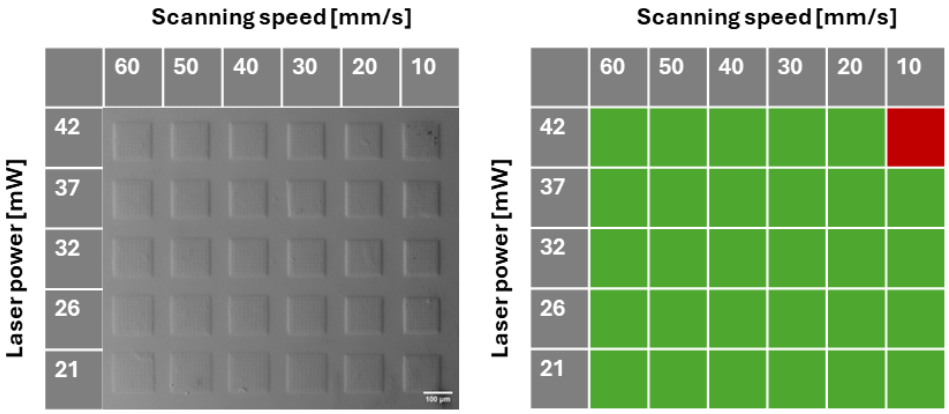

Figure S9: Printability window of collagen ink for various combinations of laser powers and scanning speeds for printing cubic lattices of 100 µm × 100 µm × 70 µm dimension. Green and red color coding correspond to printing with stable and overexposure parameters, respectively. Scale bar: 100 µm.

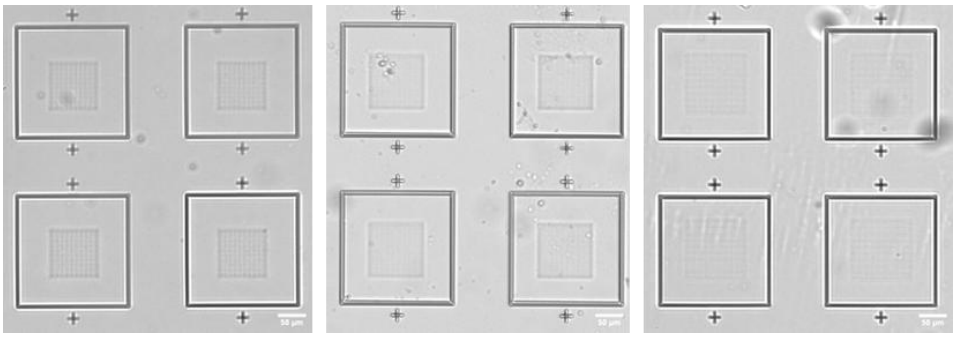

Figure S10: Stability of the printed collagen microstructures in various pH conditions (from left to right 2.56, 7.00, 10.82). To enhance the visibility of the crosslinked collagen methacrylamide, the hydrogels were printed inside of a frame of a commercial material (IP-S, Nanoscribe GmbH).

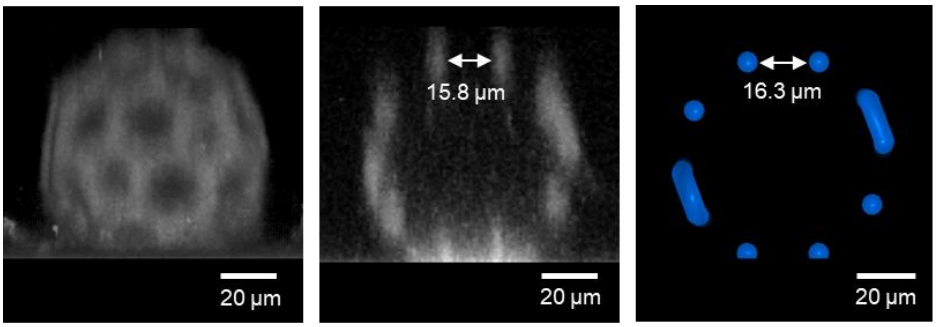

Figure S11: Side view on volumetric 3D reconstruction (left), vertical cross section (center) through the center of the printed buckyball structure (75 µm × 75 µm × 70 µm, 42 mW laser power, 20 mm/s scanning speed) after confocal fluorescence microscopy, and model of cross-section (right).

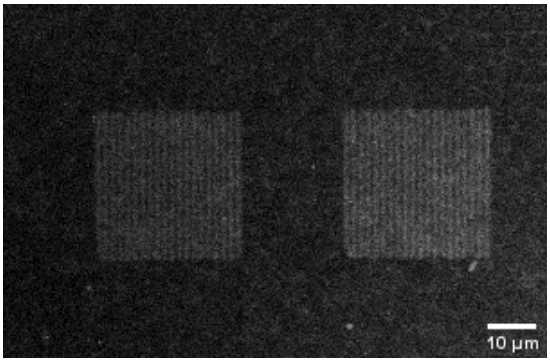

Figure S12: Resolution tests with parallel printed lines of 30 µm length with 1.5 µm spacing in-between. The printing parameters were 40 mW and 3 mm/s.

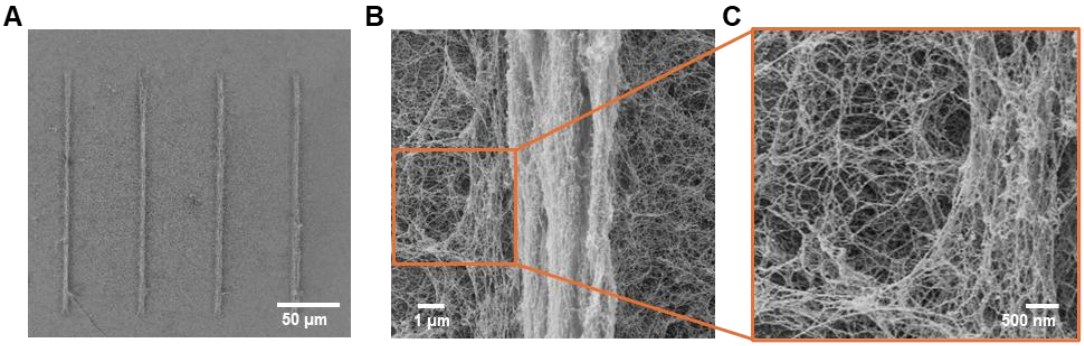

Figure S13: SEM images of critical point dried 3D printed collagen microstructures. The printed bars (A) with original dimensions of 200 µm × 10 µm × 10 µm collapsed under these preparation conditions to about 30% in width (B) and show an irregular fibrillar network (C).

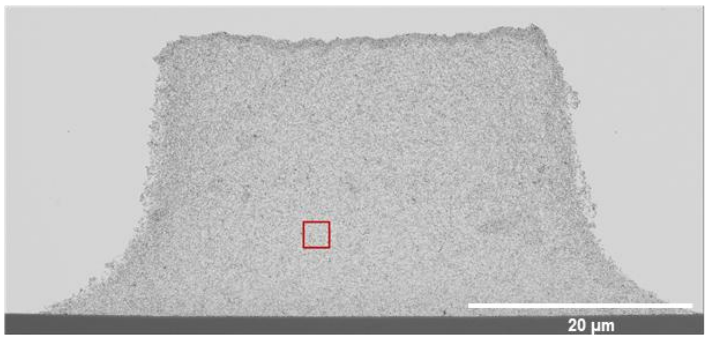

Figure S14: SEM image of cross section of epoxide embedded printed collagen. Shrinkage of the initially printed blocks (50 µm × 50 µm × 50 µm) to around 70% in each dimension occurred during staining and fixation with tannic acid and OsO_4. Red square indicates the region used for analysis of fibril diameters.

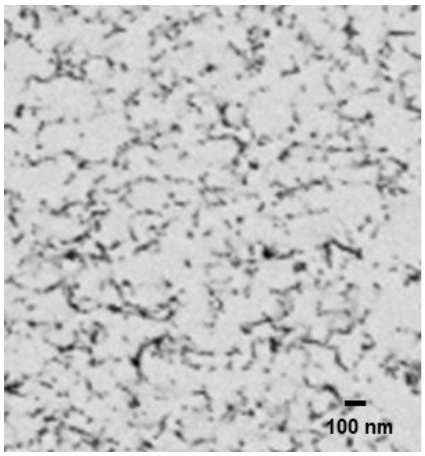

Figure S15: Zoom in SEM image of cross section of epoxide embedded printed collagen showing collagen fibrils of around 13 nm diameter. Note that SEM imaging at the low primary energy (1.5 keV) used here produces signal only from a thin surface layer of the section leading to seeming breaks or discontinuities in the collagen network.

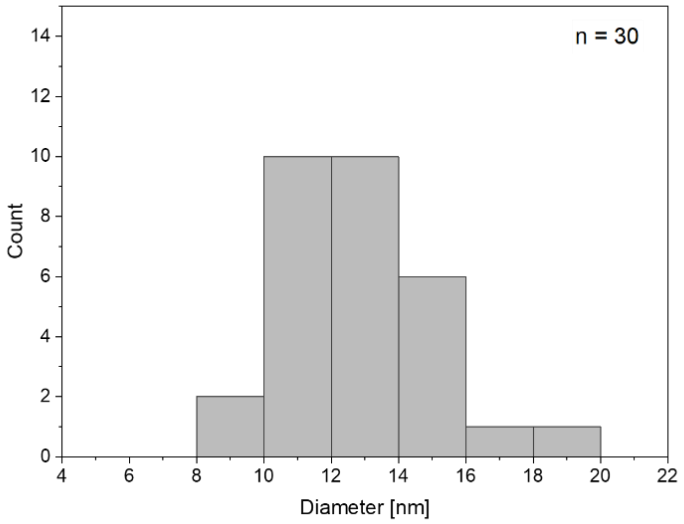

Figure S16: Histogram of n = 30 measured fibril diameters in the SEM cross section image. The average of measured diameters was calculated to 13.2 nm ± 2.4 nm.

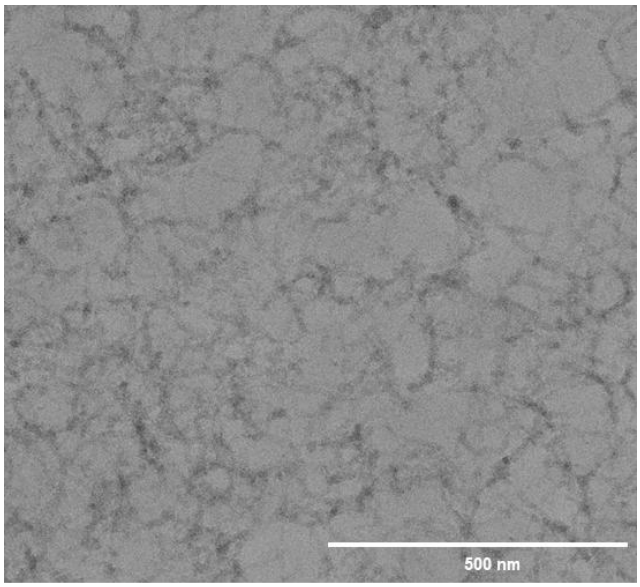

Figure S17: TEM image of cross section of epoxide embedded printed collagen showing collagen fibrils of around 13 nm diameter. Since in TEM a projection image is recorded a homogeneous fibrous network without discontinuities is visualized. Contrast in this image is created by the metals used to stain the embedded sample.

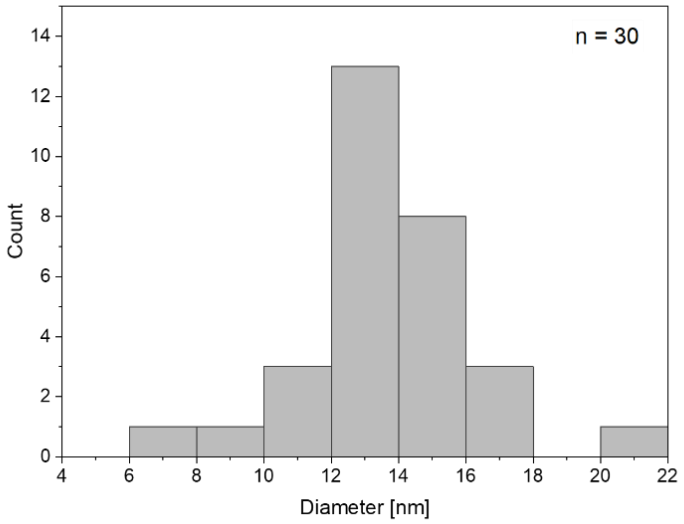

Figure S18: Histogram of n = 30 measured fibril diameters in the TEM cross section image. The average of measured diameters was calculated to 12.6 nm ± 2.3 nm.

Table S1: Fibril diameters obtained from different electron microscopy techniques for N = 30 averaged fibrils.

	Cryo-TEM (ink)	**SEM (printed)**	**TEM (printed)**
treatment	vitrified	stained + embedded	stained + embedded
sample	thinned liquid film	ultrathin section	ultrathin section
electron energy	300 keV	1.5 keV	300 keV
fibril diameter	12.3 nm ± 2.5 nm	13.2 nm ± 2.4 nm	12.6 nm ± 2.3 nm

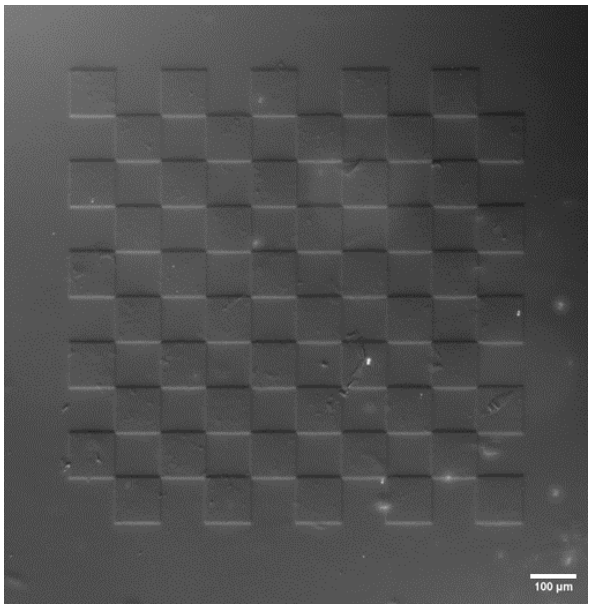

Figure S19: Optical microscopy image (acquired with CDIC contrast) of printed check board structure of collagen blocks for biocompatibility tests. Scale bar: 100 µm.

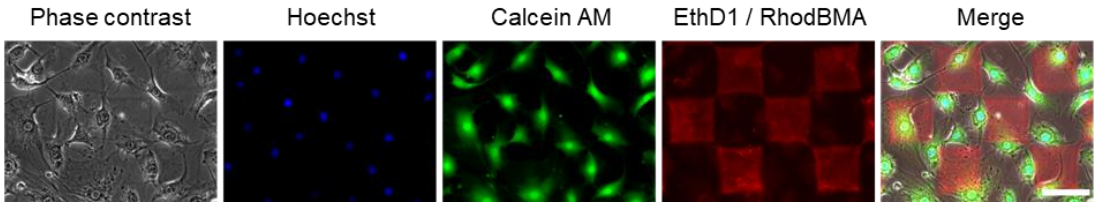

Figure S20: Cell viability assay REF cells on 2PPL printed collagen blocks. Cell nuclei are labelled with Hoechst (blue), live cells with Calcein AM (green) and dead cells labelled with EthD-1 (red). The RhodBMA-labelled collagen appears in the same color as the dead-stain (red). Within three independent experiments, the majority of cells did not appear positive for EthD1 labelling. Scale bar: 100 µm.

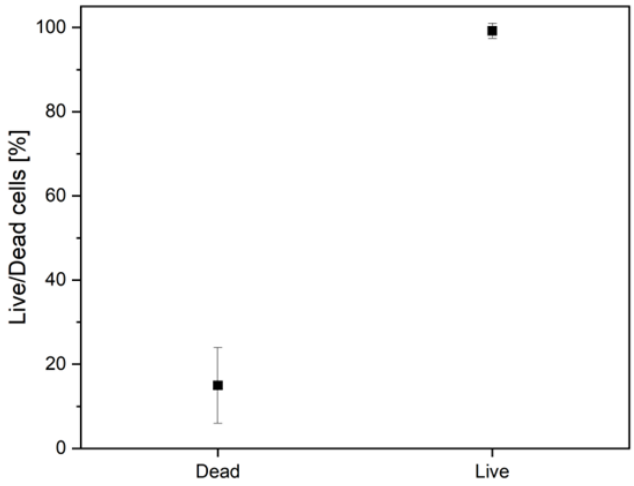

Figure S21: Results from statistical analysis of live/dead assay verifying >99% of cells to be alive. A fraction of 15% for dead cells can be traced back to the autofluorescence of the RhodBMA-labeled collagen. The total number of detected cell nuclei was N = 473.

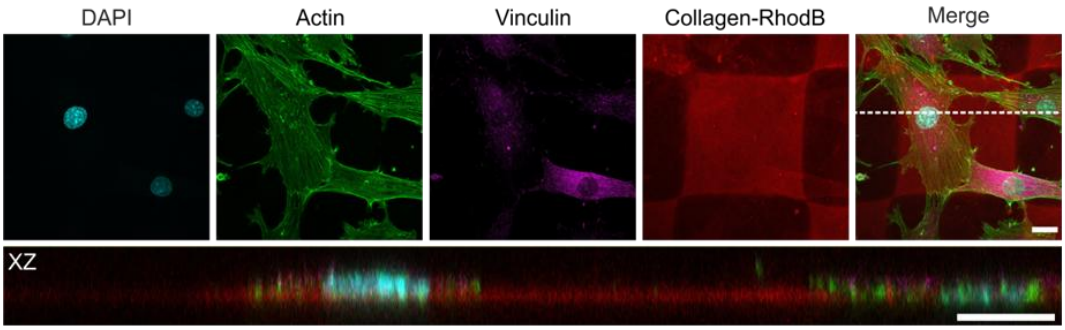

Figure S22: Confocal images of immunocytochemical staining of REF cells cultured on 3D laser printed collagen blocks. Cells adhered to the printed scaffold (red) and exhibit an undisturbed actin organization (green). Focal adhesions, as visualized by Vinculin-staining (magenta), formed on the RhodBMA-labelled collagen blocks (red). Cells adhered to the top of the scaffolds as shown by the XZ-projection. The projection plane is indicated in white in the merge image. Scale bars: 20 µm.

3. Temperature response of collagen in solution and in 3D printed structures

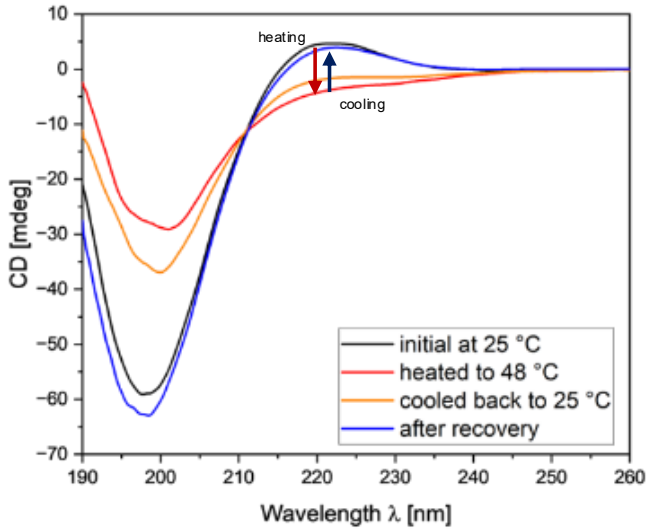

Figure S23: UV-CD spectra of 2 µg/mL ColMA in acetic acid solution (0.02 M) upon heating and cooling. Cooling of ColMA solution for 2 days shows full recovery of collagen folding bands at 200 nm and 220 nm which first disappeared upon heating.

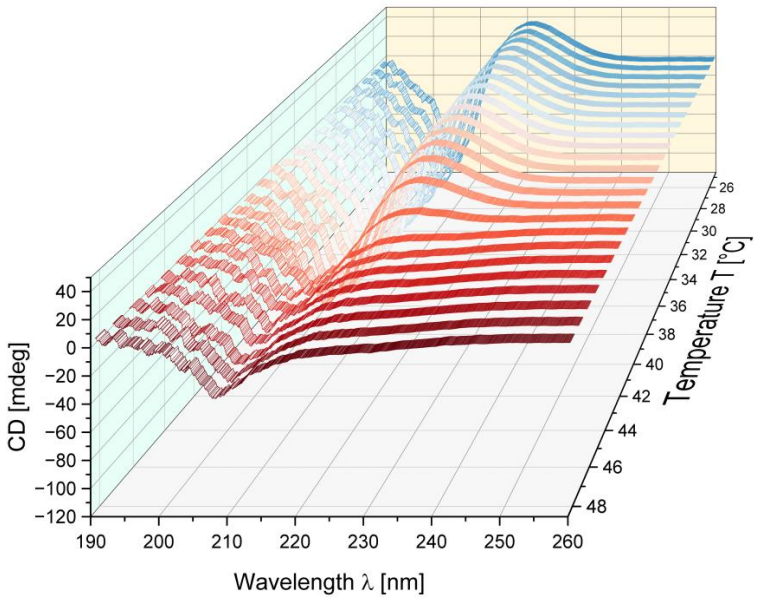

Figure S24: UV-CD spectra of 5 µg/mL ColMA in 0.02 M acetic acid solution at different temperatures.

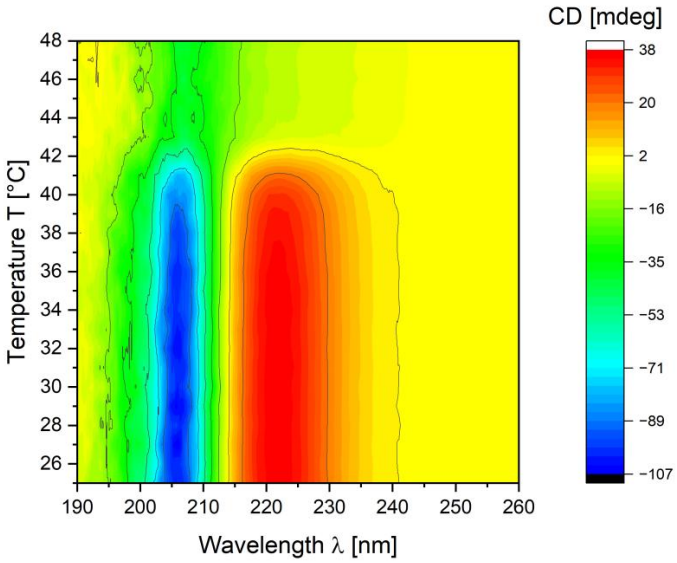

Figure S25: Contour plot of UV-CD spectra of 5 µg/mL ColMA in 0.02 M acetic acid solution at different temperatures.

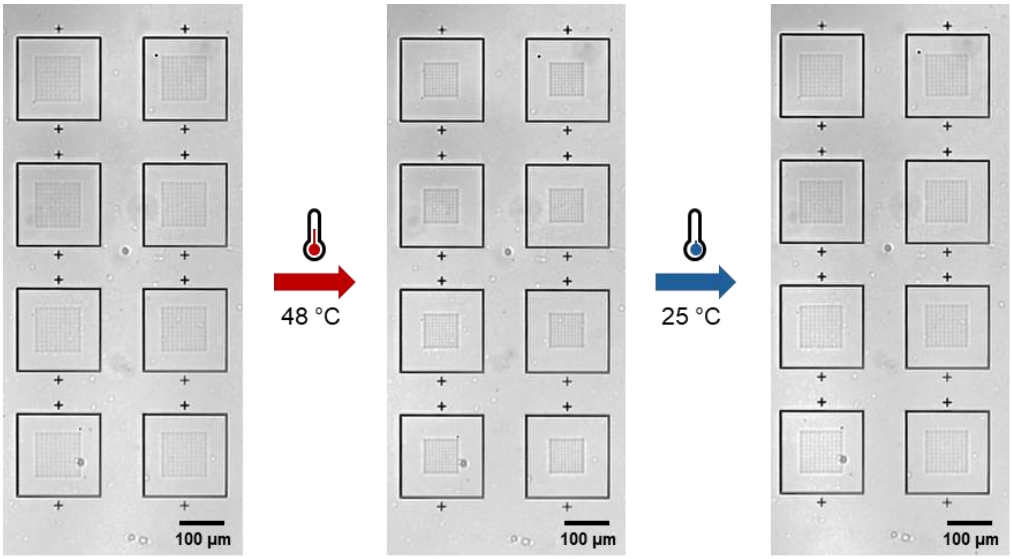

Figure S26: Response and recovery of printed collagen cubic lattices (100 µm × 100 µm × 70 µm) in printed frames of a non-responsive, passive material (IP-S, Nanoscribe GmbH) upon heating and cooling the sample by 1 °C/min.

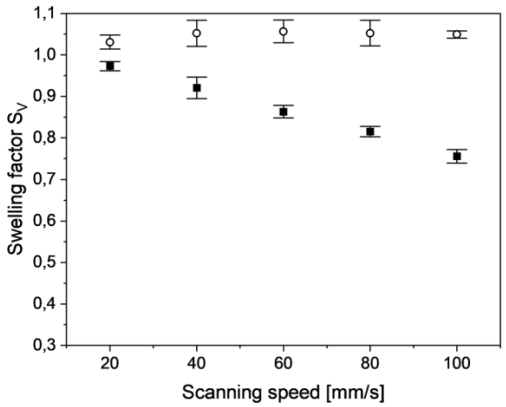

Figure S27: Recovery of collagen microstructures with 40 mW laser power and varying scanning speed (filled squares – recovery after cooling back to room temperature; empty circles – shape recovery after 1 h at room temperature). Printing parameters with higher exposure dose during printing, i.e. lower scanning speed, improve recovery rate. Full recovery of all microstructures was obtained after keeping them at room temperature for 1h.

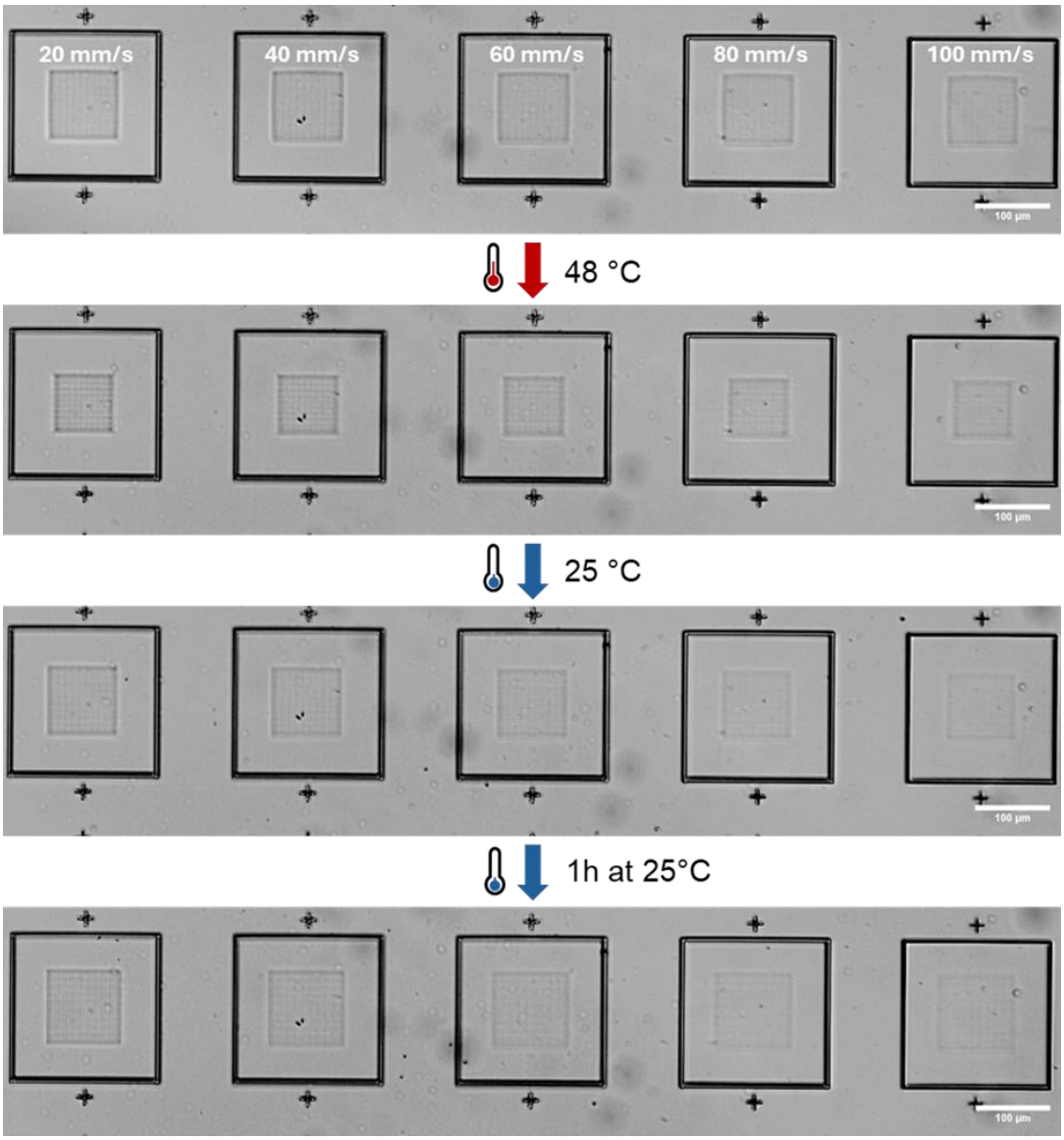

Figure S28: Response and recovery of 3D printed collagen microstructures with 40 mW laser power and varying scanning speed between 20 mm/s and 100 mm/s (from left to right). Full recovery of printed microstructures with higher scanning speed was obtained after keeping the sample at room temperature for 1h.

Table S2: Parameters employed in the stochastic molecular dynamics simulations.

Parameter type	Parameter	GROMACS arbitrary units	Normalized units
Bonded interaction	K_{bond}	100	250 k_BT/σ^2
	r	2.80616	$\sigma(2^{1/6})/2$
Repulsive non-bonded	ε	0.25	0.1 k_BT
Lennard-Jones interaction	σ	2.5	1 σ
	d_{cutoff}	10	4 σ
	Verlet buffer tolerance	$2 \cdot 10^{-4}$	~$2.5 \cdot 10^{-3}$ k_BT/τ
Angular interaction	K_θ	5000	2000 k_BT
	θ_0	180°	180°
Langevin dynamics	m	20000	1 m
	1/γ	1000	~15.8740 τ
	k_BT	2.5	1 k_BT
	D	0.125	~1.2599 σ^2/τ
	Δt	0.1	~$1.5874 \cdot 10^{-3}$ τ
	No. integration steps	10^6–$6 \cdot 10^8$ steps	
Characteristic diffusion time	τ	~62.996	1 τ
Closed package volume	V_{CP}	156250	10000 σ^3

3. MINIMAL-INVASIVE 3D LASER PRINTING OF MICROIMPLANTS IN ORGANISMO

Bibliographic reference

Cassian Afting†, Philipp Mainik†, Clara Vazquez-Martel, Tobias Abele, Verena Kaul, Girish Kale, Kerstin Goepfrich, Steffen Lemke, Eva Blasco, and Joachim Wittbrodt. “Minimal-invasive 3D laser printing of microimplants in organismo.” Adv. Sci. (2024): 2401110.
† - equal contribution

Author contribution

Philipp Mainik has contributed to the *methodology* (lead), *validation* (lead), *formal analysis* (lead), *investigation* (lead), *data curation* (lead), *writing – original-draft* (lead), *writing – review & editing* (lead), and *visualization* (lead).

Formblatt Kumulative Dissertation

1. Publikation/*Publication*:

Vollständige bibliographische Referenz/*Complete bibliographic reference:*

Cassian Afting, Philipp Mainik, Clara Vazquez-Martel, Tobias Abele, Verena Kaul, Girish Kale, Kerstin Goepfrich, Steffen Lemke, Eva Blasco, and Joachim Wittbrodt. "Minimal-invasive 3D laser printing of microimplants in organismo." Adv. Sci. (2024): 2401110.

2. Erst- oder gleichberechtigte Autorenschaft/*First or equal authorship*: Ja/*Yes*☒ Nein/*No* ☐

Veröffentlicht/*Published*	☑
Zur Veröffentlichung angenommen/*Accepted*	☐
Eingereicht/*Submitted*	☐
Noch nicht eingereicht/*Not yet submitted*	☐

4.* Beteiligungen/*Contributions**

Contributor Role	**Doktorand/in/ *Doctoral Student***	**Co-Autor/in 1/ *Co-author* 1**	**Co-Autor/in 2/ *Co-author 2***
Name, first name	Mainik, Philipp	Afting, Cassian	
Methodology	x	x	
Software			
Validation	x	x	
Formal analysis	x	x	
Investigation	x	x	
Resources			
Data Curation	x	x	
Writing-Original Draft	x	x	
Writing-Review&Editing	x	x	
Visualization	x	x	
Supervision			
Project administration			
Funding acquisition			

Kategorien des CRediT (Contributor Roles Taxonomy, https://credit.niso.org/)

Hiermit bestätige ich, dass alle obigen Angaben korrekt sind/*I confirm that all declarations made above are correct.*

Unterschrift/*Signature* _____ _____ _____

Doktorand/in/*Doctoral student* **Co-Autor/in 1/*Co-author 1*** **Co-Autor/in 2/*Co-author***

Betreuungsperson/Supervisor:

Hiermit bestätige ich, dass alle obigen Angaben korrekt sind und dass die selbstständigen Arbeitsanteile des/der Doktoranden/in an der aufgeführten Publikation hinreichend und signifikant sind/*I confirm that all declarations made above are correct and that the doctoral student's independent contribution to this publication is significant and sufficient to be considered for the cumulative dissertation.*

Prof Blasco, Eva _____ E. Blasco _____ 8.5.2025 _____

Name/*Name* Unterschrift/*Signature* Datum/*date*

Stand: Februar 2025

RESEARCH ARTICLE

ADVANCED SCIENCE Open Access

www.advancedscience.com

Minimal-Invasive 3D Laser Printing of Microimplants in Organismo

Cassian Afting, Philipp Mainik, Clara Vazquez-Martel, Tobias Abele, Verena Kaul, Girish Kale, Kerstin Göpfrich, Steffen Lemke, Eva Blasco, and Joachim Wittbrodt**

Multi-photon 3D laser printing has gathered much attention in recent years as a means of manufacturing biocompatible scaffolds that can modify and guide cellular behavior in vitro. However, in vivo tissue engineering efforts have been limited so far to the implantation of beforehand 3D printed biocompatible scaffolds and in vivo bioprinting of tissue constructs from bioinks containing cells, biomolecules, and printable hydrogel formulations. Thus, a comprehensive 3D laser printing platform for in vivo and in situ manufacturing of microimplants raised from synthetic polymer-based inks is currently missing. Here, a platform for minimal-invasive manufacturing of microimplants directly in the organism is presented by one-photon photopolymerization and multi-photon 3D laser printing. Employing a commercially available elastomeric ink giving rise to biocompatible synthetic polymer-based microimplants, first applicational examples of biological responses to in situ printed microimplants are demonstrated in the teleost fish *Oryzias latipes* and in embryos of the fruit fly *Drosophila melanogaster*. This provides a framework for future studies addressing the suitability of inks for in vivo 3D manufacturing. The platform bears great potential for the direct engineering of the intricate microarchitectures in a variety of tissues in model organisms and beyond.

1. Introduction

Multi-photon 3D laser printing has been gaining attention in recent years for offering 3D fabrication of objects on the micro- and nanoscale.[1–4] This technology has evolved originally from applications in mainly technical fields such as optics and photonics, but has also found its way into the life sciences thanks to the development of biocompatible materials. Today, this method is established in the life sciences for the precise fabrication of biocompatible scaffolds with subcellular resolution and applied in single-cell, organoid, and cultured tissue research.[4–17] The biocompatible scaffolds can be prepared either by physically encapsulating cells in a photocurable hydrogel or by printing and successive development, that is, removing excessive ink prior to cell seeding.

Application of printed 3D biocompatible scaffolds as implants possess great potential in experimental clinical and biological fundamental research.[4,18–20] For example, cell-free and biocompatible structures have been printed and surgically transplanted into the subretinal space of pig eyes.[12] Histological and immunohistochemical analysis of these eyes then suggested an infiltration of the transplanted scaffold by retinal pigmented epithelium and photoreceptors within 30 days. However, major limitations of such surgical micro-implantations remain: they are technically challenging, the procedure is highly invasive,

C. Afting, V. Kaul, G. Kale, S. Lemke, J. Wittbrodt
Centre for Organismal Studies Heidelberg (COS)
Heidelberg University
69120 Heidelberg, Germany
E-mail: jochen.wittbrodt@cos.uni-heidelberg.de

C. Afting, V. Kaul
Heidelberg International Biosciences Graduate School HBIGS
69120 Heidelberg, Germany

C. Afting, T. Abele
HeiKa Graduate School on "Functional Materials"
69120 Heidelberg, Germany

P. Mainik, C. Vazquez-Martel, E. Blasco
Institute for Molecular Systems Engineering and Advanced Materials (IMSEAM)
Heidelberg University
69120 Heidelberg, Germany
E-mail: eva.blasco@oci.uni-heidelberg.de

P. Mainik, C. Vazquez-Martel, E. Blasco
Organic Chemistry Institute (OCI)
Heidelberg University
69120 Heidelberg, Germany

T. Abele, K. Göpfrich
Zentrum für Molekulare Biologie der Universität Heidelberg (ZMBH)
Heidelberg University
69120 Heidelberg, Germany

T. Abele, K. Göpfrich
Max Planck Institute for Medical Research
69120 Heidelberg, Germany

G. Kale, S. Lemke
Institute of Biology
University of Hohenheim
70599 Stuttgart, Germany

The ORCID identification number(s) for the author(s) of this article can be found under https://doi.org/10.1002/advs.202401110

DOI: 10.1002/advs.202401110

and damages to the surrounding tissues are almost always inevitable.

A well-explored alternative for targeting in vivo tissue engineering is the injection of cell-free or cell-laden hydrogels or ink-based composites for direct polymerization within tissues. Although a variety of physical and chemical in vivo crosslinking strategies have been explored for injected liquids,[21–25] these approaches are so far lacking control over the shape of the construct in 3D.

To address this issue, light-based 3D printing methods have very recently been explored for spatially controlled photopolymerization. For example, Chen et al. have reported noninvasive light-based in vivo 3D bioprinting of a gelatin-based ink with digitally guided near-infrared photopolymerization via micromirrors.[26] Furthermore, in vivo multi-photon 3D laser printing was recently presented by Urciuolo et al. for the fabrication of cell-laden and microscaled hydrogel structures.[8] Therein, the authors injected a cell-laden photosensitive gelatin-based prepolymer in skin, brain, or muscle tissue of anesthetized alive mice and used a multi-photon confocal microscope for printing. Similar to other bioprinting approaches, these efforts were aiming at in vivo manufacturing of tissue constructs, replicating the biochemical and mechanical properties of their surrounding tissues.

In a second work, in vivo 3D laser printing was performed outside of tissues, yet within living organisms. Conductive polypyrrole-containing microstructures were printed in the lumen of the *Caenorhabditis elegans* gut after feeding the worm with a hydrogel ink composition.[5] So far, these reports illustrated the potential of hydrogel-based ink systems in developed organisms.

Here, we present a platform for in vivo, *in organismo* manufacturing of microimplants by one-photon photocrosslinking and multi-photon 3D laser printing with potential in shaping tissue morphogenesis and eliciting biological response. For this, we employ a commercially available elastomeric ink, which allows us to manufacture biocompatible, synthetic polymer-based *micro*structures of low immunogenicity in alive developing organisms. With our approach, we have developed an in vivo tissue engineering toolbox for studying the effects of minimal-invasively delivered, 3D structured *micro*implants in (developing) organisms.

2. Results

2.1. Biocompatible One-Photon Photopolymerization in Living, Early Organisms

The first step towards in vivo manufacturing of microimplants was to identify a suitable ink for in vivo one-photon photopolymerization. To this aim, we have identified several criteria that the ink needs to fulfill: i) fast photopolymerization, ii) biocompatibility (both before and after polymerization), iii) hydrophobicity (to avoid diffusion of the reactive unpolymerized species in the living system), iv) microinjection compatible viscosity of the ink, and v) a suitable refractive index. A systematic analysis of inks indicated that the commercially available photocurable ink IP-PDMS (Nanoscribe GmbH, Germany) represented a very suitable ink for this purpose. The ink is optically transparent with a refractive index of 1.45 (589 nm, 20 °C) and upon photopolymerization gives rise to an elastomeric, biocompatible material with a Young's modulus of 15 MPa and polydimethylsiloxane-like properties.[27]

As in vivo model organisms, we selected the teleost fish *Oryzias latipes* (hereafter: medaka) and the fruit fly *Drosophila melanogaster* (hereafter: *Drosophila*). Their short generation time, their long history of genetic studies, their transparent eggs, and the ease of observing and experimentally addressing early developmental processes in these organisms places them both among the most important vertebrate and invertebrate models, respectively. Since their development occurs outside the mother and at sub-centimeter scales, all tissues are easily accessible via light irradiation during early development, which makes them uniquely suited to investigate the effects of tightly controlled in vivo polymerized materials on a wide range of different living tissues, organs, and whole organisms.

To prepare these organisms for microinjection of ink and subsequent one-photon photopolymerization and multi-photon 3D laser printing, fertilized eggs were collected and then left to develop until they reached the required age. Fertilized *Drosophila* eggs were dechorionated immediately after deposition, mounted on a glass slide, and covered with hydrocarbon oil. Fertilized medaka eggs were incubated overnight until embryonic stage 19–21,[28] the egg-shell was then removed (dechorionation) and the embryos were mounted in custom-made agarose molds. Following the microinjection of the ink, either into the yolk of developing *Drosophila* embryos or the developing optic vesicle of medaka embryos, embryos were exposed globally to a short 1 min UV light pulse to photocrosslink and thus solidify the microinjected ink in an one-photon photopolymerization process using the external light source of a conventional fluorescence microscope. In case of 3D laser printing, embryos were mounted for insertion into a Professional Photonic GT2 (Nanoscribe GmbH) and thus made available for 3D printing of microstructures. Finally, embryos were re-incubated for subsequent microscopic analysis (**Figures 1**, **2**a,c).

After microinjection into either the semi-aqueous environment of the yolk of early *Drosophila* embryos (1 h post fertilization; 1 hpf) or the aqueous extracellular environment of the developing retina of medaka embryos (1 day post fertilization; 1 dpf), the IP-PDMS droplets adopted a stable and spherical shape. Even after microinjection into embryos, IP-PDMS photopolymerized efficiently (Figure S1 (Supporting Information) showing UV-cured spheres explanted from *Drosophila* embryos). Importantly, there was no indication of acute toxicity of even unpolymerized IP-PDMS on the embryos as apparent by their unaffected development, the absence of immediate deformation, shrinkage or dissolution of ink surrounding tissue regardless of the microinjected IP-PDMS deposits being UV cured or left uncured.

For *Drosophila* embryos, timelapse transmission microscopy revealed that the embryo development progressed normally through all developmental stages followed in this study (cellularization and gastrulation) both post-microinjection and -photopolymerization. To control for UV toxicity during the polymerization process, non-injected controls were exposed to the same UV light dose and likewise showed normal gross development (Figure 2b). For medaka embryos, normal development was confirmed by confocal microscopy of whole-mount nuclei stained

ADVANCED SCIENCE NEWS
www.advancedsciencenews.com

ADVANCED SCIENCE Open Access
www.advancedscience.com

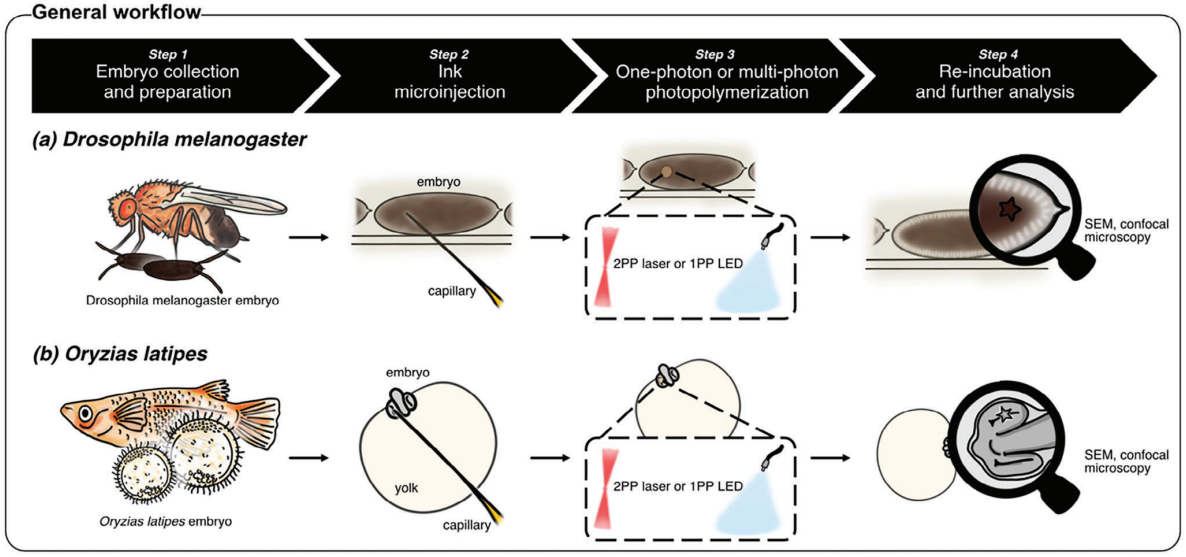

Figure 1. Biocompatible one-photon photopolymerization and multi-photon 3D laser printing workflow in living, early organisms. Schematic illustration of the one-photon photopolymerization (1PP) and multi-photon 3D laser printing (2PP) workflow in early *Drosophila melanogaster* and *Oryzias latipes* embryos.

heads at 6 dpf (5 days post-microinjection) with and without its UV curing, respectively. Notably, uncured IP-PDMS droplets consistently reduced in volume compared to UV-cured spheres, suggesting a slow in vivo resorption of IP-PDMS ink over time (Figure 2d).

2.2. In vivo One-Photon Photopolymerized IP-PDMS Permits Targeted Re-Shaping of Tissue Morphogenesis

Following the establishment of microinjection and imaging conditions, we next analyzed the displacement of uncured droplets and UV-cured IP-PDMS spheres in *Drosophila* embryos during the process of gastrulation. Specifically, we asked whether overall gastrulation dynamics within the confined egg space affected uncured droplets and UV-cured spheres differently. For this, we microinjected IP-PDMS at the anterior and posterior poles of the embryos and tracked its total movement starting with the end of cellularization in 10 min increments for 2 h in timelapse recordings acquired by transmission microscopy. We focused our analysis on embryos that had IP-PDMS spheres either in the anterior or in the posterior third of the embryo at the starting point of analysis (**Figure 3a**). The total distance traveled of uncured droplets and UV-cured spheres was significantly increased if microinjected at the posterior pole compared to the anterior pole, but did not differ depending on their curation status (Figure 3b). By contrast, if spheres were tracked only until the onset of gastrulation dynamics (i.e., from the last mitotic wave until the end of cellularization), no difference in total distance traveled between posteriorly and anteriorly microinjected deposits could be detected (Figure S2, Supporting Information). Taken together, these results suggest that increased displacement of posterior spheres during *Drosophila* gastrulation dynamics was driven mainly by the process of germ band extension, which pushes the posterior end of the embryo towards the anterior.[29]

While the overall in vivo movement dynamics of uncured droplets and UV-cured IP-PDMS spheres in *Drosophila* embryos did not differ, we could observe that UV-cured spheres had a striking capacity to alter local tissue dynamics, which was not seen with uncured droplets. This could be demonstrated exemplary for two different developmental processes, first for blastoderm formation and, second for a transient epithelial fold at the head/trunk interface, the so-called cephalic furrow (CF). While blastoderm formation was unaffected in the presence of uncured droplets microinjected at the anterior pole of an embryo, the process was altered in the presence of UV-cured spheres: following nuclear translocation from the yolk to the embryo cortex, the density of cortical nuclei was visibly lower at the anterior pole compared to non-affected regions in the middle or posterior of the embryo. As a consequence, an additional round of nuclear division was observed at the anterior pole, which resulted in a time-shifted onset of cellularization at the anterior pole and in a decoupling of the otherwise tightly regulated timing of head and trunk development. This interference with blastoderm formation could only be observed for the anterior pole and was not found at any other place of microinjection within the embryo (Figure 3c; Movie S1, Supporting Information).

Similar as for blastoderm formation, the dynamics of CF formation remained unaffected in the presence of uncured droplets. Conversely, a UV cured sphere had the capacity to alter the shape of the cephalic furrow upon contact. Consistent with the notion that such capacity to change the shape of an epithelial fold was associated with direct sphere contact, we found that the UV cured sphere traveled less than half the distance compared to the uncured droplet within 15 min upon contact with the CF (Figure S3, Supporting Information).

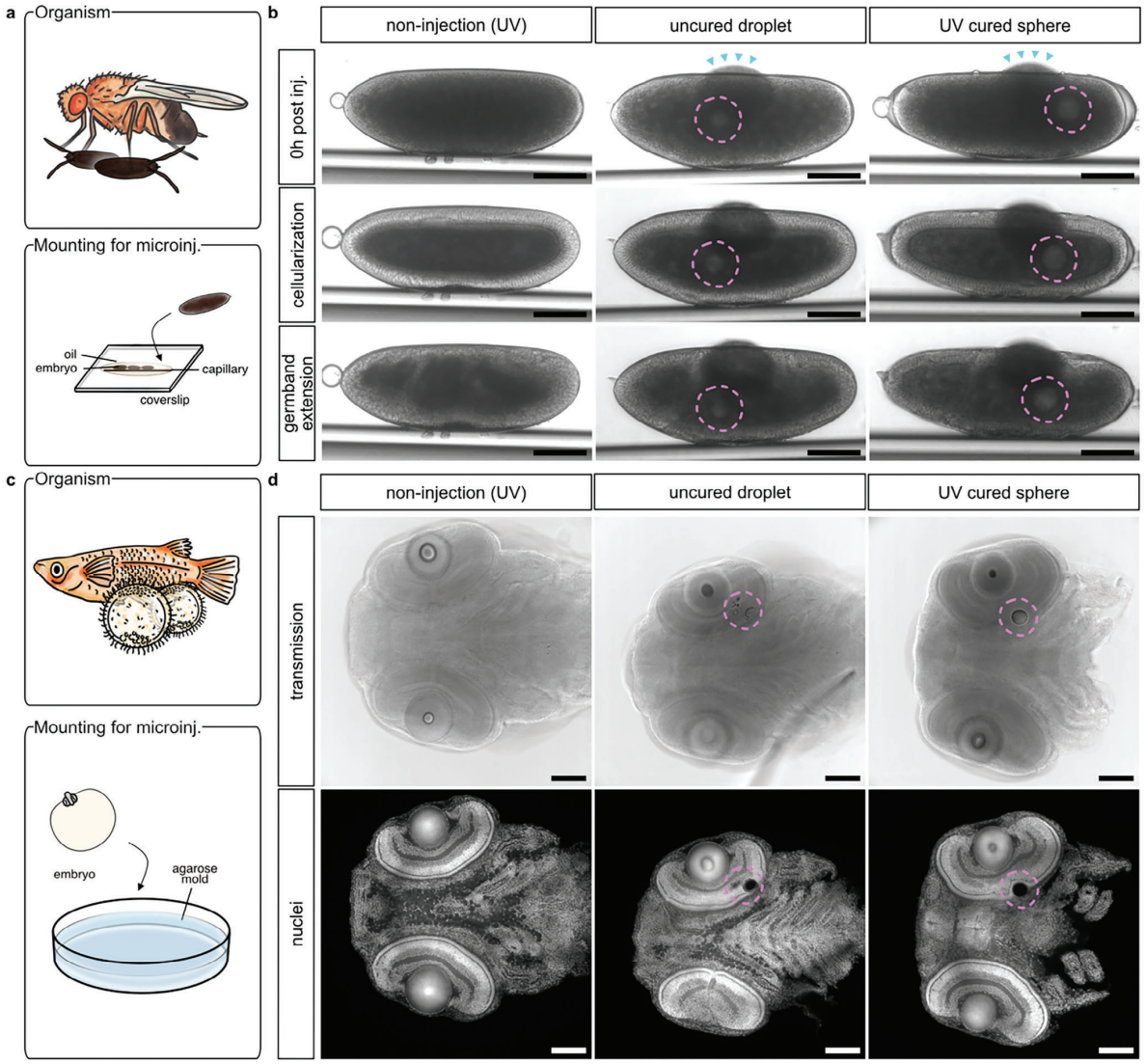

Figure 2. In vivo one-photon photopolymerization of microinjected ink does not adversely impact embryonic development. a) Schematic illustration of the mounting method used to microinject (microinj.) ink in *Drosophila melanogaster* embryos. b) Representative time-lapse transmission microscopy of early *Drosophila melanogaster* embryos shortly after IP-PDMS microinjection (top), and during the cellularization stage (middle) at ≈2.5 h post microinjection (hpi), and at ≈3 hpi during germband extension stage (bottom). Microinjected IP-PDMS deposits were either left uncured (uncured droplet) or cured by UV light exposure (UV-cured sphere). Non-injected controls (non-injection (UV)) were subjected to the same UV light regime. Because IP-PDMS is highly viscous, microinjection needles with a tip diameter of approx. 5–10 µm were used. During microinjection, slight leakages of yolk could be observed (indicated by cyan arrowheads), which however sealed off quickly and did not affect subsequent embryonic development. c) Schematic illustration of the mounting method used to microinject ink in *Oryzias latipes* embryos. d) Representative confocal microscopy of chemically fixed and whole-mount nuclear stained (Nuclei; DAPI) medaka embryo heads at 6 days post fertilization (dpf) after microinjection of IP-PDMS into their optic vesicles at 1 dpf. Dashed lines (magenta) indicate positions of microinjected deposits. Scale bars: 100 µm.

2.3. Biocompatible Multi-Photon 3D Laser Printing in Living, Early Organisms

In addition to the described one-photon photopolymerization process, IP-PDMS can be shaped with higher precision and to complex geometries using multi-photon 3D laser printing. Therefore, we adapted the workflow to 3D laser print inside of the uncured IP-PDMS droplet in living, early organisms using a Professional Photonic GT2 (Nanoscribe GmbH). For *Drosophila* embryos, we did not need to modify the one-photon polymerization pipeline to enable insertion into the substrate holder of the 3D laser printer and subsequent 3D printing (**Figure** 4a), while for

ADVANCED SCIENCE NEWS
www.advancedsciencenews.com

ADVANCED SCIENCE Open Access
www.advancedscience.com

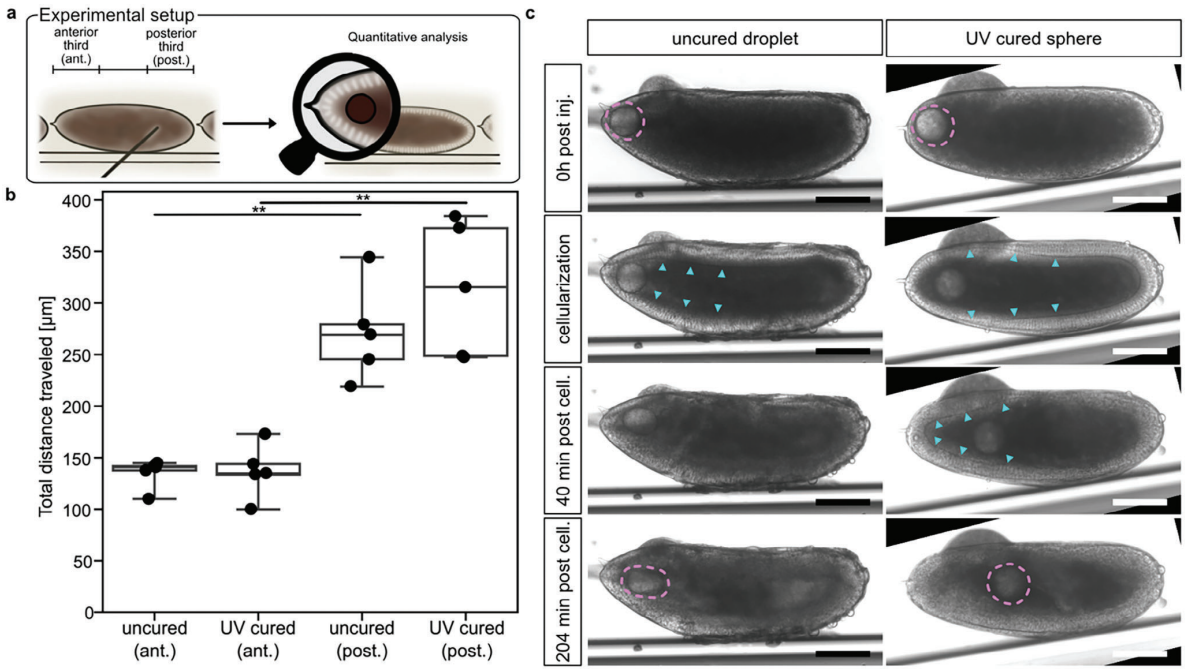

Figure 3. In vivo one-photon photopolymerized IP-PDMS spheres allow local re-shaping of tissue morphogenesis. a) Schematic illustration of microinjection scheme for quantitative analysis of uncured and UV-cured IP-PDMS deposit dynamics in *Drosophila melanogaster (Drosophila)* embryos. b) Quantification of total distance traveled of the uncured and UV-cured, microinjected IP-PDMS deposits at the anterior (ant.) and posterior (post.) poles of the *Drosophila* embryos. Spheres were tracked in 10 min increments in timelapse transmission images from the end of cellularization 2 h onwards. Boxplots include data from 5 embryos each with boxes indicating 25–75% percentiles and whiskers 10–90% percentiles. Individual data points are shown as dots. Student's *t*-test with unequal variance; **p-value: 0.002. c) Representative time-lapse transmission microscopy of early *Drosophila* embryos microinjected at the extreme anterior pole with IP-PDMS during cellularization (cell.). Microinjected IP-PDMS droplets were either left uncured (left panels) or cured by UV light exposure (right panels). Note that the uncured droplet was found to deform under the local pressure induced by the tissue morphogenesis in the developing head region, which could only be observed at the anterior pole. The UV-cured sphere did not deform but was ejected from the head region. Magenta dashed lines indicate the shape of the microinjected deposits, and cyan arrowheads indicate the cellularization front. Scale bars: 100 µm.

medaka embryos the mounting method had to be adapted. Here, insertion into the substrate holder and subsequent 3D printing was possible after immobilizing the embryo on the insertable cover glass in a low-melting point agarose dome following its microinjection with IP-PDMS. Orientation with the embryos' heads down towards the cover glass proved pivotal to not exceed the working distance of the 25x objective (Figure 4c; see Experimental Section for details).

In this way we were able to print structures in vivo with sizes down to the low microscale with even smaller feature sizes. Timelapse transmission microscopy of *Drosophila* embryos with 3D laser printed stars (40 µm × 40 µm × 13 µm) showed that gross embryonic development is not perturbed by multi-photon 3D laser printing. The printed structures were not visible at any time in transmission mode, presumably due to the embryo's thickness and the yolk's optical properties. However, the dissection of the embryos confirmed the successful microprinting of the structures (Figure 4b). Figure 4d shows transmission microscopy of exemplary medaka embryos of different stages with different 3D printed microstructures in their developing retinas (from left to right: hollow cylinder 50 µm × 50 µm × 20 µm (20 µm inner diameter), star 60 µm × 60 µm × 20 µm).

2.4. In vivo Multi-Photon 3D Laser-Printed Microstructures Spontaneously Develop and Fully Integrate into Surrounding Tissues without Significant Immunogenicity

After 3D laser printing, printed structures float in the unpolymerized ink within the embryos and are thus initially not directly contacting the cells of the adjacent tissue. In medaka embryos, structures remained floating in the ink residue for days as embryonic development continued. Nevertheless, raising medaka embryos after multi-photon 3D laser printing to the end of embryonic development at stage 41[28] (18 days post microinjection, **Figure 5a**) resulted in spontaneous and mostly complete removal of the unpolymerized ink in a strain-specific manner, presumably by slow resorption of the non-toxic IP-PDMS over time.

Whole-mount nuclear stain and imaging by confocal microscopy revealed an integration of the structures into the surrounding tissue, most frequently into the retinal outer segments layer (OSL), seamlessly without any apparent signs of immunogenic reactions, scarring, or developmental defects. Moreover, multiple nuclei are consistently assembled around the structures, locally breaking the otherwise cell soma free organization of the OSL. This was observed independently of the shape of the printed

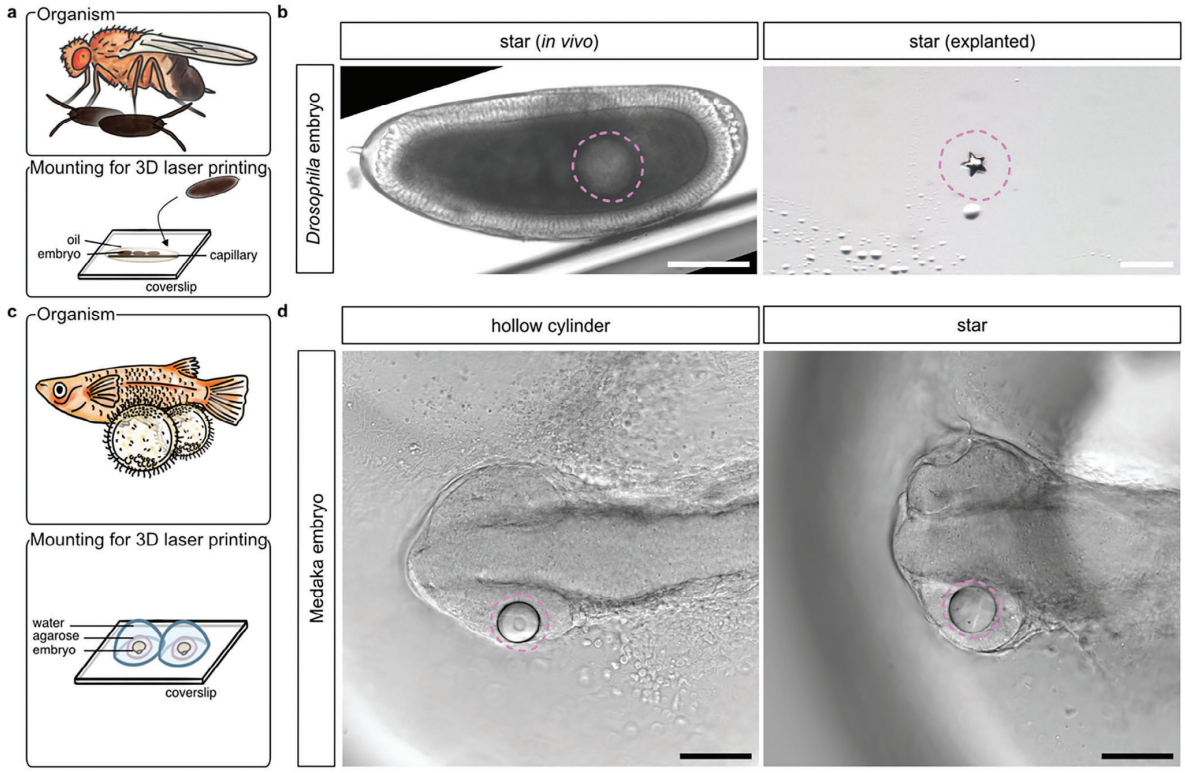

Figure 4. Microinjected ink deposits can be used for in vivo multi-photon 3D laser printing of microstructures. a) Schematic illustration of the mounting method used to enable 3D laser printing in *Drosophila melanogaster (Drosophila)* embryos. b) Representative transmission microscopy of early *Drosophila* embryos microinjected with IP-PDMS and subsequently subjected to 3D laser printing of a 40 µm × 40 µm × 13 µm star. The printed structure within the yolk of developing *Drosophila* embryos were then manually extracted by dissection and stereomicroscopically imaged. c) Schematic illustration of the mounting method used to enable 3D laser printing in *Oryzias latipes* (medaka) embryos. d) Representative transmission microscopy of stage 19–21 medaka embryos microinjected with IP-PDMS and subsequently subjected to multi-photon 3D laser printing of a 50 µm × 50 µm × 20 µm hollow cylinder (20 µm inner diameter) and a 60 µm × 60 µm × 20 µm star. Dashed lines (magenta) indicate positions of microinjected deposits. Scale bars: 100 µm.

structures and their position within the retinal layering since nuclei with morphologies different from surrounding cells were observed to neighbor printed structures intermittently even in other retinal layers like the retinal inner nuclear layer (INL; Figure S4a, Supporting Information). Cells did not actively invade the hollow cylinders with openings of 20 µm in diameter and rather stayed in closer connection to cells of the surrounding tissue (Figure 5b; contralateral control eyes in Figure S4b, Supporting Information). Scanning electron microscopy of printed structures enzymatically extracted from stage 41 embryonic medaka retinas revealed a remarkable printing precision given the particular printing environment, albeit showing a tendency towards round distortions if printed close to the edge of the ink bubble likely due to optical diffraction (Figure 5c,d rendered models of microstructures in Figure S5, Supporting Information).

To address the apparent absence of a significant immunogenic reaction to the microstructures, we employed a transgenic reporter line labeling macrophages (cxcr3a::GFP), the known key players in the immediate to long-term immune response to implanted biomaterials,[30–32] and compared the total number of macrophages in the experimental and control retina. At 18 days post ink microinjection and 3D laser printing, we consistently found comparable macrophage numbers in both retinas with no significant difference when comparing retinas with microstructures to contralateral control retinas without (Figure 5d). This indicates that there was no immunogenic response triggering the infiltration of additional macrophages in the microinjected/printed retinas as a chronic inflammatory response. Moreover, we consistently observed a macrophage population of a few cells at the sites of the microstructures inspecting the 3D printed object during immunosurveillance without triggering an adverse immunogenic reaction (Figure 5e). The cytosolic fluorescent signal of labeled macrophages was found to partially overlap with the above-mentioned nuclei.

3. Discussion

In this work, we outline a platform for one-photon photopolymerization and also adapted it to enable multi-photon 3D laser printing in early alive *Drosophila* and medaka embryos. We show how one- and multi-photon polymerizable polydimethylsiloxane can be microinjected, and UV-cured as well as 3D printed in their

ADVANCED SCIENCE NEWS
www.advancedsciencenews.com

ADVANCED SCIENCE Open Access
www.advancedscience.com

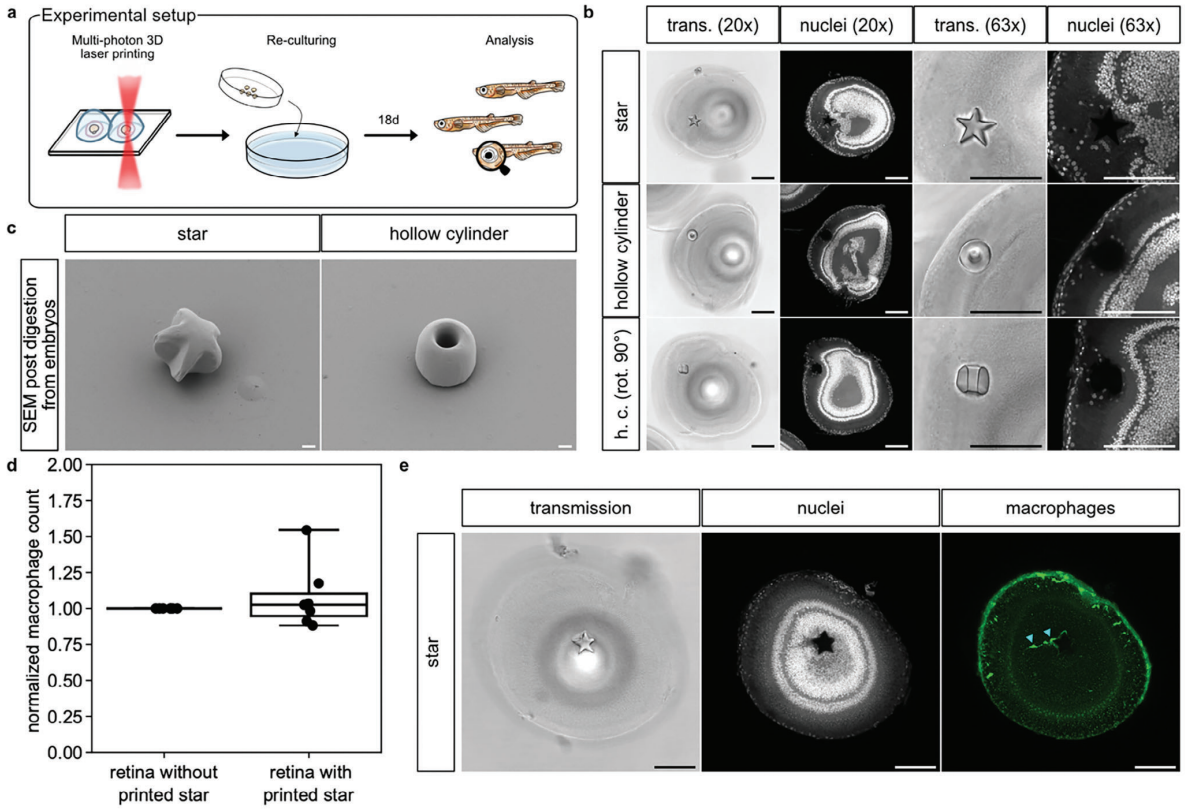

Figure 5. In vivo multi-photon 3D laser-printed microstructures develop spontaneously in the developing medaka retina, fully integrate into the tissue, and show no significant immunogenicity. a) Schematic illustration of the experimental setup that led to the images shown. b) Representative confocal microscopy of chemically fixed and whole-mount nuclear stained (Nuclei; DAPI) medaka embryo eyes (stage 41) after microinjection of IP-PDMS into their optic vesicles and subsequent 3D laser printing at 1 dpf. Printed structures measure 60 µm × 60 µm × 20 µm for the star and 50 µm × 50 µm × 20 µm for the hollow cylinder (20 µm inner diameter; shown in two orientations). Scale bars: 100 µm. c) Scanning electron microscopy of microprinted structures after enzymatic extraction from medaka embryo eyes obtained like shown in a. Scale bars: 10 µm. d) Quantification of total macrophage count in the whole retinas of n = 7 embryos with printed stars (60 µm × 60 µm × 20 µm). Cell counts were normalized to the cell counts of the contralateral control retinas of the same embryo without printed stars to account for differential cxcr3a::GFP expression levels between individual embryos. Boxplot boxes indicating 25–75% percentiles with whiskers indicating 10–90% percentiles. Individual data points are shown as dots. e) Representative confocal microscopy of chemically fixed and whole-mount nuclear and anti-GFP stained (Nuclei: DAPI; Macrophages: cxcr3a::GFP) medaka embryo retina (stage 41) after microinjection of IP-PDMS into their optic vesicle and subsequent 3D laser printing at 1 dpf. Printed star measures 60 µm × 60 µm × 20 µm. Cyan arrowheads indicate two individual macrophages in close proximity to the star. Scale bars: 100 µm.

extracellular tissue environments. Regarding requirements for in vivo printable synthetic polymers, we found it to be crucial for the ink to fulfil various criteria in terms of biocompatibility, printability, viscosity, and refractive indices in aqueous environments.

In case of in vivo one-photon photopolymerization, we observed that only after UV-induced photocrosslinking, the PDMS-like material could locally re-shape tissue morphogenesis in *Drosophila* embryos in ways that have not been possible by established methodology. From the time-lapse transmission recordings, we inferred that UV-cured spheres, as opposed to uncured droplets, interfere locally with the translocation of nuclei toward the embryo's cortex. This resulted in a reduced nuclear density at the anterior pole, which triggered an additional round of nuclear division and the subsequent time shift in cellularization at the anterior pole.

The re-shaping of cephalic furrow formation might be the consequence of an interaction of the basal cell side with the UV-cured IP-PDMS sphere, which the fluid surface interface of uncured IP-PDMS might not permit. A non-natural point of adhesive interaction of the yolk-facing cells in the emerging cephalic furrow might then be an anchor point for the tissue to re-shape around. PDMS is generally known to be biocompatible but unfavorable for cell adhesion. Coating with extracellular matrix (ECM) proteins via physisorption is regularly used to increase cell attachment on PDMS surfaces.[33–35] Specifically for multi-photon printed IP-PDMS, it has recently been shown to be able to support cell attachment of human mesenchymal stem cells after fibronectin functionalization.[9] Given that our PDMS-like material microstructures reside outside bona fide epithelia of the *Drosophila* and medaka embryos, a natural coating with ECM

or yolk resident proteins via physisorption after UV curation or 3D printing seems likely.[36] On top of that, the PDMS-like material structures are being exposed to the composition and spatial distribution of ECM and yolk resident proteins that are specific to the embryo, its developmental stage, and the tissue in question and therefore likely suitable for supporting attachment of cells of that particular tissue. Therefore, yolk protein-coated UV-cured spheres permitting both cell attachment after cellularization as well as interfering with the local cytoskeletal arrangement required for cortical nuclear translocation[37,38] represents the most likely explanation of the tissue morphogenesis phenotypes shown in this study. Future studies will address how the addition of ink components which can directly interact with surrounding cells without the need for ECM physisorption can be used to selectively program alternative biological responses.

Beyond the tissue engineering capacity of the presented technology, in vivo one-photon photopolymerization can also be utilized for biophysical studies of local forces generated *in organismo*, within the *Drosophila* embryo over the course of its development. In particular, timelapse transmission recordings of embryonic development and the visualization of uncured ink droplet deformations, combined with the ability to freeze – within seconds and with full temporal user control – the 3D shape of a droplet for subsequent ex vivo topological analysis, promises to be a powerful addition to the in vivo mechanobiology toolkit.

In late stages of medaka embryos, we found the 3D microstructures to develop and subsequently integrate into the surrounding tissue in less than 3 weeks after ink microinjection and 3D laser printing. Depending on the specific position of the 3D microstructures within the retinal layers, they were found juxtaposed to the outer segments of the photoreceptors in the OSL or the cell somata of the cells in the INL, permitting direct interaction with the cells of the tissue. This opens up the tissue microarchitecture to precise in vivo tissue engineering efforts utilizing the physicochemical features of a given printable biomaterial. Here, among others, properties like stiffness could be exploited as stiffness has been widely characterized to be a critical physical stem cell niche parameter and key determinant of differentiation,[39,40] proliferation,[41] and motility.[42]

Moreover, we found IP-PDMS microstructures to have remarkably low immunogenicity. At 18 days post ink microinjection and 3D laser printing, no macrophage infiltration of the retina was observed, showing that the in situ manufactured microstructures did not trigger an immunogenic response. Few resident macrophages were found to partially surround the printed microstructures with their cell bodies and pseudopodia, reminiscent of a recognition of the structure during immunosurveillance without them triggering an adverse immunogenic reaction to the foreign body. Inflammatory responses to immunogenic events, like an injury, generally are known to trigger massive infiltration of macrophages into the organ in question and to the site of injury even in early and late fish embryos.[43,44] The lack of an inflammatory response reflects the high degree of biocompatibility of the material as well as the minimal-invasive nature of the presented platform, since the tissue damage during surgical implantation releases damage-associated molecular patterns (DAMPs) and thus always results in an inflammatory response.[31,32] In vivo biocompatibility studies following mainly subcutaneous, intramuscular, and intraperitoneal implantation protocols for PDMS-based prosthetic macroscopic implants showed a high degree of biocompatibility with only mild acute and chronic inflammatory responses in the past.[45]

In conclusion, this study presents the first account of in vivo fabrication of 3D artificial microimplants inside the organ of a developing organism, using both one-photon and multi-photon polymerization. Importantly, this approach offers a framework for the minimal-invasive installation of biocompatible and non-degradable microimplants in vivo and thus provides opportunity to study and apply the in vivo bioengineering potential of materials and their shapes in 3D within tissue microarchitectures. Our pipeline allows for studying long-term interactions of complex in vivo tissue environments on micromaterials and their 3D integrity and vice versa. We identified an easily accessible, biocompatible, in vivo printable material of particularly low immunogenicity that is capable of mediating biological responses in extracellular in vivo environments. It is enticing to speculate how the presented platform is a first step towards in vivo 3D manufacturing of microimplants to treat human diseases affecting tissue or organ microarchitectures. This includes in vivo printing of microfluidic devices which can be envisioned in medical applications for targeted and controlled release of loaded therapeutics. The printed hydrophobic material could allow for loading with aqueous solutions containing drugs. Future studies towards clinical application require validation of the discovered approach inside common mammalian model systems.

4. Experimental Section

Materials: IP-PDMS (IP-polydimethylsiloxane; Nanoscribe GmbH, Germany) was used as the microinjectable, biocompatible ink in this study. The ink was protected from UV light prior to and after microinjection and mostly handled under yellow light conditions.

Fish Husbandry and Maintenance: Medaka fish (*Oryzias latipes*) stocks were maintained according to the local animal welfare standards (Tierschutzgesetz §11, Abs. 1, Nr. 1, husbandry permit AZ35-9185.64/BH, line generation permit number 35–9185.81/G-145/15 Wittbrodt). The fish are being kept as closed stocks in constantly recirculating systems at 28 °C with a 14 h light/10 h dark cycle. The following medaka lines were used in this study: Heino strain as an albinism exhibiting mutant[46] and cxcr3a::GFP.[47]

Fly Line and Embryo Handling: *OregonR* line was used as wildtype *Drosophila melanogaster*. Embryos were collected on apple juice containing agar plates (1:4 mix) with yeast paste at room temperature and subsequently prepared for microinjection. Embryos were dechorionated using bleach for 45 s and afterward washed thoroughly with tap water. Dechorionated embryos were transferred on a 22 × 22 mm cover glass, aligned against a glass capillary, and dried at room temperature for 7.5 min for slight volume reduction. Embryos were finally covered with a mixture of hydrocarbon oil (700 and 27 at a 4:1 ratio; Sigma Aldrich) and subjected to microinjection in less than 1 h post fertilization. One-photon photopolymerization, multi-photon 3D laser printing, and further microscopic analysis were performed typically within an hour of microinjection with embryos left mounted onto the cover glass.

Fish Embryo Handling: Medaka embryos were collected at day 0 shortly after fertilization and incubated in embryo rearing medium (ERM; 17 mM NaCl, 40 mM KCl, 0.27 mM $CaCl_2$, 0.66 mM $MgSO_4$, 17 mM HEPES) at temperatures between 18 and 32 °C depending on the desired timing of the target stage. Stage 19–21[28] (1 day post fertilization; dpf) embryos were subjected to dechorionation using hatching enzyme, washed and kept in 100 U ml^{-1} penicillin-streptomycin (P/S) containing ERM. Embryos were transferred into 1% agarose molds commonly used for transplantations,[48] oriented heads down for microinjection, and punc-

ADVANCED SCIENCE NEWS
www.advancedsciencenews.com

ADVANCED SCIENCE Open Access
www.advancedscience.com

tured at the vegetal pole. Microinjected embryos to be subjected to UV curation of the microinjected ink were transferred into 100 µl of P/S containing ERM. For multi-photon 3D laser printing, embryos were imbedded in 1% low-melting point agarose (Carl Roth, Cat#: 6351.5) solved in ERM onto a 22 × 22 mm cover glass and oriented with the heads towards the glass, minimizing the distance to the printer's objective. UV-curation and 3D laser printing were conducted within an hour of microinjection. Low-melting point agarose domes were moisturized with ERM and inserted into the Photonic Professional GT2 sample holder. After printing, embryos were manually extracted from the agarose using tweezers. Finally, embryos were re-incubated on glass ware in 100 U ml^{-1} P/S containing ERM until either 6 dpf or hatchling stage (s41.[28] 19 dpf) with daily assessment of their gross morphology by stereomicroscopy. In order to prevent unwanted UV-curation of unprinted IP-PDMS within the embryos, embryos were raised in total darkness until stage s40.[28]

Microinjection of Embryos: For microinjection, borosilicate micropipettes (1 mm OD × 0.58 mm ID × 100 mm L; Warner Instruments, Cat#: 30-0016) were pulled on a Flaming/Brown micropipette puller P-97 (Sutter instruments Co.) with the following settings: Heat 505, Pull 25, Velocity 250, Time 10, 1 cycle to create pulled pipettes with a slender taper. Pulled micropipettes were cut open manually to have a small, beveled opening of ≈5–10 microns. Microinjections were performed with either a CellTram 4m oil microinjector (Eppendorf AG) or homemade oil microinjector and a standard manual micromanipulator under an epifluorescence stereomicroscope (Olympus MVX10; MV PLAPO 1x objective).

One-Photon Photocrosslinking: For one-photon photocrosslinking of the ink (UV curing) medaka embryos kept in 100 µl of P/S containing ERM or *Drosophila* embryos mounted on the cover glass were exposed for 60 s at a 1 cm distance to unfiltered Leica EL6000 light (100% intensity; Lamp: HXP-R120W/45C VIS, power input 120 W, Osram Licht AG, Munich, Germany). Successful solidification was evaluated for every individual experiment by dissection of the embryos, removal of the UV-cured sphere, and manual crushing or drying of it.

Multi-Photon 3D Laser Printing: Multi-photon 3D laser printing was performed with the commercial 3D printing system Photonic Professional GT2 (Nanoscribe GmbH) with a laser wavelength of 780 nm and a 25x objective (NA = 0.8). STL files of desired 3D structures were transformed into Nanoscribe GWL printing files using the Describe software. In this software, slicing and hatching were set to 300 nm for all geometries, as well as galvo and piezo modes were selected for xy and z movement of the laser, respectively.

Before printing in the microinjected droplet, precise laser positioning was required in *xyz* dimensions. For this purpose, a glass slide with pure IP-PDMS was first prepared for printing in oil immersion mode with Immersol 518 F from Carl Zeiss AG. Subsequently, simple crosshair structures were printed to align the *xy* position of the laser to an external crosshair in the camera. Afterward, the glass slide was removed from the substrate holder and replaced by the glass slides with the embryos (medaka and *Drosophila*).

The first initial *xy* positioning was followed by preparing the slides for printing in oil immersion mode and inserting the equipped substrate holder in the printer. The ink droplet in the embryo was positioned in the center of the external camera crosshair for *xy* positioning. Now, moving of the stage (in *z* axis) was used to position the droplet in the focus plane. After final *xyz* positioning, 3D laser printing of desired 3D microstructures was performed with a scan speed of 20 mm $^{-1}$s and laser power of 30 mW. After printing, the oil on the bottom of the glass slides was removed with HPLC-grade isopropanol.

Fly Embryo Live Imaging: Following either one-photon photocrosslinking or multi-photon 3D laser printing, cover glasses with *Drosophila* embryos mounted on were adhered onto standard glass microscopy slides. Live embryos were timelapse imaged at a framerate of 1 frame every 1 min over the course of 7 h or 1 frame every 4 min over the course of 10 h for additional z-stack acquisition, resulting in videos capturing their gross development after intervention. 633 nm/552 nm laser-powered transmission images were acquired on a Leica SP5 DMI6000CS/SP8 DMi8 inverted confocal microscope using the 10x objective with 2-2.5x digital zoom. Microinjected deposits were tracked using manual ROI specification in ImageJ.[49]

Fluorescent Labeling and Fish Embryo Imaging: For whole-mount fluorescent staining, embryos were fixed overnight in 4% PFA at 4 °C and washed with PTW (0.05% Tween20 dissolved in PBS). Either full heads, eyes or retinas were manually dissected from the embryos using tweezers. Dissected samples were bleached (either 0.3% (Heinostrain) or 3% (cxcr3a::GFP) H_2O_2, 0.5% KOH; dissolved in PTW) for 15–30 min at room temperature and washed 5 times with PTW. Sample permeabilization was performed with acetone for 15 min at −20 °C. Samples were blocked with 4% sheep serum, 1% BSA, and 1% DMSO in PTW for 1 h at room temperature. Nuclear stain was carried out overnight at 4 °C with DAPI (10 µg ml^{-1} in DMSO, Carl Roth, Cat#: 6335.1) dissolved in PTW. Cxcr3a::GFP samples were incubated with primary antibodies against GFP for 48 h at 4 °C (chicken anti-GFP (Thermo Fisher Scientific, Cat#: A10262; 1:300)). Samples were washed five times with PTW and subsequently incubated with the respective secondary antibodies (1:500) for 24 h at 4 °C (donkey anti-chicken Alexa Fluor 488 (Jackson ImmunoResearch Europe Ltd., Cat#: 703-545-155)). In preparation for imaging, embryos were washed five times in PTW and finally transferred into optical clearing solution[50] (20% (wt/vol) urea (Sigma–Aldrich, Cat#: V900119), 30% (wt/vol) D-sorbitol (Sigma–Aldrich, Cat#: V900390), 5% (wt/vol) glycerol (Sigma–Aldrich, Cat#: V900122) dissolved in DMSO (Sigma Aldrich, Cat#: V900090)). Imaging was performed on a Leica TCS Sp8 DMi8 inverted confocal microscope (20x and 63x oil immersion objective).

Macrophages were manually counted in whole retinas using the Cell Counter plugin in ImageJ.[49]

Scanning Electron Microscopy (SEM): 3D laser printed structures were extracted from fixed medaka embryo samples via overnight incubation at 60 °C in extraction buffer (100 nM Tris-HCl pH 8.5, 10 mM EDTA, 200 mM NaCl, 1% SDS, 1 mg ml^{-1} Proteinase K (Sigma–Aldrich, Cat#: 3 115 852 001)), then washed with isopropanol, and transferred onto glass coverslips. The glass coverslips containing the 3D structures were then sputter coated with a 12 nm layer of Pt/Pd (80:20) and imaged using a field-emission scanning electron microscope (Ultra 55, Carl Zeiss Microscopy) operated at a primary electron energy of 3 keV with the chamber SE2 detector and a tilting angle of 30°.

Statistical Analysis: Two-tailed Student's *t*-test with unequal variance was used for the calculation of significant differences. Differences between two groups with p-values < 0.05 were considered statistically significant.

Supporting Information

Supporting Information is available from the Wiley Online Library or from the author.

Acknowledgements

The authors thank Maily Scorcelletti for help with setting up *Drosophila melanogaster* experiments. The authors thank Prof. Dr. Rasmus Schröder (Heidelberg University) for the access to the electron microscopy facilities. C.A. was partially funded by the Structured Doctoral programme (*Strukturiertes Doktorandenprogramm zum Erwerb des Dr. med. und Dr. rer. nat.*) of Heidelberg University. K.G., E.B., and J.W. acknowledge the funding from the Excellence Cluster "3D Matter Made to Order" (EXC-2082/1-390761711). E.B., K.G., and T.A. further acknowledge funding from the Carl Zeiss Foundation through the "Carl-Zeiss-Foundation-Focus@HEiKA". C.V.M. acknowledges the Fonds der Chemischen Industrie for the support during her PhD studies through the Kekulé Fellowship.

Open access funding enabled and organized by Projekt DEAL.

Conflict of Interest

The authors declare no conflict of interest.

Author Contributions

C.A. and P.M. contributed equally to this work. C.A., P.M., E.B., and J.W. performed conceptualization. C.A., P.M., C.V.M., T.A., V.K., G.K., K.G., S.L., E.B., and J.W. performed investigation. C.A., P.M., and C.V.M. performed visualization. S.L., K.G., E.B., and J.W. performed funding acquisition. E.B., and J.W. performed project administration. S.L., K.G., E.B., and J.W. performed supervision. C.A., P.M., E.B., and J.W. Wrote – original draft.

Data Availability Statement

The data that support the findings of this study are openly available in heiDATA, the Open Research Data institutional repository for Heidelberg University at https://doi.org/10.11588/data/MVBFOY, reference number [51].

Keywords

3D laser printing, additive manufacturing, bioengineering, *Drosophila melanogaster*, microimplants, *Oryzias latipes*, two-photon lithography

Received: January 30, 2024
Revised: May 10, 2024
Published online: June 12, 2024

[1] S. C. Ligon, R. Liska, J. Stampfl, M. Gurr, R. Mülhaupt, *Chem. Rev.* **2017**, *117*, 10212.
[2] A. Jaiswal, C. K. Rastogi, S. Rani, G. P. Singh, S. Saxena, S. Shukla, *iScience* **2023**, *26*, 106374.
[3] V. Harinarayana, Y. C. Shin, *Opt. Laser Technol.* **2021**, *142*, 107180.
[4] C. Greant, B. Van Durme, J. Van Hoorick, S. Van Vlierberghe, *Adv. Funct. Mater.* **2023**, *33*, 2212641.
[5] S. J. Baldock, P. Kevin, G. R. Harper, R. Griffin, H. H. Genedy, M. J. Fong, Z. Zhao, Z. Zhang, Y. Shen, H. Lin, C. Au, J. R. Martin, M. D. Ashton, M. J. Haskew, B. Stewart, O. Efremova, R. N. Esfahani, H. C. A. Emsley, J. B. Appleby, D. Cheneler, D. M. Cummings, A. Benedetto, J. G. Hardy, *Adv. Mater. Technol.* **2023**, *8*, 2201274.
[6] M. Taale, B. Schamberger, F. Taheri, Y. Antonelli, A. Leal-Egaña, C. Selhuber-Unkel, *Adv. Funct. Mater* **2024**, *34*, 2302356.
[7] A. Urciuolo, G. G. Giobbe, Y. Dong, F. Michielin, L. Brandolino, M. Magnussen, O. Gagliano, G. Selmin, V. Scattolini, P. Raffa, P. Caccin, S. Shibuya, D. Scaglioni, X. Wang, J. Qu, M. Nikolic, M. Montagner, G. L. Galea, H. Clevers, M. Giomo, P. De Coppi, N. Elvassore, *Nat. Commun.* **2023**, *14*, 3128.
[8] A. Urciuolo, I. Poli, L. Brandolino, P. Raffa, V. Scattolini, C. Laterza, G. G. Giobbe, E. Zambaiti, G. Selmin, M. Magnussen, L. Brigo, P. De Coppi, S. Salmaso, M. Giomo, N. Elvassore, *Nat. Biomed. Eng.* **2020**, *4*, 901.
[9] N. Munding, M. Fladung, Y. Chen, M. Hippler, A. D. Ho, M. Wegener, M. Bastmeyer, M. Tanaka, *Adv. Funct. Mater.* **2024**, *34*, 2301133.
[10] A. Ovsianikov, A. Deiwick, S. Van Vlierberghe, M. Pflaum, M. Wilhelmi, P. Dubruel, B. Chichkov, *Materials* **2011**, *4*, 288.
[11] A. Ovsianikov, M. Malinauskas, S. Schlie, B. Chichkov, S. Gittard, R. Narayan, M. Löbler, K. Sternberg, K.-P. Schmitz, A. Haverich, *Acta Biomater.* **2011**, *7*, 967.
[12] J. R. Thompson, K. S. Worthington, B. J. Green, N. K. Mullin, C. Jiao, E. E. Kaalberg, L. A. Wiley, I. C. Han, S. R. Russell, E. H. Sohn, C. A. Guymon, R. F. Mullins, E. M. Stone, B. A. Tucker, *Acta Biomater.* **2019**, *94*, 204.
[13] J. Van Hoorick, L. Tytgat, A. Dobos, H. Ottevaere, J. Van Erps, H. Thienpont, A. Ovsianikov, P. Dubruel, S. Van Vlierberghe, *Acta Biomater.* **2019**, *97*, 46.
[14] L. Tytgat, A. Dobos, M. Markovic, L. Van Damme, J. Van Hoorick, F. Bray, H. Thienpont, H. Ottevaere, P. Dubruel, A. Ovsianikov, S. Van Vlierberghe, *Biomacromolecules* **2020**, *21*, 3997.
[15] X. Wang, X.-H. Qin, C. Hu, A. Terzopoulou, X.-Z. Chen, T.-Y. Huang, K. Maniura-Weber, S. Pané, B. J. Nelson, *Adv. Funct. Mater.* **2018**, *28*, 1804107.
[16] E. Zerobin, M. Markovic, Z. Tomásiková, X.-H. Qin, D. Ret, P. Steinbauer, J. Kitzmüller, W. Steiger, P. Gruber, A. Ovsianikov, R. Liska, S. Baudis, *Prog. Polym. Sci* **2020**, *58*, 1288.
[17] O. Kufelt, A. El-Tamer, C. Sehring, S. Schlie-Wolter, B. N. Chichkov, *Biomacromolecules* **2014**, *15*, 650.
[18] J. Jang, J.-Y. Kim, Y. C. Kim, S. Kim, N. Chou, S. Lee, Y.-H. Choung, S. Kim, J. Brugger, H. Choi, J. H. Jang, *Adv. Healthcare Mater.* **2019**, *8*, e1900379.
[19] A. Ovsianikov, B. Chichkov, O. Adunka, H. Pillsbury, A. Doraiswamy, R. J. Narayan, *Appl. Surf. Sci.* **2007**, *253*, 6603.
[20] H. Kavand, M. Visa, M. Köhler, W. van der Wijngaart, P.-O. Berggren, A. Herland, *Adv. Mater.* **2024**, *36*, 2306686.
[21] X. Wang, N. Rivera-Bolanos, B. Jiang, G. A. Ameer, *Adv. Funct. Mater.* **2019**, *29*, 1809009.
[22] K. S. Lim, B. J. Klotz, G. C. J. Lindberg, F. P. W. Melchels, G. J. Hooper, J. Malda, D. Gawlitta, T. B. F. Woodfield, *Macromol. Biosci.* **2019**, *19*, 1900098.
[23] R.-Z. Lin, Y.-C. Chen, R. Moreno-Luna, A. Khademhosseini, J. M. Melero-Martin, *Biomaterials* **2013**, *34*, 6785.
[24] S. Chung, H. Lee, H.-S. Kim, M.-G. Kim, L. P. Lee, J. Y. Lee, *Nanoscale* **2016**, *8*, 14213.
[25] K. Y. Lee, D. J. Mooney, *Prog. Polym. Sci.* **2012**, *37*, 106.
[26] Y. Chen, J. Zhang, X. Liu, S. Wang, J. Tao, Y. Huang, W. Wu, Y. Li, K. Zhou, X. Wei, S. Chen, X. Li, X. Xu, L. Cardon, Z. Qian, M. Gou, *Sci. Adv.* **2020**, *6*, eaba7406.
[27] Nanoscribe GmbH & Co. KG. IP-PDMS photoresin, Biocompatible elastomers for life sciences, https://www.nanoscribe.com/en/products/ip-resins/ip-pdms (accessed: November 2023).
[28] T. Iwamatsu, *Mech. Dev.* **2004**, *121*, 605.
[29] C. Collinet, T. Lecuit, *Nat. Rev. Mol. Cell Biol.* **2021**, *22*, 245.
[30] S. Franz, S. Rammelt, D. Scharnweber, J. C. Simon, *Biomaterials* **2011**, *32*, 6692.
[31] J. O. Abaricia, N. Farzad, T. J. Heath, J. Simmons, L. Morandini, R. Olivares-Navarrete, *Acta Biomater.* **2021**, *133*, 58.
[32] L. Kämmerling, L. E. Fisher, E. Antmen, G. M. Simsek, H. M. Rostam, N. E. Vrana, A. M. Ghaemmaghami, *J. Immunol. Regener. Med.* **2021**, *12*, 100040.
[33] L. Wang, B. Sun, K. S. Ziemer, G. A. Barabino, R. L. Carrier, *J. Biomed. Mater. Res., Part A* **2010**, *93A*, 1260.
[34] J. N. Lee, X. Jiang, D. Ryan, G. M. Whitesides, *Langmuir* **2004**, *20*, 11684.
[35] F. Akther, S. B. Yakob, N.-T. Nguyen, H. T. Ta, *Biosensors* **2020**, *10*, 182.
[36] Y. Hong, I. Koh, K. Park, P. Kim, *ACS Biomater. Sci. Eng.* **2017**, *3*, 3546.
[37] W. Sullivan, P. Fogarty, W. Theurkauf, *Development* **1993**, *118*, 1245.
[38] G. von Dassow, G. Schubiger, *J. Cell Biol.* **1994**, *127*, 1637.
[39] A. J. Engler, S. Sen, H. L. Sweeney, D. E. Discher, *Cell* **2006**, *126*, 677.
[40] K. Saha, A. J. Keung, E. F. Irwin, Y. Li, L. Little, D. V. Schaffer, K. E. Healy, *Biophys. J.* **2008**, *95*, 4426.
[41] N. D. Leipzig, M. S. Shoichet, *Biomaterials* **2009**, *30*, 6867.
[42] W. J. Hadden, J. L. Young, A. W. Holle, M. L. McFetridge, D. Y. Kim, P. Wijesinghe, H. Taylor-Weiner, J. H. Wen, A. R. Lee, K. Bieback, B.-N. Vo, D. D. Sampson, B. F. Kennedy, J. P. Spatz, A. J. Engler, Y. S. Choi, *Proc Natl Acad Sci U S A* **2017**, *114*, 5647.
[43] R. A. Morales, M. L. Allende, *Front. Immunol.* **2019**, *10*, 00253.

[44] L. L. Leach, N. J. Hanovice, S. M. George, A. E. Gabriel, J. M. Gross, *Proc. Natl. Acad. Sci. USA* **2021**, *118*, e2017198118.
[45] M. C. Bélanger, Y. Marois, *J. Biomed. Mater. Res* **2001**, *58*, 467.
[46] F. Loosli, R. W. Köster, M. Carl, R. Kühnlein, T. Henrich, M. Mücke, A. Krone, J. Wittbrodt, *Mech. Dev.* **2000**, *97*, 133.
[47] N. Aghaallaei, B. Bajoghli, H. Schwarz, M. Schorpp, T. Boehm, *Proc. Natl. Acad. Sci. USA* **2010**, *107*, 18079.
[48] J. F. Fuhrmann, J. Onistschenko, L. Centanin, *Bio-Protoc.* **2021**, *11*, e4166.
[49] C. A. Schneider, W. S. Rasband, K. W. Eliceiri, *Nat. Methods* **2012**, *9*, 671.
[50] X. Zhu, L. Huang, Y. Zheng, Y. Song, Q. Xu, J. Wang, K. Si, S. Duan, W. Gong, *Proc. Natl. Acad. Sci. USA* **2019**, *116*, 11480.
[51] C. Afting, P. Mainik, C. Vazquez-Martel, T. Abele, V. Kaul, G. Kale, K. Göpfrich, S. Lemke, E. Blasco, J. Wittbrodt, "Minimal-Invasive 3D Laser Printing of Microimplants in Organismo [data]", heiDATA, 1.0, **2024**, https://doi.org/10.11588/data/MVBFOY.

Supplemental Information

Fig. S1: UV cured spheres explanted from *Drosophila* embryos after timelapse microscopy.

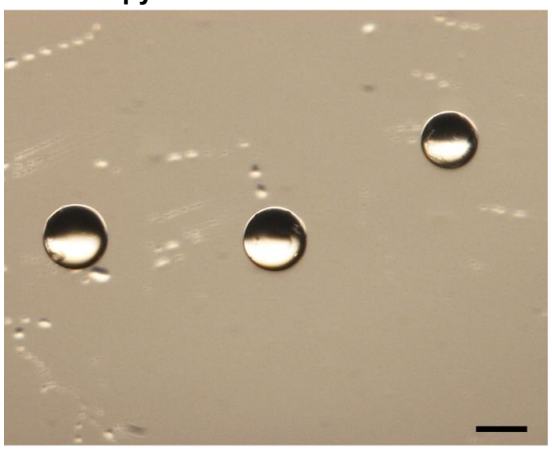

Scale bar: 100 µm.

Fig. S2: Total distance traveled of uncured droplets and UV cured spheres in *Drosophila* embryos before cellularization.

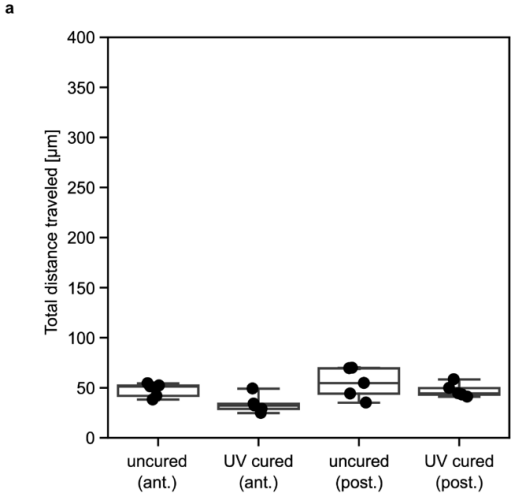

a Quantification of total distance traveled of the uncured and UV cured, microinjected IP-PDMS deposits at the anterior (ant.) and posterior (post.) poles of the *Drosophila* embryos. Spheres were tracked in 10 min increments in timelapse microscopy images from the last mitotic wave until end of cellularization. Boxplots include data from 5 embryos each with boxes indicating 25-75% percentiles and whiskers 10-90% percentiles. Individual data points shown as dots.

Fig. S3: *In vivo* one-photon photopolymerized IP-PDMS spheres allow local re-shaping of the *Drosophila* cephalic furrow.

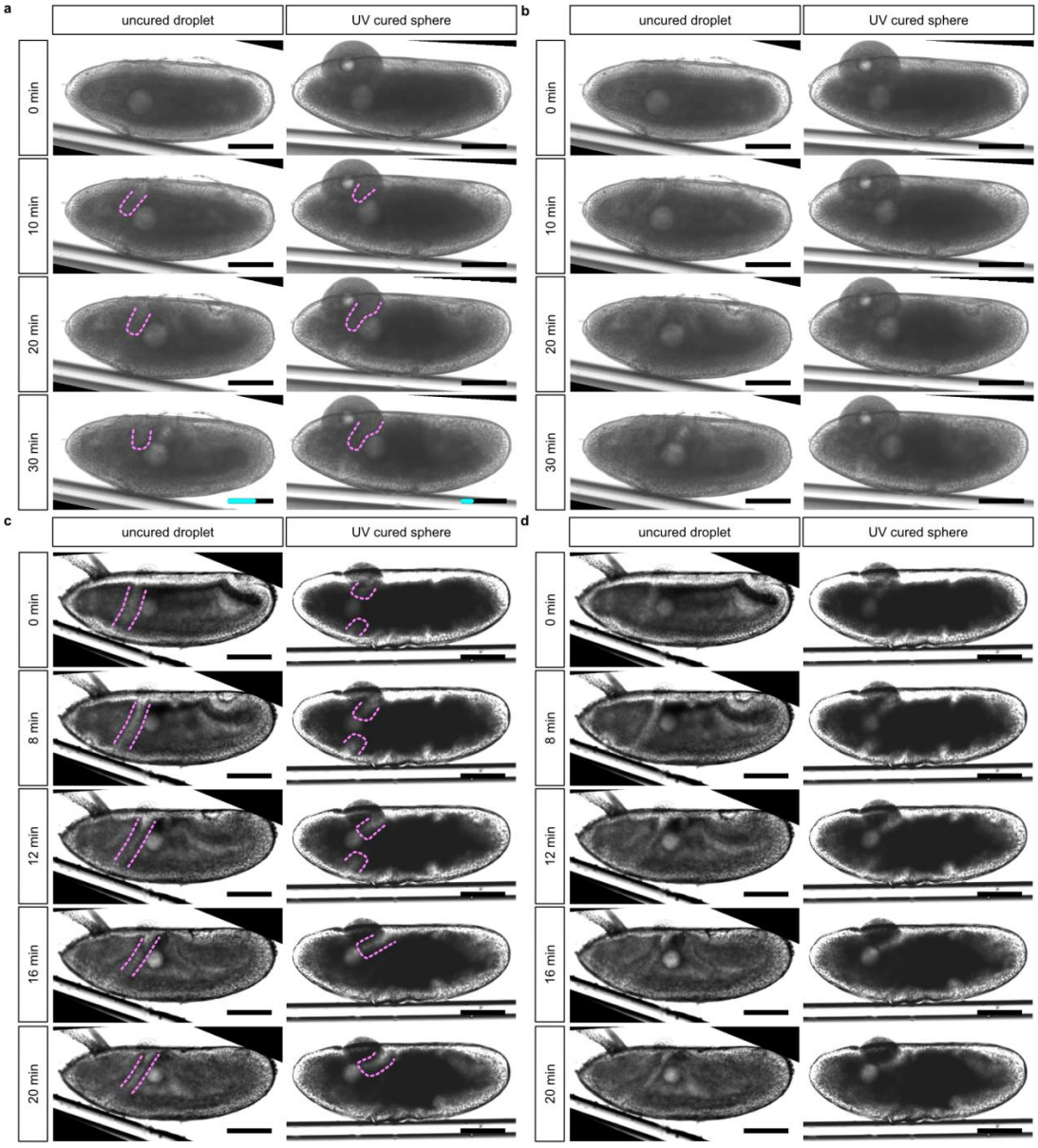

a/b Representative timelapse transmission microscopy of early *Drosophila* embryos during cephalic furrow formation microinjected with IP-PDMS with (a) and without (b) overlays. Microinjected IP-PDMS deposits were either left uncured (left panels) or cured by UV light exposure (right panels). Cyan scale bar insets indicate the total distance traveled of the spheres within 15 min after the first contact with the emerging cephalic furrow. **c/d** Additional example of timelapse transmission microscopy of early *Drosophila* embryos during cephalic furrow formation microinjected with IP-PDMS with (c) and without (d) overlays. Magenta dashed lines indicate the gross morphology of the cephalic furrow. Scale bars: 100 µm.

Fig. S4: Multi-photon 3D laser printed star in bipolar cell layer and contralateral control eyes of the stage 41 medaka embryos shown in Figure 5.

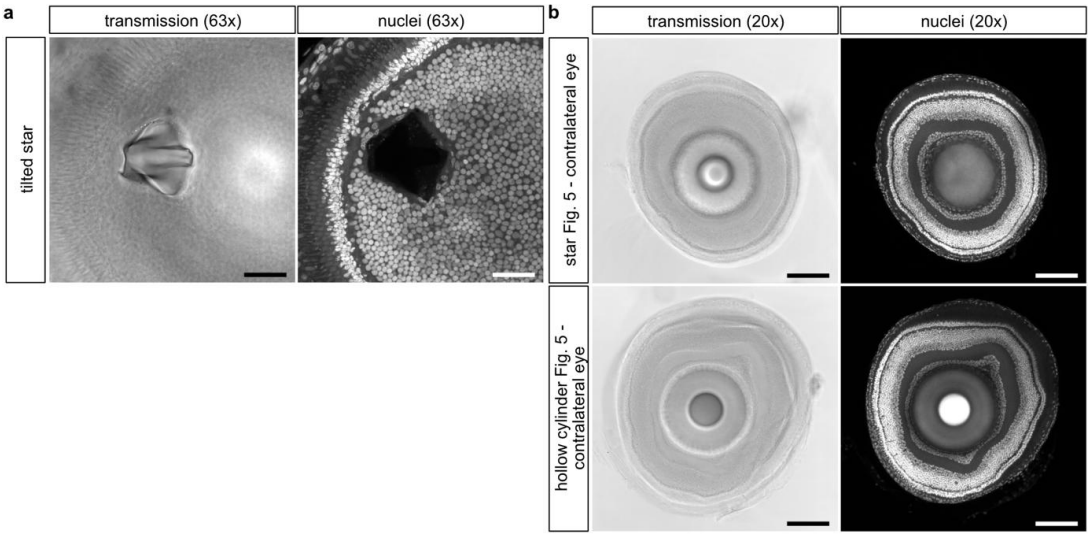

a Representative confocal microscopy of chemically fixed and whole-mount nuclear stained (Nuclei; DAPI) medaka embryo eyes at 19 days post fertilization (dpf) after microinjection of IP-PDMS into their optic vesicles and subsequent 3D laser printing at 1dpf. The slightly tilted star measures 60 µm x 60 µm x 20 µm and is integrated into the retinal inner nuclear cell layer (INL). **b** Contralateral, uninjected eyes of the medaka embryos shown in Figure 5b. Scale bars: 100 µm.

Fig. S5: 3D rendered models of in vivo 3D printed microstructures shown in Fig. 4 and 5.

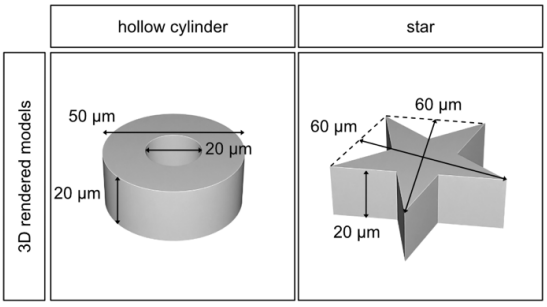

Movie S1: UV cured spheres at the extreme anterior pole trigger an additional round of anterior nuclear division resulting in a time shift of cellularization onset.

Representative timelapse transmission microscopy of early *Drosophila* embryos microinjected at the extreme anterior pole with IP-PDMS during cellularization. Microinjected IP-PDMS deposit was cured by UV light exposure. Corresponding timelapse movie to Fig. 3c (right panel). Scale bar: 100 µm.

IV. Summary & Discussion

This PhD thesis covered the material design of new synthetic and natural-based biomaterial inks for 3D/4D MPLP as well as interdisciplinary in-depth material characterization using established methods from disciplines such as engineering, (bio)physics, biology, and medicine. The characterization of (printed) biomaterial inks included, for example, printability studies, advanced imaging techniques, mechanical analysis, experimental and theoretical evaluation of stimuli-responsive behavior, as well as biocompatibility and *in vivo* studies. The performed investigations provided key information for evaluating the potential of the designed biomaterials for advancing future bioapplications.

Deep Eutectic Inks for Multiphoton 3D Laser Printing

The first project aimed to overcome current limitations by improving the printability and accessibility of synthetic biomaterial inks. For this purpose, the traditional ink design, *i.e.* the use of synthetic prepolymers or multifunctional monomers to achieve printability, was replaced by establishing supramolecular interactions in inks. This was achieved by introducing a new class of deep eutectic inks (DEIs) for MPLP.

The ink design based on DEIs enabled the simple, yet versatile preparation of the DEIs by exploring various monofunctional monomers. In detail, three polymerizable deep eutectics have been introduced based on acrylic acid, 2-hydroxyethyl acrylate, and *N*,*N*-dimethylacrylamide. These selected acrylic monomers were mixed at elevated temperatures in varying molar ratios with zinc chloride as a Lewis acid. The eutectics were liquid at room temperature and showed the expected thermal behavior upon analysis by DSC. After characterizing the viscosity, spectroscopic properties, and the thermal behavior, the three mixtures were formulated into inks for MPLP. This was achieved by adding a suitable and adding minor amounts of static crosslinkers.

Compared to inks without supramolecular crosslinking, the presented DEIs allowed the use of significantly lower exposure doses with a similar printing performance compared to commercially available stiff materials. Moreover, the high sensitivity enabled dip-in mode printing allowing MPLP in the millimeter scale.

After MPLP, the printed structures were developed in a suitable solvent to remove uncured ink which disrupted the supramolecular bonds. Removing the supramolecular crosslinking led to previously inaccessible soft structures as analyzed in compression experiments. Furthermore, the printed DEIs showed high elasticity as observed in the compression experiments and in qualitative elongation of a printed spring structure. The presented DEIs were also successfully mixed with acrylamide or NIPAAm to incorporate other functionalities. For example, the acrylic acid and NIPAAm containing printed DEI showed multi-responsive behavior upon stimuli such as temperature, calcium, and pH. Using this ink for the preparation of the multimaterial structures gave access to stimuli-responsive hydrogel structures with anisotropic actuation.

This work lays the foundation for increasing the printing speed and accessibility of soft 3D biomaterial structures with application in cell scaffold fabrication, bioelectronics, and soft robotics. For this purpose, the results of this project provided the basis for a patent filing together with Heidelberg University. The simplicity and versatility of accessible monomers for DEI preparation offers a highly attractive way for designing inks in the future. This includes especially the preparation of inks starting from monomers and adding multifunctional crosslinkers or pre-polymers only in cases where it serves an additional architectural purpose or cannot be omitted.

Responsive 3D Printed Microstructures Based on Collagen Folding and Unfolding

The second project explored the use of a natural-based, room-temperature stable collagen ink and its use for MPLP of responsive structures based on collagen folding and unfolding.

First, the room-temperature stable collagen ink was established by dissolving collagen methacrylamide in the presence of acetic acid, fluorescent co-monomer, and photoinitiator. Despite its very low (less than 0.5 wt%) polymerizable mass, the hydrogel ink showed a broad printability window and allowed for MPLP of free-standing 3D structures which have not been shown for natural collagen before. After development in water, the printed structures were first analyzed for their structural quality using optical microscopy. Good structural fidelity with micron-resolution was confirmed by confocal fluorescence microscopy.

In addition to analyzing the printed microstructures, the nanostructure of the printed collagen was studied using scanning and transmission electron microscopy techniques. To avoid collapse of the structures in the high vacuum, the printed collagen was embedded in

an epoxy resin. Analysis of the nanostructures revealed a fibrillar and porous collagen network with similar fibril diameters as measured for the dissolved collagen fibrils in the ink. Next, the 3D printed collagen was studied for its biocompatibility using rat embryonic fibroblasts. The printed structures were cell-adhesive, showed excellent cell viability, and the cells exhibited healthy focal contacts.

After having developed the ink and characterized the structures, the printed collagen was studied for its temperature-responsive behavior. For this purpose, the printed structures observed by optical microscopy upon heating in a heating stage. The collagen microstructures started to shrink around 60% in volume around 40-41 °C and recovered upon cooling back to room temperature. This process was fully reversible in multiple cycles. To investigate the origin of this effect, circular dichroism spectroscopy was performed to study collagen unfolding in the ink upon heating. The melting temperature of the collagen fibrils was found to be 40-41 °C, correlating with the temperature required for the microstructure shrinkage. In addition to the experimental observation, the origin of the shrinkage was further evaluated by theoretical simulations. For this purpose, the expected lowering in persistence length due to collagen unfolding was used to simulate the change in volume of the crosslinked structures in molecular dynamics simulations.

The presented collagen ink offers a natural-based biomaterial ink for advanced applications such as cell scaffolds in tissue engineering. The room temperature stability over weeks, easy preparation, and accessible fabrication of free-standing complex 3D structures are important advantages of the reported ink and aim to facilitate the accessibility and handling for interested users across different disciplines. Moreover, the responsive collagen folding motif offers a previously unexplored mechanism for designing stimuli-responsive biomaterials for MPLP.

Minimal-Invasive 3D Laser Printing of Microimplants in Organismo

In the third project, a new approach for introducing MPLP in living and developing organisms was successfully achieved. To this aim, a process based on the ink microinjection, MPLP, and structure as well as embryo development analysis was established for printing in fruit flies and medaka fish. This process was found to include several important criteria which were identified by testing various inks. In detail, the ink had to possess a suitable viscosity for microinjection and be hydrophobic to form a stable ink droplet in the rather hydrophilic

environment. Moreover, the ink had to be biocompatible in its liquid form as well as allowing the fabrication of biocompatible biomaterial. Moreover, in this form, the ink had to be printable in MPLP, and uncured ink had to dissipate over several days after printing. All these criteria were evaluated, and different compositions were tested before a PDMS-based ink was identified to fulfill all the requirements.

After successful microinjection, the embryo was oriented on the glass slide to stay below the working distance of the objective in oil immersion mode printing. After alignment in the *xy* plane, the laser was focused inside the liquid droplet using the stage movement in *z* direction. By following this alignment procedure, microstructures of dimensions around 60 µm × 60 µm × 20 µm were successfully printed *in organismo*. The printed PDMS-based ink as well as the printed structures were found to not show any adverse effects on the developing medaka embryos within 18 days after MPLP. Moreover, uncured ink dissipated during the embryonic development process.

In summary, the established protocol together with the systematic study of the ink requirements offers an efficient way to fabricate *in organismo* and shows that MPLP can be used to fabricate biomaterials in 3D – even in developing organisms.

V. Final Reflection

Shaping biomaterials in 3D holds great potential for tissue engineering applications such as cell scaffolds or implants. In this context, the rapidly evolving field of MPLP offers a promising technique to prepare 3D structures with subcellular resolution from biomaterial inks. This thesis covered several important aspects for broadening and advancing this field by introducing new previously unattainable synthetic as well as natural-based biomaterials inks for fast 3D fabrication.

The synthetic approach based on DEIs opens a plethora of possibilities for future ink design. Enabling MPLP of monofunctional monomer inks with low exposure doses allows for preparing soft biomaterials with subcellular resolution. These soft materials present, for example, excellent candidates for preparing tunable synthetic cell scaffolds for tissue engineering. Moreover, they could be combined with conductive electrodes for bioelectronic applications as soft implants for biosensors or even stimulation of tissues. Furthermore, the presented approach to using supramolecular bonds for the design of MPLP inks could be expanded towards other functional material inks. Thereby, it would allow for increased functionality without compromising printability. These functional materials could be used in the development of soft robotics. The simplicity and the broad range of accessible monofunctional monomers for PDESs offers an excellent foundation for using this concept in the future. For this purpose, exploring PDESs based on more hydrophobic systems could expand the range even further. [160,161] In addition to focusing on the polymerizable monomers, tuning the PDES by choosing, for example, different metal halides could employ additional properties for post-printing procedures. [160] In these post-printing procedures, the residual metal ions in printed DEIs could serve as templates for preparing catalytically active or conductive materials.

The presented natural-based collagen biomaterial was printed with a commercial setup and allows for the fabrication of printed cell scaffolds for advanced 3D cell culture experiments and tissue engineering. A promising addition to this material could include the alignment of the collagen fibrils prior to photocrosslinking. This could be achieved, for example, by ultrasound. [162] The alignment could be used to guide cell organization or spreading. [137] The printed collagen could also be combined with other printable biomolecules to stimulate

attached cells. This could be achieved for example by adding synthetic biomolecules or other components of the extracellular matrix. Moreover, the porous printed collagen could also serve as a template for performing biomineralization processes. For example, calcium phosphate could be crystallized between the (aligned) collagen fibrils and provide a mimetic bone structure. [163] In addition to using static collagen, temperature-responsive behavior could be used to stimulate cells. For this purpose, the presented temperature response could be studied for different sources of natural collagen depending on the targeted temperature range for the response. [141] A more synthetic approach by designing collagen-mimetic polypeptides could enable the study of differences in temperature-responsive self-assembly in an even larger range.[164]

The presented work on 3D printing of biomaterials in developing organisms showed the minimal-invasive installation of biocompatible and non-degradable microimplants *in vivo*. The presented workflow opens new opportunities to apply materials and their shapes in 3D within tissues. *In vivo* MPLP could be used for medical applications such as microimplants or targeted drug delivery by printed microfluidic devices. In addition to the development of new applications, future research directions could involve the design of new materials with additional shape-morphing or degradable behavior.

In conclusion, the rise of light-based 3D printing, particularly MPLP, in the last two decades has offered promising new applications by microfabrication, where high precision is needed. I believe that advancing new biomaterial inks holds great potential for bioapplications and will offer prosperous new possibilities for science, industry and society.

VI. References

[1] R. Mülhaupt, *Angew. Chem.* **2004**, *43*, 1054.

[2] J. W. Nicholson, *Chemistry of Polymers*, The Royal Society of Chemistry **2006**.

[3] E. Saldívar-Guerra, E. Vivaldo-Lima, *Handbook of Polymer Synthesis, Characterization, and Processing*, Wiley **2013**.

[4] R. Geyer, J. R. Jambeck, K. L. Law, *Sci. Adv.* **2017**, *3*, e1700782.

[5] S. Koltzenburg, M. Maskos, O. Nuyken, *Polymer chemistry*, Springer **2017**.

[6] S. Chandran, J. Baschnagel, D. Cangialosi, K. Fukao, E. Glynos, L. M. C. Janssen, M. Müller, M. Muthukumar, U. Steiner, J. Xu, S. Napolitano, G. Reiter, *Macromolecules* **2019**, *52*, 7146.

[7] G. Odian, *Principles of Polymerization*, Wiley **2004**.

[8] M. A. S. N. Weerasinghe, O. J. Dodo, C. W. H. Rajawasam, I. O. Raji, S. V. Wanasinghe, D. Konkolewicz, N. de Alwis Watuthanthrige, *Polym. Chem.* **2023**, *14*, 4503.

[9] M. Attaran, *Bus. Horiz.* **2017**, *60*, 677.

[10] S. C. Ligon, R. Liska, J. Stampfl, M. Gurr, R. Mülhaupt, *Chem. Rev.* **2017**, *117*, 10212.

[11] P. Somers, A. Münchinger, S. Maruo, C. Moser, X. Xu, M. Wegener, *Nat. Rev. Phys.* **2024**, *6*, 99.

[12] H. J. Levinson, *Principles of Lithography, Fourth Edition*, SPIE **2019**.

[13] C. W. Hull, *Apparatus for production of three-dimensional objects by stereolithography*, US4575330A, Patent **1986**.

[14] M. Vaezi, H. Seitz, S. Yang, *Int. J. Adv. Manuf. Technol.* **2013**, *67*, 1721.

[15] C. Sun, N. Fang, D. M. Wu, X. Zhang, *Sens. Actuators A: Phys.* **2005**, *121*, 113.

[16] C. Yu, J. Schimelman, P. Wang, K. L. Miller, X. Ma, S. You, J. Guan, B. Sun, W. Zhu, S. Chen, *Chem. Rev.* **2020**, *120*, 10695.

[17] A. D. Benjamin, R. Abbasi, M. Owens, R. J. Olsen, D. J. Walsh, T. B. LeFevre, J. N. Wilking, *Biomed. Phys. Eng. Express* **2019**, *5*, 25035.

[18] K. Arcaute, B. K. Mann, R. B. Wicker, *Ann. Biomed. Eng.* **2006**, *34*, 1429.

[19] P. F. Jacobs, *Rapid prototyping & manufacturing: fundamentals of stereolithography*, Society of Manufacturing Engineers **1992**.

[20] R. Chaudhary, P. Fabbri, E. Leoni, F. Mazzanti, R. Akbari, C. Antonini, *Prog. Addit. Manuf.* **2023**, *8*, 331.

[21] L. T. Nguyen, F. E. Du Prez, *Mater. Horiz.* **2024**, *11*, 6408.

[22] A. Faldi, M. Tirrell, T. P. Lodge, E. von Meerwall, *Macromolecules* **1994**, *27*, 4184.

[23] D. A. Walker, J. L. Hedrick, C. A. Mirkin, *Science* **2019**, *366*, 360.

[24] J. R. Tumbleston, D. Shirvanyants, N. Ermoshkin, R. Janusziewicz, A. R. Johnson, D. Kelly, K. Chen, R. Pinschmidt, J. P. Rolland, A. Ermoshkin, E. T. Samulski, J. M. DeSimone, *Science* **2015**, *347*, 1349.

[25] J. M. DeSimone, A. Ermoshkin, N. Ermoshkin, E. T. Samulski, *Continuous liquid interphase printing*, WO2014126837A2, Patent **2016**.

[26] P. N. Bernal, S. Florczak, S. Inacker, X. Kuang, J. Madrid-Wolff, M. Regehly, S. Hecht, Y. S. Zhang, C. Moser, R. Levato, *Nat. Rev. Mater.* **2025**.

[27] M. Regehly, Y. Garmshausen, M. Reuter, N. F. König, E. Israel, D. P. Kelly, C.-Y. Chou, K. Koch, B. Asfari, S. Hecht, *Nature* **2020**, *588*, 620.

[28] S. N. Sanders, T. H. Schloemer, M. K. Gangishetty, D. Anderson, M. Seitz, A. O. Gallegos, R. C. Stokes, D. N. Congreve, *Nature* **2022**, *604*, 474.

[29] B. E. Kelly, I. Bhattacharya, H. Heidari, M. Shusteff, C. M. Spadaccini, H. K. Taylor, *Science* **2019**, *363*, 1075.

[30] S. Maruo, O. Nakamura, S. Kawata, *Opt. Lett.* **1997**, *22*, 132.

[31] E. Skliutas, G. Merkininkaitė, S. Maruo, W. Zhang, W. Chen, W. Deng, J. Greer, G. von Freymann, M. Malinauskas, *Nat. Rev. Methods Primers* **2025**, *5*, 15.

[32] V. Hahn, F. Mayer, M. Thiel, M. Wegener, *Opt. Photonics News* **2019**, *30*, 28.

[33] M. Deubel, G. von Freymann, M. Wegener, S. Pereira, K. Busch, C. M. Soukoulis, *Nat. Mater.* **2004**, *3*, 444.

[34] S. O'Halloran, A. Pandit, A. Heise, A. Kellett, *Adv. Sci.* **2023**, *10*, e2204072.

[35] P. N. Prasad, B. A. Reinhardt, *Chem. Mater.* **1990**, *2*, 660.

[36] O. Stenzel, *Light–Matter Interaction*, Springer **2022**.

[37] F. Cantoni, D. Maher, E. Bosler, S. Kühne, L. Barbe, D. Oberschmidt, C. Marquette, R. Taboryski, M. Tenje, A.-I. Bunea, *Addit. Manuf.* **2023**, *76*, 103761.

[38] M. Thiel, H. Fischer, *Method and device for a spatially resolved introduction of an intensity pattern comprising electro-magnetic radiation into a photosensitive substance as well as applications thereof*, US20120218535A1, Patent **2016**.

[39] T. Koch, W. Zhang, T. T. Tran, Y. Wang, A. Mikitisin, J. Puchhammer, J. R. Greer, A. Ovsianikov, F. Chalupa-Gantner, M. Lunzer, *Adv. Mater.* **2024**, *36*, e2308497.

[40] C. Greant, B. van Durme, J. van Hoorick, S. van Vlierberghe, *Adv. Funct. Mater.* **2023**, *33*, 2212641.

[41] P. Kiefer, V. Hahn, M. Nardi, L. Yang, E. Blasco, C. Barner-Kowollik, M. Wegener, *Adv. Opt. Mater.* **2020**, *8*, 2000895.

[42] P. Müller, R. Müller, L. Hammer, C. Barner-Kowollik, M. Wegener, E. Blasco, *Chem. Mater.* **2019**, *31*, 1966.

[43] P. Kiefer, V. Hahn, S. Kalt, Q. Sun, Y. M. Eggeler, M. Wegener, *Light: Adv. Manuf.* **2024**, *4*, 1.

[44] P. Somers, S. Koch, P. Kiefer, M. L. Meretska, M. Wegener, *Opt. Mater. Express* **2024**, *14*, 2370.

[45] P. Somers, Z. Liang, J. E. Johnson, B. W. Boudouris, L. Pan, X. Xu, *Light Sci. Appl.* **2021**, *10*, 199.

[46] T. Aderneuer, O. Fernández, R. Ferrini, *Opt. Express* **2021**, *29*, 39511.

[47] W. H. Carothers, *Trans. Faraday Soc.* **1936**, *32*, 39.

[48] J. P. Fouassier, J. Lalevée, *Photoinitiators for Polymer Synthesis*, Wiley **2012**.

[49] A. Bagheri, J. Jin, *ACS Appl. Polym. Mater.* **2019**, *1*, 593.

[50] T.-L. Huang, Y.-C. Chen, *J. Photochem. Photobiol. A: Chem.* **2022**, *429*, 113900.

[51] Y. Bao, *Macromol. Rapid Commun.* **2022**, *43*, e2200202.

[52] T. Wloka, M. Gottschaldt, U. S. Schubert, *Chem. Eur. J.* **2022**, *28*, e202104191.

[53] T. H. Koch, A. H. Jones, *J. Am. Chem. Soc.* **1970**, *92*, 7503.

[54] A. Sharaf, J. P. Frimat, G. J. Kremers, A. Accardo, *Micro Nano Eng.* **2023**, *19*, 100188.

[55] S. C. Gauci, A. Vranic, E. Blasco, S. Bräse, M. Wegener, C. Barner-Kowollik, *Adv. Mater.* **2024**, *36*, e2306468.

[56] L. Chen, Q. Wu, G. Wei, R. Liu, Z. Li, *J. Mater. Chem. C* **2018**, *6*, 11561.

[57] A. B. Lowe, *Polym. Chem.* **2010**, *1*, 17.

[58] S. O. Catt, M. Hackner, J. P. Spatz, E. Blasco, *Small* **2023**, *19*, e2300844.

[59] A. Jaiswal, C. K. Rastogi, S. Rani, G. P. Singh, S. Saxena, S. Shukla, *iScience* **2023**, *26*, 106374.

[60] B. Weidinger, G. Yang, N. von Coelln, H. Nirschl, I. Wacker, P. Tegeder, R. R. Schröder, E. Blasco, *Adv. Sci.* **2023**, *10*, e2302756.

[61] J.-W. Kim, M. J. Allen, E. A. Recker, L. M. Stevens, H. L. Cater, A. Uddin, A. Gao, W. Eckstrom, A. J. Arrowood, G. E. Sanoja, M. A. Cullinan, B. D. Freeman, Z. A. Page, *Nat. Mater.* **2025**, *24*, 1116.

[62] K. S. Mason, J.-W. Kim, E. A. Recker, J. M. Nymick, M. Shi, F. A. Stolpen, J. Ju, Z. A. Page, *ACS Cent. Sci.* **2025**, *11*, 975.

[63] D. S. Branciforti, S. Lazzaroni, C. Milanese, M. Castiglioni, F. Auricchio, D. Pasini, D. Dondi, *Addit. Manuf.* **2019**, *25*, 317.

[64] B. Wu, A. Sufi, R. Ghosh Biswas, A. Hisatsune, V. Moxley-Paquette, P. Ning, R. Soong, A. P. Dicks, A. J. Simpson, *ACS Sustain. Chem. Eng.* **2020**, *8*, 1171.

[65] G. Zhu, H. A. Houck, C. A. Spiegel, C. Selhuber-Unkel, Y. Hou, E. Blasco, *Adv. Funct. Mater.* **2024**, *34*, 2300456.

[66] A. P. Dhand, R. H. Bean, V. Chiaradia, A. J. Commisso, D. Dranseike, H. E. Fowler, J. M. Fraser, H. Howard, T. Kaneko, J.-W. Kim, J. M. Kronenfeld, K. S. Mason, C. J. O'Dea, F. Pashley-Johnson, D. H. Porcincula, M. I. Segal, S. Yu, M. A. Saccone, *RSC Appl. Polym.* **2025**, *3*, 574.

[67] G. Altin-Yavuzarslan, S. M. Brooks, S.-F. Yuan, J. O. Park, H. S. Alper, A. Nelson, *Adv. Funct. Mater.* **2023**, *33*, 2300332.

[68] G. Altin-Yavuzarslan, N. Sadaba, S. M. Brooks, H. S. Alper, A. Nelson, *Small* **2024**, *20*, 2306564.

[69] R. Levato, O. Dudaryeva, C. E. Garciamendez-Mijares, B. E. Kirkpatrick, R. Rizzo, J. Schimelman, K. S. Anseth, S. Chen, M. Zenobi-Wong, Y. S. Zhang, *Nat. Rev. Methods Primers* **2023**, *3*.

[70] Y. Li, R. K. Kankala, L. Wu, A.-Z. Chen, S.-B. Wang, *ACS Appl. Polym. Mater.* **2023**, *5*, 991.

[71] C. Lu, X. Wang, Q. Jia, S. Xu, C. Wang, S. Du, J. Wang, Q. Yong, F. Chu, *Carbohydr. Polym.* **2024**, *324*, 121496.

[72] L. Cai, G. Chen, B. Su, M. He, *Chem. Eng. J.* **2021**, *426*, 130545.

[73] L. Cai, G. Chen, J. Tian, B. Su, M. He, *Chem. Mater.* **2021**, *33*, 2072.

[74] C. Zhang, H. Zheng, J. Sun, Y. Zhou, W. Xu, Y. Dai, J. Mo, Z. Wang, *Adv. Mater.* **2022**, *34*, 2105996.

[75] E. L. Smith, A. P. Abbott, K. S. Ryder, *Chem. Rev.* **2014**, *114*, 11060.

[76] B. B. Hansen, S. Spittle, B. Chen, D. Poe, Y. Zhang, J. M. Klein, A. Horton, L. Adhikari, T. Zelovich, B. W. Doherty, B. Gurkan, E. J. Maginn, A. Ragauskas, M. Dadmun, T. A.

Zawodzinski, G. A. Baker, M. E. Tuckerman, R. F. Savinell, J. R. Sangoro, *Chem. Rev.* **2021**, *121*, 1232.

[77] J. Wang, S. Zhang, Z. Ma, L. Yan, *Green Chem. Eng.* **2021**, *2*, 359.

[78] P. Mainik, C. A. Spiegel, E. Blasco, *Adv. Mater.* **2024**, *36*, e2310100.

[79] M. Carlotti, V. Mattoli, *Small* **2019**, *15*, e1902687.

[80] C. A. Spiegel, M. Hippler, A. Münchinger, M. Bastmeyer, C. Barner-Kowollik, M. Wegener, E. Blasco, *Adv. Funct. Mater.* **2020**, *30*, 1907615.

[81] M. Wei, Y. Gao, X. Li, M. J. Serpe, *Polym. Chem.* **2017**, *8*, 127.

[82] S. Tibbits, *Archit. Des.* **2014**, *84*, 116.

[83] M. Behl, A. Lendlein, *Mater. Today* **2007**, *10*, 20.

[84] L. V. Elliott, E. E. Salzman, J. R. Greer, *Adv. Funct. Mater.* **2021**, *31*, 2008380.

[85] C. A. Spiegel, M. Hackner, V. P. Bothe, J. P. Spatz, E. Blasco, *Adv. Funct. Mater.* **2022**, *32*, 2110580.

[86] K. M. Herbert, H. E. Fowler, J. M. McCracken, K. R. Schlafmann, J. A. Koch, T. J. White, *Nat. Rev. Mater.* **2022**, *7*, 23.

[87] E. M. Terentjev, *Macromolecules* **2025**, *58*, 2792.

[88] Z. Huang, G. C.-P. Tsui, K.-W. Yeung, C. Li, C.-Y. Tang, M. Yang, M. Zhang, W.-Y. Wong, *Mater. Des.* **2023**, *232*, 112101.

[89] L.-Y. Hsu, P. Mainik, A. Münchinger, S. Lindenthal, T. Spratte, A. Welle, J. Zaumseil, C. Selhuber-Unkel, M. Wegener, E. Blasco, *Adv. Mater. Technol.* **2023**, *8*, 2200801.

[90] S. Woska, A. Münchinger, D. Beutel, E. Blasco, J. Hessenauer, O. Karayel, P. Rietz, S. Pfleging, R. Oberle, C. Rockstuhl, M. Wegener, H. Kalt, *Opt. Mater. Express* **2020**, *10*, 2928.

[91] H. Zeng, D. Martella, P. Wasylczyk, G. Cerretti, J.-C. G. Lavocat, C.-H. Ho, C. Parmeggiani, D. S. Wiersma, *Adv. Mater.* **2014**, *26*, 2319.

[92] H. Zeng, P. Wasylczyk, C. Parmeggiani, D. Martella, M. Burresi, D. S. Wiersma, *Adv. Mater.* **2015**, *27*, 3883.

[93] A. Münchinger, V. Hahn, D. Beutel, S. Woska, J. Monti, C. Rockstuhl, E. Blasco, M. Wegener, *Adv. Mater. Technol.* **2022**, *7*, 2100944.

[94] A. Münchinger, L.-Y. Hsu, F. Fürniß, E. Blasco, M. Wegener, *Mater. Today* **2022**, *59*, 9.

[95] M. Del Pozo, C. Delaney, C. W. M. Bastiaansen, D. Diamond, A. P. H. J. Schenning, L. Florea, *ACS nano* **2020**, *14*, 9832.

[96] M. Neumann, G. Di Marco, D. Iudin, M. Viola, C. F. van Nostrum, B. G. P. van Ravensteijn, T. Vermonden, *Macromolecules* **2023**, *56*, 8377.

[97] L. Ionov, *Mater. Today* **2014**, *17*, 494.

[98] M. C. Koetting, J. T. Peters, S. D. Steichen, N. A. Peppas, *Mater. Sci. Eng. R Rep.* **2015**, *93*, 1.

[99] Y.-W. Lee, J.-K. Kim, U. Bozuyuk, N. O. Dogan, M. T. A. Khan, A. Shiva, A.-M. Wild, M. Sitti, *Adv. Mater.* **2023**, *35*, e2209812.

[100] H. G. Schild, *Prog. Polym. Sci.* **1992**, *17*, 163.

[101] M. Hippler, E. Blasco, J. Qu, M. Tanaka, C. Barner-Kowollik, M. Wegener, M. Bastmeyer, *Nat. Commun.* **2019**, *10*, 232.

[102] C. Barwig, A. Sonn, T. Spratte, A. Mishra, E. Blasco, C. Selhuber-Unkel, S. Pashapour, *Adv. Intell. Syst.* **2024**, *6*, 2300829.

[103] T. Spratte, S. Geiger, F. Colombo, A. Mishra, M. Taale, L.-Y. Hsu, E. Blasco, C. Selhuber-Unkel, *Adv. Mater. Technol.* **2023**, *8*, 2200714.

[104] H. B. D. Tran, C. A. Spiegel, E. Blasco, *Macromol. Mater. Eng.* **2025**.

[105] M. Hippler, K. Weißenbruch, K. Richler, E. D. Lemma, M. Nakahata, B. Richter, C. Barner-Kowollik, Y. Takashima, A. Harada, E. Blasco, M. Wegener, M. Tanaka, M. Bastmeyer, *Sci. Adv.* **2020**, *6*.

[106] D. F. Williams, *Biomaterials* **2009**, *30*, 5897.

[107] M. Wang, B. Duan, *Encyclopedia of Biomedical Engineering: Materials and Their Biomedical Applications*, Elsevier **2019**.

[108] L. Crawford, M. Wyatt, J. Bryers, B. Ratner, *Adv. Healthc. Mater.* **2021**, *10*, e2002153.

[109] R. Srinivasaraghavan Govindarajan, S. Sikulskyi, Z. Ren, T. Stark, D. Kim, *Polymers* **2023**, *15*.

[110] O. Eivgi, C. Vazquez-Martel, J. Lukeš, E. Blasco, *Small methods* **2025**.

[111] P. F. J. van Altena, A. Accardo, *Polymers* **2023**, *15*.

[112] Nanoscribe GmbH, *IP-PDMS ink: https://www.nanoscribe.com/en/products/ip-photoresins/ip-pdms/*, Last Access: August 2025.

[113] F. Colombo, M. Taale, F. Taheri, M. Villiou, T. Debatin, G. Dulatahu, P. Kollenz, M. Schmidt, C. Schlagheck, J. Wittbrodt, C. Selhuber-Unkel, *Adv. Funct. Mater.* **2024**, *34*, 2303601.

[114] N. Munding, M. Fladung, Y. Chen, M. Hippler, A. D. Ho, M. Wegener, M. Bastmeyer, M. Tanaka, *Adv. Funct. Mater.* **2024**, *34*, 2301133.

[115] J. Liu, H. Zheng, P. S. P. Poh, H.-G. Machens, A. F. Schilling, *Int. J. Mol. Sci.* **2015**, *16*, 15997.

[116] A. Dobos, J. van Hoorick, W. Steiger, P. Gruber, M. Markovic, O. G. Andriotis, A. Rohatschek, P. Dubruel, P. J. Thurner, S. van Vlierberghe, S. Baudis, A. Ovsianikov, *Adv. Healthc. Mater.* **2020**, *9*, e1900752.

[117] N. Schwegler, T. Gebert, M. Villiou, F. Colombo, B. Schamberger, C. Selhuber-Unkel, F. Thomas, E. Blasco, *Small* **2024**, *20*, e2401344.

[118] C. Peters, M. Hoop, S. Pané, B. J. Nelson, C. Hierold, *Adv. Mater.* **2016**, *28*, 533.

[119] D. Sivun, E. Murtezi, T. Karimian, K. Hurab, M. Marefat, E. Klimareva, C. Naderer, B. Buchroithner, T. A. Klar, G. Gvindzhiliia, A. Horner, J. Jacak, *Mater. Today Bio* **2024**, *25*, 100994.

[120] T. Abele, T. Messer, K. Jahnke, M. Hippler, M. Bastmeyer, M. Wegener, K. Göpfrich, *Adv. Mater.* **2022**, *34*, e2106709.

[121] B.-M. Chen, T.-L. Cheng, S. R. Roffler, *ACS nano* **2021**, *15*, 14022.

[122] Y. Ju, W. S. Lee, E. H. Pilkington, H. G. Kelly, S. Li, K. J. Selva, K. M. Wragg, K. Subbarao, T. H. O. Nguyen, L. C. Rowntree, L. F. Allen, K. Bond, D. A. Williamson, N. P. Truong, M. Plebanski, K. Kedzierska, S. Mahanty, A. W. Chung, F. Caruso, A. K. Wheatley, J. A. Juno, S. J. Kent, *ACS nano* **2022**, *16*, 11769.

[123] C. Frantz, K. M. Stewart, V. M. Weaver, *J. Cell Sci.* **2010**, *123*, 4195.

[124] K. Yue, G. Trujillo-de Santiago, M. M. Alvarez, A. Tamayol, N. Annabi, A. Khademhosseini, *Biomaterials* **2015**, *73*, 254.

[125] D. Elieh-Ali-Komi, M. R. Hamblin, *Int. J. Adv. Res.* **2016**, *4*, 411.

[126] G. N. Iaconisi, P. Lunetti, N. Gallo, A. R. Cappello, G. Fiermonte, V. Dolce, L. Capobianco, *Int. J. Mol. Sci.* **2023**, *24*.

[127] M. Rothammer, M.-C. Heep, G. von Freymann, C. Zollfrank, *Cellulose* **2018**, *25*, 6031.

[128] H. Yu, J. Liu, Y.-Y. Zhao, F. Jin, X.-Z. Dong, Z.-S. Zhao, X.-M. Duan, M.-L. Zheng, *ACS Appl. Bio Mater.* **2019**, *2*, 3077.

[129] O. Kufelt, A. El-Tamer, C. Sehring, S. Schlie-Wolter, B. N. Chichkov, *Biomacromolecules* **2014**, *15*, 650.

[130] O. Kufelt, A. El-Tamer, C. Sehring, M. Meißner, S. Schlie-Wolter, B. N. Chichkov, *Acta Biomater.* **2015**, *18*, 186.

[131] U. Bozuyuk, O. Yasa, I. C. Yasa, H. Ceylan, S. Kizilel, M. Sitti, *ACS nano* **2018**, *12*, 9617.

[132] A. Berg, R. Wyrwa, J. Weisser, T. Weiss, R. Schade, G. Hildebrand, K. Liefeith, B. Schneider, R. Ellinger, M. Schnabelrauch, *Adv. Eng. Mater.* **2011**, *13*.

[133] X.-H. Qin, P. Gruber, M. Markovic, B. Plochberger, E. Klotzsch, J. Stampfl, A. Ovsianikov, R. Liska, *Polym. Chem.* **2014**, *5*, 6523.

[134] E. Armingol, A. Officer, O. Harismendy, N. E. Lewis, *Nat. Rev. Genet.* **2021**, *22*, 71.

[135] J. Nicolas, S. Magli, L. Rabbachin, S. Sampaolesi, F. Nicotra, L. Russo, *Biomacromolecules* **2020**, *21*, 1968.

[136] K. Tarnutzer, D. Siva Sankar, J. Dengjel, C. Y. Ewald, *Sci. Rep.* **2023**, *13*, 4490.

[137] J. Sapudom, S. Karaman, B. C. Quartey, W. K. E. Mohamed, N. Mahtani, A. Garcia-Sabaté, J. Teo, *Adv. Sci.* **2023**, *10*, e2301353.

[138] C. Jiang, A. Centonze, Y. Song, A. Chrisnandy, E. Tika, S. Rezakhani, Z. Zahedi, G. Bouvencourt, C. Dubois, A. van Keymeulen, M. Lütolf, A. Sifrim, C. Blanpain, *Nat. Commun.* **2024**, *15*, 10482.

[139] M. Meyer, *Biomed. Eng. Online* **2019**, *18*, 24.

[140] B. P. Carr, Z. Chen, J. H. Y. Chung, G. G. Wallace, *Polymers* **2022**, *14*, 4270.

[141] X. Zhang, S. Xu, L. Shen, G. Li, *J. Leather Sci. Eng.* **2020**, *2*, 19.

[142] J. P. R. O. Orgel, T. C. Irving, A. Miller, T. J. Wess, *Proc. Natl. Acad. Sci. U.S.A.* **2006**, *103*, 9001.

[143] C. Zapp, A. Obarska-Kosinska, B. Rennekamp, M. Kurth, D. M. Hudson, D. Mercadante, U. Barayeu, T. P. Dick, V. Denysenkov, T. Prisner, M. Bennati, C. Daday, R. Kappl, F. Gräter, *Nat. Commun.* **2020**, *11*, 2315.

[144] A. Gautieri, A. Russo, S. Vesentini, A. Redaelli, M. J. Buehler, *J. Chem. Theory Comput.* **2010**, *6*, 1210.

[145] J.-D. Malcor, N. Ferruz, S. Romero-Romero, S. Dhingra, V. Sagar, A. A. Jalan, *ACS Appl. Polym. Mater.* **2025**, *16*, 2702.

[146] E. E. Antoine, P. P. Vlachos, M. N. Rylander, *Tissue Eng. Part B Rev.* **2014**, *20*, 683.

[147] J. Gross, D. Kirk, *J. Biol. Chem.* **1958**, *233*, 355.

[148] E. O. Osidak, V. I. Kozhukhov, M. S. Osidak, S. P. Domogatsky, *Int. J. Bioprinting* **2020**, *6*, 270.

[149] A. Bell, M. Kofron, V. Nistor, *Biofabrication* **2015**, *7*, 35007.

[150] L. P. Cunningham, M. P. Veilleux, P. J. Campagnola, *Opt. Express* **2006**, *14*, 8613.

[151] L. Tytgat, M. Markovic, T. H. Qazi, M. Vagenende, F. Bray, J. C. Martins, C. Rolando, H. Thienpont, H. Ottevaere, A. Ovsianikov, P. Dubruel, S. van Vlierberghe, *J. Mater. Chem. B* **2019**, *7*, 3100.

[152] A. Shrestha, B. N. Allen, L. A. Wiley, B. A. Tucker, K. S. Worthington, *J. Ocul. Pharmacol. Ther.* **2020**, *36*, 42.

[153] D. Liu, M. Nikoo, G. Boran, P. Zhou, J. M. Regenstein, *Annu. Rev. Food Sci. Technol.* **2015**, *6*, 527.

[154] R. Schrieber, H. Gareis, *Gelatine Handbook*, Wiley **2007**.

[155] A. Ovsianikov, A. Deiwick, S. van Vlierberghe, P. Dubruel, L. Möller, G. Dräger, B. Chichkov, *Biomacromolecules* **2011**, *12*, 851.

[156] A. Ovsianikov, S. Mühleder, J. Torgersen, Z. Li, X.-H. Qin, S. van Vlierberghe, P. Dubruel, W. Holnthoner, H. Redl, R. Liska, J. Stampfl, *Langmuir* **2014**, *30*, 3787.

[157] F. A. Pennacchio, C. Fedele, S. de Martino, S. Cavalli, R. Vecchione, P. A. Netti, *ACS Appl. Mater. Interfaces* **2018**, *10*, 91.

[158] D. Gong, N. Celi, L. Xu, D. Zhang, J. Cai, *Mater. Today Chem.* **2022**, *23*, 100694.

[159] X. Wang, X.-H. Qin, C. Hu, A. Terzopoulou, X.-Z. Chen, T.-Y. Huang, K. Maniura-Weber, S. Pané, B. J. Nelson, *Adv. Funct. Mater.* **2018**, *28*, 1804107.

[160] K. A. Omar, R. Sadeghi, *J. Mol. Liq.* **2023**, *384*, 121899.

[161] J. Cao, E. Su, *J. Clean. Prod.* **2021**, *314*, 127965.

[162] E. G. Norris, D. Dalecki, D. C. Hocking, *Mater. Today Bio* **2019**, *3*, 100018.

[163] F. Nudelman, A. J. Lausch, N. A. J. M. Sommerdijk, E. D. Sone, *J. Struct. Biol.* **2013**, *183*, 258.

[164] F. W. Kotch, R. T. Raines, *Proc. Natl. Acad. Sci. U.S.A.* **2006**, *103*, 3028.

NATURWISSENSCHAFTLICH-MATHEMATISCHE GESAMTFAKULTÄT

COMBINED FACULTY OF NATURAL SCIENCES AND MATHEMATICS

RUPRECHT-KARLS-
UNIVERSITÄT
HEIDELBERG

Eidesstattliche Versicherung gemäß § 8 der Promotionsordnung für die Naturwissenschaftlich-Mathematische Gesamtfakultät der Universität Heidelberg / Sworn Affidavit according to § 8 of the doctoral degree regulations of the Combined Faculty of Natural Sciences and Mathematics

1. Bei der eingereichten Dissertation zu dem Thema / The thesis I have submitted entitled

   3D/4D microprinting of biomaterials

   handelt es sich um meine eigenständig erbrachte Leistung / is my own work.

2. Ich habe nur die angegebenen Quellen und Hilfsmittel (inkl. KI-basierter Hilfsmittel) benutzt und mich keiner unzulässigen Hilfe Dritter bedient. Insbesondere habe ich wörtlich oder sinngemäß aus anderen Werken übernommene Inhalte als solche kenntlich gemacht. / I have only used the sources indicated (incl. AI-based tools) and have not made unauthorised use of services of a third party. Where the work of others has been quoted or reproduced, the source is always given.

3. Die Arbeit oder Teile davon habe ich wie folgt/bislang nicht[1)] an einer Hochschule des In- oder Auslands als Bestandteil einer Prüfungs- oder Qualifikationsleistung vorgelegt. / I have not yet/have already[1)] presented this thesis or parts thereof to a university as part of an examination or degree.

   Titel der Arbeit / Title of the thesis: 3D/4D microprinting of biomaterials

   Hochschule und Jahr / University and year: Universität Heidelberg, 2025

   Art der Prüfungs- oder Qualifikationsleistung / Type of examination or degree: Promotion

4. Die Richtigkeit der vorstehenden Erklärungen bestätige ich. / I confirm that the declarations made above are correct.

5. Die Bedeutung der eidesstattlichen Versicherung und die strafrechtlichen Folgen einer unrichtigen oder unvollständigen eidesstattlichen Versicherung sind mir bekannt. / I am aware of the importance of a sworn affidavit and the criminal prosecution in case of a false or incomplete affidavit

Ich versichere an Eides statt, dass ich nach bestem Wissen die reine Wahrheit erklärt und nichts verschwiegen habe. / I affirm that the above is the absolute truth to the best of my knowledge and that I have not concealed anything.

Heidelberg, 08.08.2025
Ort und Datum / Place and date

.....
Unterschrift / Signature

[1)] Nicht Zutreffendes streichen. Bei Bejahung sind anzugeben: der Titel der andernorts vorgelegten Arbeit, die Hochschule, das Jahr der Vorlage und die Art der Prüfungs- oder Qualifikationsleistung. / Please cross out what is not applicable. If applicable, please provide: the title of the thesis that was presented elsewhere , the name of the university, the year of presentation and the type of examination or degree.

The German text is legally binding.